Non Gravitational Heating Mechanisms in Galaxy Clusters

Dissertation der Fakultät für Physik
der
Ludwig-Maximilians-Universität München

vorgelegt von Debora Šijački
aus Belgrad, Serbien

München, den 25. März 2007

Non Gravitational Heating Mechanisms in Galaxy Clusters

Dissertation der Fakultät für Physik
der
Ludwig-Maximilians-Universität München

vorgelegt von Debora Šijački
aus Belgrad, Serbien

München, den 25. März 2007

Erstgutachter:	Prof. Dr. Simon D. M. White
Zweitgutachter:	Prof. Dr. Hans Böhringer
Tag der mündlichen Prüfung:	17. September 2007

Mojim dragim roditeljima i mojoj baki Desi
za svu ljubav, podršku i razumevanje
tokom svih ovih godina

Contents

Zusammenfassung

Das Studium der kosmischen Strukturbildung ist eines der faszinierendsten Felder der modernen Astrophysik und zugleich eine enorme Herausforderung. Im derzeit favorisierten kosmologischen Modell, der sogenannten ΛCDM Kosmogonie, wachsen die Strukturen der Dunklen Materie hierarchisch, wobei sich in der frühesten Epoche zuerst nur kleine Klumpen bilden. Das darauffolgende Verschmelzen dieser Halos dunkler Materie führt in weiterer Folge zur Bildung immer massiverer Objekte, die schlußendlich ein komplexes kosmisches Netzwerk aus Filamenten, Galaxienhaufen und Voids, kosmischen Hohlräumen dazwischen, bilden. Wir wissen zwar relativ gut, wie sich diese Dunkle-Materie Strukturen mit der Zeit entwickeln, der Zusammenhang zwischen der "dunklen" und der "leuchtenden" Materie im Universum ist jedoch nach wie vor bei weitem nicht verstanden und wirft viele noch ungelöste Fragen auf, für theoretische Untersuchungen genauso wie für die beobachtende Astronomie. Galaxienhaufen (engl.: cluster), die größten virialisierten Objekte im Universum, sind besonders interessante Studienobjekte, denn sie stellen ideale Laboratorien für die Untersuchung der physikalischen Prozesse, welche in der Strukturbildung eine Rolle spielen, dar. So etwa jener Prozesse, die die Eigenschaften von Galaxien, dem intergalaktischen und intracluster Medium (IGM) und aktiver Galaxienkerne (engl.: active galactic nuclei, AGN) bestimmen. Letztere haben ihren Ursprung in supermassiven Schwarzen Löchern, die sich im Zentrum des Galaxienhaufens befinden. Gerade heute ist die Untersuchung von Galaxienhaufen besonders vielversprechend, zum einen aufgrund der Fülle neuer Daten von Röntgenteleskopen wie XMM-Newton und Chandra oder von optischen Durchmusterungen wie dem SDSS, und zum anderen dank der neuen Möglichkeiten durch Computersimulationen als theoretisches Werkzeug. Diese können die Bildung kosmologischer Strukturen weit in das nichtlineare Regime hinein nachvollziehen und sind neuerdings zuverlässig genug, daß zum erstenmal physikalische Prozesse wie AGN Aktivität und deren Effekt auf die Galaxienentwicklung miteinbezogen werden können.

Ziel dieser Dissertation war es, den Prozeß der AGN verursachten Aufheizung des intracluster Mediums in selbst-konsistente Simulationen der kosmologischen Strukturbildung zu integrieren und die Bedeutung dieses Rückkopplungsmechanismus für die Bildung und Entwicklung von Galaxien und Galaxienhaufen zu erforschen. Im ersten Teil meiner Arbeit diskutiere ich ein phänomenologisches Modell für die Aufheizung des Zentrums von Galaxienhaufen durch heiße Blasen, die wiederholt von den AGN ausgehen. Numerische Vorhersagen dieses Modells weisen darauf hin, daß solche heißen Gasblasen, die leichter als ihre Umgebung sind und im IGM aufsteigen, eine energetisch plausible Lösung des sogenannten "Cooling Flow" Problems darstellen und somit die Eigenschaften simulierter Galaxienhaufen deutlich verbessern. Eine weitere Erkenntnis daraus war, daß ein aufgrund der lokalen Gaseigenschaften sich selbst regulierender Rückkopplungsmechnismus vonnöten ist, um das Zusammenspiel zwischen AGN und ihrer Umgebung zu verstehen. Darüberhinaus

müssen Transportprozesse wie z.B. Viskosität zuverlässiger modelliert werden, da sie einen wichtigen Mechanismus zur Wärmeableitung der von den AGN ausgehenden thermischen Energie in das umgebende IGM darstellen könnten.

Daher habe ich im zweiten Teil meiner Dissertation die selbst-konsistente Modellierung eines viskosen Fluidums im Simulationscode implementiert und in weiterer Folge auf die Gasatmosphäre von Galaxienhaufen angewendet. Konkret habe ich die Effizienz der Aufheizung des Gases durch AGN als Funktion der intracluster Viskosität untersucht und dabei gefunden, daß Wärmedissipation durch Viskosität tatsächlich einen wichtigen nicht-lokalen Aufheizungsmechanismus im Zentrum von Galaxienhaufen darstellt. Desweiteren schwächt eine höhere Gasviskosität mögliche Strömungsinstabilitäten ab, was zu einer erhöhten Lebensdauer der vom AGN erzeugten heißen Gasblasen führt, wodurch diese eine größere Entfernung vom Haufenzentrum erreichen. Damit stimmen die Simulationsergebnisse recht gut mit den Beobachtungen überein.

Schlußendlich habe ich im dritten Teil meiner Dissertation ein verfeinertes Modell für die AGN bedingten Rückkopplungsmechnismen in kosmologischen Simulationen der Strukturbildung entwickelt. Dabei wird die Bildung und das Wachstum von schwarzen Löchern (engl.: black holes, BH) als selbst-regulierende Rückkopplungsschleife beschrieben, in der die Aufheizung durch den AGN von der Akkretionsrate des schwarzen Loches abhängt. Zwei unterschiedliche Arten von Rückkopplung wurden realisiert: eine für BHs mit hoher Akkretionsrate welche sich als Quasare manifestieren und eine für BHs mit deutlich niedrigerer Akkretion, jedoch mit trotzdem beträchtlicher mechanischer Leistung. Diese neuartige Implementierung stellt ein sehr mächtiges Werkzeug dar, mit dem zum erstenmal mittels hydrodynamischer Simulationen die gemeinsame Entwicklung von schwarzen Löchern und dem Galaxienhaufen in den sie eingebettet sind im vollen kosmologischen Kontext untersucht werden kann. Die bisherigen Ergebnisse können als sehr vielversprechend angesehen werden. Die vorhergesagte Population schwarzer Löcher ist realistisch und die Eigenschaften der simulierten Galaxien stimmen viel besser mit den Beobachtungen überein als bisher. Desweiteren wird die beobachtete Relation zwischen der Masse und der stellaren Geschwindigkeitsdispersion korrekt reproduziert. Womit bestätigt wird, daß ein Modell der Galaxienevolution die Bildung und Entwicklung schwarzer Löcher und gleichzeitig die dadurch bedingten Rückkopplungseffekte beinhalten muß, um erfolgreich zu sein.

Summary

The study of the formation and growth of cosmic structures is one of the most fascinating and challenging fields of astrophysics. In the currently favoured cosmological model, the so-called ΛCDM cosmogony, dark matter structures grow hierarchically, with small clumps forming first at very early epochs. The merging of these dark matter halos in the following evolution leads to the formation of more massive objects with time, ultimately resulting in a complex cosmic web composed of filaments of dark matter and galaxies, rich galaxy clusters, and voids in between. While we have some knowledge how these dark matter structures evolve with cosmic time, the relationship between the "dark" and the "luminous" content of the Universe is still far from being fully understood and it poses many puzzling questions, both for observational and theoretical investigations. Galaxy clusters, the largest virialized objects in the Universe, are especially interesting for cosmological studies because they are ideal laboratories to study the physical processes relevant in structure formation, like those that shape the properties of galaxies, the intergalactic and intracluster media, and the active galactic nuclei (AGN) that originate from supermassive black holes (BHs) in cluster centres. The study of clusters is remarkably promising right now, both because of the wealth of new data from X-ray telescopes such as XMM-Newton and Chandra or from optical surveys such as SDSS, and also due to the increasing power of cosmological simulations as a theoretical tool. The latter can track the growth of cosmological structures far into the highly non-linear regime, and have recently become faithful enough to include for the first time physical processes such as AGN activity and its effect on galaxy evolution.

The aim of this Thesis was to incorporate AGN heating process in fully self-consistent cosmological simulations of structure formation, and to constrain the relevance of this feedback mechanism for galaxy and galaxy cluster formation and evolution. In the first part of the Thesis I have discussed a phenomenological model for AGN heating in galaxy cluster cores. This model was designed to address the question of cooling flows in massive galaxy clusters by heating the innermost regions with recurrent, hot AGN-driven bubbles. Numerical results from this model have indicated that AGN heating, in the form of buoyant bubbles, provides an energetically plausible solution to the cooling flow problem, improving in a number of ways the properties of simulated galaxy clusters. On the other hand, from this study it emerged that a self-regulated feedback mechanism, sensitive to the local gas properties, is needed to address with a greater realism how AGN interact with their surroundings. Furthermore, the relevance of transport processes, such as viscosity, had to be explored rigorously, because it may represent a mechanism needed for coupling the heat into the intracluster medium.

Hence, in the second part of the Thesis I have developed a self-consistent treatment for viscous fluids and incorporated in the simulation code, which I then applied to gaseous

cluster atmospheres. I have analyzed the AGN heating efficiency as a function of the intracluster viscosity, finding that viscous dissipation processes indeed provide a non-local heating mechanism in cluster cores. Moreover, an increased gas viscosity changes the properties of AGN-driven bubbles, since it stabilizes them against fluid instabilities, and thus increases their life-time and maximum cluster-centric distance reached, bringing the simulations in broad agreement with observational findings.

Finally, in the third part of my Thesis, I have explored a more sophisticated model of AGN feedback in cosmological simulations of structure formation. In this novel implementation, a prescription for BH seeding and growth has been developed which allows for a self-regulated feedback loop where AGN heating depends on the amount of gas that is accreted by the BH. Two distinct modes of feedback have been incorporated: one corresponding to BHs with high accretion rates that shine as bright quasars, and the other to BHs growing at much reduced rates, but having significant mechanical luminosity. This novel AGN prescription represents a very powerful tool to analyze, for the first time, the joint evolution of BHs and their hosts with hydrodynamical simulations in the full cosmological framework. The first results obtained can be considered rather promising. A realistic population of BHs is produced, and the properties of simulated host galaxies are in much better agreement with observations. Also, the observed relationship between black hole mass and stellar velocity dispersion is reproduced. This confirms that successful models for galaxy formation need to simultaneously treat the build up of supermassive black holes and account for their feedback effects.

1 Introduction

1.1 Cosmic structure formation

Remarkable progress in observational cosmology has revolutionized our understanding of the observable Universe, leading to the establishment of a standard model for cosmic structure formation[1]:

i) The dynamics of the Universe is described by Einstein's theory of general relativity, and the mass distribution of the Universe on large scales is fairly homogeneous. Thus, the spacetime metric of the Universe can be described by the Robertson-Walker metric and its dynamical evolution by Friedman models, as I will discuss more in detail in the next section.

ii) The Universe started with a rapid expansion from a very hot and dense state. Crucial information about this early phase is locked-up in the cosmic microwave background (CMB) radiation, which is permeating the Universe and is well described by thermal blackbody radiation. The CMB provides direct evidence for the hot Big Bang model. In the last years, several experiments, among them COBE, BOOMERanG and WMAP, have successfully measured tiny fluctuations in the temperature map of the last scattering surface of the CMB, which in turn allowed a determination of the primary cosmological parameters with good quantitative accuracy. Together with independent measurements obtained from galaxy clustering and distant type Ia supernovae, a consistent "concordance" model of cosmology has emerged. The total density parameter in this model, expressed in units of the critical density, is very close to unity, i.e. the geometry of space is flat, as predicted by inflationary models.

The contribution of the baryonic matter is only $\Omega_b \sim 0.04$, in good agreement with Big Bang nucleosynthesis predictions. On the other hand, dynamical estimates of the

[1] A comprehensive overview of the standard cosmological model can be found in several cosmology textbooks, e.g. Peebles [1980, 1993], Padmanabhan [1993], Coles and Lucchin [1995], Peacock [1999].

matter density parameter require a higher value, of the order of ~ 0.3. This discrepancy is reconciled by the introduction of non-baryonic dark matter, which in the currently favoured cold dark matter (CDM) model is weakly interacting (effectively being collisionless) and has negligible thermal velocities at the time of decoupling. However, up to the present day, we have no certainty about the physical identity of the dark matter particle, apart from knowing its basic properties, namely that it should be collisionless and heavy enough to be non-relativistic. The nature of the dark matter is one of the most important open questions in modern cosmology.

Finally, to explain the difference between the matter density parameter $\Omega_{\rm m}$ and the flat geometry of the Universe, a dark energy component Ω_Λ is invoked in the standard model, which is smoothly distributed, is important only on large scales and has a negative pressure, which actually lets it accelerate the expansion of the Universe! The simplest theory incorporating effects of such a component is the ΛCDM model, a model with a cosmological constant. Unfortunately, the nature of the dark energy is even less clear than that of the dark matter, posing a fundamental puzzle for field theories. Nevertheless, trying to obtain empirical constraints for the time evolution of the dark energy has become a very active field in cosmology. In Figure 1.1, a compilation of current observational constraints on the cosmological density parameters in the $\Omega_{\rm m} - \Omega_\Lambda$ plane is shown. The constraints from supernovae [Riess et al., 2004], CMB data [Spergel et al., 2003], and galaxy clusters [Schuecker et al., 2003] all intersect at a consistent place, that of the concordance cosmology.

iii) Cosmic structures form via gravitational instability in a bottom-up fashion. Quantum fluctuations amplified during inflation provide the seeds from which cosmic structures have formed. In the CMB, density fluctuations of order of 10^{-5} at redshift of $z \sim 1100$ have been detected which correspond to these seeds. Given their tiny density contrast, the initial growth of cosmic structures can be described well by linear perturbation theory. However, cosmic structures today are highly non linear. One of the primary goals of cosmology is to understand in detail how the multitude and richness of locally observed galaxies, massive galaxy clusters and filaments has arisen from such small seeds. The driving process for structure formation is gravity, but if we wish to understand all aspects of the evolution, growth and properties of cosmic structures a highly intricate and complex array of additional physical processes needs to be considered.

1.1.1 The homogeneous Universe

One of the fundamental assumptions in cosmology is the *cosmological principle*: on large enough scales, the Universe is approximately homogeneous and isotropic, i.e. there are no preferred direction or spatial locations. While a look towards the Milky Way on a starry night will convince us that this obviously is not the case locally, the large-scale distribution of galaxies and galaxy clusters appears fairly homogeneous and isotropic on scales above $\sim 100\,{\rm Mpc}$, despite forming an intricate cosmic web on smaller scales. The most stringent observational peace of evidence supporting the cosmological principle is the detected high degree of isotropy of the CMB, which only exhibits temperature fluctuations of order $\delta T/T \sim 10^{-5}$ once the dipole of our peculiar motion relative to the CMB is subtracted.

Assuming that the cosmological principle holds, the spacetime metric of the Universe is given by the Robertson-Walker metric, viz.

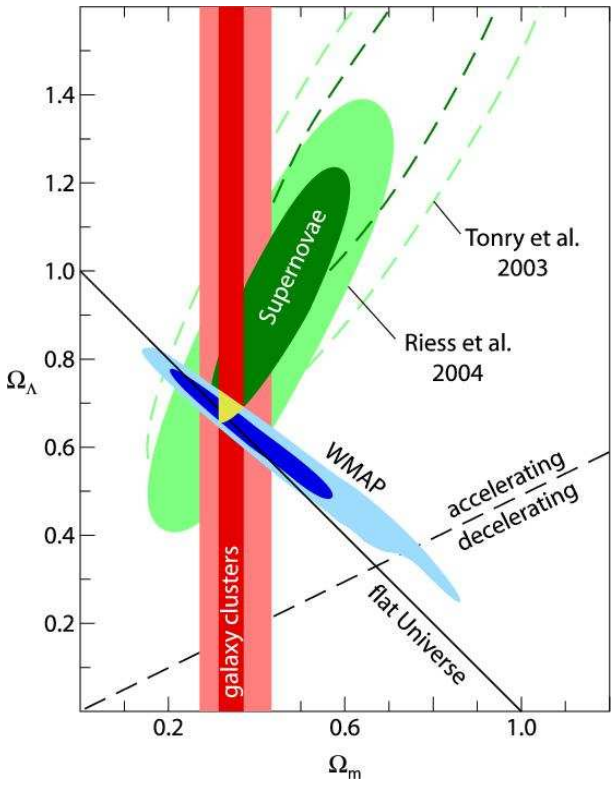

Figure 1.1: Cosmological constraints in the $\Omega_\mathrm{m} - \Omega_\Lambda$ plane. The three data sets shown, based on supernovae, CMB and galaxy cluster measurements, provide completely independent methods to determine the cosmological parameters.

$$\mathrm{d}s^2 \;=\; (c\,\mathrm{d}t)^2 - a(t)^2\left[\frac{\mathrm{d}r^2}{1-Kr^2} + r^2(\mathrm{d}\theta^2 + sin^2\theta\,\mathrm{d}\phi^2)\right], \tag{1.1}$$

where r, θ, and ϕ are spherical comoving coordinates, and t is the proper time. The growth of the spatial extent of the Universe can be parameterized with the function $a(t)$, that is called expansion factor, and by definition $a_0 = a(t_0) = 1$ at the present time. The information about the curvature of the spacetime is in the parameter K, that for suitably rescaled r can be -1, 0 or 1, corresponding to an open (hyperbolic), flat (Euclidean) or closed (spherical) geometry of spatial timeslices at fixed t. Einstein's field equations relate the geometrical properties of the spacetime with its stress-energy tensor. Assuming that the Universe can be described by a homogeneous and isotropic distribution of an ideal fluid, one obtains the Friedmann equations,

$$\frac{\ddot{a}}{a} \;=\; -\frac{4\,\pi\,G}{3}\left(\rho + \frac{3p}{c^2}\right) + \frac{\Lambda\,c^2}{3}\,, \tag{1.2}$$

$$\left(\frac{\dot{a}}{a}\right)^2 \;=\; \frac{8\,\pi\,G}{3}\rho - \frac{K\,c^2}{a^2} + \frac{\Lambda\,c^2}{3}\,. \tag{1.3}$$

These equations have been written in form that allows for a non-vanishing cosmological constant Λ. The evolution of the expansion parameter can be obtained from the Friedmann equations if the equation of state that relates p and ρ is specified. For most of the cosmologically relevant cases the equation of state can be written in the form

$$p \,=\, w\,\rho\,c^2\,, \tag{1.4}$$

where w is typically in the interval of $[0,1]$. The case $w=0$ corresponds to a *dust universe*. An ideal, non-relativistic fluid can be well approximated with $w=0$, and this equation of state is relevant for the matter-dominated evolution of the Universe. Instead, in the early phases of evolution, the Universe is radiation-dominated with $w=1/3$, corresponding to the fluid of relativistic, non-degenerate particles that are in thermodynamic equilibrium.

It is convenient to define today's *critical density* of the Universe as

$$\rho_{\rm cr} \,=\, \frac{3\,H_0^2}{8\,\pi\,G}\,, \tag{1.5}$$

where H_0 is the Hubble constant given by $\dot{a}/a$ at the present time. The value of the Hubble constant at $z=0$ is often parameterized as $100\,h\,{\rm km\,s^{-1}\,Mpc^{-1}}$, where h is a dimensionless factor (currently the estimated value is ~ 0.7). Having defined the critical density of the Universe it is possible to express the total density parameter at the present time as

$$\Omega_{{\rm tot},\,0} \,=\, \frac{\rho}{\rho_{\rm cr}}\,, \tag{1.6}$$

with $\Omega_{{\rm tot},\,0} > 1, = 1$ or < 1 corresponding to the cases of a closed, flat or open geometry, respectively. In the standard ΛCDM cosmology it is believed that the main contribution to $\Omega_{{\rm tot},\,0}$ comes from the cosmological constant, with $\Omega_{\Lambda,\,0} \,=\, \frac{\Lambda\,c^2}{3\,H_0^2} \,=\, 0.73$, while the remaining part is due to the density parameters of dark matter and baryons, such that the geometry of the Universe is flat. The relativistic particles and radiation have negligible density parameters today.

The Friedmann equations and the adiabatic expansion of the Universe yield the relation

$$\rho_w\,a^{3(1\,+\,w)} = \rho_{w,\,0}\,a_0^{3(1\,+\,w)} \tag{1.7}$$

between the density and the expansion factor. Hence, the time evolution of the Hubble constant can be written in the form

$$H^2(t) \equiv \left(\frac{\dot{a}}{a}\right)^2 \,=\, H_0^2\left(\frac{a_0}{a}\right)^2\left[\Omega_{w,\,0}\left(\frac{a_0}{a}\right)^{1\,+\,3w} + 1 - \Omega_{w,\,0}\right], \tag{1.8}$$

with $\Omega_{w,\,0} \,=\, \rho_{w,\,0}/\rho_{\rm cr}$ for the components of the Universe having different equations of state. In the case of the ΛCDM cosmology, Eq. [1.8] can be expressed in a simplified form as

$$H^2(t) \,=\, H_0^2\left[\Omega_{{\rm m},\,0}\left(\frac{a_0}{a}\right)^3 + \Omega_{\Lambda,\,0}\right], \tag{1.9}$$

where the part due to the cosmological constant has been treated as a fluid with $w=-1$. The ratio of the present day expansion factor to the expansion factor at some previous

time defines a very useful variable in cosmology, the *redshift*, i.e. $z = \frac{a_0}{a} - 1$. This quantity can be directly measured from observed spectra of an astrophysical object of interest

$$z \,=\, \frac{\lambda_{\rm obs} - \lambda_{\rm em}}{\lambda_{\rm em}}\,. \tag{1.10}$$

Here $\lambda_{\rm obs}$ is the observed wavelength, e.g. determined today on the Earth, and $\lambda_{\rm em}$ is the emitted wavelength at time t in the rest frame of the object in consideration. Correcting for, or within the uncertainty of, peculiar motions, the cosmological redshift serves then both as a variable of distance and lookback time.

1.1.2 Structure growth: the linear theory

In the currently favoured cosmological scenario, structures have formed from very tiny density perturbations, $\delta\rho/\rho \sim 10^{-5}$. Thus, the early growth of structure can be well approximated with the linear perturbation theory. This remains valid while the density contrast of a given perturbation is much less than unity, i.e.

$$\delta(\mathbf{r},t) \,=\, \frac{\rho(\mathbf{r},t) - \rho_{\rm b}}{\rho_{\rm b}} \ll 1\,, \tag{1.11}$$

where $\rho_{\rm b}$ represents the unperturbed background density. A simple criterion to decide whether a perturbation will grow or not in time is based on the Jeans length,

$$\lambda_{\rm J} \simeq \frac{v_{\rm s}}{\sqrt{G\rho_{\rm b}}}\,, \tag{1.12}$$

where $v_{\rm s}$ is the sound speed. The meaning of the Jeans criterion is the following: a spherical fluctuation having a certain overdensity $\delta(\mathbf{r},t)$ will grow in time if its gravitational force exceeds the pressure force, thus implying that its radius λ has to be larger than $\lambda_{\rm J}$. In other words, $\delta(\mathbf{r},t)$ will increase in time if the gravitational free-fall time, $\tau_{\rm ff} \sim 1/\sqrt{G\rho}$, is less than the characteristic hydrodynamical time $\tau_{\rm h} \sim \lambda/v_{\rm s}$.

Let us now consider the fundamental equations governing an ideal, non relativistic fluid, in the physical rest frame of an expanding Universe. These are:

1. The mass conservation,
$$\frac{\partial\rho}{\partial t} + \nabla(\rho\mathbf{v}) = 0\,. \tag{1.13}$$
2. The Euler equation,
$$\frac{\partial\mathbf{v}}{\partial t} + (\mathbf{v}\cdot\nabla)\mathbf{v} + \frac{1}{\rho}\nabla p + \nabla\varphi = 0\,. \tag{1.14}$$
3. The equation of state,
$$p = p(\rho, S)\,. \tag{1.15}$$
4. The Poisson equation,
$$\nabla^2\varphi = 4\pi G\rho\,. \tag{1.16}$$
5. The entropy evolution,
$$\frac{{\rm d}S}{{\rm d}t} = 0\,. \tag{1.17}$$

In order to analyze linear growth of fluctuations we seek solutions that are the sum of the unperturbed solutions and small perturbations around those. In particular, for the unperturbed solutions in an expanding Universe we adopt the Friedmann solutions and we write the small perturbations in the following form:

$$\rho = \rho_{\rm b} + \delta\rho$$

$$\mathbf{v} = H\mathbf{r} + \mathbf{u}$$

$$p = p_{\rm b} + \delta p$$

$$\varphi = \varphi_b + \delta\varphi\,.$$

Here $\delta\rho$ is a small perturbation in density with respect to the underlying background density, $\delta\varphi$ is the corresponding perturbation in the gravitational potential, while the perturbation in the velocity is given by the peculiar velocity $\mathbf{u}$. Note that the factor $H\mathbf{r}$ vanishes in the comoving reference frame, being caused by the expansion of the background Universe. Passing to Fourier space and after some algebra a unique equation can be derived for the evolution of the small density perturbation in the expanding Universe, viz.

$$\ddot{\delta}_k + 2\frac{\dot{a}}{a}\dot{\delta}_k + \delta_k\left(\frac{k^2 v_s^2}{a^2} - 4\pi G\rho_b\right) = 0\,. \tag{1.18}$$

Note that here k is the comoving wave number, with $k_{\rm ph} = k/a(t) = 2\pi/\lambda$. Solving this second-order equation for the case of an Einstein-de Sitter Universe characterized by $\Omega_m = 1$, it can be seen that there are two solutions, one growing in time, $\delta \propto t^{2/3} \propto a$, and the other decaying as $\delta \propto t^{-1} \propto a^{-3/2}$ in time. These solutions will be useful when discussing the spherical collapse model in the next section.

1.1.3 The non-linear spherical collapse model

When the density contrast of a perturbation approaches unity, the Jeans theory cannot be applied any more because its assumptions cease to be valid. However, one can still analytically follow the growth of perturbations with $\delta \simeq 1$ in certain simple situations.

Let us consider a spherical top-hat perturbation at some initial time $t_{\rm i}$, with overdensity much smaller than unity, with no peculiar velocity and negligible pressure. We can treat this perturbation as a small fluctuation induced on the underlying Universe, and for simplicity, we can assume that it can be described by an Einstein-de Sitter model ($\Omega_{\rm m} = 1$) at $t_{\rm i}$. From the previous section we know that the density contrast admits two solutions with the following form

$$\delta_i \equiv \delta(t_i) = \delta_+(t_i)\left(\frac{t}{t_i}\right)^{2/3} + \delta_-(t_i)\left(\frac{t}{t_i}\right)^{-1}, \tag{1.19}$$

where $\delta_+(t_i)$ is the growing mode and $\delta_-(t_i)$ is the decaying mode. Requiring that the initial peculiar velocity is zero, one finds $\delta_+ = \frac{3}{5}\delta_i$, while the decaying mode will become

negligible after some time. If we demand that the perturbation decouples from the background expansion of the Universe at a certain time and starts to collapse, the following equation needs to be satisfied

$$\delta_+ = \frac{3}{5}\delta_i > \frac{3}{5}\frac{1-\Omega_0}{\Omega_0(1+z_\mathrm{i})}\,. \tag{1.20}$$

Thus, if $\Omega_0 \geq 1$ Eq. [1.20] will be satisfied for any value of δ_i, while for a Universe with $\Omega_0 < 1$ Eq. [1.20] is more stringent, allowing only certain perturbations to collapse. Within the same formalism one can calculate that the density of the perturbation at the time of the maximum compression will be ~ 180 times the density of the underlying Einstein-de Sitter Universe, while in linear theory the extrapolated overdensity at this time is only 1.68.

1.1.4 Numerical methods

While the linear theory represents a very useful tool for addressing the early growth of structures, its results cannot be readily extrapolated into the highly non-linear regime, as we have seen in the previous section. However, more accurate analytic calculations in the non-linear regime are very complex, and limited to special configurations and symmetries. This leaves the numerical approach as the only general method for following the fully non-linear evolution of structure growth, which is especially relevant for studying the formation and evolution of galaxies, galaxy clusters and large-scale structure. Moreover, the relevance of numerical methods nowadays lies not only in tracking accurately the structure formation processes due to the gravity, but also in solving the coupled and complex hydrodynamical processes that occur in the baryonic component. The ultimate goal of numerical simulations is to self-consistently and *ab initio* compute all physical processes relevant for the astrophysical problem in consideration. Unfortunately, for most of the interesting issues, this is beyond the present-day capabilities of any numerical code. One of the big obstacles is the limited mass and spatial resolution that can be achieved in current state-of-the-art simulations. Thus, often subresolution techniques need to be invoked to incorporate physical processes occurring at unresolved scales. Other, equally severe limitations arise from our ignorance of some of the key physical mechanisms that are actually acting in astrophysical problems of interest. For example, the treatment of star formation is one of the fundamental issues in astrophysics that faces this difficulty. Nevertheless, remarkable progress has been made in astrophysical simulations over the past few years, both thanks to drastically improved numerical schemes and the increased performance of computer hardware.

1.1.4.1 N-body techniques

A number of methods have been developed in the literature to track the time evolution of three-dimensional self-gravitating fluids. Since dark matter dominates the total mass, it is essential to represent this collisionless component well, which can only be done efficiently by discretizing it in terms of particles as an N-body problem. This leads to the numerical task of computing the gravitational forces between N particles.

The most obvious solution relies on direct summation, which is called the particle-particle (PP) method. However, this method cannot handle systems with a large number of particles, say $N > 10^5$, because its computational cost is proportional to the number of particle pairs ($\sim N^2$) present in the simulated volume. Thus, several alternatives have been suggested, like e.g. the particle-mesh (PM) method [e.g. Klypin and Shandarin, 1983], where the gravitational potential is calculated on a regular grid with periodic boundary conditions, allowing one to take advantage of Fast Fourier Transform (FFT) algorithms for solving the Poisson equation. Even though the computational costs in the PM method scale much more favourably with particle number, the force resolution on small scales is rather poor, since it is limited by the finite size of the grid. A significant improvement on this has been achieved in the P^3M method [Efstathiou et al., 1985, Couchman, 1991], where the long range forces are computed on a grid, while the PP method is adopted for the short-range forces on the scale of individual cells, thus making a compromise between the computational time and a high force resolution.

An alternative to the P^3M method is to use an Adaptive Mesh Refinement (AMR) technique [e.g. Norman and Bryan, 1999], where a hierarchy of grids is constructed, with the finest ones placed in regions where the highest force resolution needs to be achieved. Poisson's equation can then be solved in real-space on this grid using iterative multigrid methods. Still a different strategy is adopted in the so-called tree (TREE) algorithms proposed by Barnes and Hut [1986]. They are based on a hierarchical multipole expansion, and can preserve a fast computation time and good force resolution independent of the clustering state of the particles. The key point of TREE methods is to divide the simulated volume in a hierarchy of cells, such that every cell that contains more than one particle is subdivided into subcells, until the smallest cells all contain at most one particle. The gravitational forces at small distances are then calculated as in the PP method, while the long-range forces are approximated by multipole expansions for groups of distant particles. This makes the TREE method quite flexible in adapting to the particular clustering state in the simulated volume. The 'Lagrangian nature' makes it also ideally suited for a coupling with hydrodynamical Lagrangian techniques, such as the Smoothed Particle Hydrodynamics (SPH) method developed by Lucy [1977] and Gingold and Monaghan [1977], that I will address later on.

1.1.4.2 Numerical hydrodynamics

In order to follow the gas evolution in cosmological simulations of structure formation, hydrodynamical processes have to be treated besides gravity. The simplest case corresponds to that of non-relativistic, non-radiative simulations of an ideal gas, which however provides only a model of very limited applicability. As a next step, radiative cooling and heating processes need to be taken into account, which leads to much greater realism for the formation and growth of galaxies. If gas is allowed to cool radiatively within dark matter halos, it will become much denser, reaching eventually the physical conditions necessary for star formation. However, as soon as radiative cooling is incorporated into a simulation code, one also needs to consider feedback processes to prevent excessive gas cooling that otherwise occurs. A natural candidate for heating is star formation itself: during certain stages of their evolution stars can loose large amounts of mass due to stellar

winds (e.g. during the AGB phase), while in the final stages of their life, massive stars explode as supernovae, thereby shock heating the surrounding medium and polluting the intergalactic medium with metals.

Moreover, it has been observationally established that powerful starburst activity can give rise to the phenomenon of 'galactic winds' [McCarthy et al., 1987, Heckman et al., 1987], large-scale outflows from galaxies that enrich and heat the intergalactic medium. Galaxies with high star formation rates can expel some of their gas due to the winds, and this gas may fall back onto the galaxies at a later time, in the form of galactic fountains. However, both from an observational and theoretical point of view, it seems clear by now that feedback from star formation is not sufficient to explain all galaxy properties. In particular, numerous observational findings [Kormendy and Richstone, 1995, Magorrian et al., 1998] provide evidence that supermassive black holes are an important ingredient of structure formation. For example, it has been established that black hole masses are tightly linked to the properties of host halos [Ferrarese and Merritt, 2000, Gebhardt et al., 2000, Tremaine et al., 2002, Marconi and Hunt, 2003], indicating that a mutual interaction must be taking place. Moreover, in a number of objects – massive ellipticals and central cluster galaxies – direct evidence for such an interaction has been discovered [e.g. Owen et al., 2000, Blanton et al., 2001]. These issues will be discussed extensively in Chapters 2 and 4, where hydrodynamical simulations are used to study the co-evolution of supermassive black holes and their host galaxies.

For a hydrodynamical treatment of feedback processes, one needs to simulate gas dynamics. One of several available techniques to treat gas hydrodynamics in cosmological simulations is provided by SPH. The main idea of the SPH method is to represent a given thermodynamical function with an interpolant constructed from the values at a set of disordered points. Thus, the gas is treated with an ensemble of particles, that are characterized by their position, velocity and mass, and internal thermodynamic variables. This particle-based nature allows for an accurate treatment of the self-gravity with an accuracy that is well matched to the N-body method needed for the dark matter. Furthermore, the intrinsic Lagrangian nature of SPH is particularly well suited for cosmological simulations of structure formation, where the density contrast is very large, and the highest resolution is required at the peaks of the density field. In fact, SPH automatically adjusts its resolution locally to the clustering state and can easily deal with an arbitrary geometry. Also, the SPH method can be extended to the case of real gases, subject to thermal conduction, or viscosity, as discussed in more detail in Chapter 3.

For the above reasons, the TREESPH method has been adopted in this thesis for all simulations that we performed. A more detailed description of SPH can be found in Chapter 3.

1.2 Galaxy clusters: evolution and properties

Clusters of galaxies are the largest virialized objects in the Universe. They form from the highest peaks in the primordial density fluctuation field, and given their rarity they are very sensitive probes of underlying cosmology. In particular, their local abundance depends strongly on the amplitude of the power spectrum of fluctuations, σ_8, and on the matter density parameter $\Omega_{\mathrm{m},0}$, while the redshift evolution of the galaxy cluster abundance can

break the degeneracy between these two cosmological parameters [Bahcall et al., 1997]. Yet another independent estimate of $\Omega_{\mathrm{m},0}$ can be obtained from galaxy clusters assuming that they contain a fair, universal sample of the material mix in the Universe [White et al., 1993a].

Furthermore, galaxy clusters represent ideal laboratories to study physical processes that shape the evolution of galaxies and halos. Optical and X–ray observations have established that they contain up to ~ 1000 member galaxies, as well as intracluster stars and hot intracluster gas ($\sim 10^8\,\mathrm{K}$). The latter makes them one the most luminous X–ray sources in the sky. However, their gravity is dominated by the dark matter component, that contributes $\sim 80\%$ of their total mass[2]. The second most important component to the mass is the hot ICM, which contains most of the baryons in clusters while the galaxies usually contribute only $\sim 2-5\%$ to the total mass. Given their size, galaxy clusters are dynamically young systems that form late, with $t_{\mathrm{dyn}} \sim t_{\mathrm{Hubble}}$. Also, they are powerful gravitational lenses, as illustrated in Figure 1.2. The gravitational lensing observations allow to estimate cluster masses that can be directly compared with the measurements obtained by optical and X–ray methods, which assume that galaxy cluster are in dynamical equilibrium [e.g. Allen, 1998].

Dark matter and galaxies in clusters can be well approximated as collisionless systems, while for the intracluster gas a collisional hydrodynamical treatment is essential. In a simple model, galaxy clusters can be represented as spherical and static systems, implying that the Jeans equation can be used to describe the relation between gravitational potential, density field and velocity distribution of collisionless components of the system, viz.

$$M(<r) \;=\; -\frac{r\sigma_r^2(r)}{G}\left[\frac{d\log\rho}{d\log r} + \frac{d\log\sigma_r^2}{d\log r} + 2\beta(r)\right]. \tag{1.21}$$

Here $M(<r)$ is the total mass of the system inside the radius r, while $\beta(r)$ is a measure of the anisotropy of the velocity distribution. It is defined as $\beta(r) = 1 - \sigma_t^2(r)/\sigma_r^2(r)$, with $\sigma_t^2(r)$ and $\sigma_r^2(r)$ being tangential and radial velocity dispersions, respectively. Note that $\rho(r)$, $\sigma_r^2(r)$ and $\beta(r)$ correspond to any tracer of the potential that is in dynamical equilibrium.

Instead, for the intracluster gas, a hydrostatic equilibrium in a static and spherical potential can be assumed, described by

$$M(<r) \;=\; -\frac{rkT(r)}{G\mu m_p}\left[\frac{d\log\rho_g}{d\log r} + \frac{d\log T(r)}{d\log r}\right]. \tag{1.22}$$

The equation of hydrostatic equilibrium is analogous to the Jeans equation, with the gas temperature T replacing the velocity dispersion, and with $\beta = 0$ due to the collisional nature of the gas which gives rise to isotropic gas pressure.

To the first approximation, the intracluster gas can be well described as a fully ionized, tenuous plasma with characteristic temperature of $10^8\,\mathrm{K}$ and density $n \sim 10^{-3}\,\mathrm{cm}^{-3}$. The extended X-ray emission detected in clusters can be explained by thermal bremsstrahlung

[2] Already in 1933 Zwicky was the first one to point out that the velocities of galaxies in the Coma cluster were way to high for the underlying mass distribution composed of galaxies only and being in equilibrium, thus he hypothesized the existence of "dark matter" and pointed out the missing mass problem.

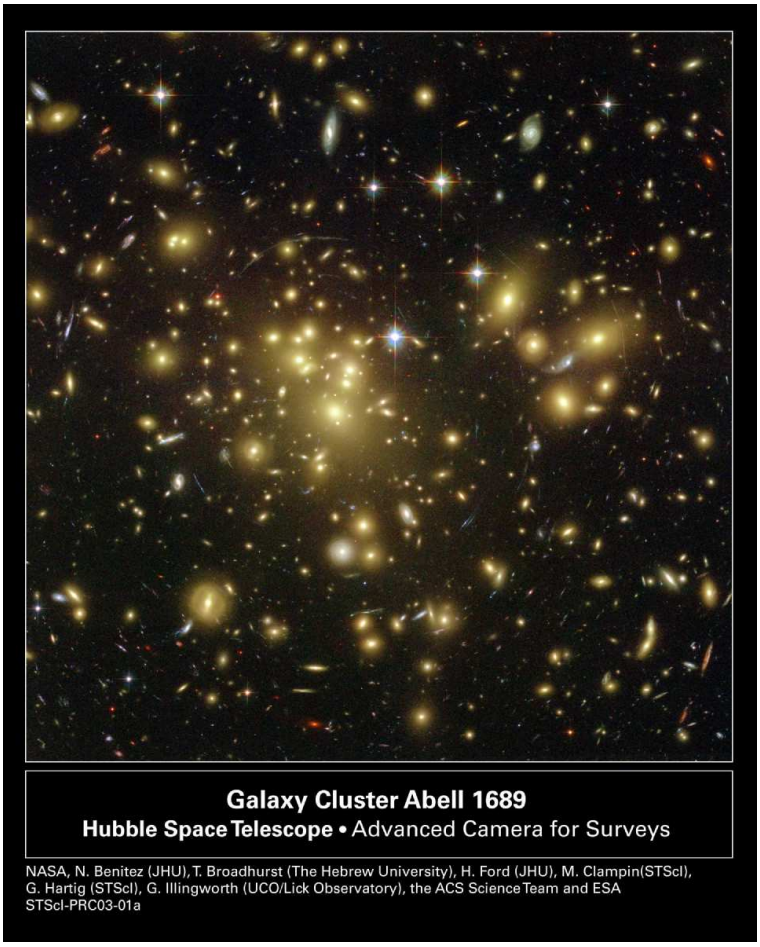

Figure 1.2: A beautiful picture of a rich galaxy cluster taken with the Hubble Space Telescope with over 13 hours of exposure time. This galaxy cluster is 675 Mpc away from us and the image shows the central 630 kpc of the cluster. A large number of galaxies that are part of the cluster can be seen, with additional galaxies in the foreground and background up to redshift of ~ 6. This galaxy cluster acts as a powerful gravitational lens, producing a number of bluish and reddish arcs that represent the distorted images of faint background galaxies.

of the hot intracluster plasma. Thus, one can estimate the characteristic time scale necessary for the intracluster plasma to cool via bremsstrahlung emission, which is the so-called cooling time. For most of the gas in a cluster this time is typically longer than the Hubble time. However, for a class of galaxy clusters, the cooling time in the innermost regions can be substantially shorter, suggesting that the gas should in principle cool off from the cluster atmosphere and flow towards the centre. This class of objects has therefore been named *cooling flow clusters* [for a review see Fabian, 1994]. However, as I will discuss next and address in much more detail in a good part of this thesis, this name is inappropriate, in the sense that gas is actually *not* cooling off in the centre of these systems at all, or is at least cooling at much reduced rates compared to what one would naively expect. This

discovery constitutes what has become known as the *cooling flow problem*, and it represents one of the major challenges in understanding galaxy cluster physics.

1.2.1 The cooling flow problem

First observational evidence for cooling flow clusters has been provided by the Uhuru X–ray telescope [Lea et al., 1973], and was later confirmed by the Einstein observatory and ROSAT. These X–ray telescopes have unambiguously detected peaked surface brightness profiles in the innermost regions of a number of clusters, indicating that the intracluster gas density must rise significantly towards the centre. The cooling times in the central $\sim 100\,\mathrm{kpc}$ of these systems have been estimated to be significantly shorter than the Hubble time, implying rather high mass deposition rates of up to $1000\,M_{\odot}/\mathrm{yr}$. However, apart from X–rays, no compelling evidence for cooling flows with such high mass fluxes has been found in any other band.

A major breakthrough in the field has been achieved with the newest generation of X–ray telescopes: XMM-Newton and Chandra. With these telescopes it was possible for the first time to take accurate spectra of the central regions of clusters, which surprisingly have shown a lack of very cold gas with $< 1keV$ [e.g. McNamara et al., 2000, Böhringer et al., 2002]. On the other hand, the high spatial resolution of these telescopes permitted to observe with unprecedented detail a number of features in the X–ray emitting gas, including cavities, irregularities and ripples in the central regions of cooling flow clusters [e.g. Forman et al., 2006, Fabian et al., 2006]. Observations in other bands that are sensitive to molecular gas and star formation have meanwhile confirmed the earlier findings [Edge, 2001, Edge et al., 2002], and shown that there appears to be no appreciable influx of cold gas onto the central cluster galaxy. Observationally it thus appears that the gas is indeed not cooling out with the high rates expected from the X-ray luminosity, instead it is kept hot somehow.

These puzzling observational findings have initiated very vigorous theoretical research [e.g. Binney and Tabor, 1995, Churazov et al., 2001, 2002, Quilis et al., 2001, Ruszkowski and Begelman, 2002], that has been trying to interpret and understand this novel scenario. Arguably the most promising emerging picture from a number of theoretical studies is the following: In order to prevent excessive gas cooling in the central cluster regions, a heating mechanism is required, and the best candidate for this feedback process appears to lie in a central radio source powered by active galactic nuclei (AGN).[3] This scenario has found support by a growing body of observational evidence, showing that the intracluster plasma is displaced and heated by AGN-inflated bubbles, as illustrated in two very nice examples in Figure 1.3.

1.3 Thesis outline

The aim of my PhD Thesis is to better understand which physical processes are crucial for the formation and evolution of the galaxy cluster population as a whole. For this purpose I carried out numerical simulations that followed both the evolution of the dark matter

[3] Note that the idea of central cluster heating by radio sources is actually quite old: some of the pioneering works suggesting it date back to 1970s [e.g. Gull and Northover, 1973, Blandford and Rees, 1978].

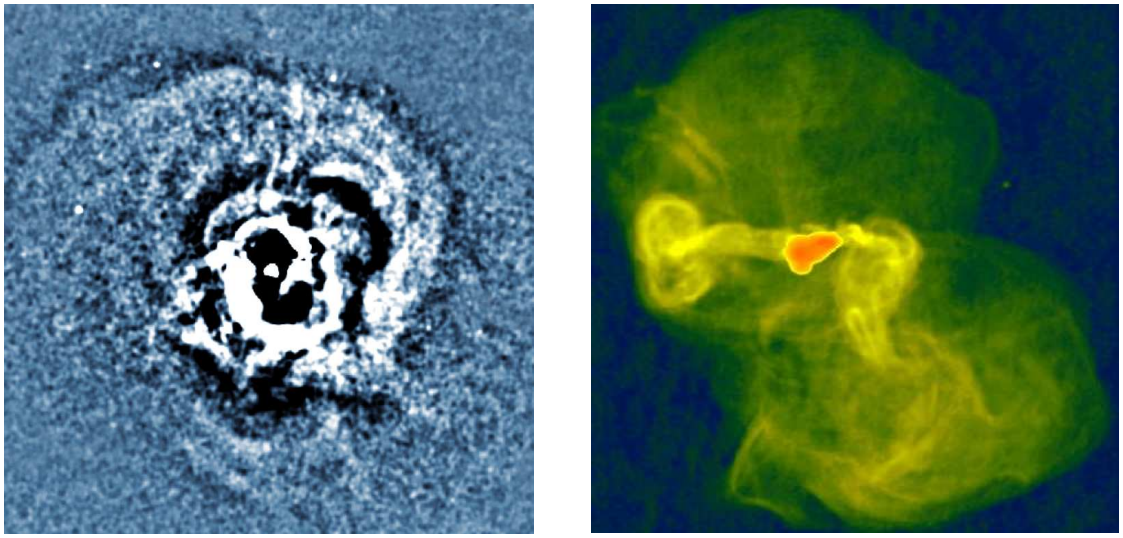

Figure 1.3: The left-hand panel shows an unsharp-masked image of the central region of the Perseus cluster, highlighting radio bubbles and a number of irregularities or ripples in the X–ray emission, probably caused by bubble expansion [Fabian et al., 2006]. The right-hand panel is a radio image of the M87 galaxy in the Virgo cluster, representing an extraordinary example of a jet-inflated radio bubble in the cluster core [Owen et al., 2000].

and the baryons in a ΛCDM cosmology, and also modelled an array of different physical processes and their complex interplay. The simulations have been performed with the parallel TREESPH code GADGET-2, that has been developed by Springel et al. [2001b] and Springel [2005]. Besides gravitational and non-radiative hydrodynamical processes, GADGET-2 incorporates a treatment of radiative cooling, and of heating of the gas by a spatially uniform, time-dependent UV background. Star formation and associated supernovae feedback are implemented using a subresolution multiphase scheme [Springel and Hernquist, 2003a]. For my own work, I have extended the code with models for further physical processes, as described below.

AGN-driven bubble heating of galaxy clusters. Based on the framework of physical processes included in GADGET-2 I have implemented an additional heating mechanism provided by AGN situated at the centres of galaxy groups and clusters, as outlined in detail in Chapter 2. The AGN heating model is of a phenomenological nature and its aim was to mimic the observed morphology of AGN-driven bubbles. One of our goals was to investigate the impact of these bubbles on the well-known cooling flow problem, using self-consistent cosmological simulations of galaxy cluster formation.

Physical viscosity simulations of cluster formation. Recent observations of galaxy clusters have suggested the possibility that the gas viscosity of the ICM in hot clusters may not be negligible, and that viscous transport processes could play an important role in dissipating energy generated by AGN-driven bubbles or during merger events. In order to explore

the relevance of this physical process in the context of galaxy cluster formation, I have implemented a fully self-consistent treatment of physical viscosity in GADGET-2, allowing both a shear and a bulk viscosity, as described in Chapter 3. The implementation consists of a novel discretization of the Navier-Stokes and general heat transfer equations within the SPH framework, and adopts the Braginskii parameterization for the shear viscosity coefficient. I have tested the implementation extensively on a set of hydrodynamical problems with known analytic solutions, recovering these solutions accurately. I then applied the code to simulations of galaxy clusters, analyzing in particular how viscosity affects the heating induced by AGN inflated bubbles, and how the properties of galaxy clusters are altered with cosmic time.

A unified model of AGN feedback in cosmological simulations of galaxy clusters. In the newly emerging picture for the joint evolution of galaxies and super-massive black holes, the interplay between AGN and their host objects may be composed of two modes. At high redshifts, and in particular triggered by the merging activity of host halos, large amounts of gas can be efficiently funneled towards the embedded black holes at halo centres, triggering powerful quasar activity. If a small amount of the quasar bolometric luminosity couples thermally with the surrounding gas, a very effective feedback mechanism can be established, able to quench further gas accretion and star formation once the black hole has become sufficiently massive, as explicitly demonstrated by numerical simulations of Di Matteo et al. [2005b]. However, at lower redshifts and for black holes accreting with low rates, the mechanical luminosity of radio galaxies, in the form of jets and radio bubbles, could provide a different mode of heating by AGN, which would be especially important in the cooling flow clusters, which are often associated with central radio activity. My goal has therefore been to integrate these two modes of AGN feedback in a unified simulation model, described in Chapter 4, incorporating both the model of black hole growth and feedback as formulated by Springel et al. [2005c] as well as the bubble model for radio activity that I have illustrated in Chapter 2.

2

Hydrodynamical simulations of cluster formation with central AGN heating

D. Sijacki and V. Springel, 2006, MNRAS, 366, 397

Abstract

We analyse a hydrodynamical simulation model for the recurrent heating of the central intracluster medium (ICM) by active galactic nuclei (AGN). Besides the self-gravity of the dark matter and gas components, our approach includes the radiative cooling and photoheating of the gas, as well as a subresolution multiphase model for star formation and supernova feedback. Additionally, we incorporate a periodic heating mechanism in the form of hot, buoyant bubbles, injected into the intragalactic medium (IGM) during the active phases of the accreting central AGN. We use simulations of isolated cluster halos of different masses to study the bubble dynamics and the heat transport into the IGM. We also apply our model to self-consistent cosmological simulations of the formation of galaxy clusters with a range of masses. Our numerical schemes explore a variety of different assumptions for the spatial configuration of AGN-driven bubbles, for their duty cycles and for the energy injection mechanism, in order to obtain better constraints on the underlying physical picture. We argue that AGN heating can substantially affect the properties of both the stellar and gaseous components of clusters of galaxies. Most importantly, it alters the properties of the central dominant (cD) galaxy by reducing the mass deposition rate of freshly cooled gas out of the ICM, thereby offering an energetically plausible solution to the cooling-flow problem. At the same time, this leads to reduced or eliminated star formation in the central cD galaxy, giving it red stellar colours as observed.

keywords: methods: numerical – galaxies: clusters: general – cooling flows – cosmology: theory

2.1 Introduction

Clusters of galaxies are the largest virialised objects in the Universe and are thought to contain a representative fraction of baryons [White et al., 1993b]. Most of these baryons can be found in the diffuse gas of the intracluster medium (ICM), which is directly observable in X-rays, making clusters of galaxies an almost ideal laboratory for studying the physical processes that shape galaxies and halos in the Universe. Clusters of galaxies are also a useful cosmological probe [for a recent review see Voit, 2004], and therefore have been a prime target for theoretical modelling early on, both numerically and analytically.

A first order approximation for the ICM is to represent it as an ideal, non-radiative gas. This leads to the predications of scale invariant relations between X-ray luminosity, mass and temperature [Kaiser, 1986]. However, it has long been established that the observed relations do not agree in detail with these assumptions, e.g. the observed $L_{\rm X}$–T relation is much steeper than expected based on this simple model. In addition, recent observations with radio and X-ray telescopes have revealed a stunning complexity of the ICM physics, including phenomena such as cold fronts, radio ghosts, cluster turbulence, and apparently nearly uniform enrichment to high metallicity.

However, possibly the most puzzling observational fact is the "cooling-flow" problem. Since the cooling time in the central regions of galaxy clusters is smaller than the age of the clusters themselves, a central inflow of cool gas is expected to occur [e.g. Fabian and Nulsen, 1977, Cowie and Binney, 1977, Fabian, 1994]. The rate of gas cooling can be estimated by energetic arguments if one assumes that X-ray cooling radiation is fed by the thermal reservoir of the hot cluster plasma. Based on this, the estimated rate of accretion onto the central galaxy is rather high in many cases [e.g. Fabian et al., 1984, White et al., 1994, 1997, Allen, 2000, Allen et al., 2001a], implying that a significant amount of gas cooler than $1-2\,\mathrm{keV}$ should be present in the centre. However, up to the present time, optical and X–ray observations have failed to detect the required amount of this cool gas, suggesting that it is simply not there [e.g. McNamara et al., 2000, Peterson et al., 2001, Tamura et al., 2001, Balogh et al., 2001, Kaastra et al., 2001, Edge, 2001, Edge et al., 2002, Edge and Frayer, 2003, Fabian et al., 2001, Böhringer et al., 2002, Peterson et al., 2003, Salomé and Combes, 2004]. The low current star formation rates of central galaxies [e.g. O'Connell and McNamara, 1989, Johnstone et al., 1987, Allen et al., 1995] provide additional support for the absence of strong cooling flows. Apparently, there must be a physical process that offsets the radiative cooling in the centre, preventing the gas from falling out of the ICM in a cooling flow.

Theoretical studies have therefore often invoked some sort of non–gravitational heating to explain the cluster scaling relations [e.g. Kaiser, 1991, Navarro et al., 1995, Bower, 1997, Tozzi and Norman, 2001, Borgani et al., 2001, Voit and Bryan, 2001, Babul et al., 2002, Voit et al., 2002, 2003, Oh and Benson, 2003, Tornatore et al., 2003, Borgani et al., 2004]. The main unsolved issue in these models remains the origin and nature of the physical sources that cause the extra–heating of the ICM. Perhaps the most obvious heat source is supernovae associated with star formation, but it seems questionable that they are able to supply the required amount of feedback energy. Curiously, radiative cooling alone may also account for the steepness of the $L_{\rm X}$–T relation by eliminating gas more efficiently in low-mass systems [e.g. Lewis et al., 2000, Voit and Bryan, 2001, Muanwong et al., 2001,

Yoshida et al., 2002, Wu and Xue, 2002, Voit et al., 2002, McCarthy et al., 2004], but this produces a drastic overprediction of the amount of cold gas (apart from a problem with the L_X–T zero-point) and is therefore disfavoured. Models that self-consistently incorporate SNe heating and radiative cooling processes are also only found to have limited success [e.g. Borgani et al., 2004]. The over–cooling problem therefore remains unsolved. Another problem is posed by simulated temperature profiles, which typically exhibit a trend to increase towards the cluster centre, in disagreement with observational inferences [e.g. Allen et al., 2001b, De Grandi and Molendi, 2002].

An array of different physical hypothesis have been proposed to solve the cooling-flow paradox, including thermal conduction, magnetic fields, cosmic rays, and hot buoyant bubbles from AGN jets. Thermal conduction may in principle offset central cooling losses by inducing a heat current from outer, hotter regions of clusters [e.g. Narayan and Medvedev, 2001], provided the conductivity is not strongly suppressed by tangled magnetic fields. Analysis of static cluster models with conduction have been able to provide good matches to observed temperature profiles in some cases [e.g Voigt et al., 2002, Zakamska and Narayan, 2003, Voigt and Fabian, 2003] but detailed self-consistent numerical simulations which followed conduction still encountered the cooling flow problem [e.g. Jubelgas et al., 2004, Dolag et al., 2004], making it questionable whether this can be the real solution.

The more widely favoured hypothesis is instead that the central AGN may supply the required amount of energy. Accretion onto supermassive black holes is thought to liberate of order $\sim 10\%$ of the accreted rest mass energy, implying that even for low accretion rates onto a supermassive black hole, offsetting the cooling flows is energetically quite possible. In fact, such accretion powers high-redshift quasars, the most luminous sources in the universe. Quasar activity is likely to be triggered by mergers of galaxies, where cold gas is forced to the nuclei by gravitational tidal forces. This accretion and the associated quasar feedback has recently been incorporated into simulations, and shown to play a potentially important role in shaping the properties of elliptical galaxies [Springel et al., 2005b].

In clusters of galaxies, however, it seems clear that the central AGN activity that causes bubbles is of a different nature, and needs not be triggered by galaxy mergers. Observationally, many clusters of galaxies show evidence for X-ray cavities filled with radio plasma [e.g. Owen et al., 2000, Blanton et al., 2001], which are thought to be inflated by relativistic jets from the AGN. Theoretically, it has been shown that these bubbles may rise buoyantly and raise some of the central cool gas [e.g. Churazov et al., 2001], allowing it to mix with the hotter gas further out. Together with the accompanying mechanical and possibly viscous heating, this can then constitute an efficient feedback mechanism.

In this paper, we focus on the phenomenology of this bubble feedback, without addressing the small scale physics of the accretion onto the black hole. This extends earlier simulation studies which all employed hydrodynamical mesh codes, but which focused exclusively on highly idealised cluster models [e.g. Churazov et al., 2001, Quilis et al., 2001, Ruszkowski and Begelman, 2002, Churazov et al., 2002, Brüggen et al., 2002, Brüggen and Kaiser, 2002, Brüggen, 2003, Nulsen et al., 2003, Dalla Vecchia et al., 2004, Hoeft and Brüggen, 2004]. A first goal of our work is to demonstrate that such simulations are also possible with the smoothed particle hydrodynamics (SPH) technique, and give results consistent with earlier studies. This is important because the Lagrangian nature of SPH is ideal for cosmological simulations of structure formation, and if applicable for

bubble feedback, will allow us to carry out the first self-consistent cosmological simulations with AGN-driven bubble heating. An equally important goal of our simulations is to gain new insights into the efficiency of bubble feedback associated with AGN for modifying the thermodynamic state of the ICM and the properties of cluster galaxies over the course of cosmic history. Our modelling can hence inform semi-analytic models of galaxy formation that have just begun to include AGN feedback [e.g. Croton et al., 2006], and provide crucial input for future hydrodynamic simulations that try to incorporate the growth of supermassive black holes both from the quasar- and the radio-mode.

The outline of this paper is as follows. In Section 2.2, we describe the characteristics of our simulation code and the numerical method adopted to introduce bubble heating. In Section 2.3 we analyse the AGN heating in isolated galaxy halos, spanning a wide range in mass, and we present some Chandra-like photon images of simulated bubbles. The effects of AGN heating in cosmological simulations of galaxy cluster formation is discussed in Section 2.4. Finally, in Section 2.5 we discuss successes and limitations of our model, and we present our conclusions.

2.2 Methodology

2.2.1 Basic code properties

Our simulations have been performed with the parallel TreeSPH-code GADGET-2 [Springel, 2005, Springel et al., 2001b]. We use the 'entropy formulation' for SPH suggested by Springel and Hernquist [2002], which manifestly conserves both energy and entropy when adaptive smoothing lengths are used. Besides gravitational and hydrodynamical processes, we include radiative cooling of the gas component, together with heating by a spatially uniform, time dependent UV background modelled as in Katz et al. [1996]. The gas consists of an optically thin primordial plasma of hydrogen and helium. In addition, a multiphase subresolution model for the treatment of star formation and associated feedback mechanisms has been adopted [Springel and Hernquist, 2003a]. In this model, stars form from dense cold gas clouds assumed to reside at pressure equilibrium in a surrounding hot phase of the interstellar medium. Supernova explosions heat the hot medium and evaporate cold clouds, thereby providing a self-regulation cycle for star formation, and a net pressurisation for the highly overdense ISM. Additionally, we use a simple prescription for metal enrichment, which assumes that each star-forming gas element can be locally approximated by a closed box model in which perfect and instantaneous mixing of metals between cold clouds and ambient gas occurs, as explained in detail in Springel and Hernquist [2003a].

2.2.2 Phenomenological description of AGN heating in clusters

Besides considering the physical processes already implemented in GADGET-2, we have implemented for this study a new model that accounts for heating by the central AGN in clusters of galaxies. This model does not attempt to provide a fully self-consistent ab initio treatment of the complex physical processes related to accretion onto supermassive black holes in clusters and the associated AGN activity. Rather, we try to mimic the observed phenomenology of hot bubbles in clusters directly in our simulations, without

addressing the jet physics that presumably inflates the bubbles in the first place. We therefore assume as a starting point that such bubbles are generated during phases in which an AGN is "switched on", and introduce them into the IGM in a phenomenological fashion. This allows us to study how the bubbles affect the properties of the central ICM as a function of their characteristics, in particular with respect to distributing their energy content to the surrounding cooler gas.

For definiteness, we assume in our model that a certain amount of thermal energy is injected in the form of centrally concentrated bubbles spaced in uniform time intervals. We parameterise this scheme in terms of the AGN duty cycle, the amount of energy $E_{\rm bub}$ injected, and by the radius $R_{\rm bub}$ and distance $d_{\rm bub}$ of the buoyant bubbles from the cluster centre, respectively.

We first test our scheme for AGN-heating on isolated, axisymmetric halo models. These systems are clean laboratories which permit us to compare directly with analogous modelling in the literature [e.g. Churazov et al., 2001, Quilis et al., 2001, Dalla Vecchia et al., 2004], and hence to evaluate whether SPH is suitable for such simulations. Moreover, these simplified models give us the possibility to explore straightforwardly and with comparatively low computational cost a large number of cases. In this way we can investigate the importance of different physical parameters of the bubbles, thus constraining their dynamical evolution and the heat transport into the ICM.

As a second step, we apply the model for bubble heating to fully self-consistent cosmological simulations of galaxy cluster formation. Here, we also investigate different redshift-dependent energy injection schemes, allowing us to gain some insight in how the AGN activity influences the hierarchical galaxy cluster growth and the characteristics of the central cluster galaxy, and to elucidate the relative importance of AGN heating with respect to the other physics included. We consider a set a galaxy clusters spanning a range in mass because we expect the efficiency of bubble heating to have a significant mass dependence.

Both for isolated halos and in cosmological simulations, we explored two different schemes for spatially placing the bubbles around the cluster centres. In the first scheme, the bubbles are introduced randomly within a sphere with a radius given by $d_{\rm bub}$ around the centre, while in the second approach, two symmetric bubbles are placed randomly along a fixed axis of length $2 \times d_{\rm bub}$, which has an orientation preserved in time during subsequent bubble events. The latter hence mimics a situation where the AGN jet that inflates the bubbles has directional stability over time, which could arise due to some coupling with the host galaxy's angular momentum, for example. At the present time there is no clear evidence either way concerning what is the preferred scenario, therefore our main aim is to investigate the possible differences in the ICM properties between these two bracketing scenarios.

2.2.3 Constraining the model parameters

Our choice for the values of $R_{\rm bub}$ and $d_{\rm bub}$ has been guided by observational constraints on X–ray cavities in clusters, and also by the values typically adopted in previous numerical works, for easier comparison. For simplicity, we restricted most of our simulations to the case where the values of $R_{\rm bub}$ and $d_{\rm bub}$ depend only on the mass of the halo under

consideration, and on the redshift in the case of cosmological simulations. Specifically, we adopted

$$R_{\rm bub} \propto M_{200}(z)^{1/3} \times \frac{1+z}{(\Omega_{0m}(1+z)^3+\Omega_{0\Lambda})^{1/3}}\,, \tag{2.1}$$

where $M_{200}(z)$ is the virial mass of the host galaxy cluster at given redshift of AGN activity, and the same scaling has been adopted for $d_{\rm bub}$. For the simulations of isolated halos, we used the same dependence of $R_{\rm bub}$ and $d_{\rm bub}$ on cluster mass, setting $z = 0$.

We study multiple bubble injection events in order to analyze how AGN heating couples with radiative cooling losses over a sufficiently long time interval. Thus, our modeling requires prescriptions both for the AGN duty cycle and for the time evolution of the energy content stored in the bubbles. However, most of the observed AGN-driven bubbles are found at low redshifts [e.g. Bîrzan et al., 2004], and only recently some observational evidence for X–ray cavities in more distant galaxy clusters has been found [McNamara et al., 2005]. Therefore, the properties and presence of radio-bubbles at higher redshifts, and their evolution with time, are observationally rather unconstrained. We hence limit ourselves in this work to simple parametric prescriptions for the evolution of $E_{\rm bub}$, derived from basic theoretical considerations and empirical laws, which hopefully bracket reality. Typically, we started injecting bubbles at redshift $z = 3$, which is the epoch that roughly corresponds to the peak of the comoving quasar space density, but we also tested an earlier epoch given by $z = 6$ for the start of the bubble activity. For our modeling of the evolution of $E_{\rm bub}$ with time, we adopted two scenarios with rather different behaviour. In the first one, most of the energy is released at late epochs, while in the second one, the bubble energy is coupled more closely to an assumed BH accretion rate (BHAR) model for the growth of the black hole population as a whole, such that the energy release is more pronounced at high redshifts.

More specifically, our first model is loosely motivated by the Magorrian relationship, which implies $M_{\rm BH} \propto \sigma^4$. A relation between the bubble mechanical luminosity and the black hole accretion rate, $\dot{M}_{\rm BH}$, can be derived by assuming that only a small fraction of the total bolometric luminosity thermally couples with the ICM. Hence, $L_{\rm bub} = f \times L_{\rm bol} = f \times \epsilon \dot{M}_{\rm BH} c^2$. The factor f sets the efficiency of thermal coupling with the ICM, and is typically assumed to lie in the range of 1-5%, while ϵ is the radiative efficiency factor. Assuming that the mechanical luminosity for Eddington-limited accretion is directly proportional to the black hole mass, the energy content $E_{\rm bub}$ of the bubbles is then proportional to $M_{200}(z)^{4/3}$, provided the mass of the central cluster galaxy scales self-similarly with the cluster mass. Hence, it follows that in this model the bubble energy content is determined by the mass assembly of the host galaxy cluster with time.

In our second scenario, we instead relate the amount of bubble energy to the average growth rate of supermassive central black holes. To describe the latter, we employ an estimate of the BHAR by Di Matteo et al. [2003], who give an analytic fit

$$\dot{\rho}(z) = \epsilon_{\rm BH} \frac{b \exp[a(z-z_m)]}{b-a+a\exp[b(z-z_m)]}\,, \tag{2.2}$$

for their numerical results, with the parameters $a = 5/4$, $b = 3/2$, $z_m = 4.8$, and $\epsilon_{\rm BH} = 3 \times 10^{-4} {\rm M}_\odot\,{\rm yr}^{-1}\,{\rm Mpc}^{-3}$. Thus, for every duty cycle of AGN activity we can directly relate

$\dot{M}_{\rm BH}$ with $E_{\rm bub}$ in the following way,

$$\frac{E_{\rm bub}}{E_{\rm norm}} = f \times \epsilon \times c^2 \int_{z_1}^{z_2} \dot{\rho}(z)\,{\rm d}z\,, \tag{2.3}$$

where a normalisation factor, $E_{\rm norm}$, has been introduced which we set such that the total energy injected over all duty cycles is the same in our two schemes. We note that the different temporal evolution of the BH mass in this approach implies a significantly reduced energy content of the bubbles at low redshifts. Finally, there is still one free constant of integration which we choose by requiring that the assumed mass of the black hole is the same at $z = 0$ in both scenarious.

A number of observational and theoretical works [e.g. Bîrzan et al., 2004, Sanderson et al., 2005, McNamara et al., 2005, Nulsen et al., 2005b,b, Donahue et al., 2005, Voit and Donahue, 2005] have constrained the plausible time interval between two successive bubble injection episodes to be of order of $\Delta t_{\rm bub} \sim 10^8$yrs. Clearly, $\Delta t_{\rm bub}$ could vary both for clusters of different mass and also in time, especially if the bubble activity is triggered by a self-regulated mechanism that operates between AGN feedback and the cooling flow. Nevertheless, given our simple phenomenological approach and lack of any better observational constraints, we adopt the value of $\Delta t_{\rm bub} = 10^8$yrs for all of our cluster simulations, independent of the cosmological epoch.

While some of our prescriptions for bubble parameters are motivated by "quasar-like" phenomena, our models are really meant to reflect a mode of feedback by supermassive black holes different from that of ordinary quasars. Instead of being triggered by mergers and being fueled with dense and cold ISM gas, the bubbles are a model for the radio activity observed in clusters. Note that there are also newly emerging theoretical models [e.g. Croton et al., 2006, Churazov et al., 2005] on how both quasar activity at higher redshifts and AGN-driven radio bubbles at lower redshifts can be described within a common unified framework. We will discuss this possibility in more detail in our conclusions.

2.3 AGN heating of isolated galaxy clusters

We here analyse simulations of isolated halos, consisting of a static NFW dark matter halo [Navarro et al., 1996, 1997] with a gaseous component that is initially in hydrostatic equilibrium and chosen to follow a density distribution similar to the NFW dark matter profile, but slightly softened at the centre according to

$$\rho_g(r) \;=\; \frac{r_s\, f_b\, \delta_0\, \rho_{\rm crit}}{(r + r_0)(1 + r/r_s)^2}, \tag{2.4}$$

where r_0 is a parameter introduced to mimic a gas core radius. The baryonic fraction is given by f_b, while $\rho_{\rm crit}$ is the critical density, δ_0 is the characteristic overdensity and r_s is the scale radius. The gas follows the equation of state of an ideal monoatomic gas with adiabatic index $\gamma = 5/3$. Besides, a certain amount of angular momentum has been imposed that can be quantified by the dimensionless spin parameter of a halo,

$$\lambda \;=\; \frac{J|E|^{1/2}}{GM^{5/2}}, \tag{2.5}$$

M_{200} $[h^{-1}\mathrm{M}_\odot]$	R_{200} $[h^{-1}\mathrm{kpc}]$	c	N_{gas}	m_{gas} $[h^{-1}\mathrm{M}_\odot]$	ϵ $[h^{-1}\mathrm{kpc}]$
10^{12}	206	12.0	3×10^5	4.0×10^5	1.0
10^{13}	444	8.0	3×10^5	4.0×10^6	2.0
10^{14}	957	6.5	3×10^5	4.0×10^7	5.0
10^{15}	2063	5.0	3×10^5	4.0×10^8	10.0
10^{15}	2063	5.0	1×10^6	1.2×10^8	6.5

Table 2.1: Numerical parameters of the isolated galaxy clusters. The first two columns give the virial mass and radius of the halos, evaluated at $200\,\rho_{\mathrm{crit}}$. The assumed values for the concentration parameter are in the third column, while the initial number and the mass of the gas particles is shown in the fourth and the fifth columns, respectively. The mass of the star particles is half that of the gas particles, because we set the number of generations of star particles that a gas particle may produce to two. Note that there are no parameters for the dark matter particles in these run, because we modelled the dark halo with a static NFW potential. Finally, in the last column, the gravitational softening length ϵ for the gas and star particles is given.

where J represents the angular momentum, M is the halo mass, and E its total energy.

The boundary conditions were chosen to be vacuum, i.e. both density and pressure are initially zero outside the virial radius (defined here as the radius enclosing a mean density equal to $200\,\rho_{\mathrm{crit}}$). We have simulated halos with a wide range of masses, with virial radii and concentration parameters as listed in Table 2.1. The baryonic fraction, $f_b = 0.12$, the spin parameter, $\lambda = 0.05$, and $r_0 = 0.02 R_{200}$ were kept fixed for all the halos. When evolved without radiative cooling, these initial models are perfectly stable for more than 1/4 of the Hubble time, as we explicitly checked. This is the timespan we subsequently consider in all our non-trivial simulations, both for the case with cooling and star formation only, and also for the case with additional AGN heating.

For the $10^{15} h^{-1}\mathrm{M}_\odot$ isolated cluster, our fiducial set of AGN heating parameters is (if not explicitly stated otherwise) $E_{\mathrm{bub}} = 5 \times 10^{60}\,\mathrm{erg}$, $R_{\mathrm{bub}} = 30\,h^{-1}\mathrm{kpc}$, $d_{\mathrm{bub}} = 50\,h^{-1}\mathrm{kpc}$, and a duty cycle of $\Delta t_{\mathrm{bub}} = 10^8\mathrm{yrs}$, all kept fix in time. The thermal energy injected in the form of bubbles has been estimated using the simple relations given in Section 2.2, assuming a $\sim (5 \times 10^8 - 3 \times 10^9)\mathrm{M}_\odot$ black hole in the cluster centre (depending on the thermal-coupling efficiency factor f). For the halos of lower mass, we assumed that the thermal content of the bubble is proportional to $M_{200}^{4/3}$, in analogy to our first scenario for scaling the bubble energy in a cosmological setting. This energy scaling is motivated by the well established observational relation between the black hole mass and the velocity dispersion of the stellar component of the bulge [e.g. Tremaine et al., 2002], given by

$$M_{\mathrm{BH}} = (1.5 \pm 0.2) \times 10^8\,\mathrm{M}_\odot \left(\frac{\sigma}{200\ \mathrm{km\ s^{-1}}} \right)^{4.02 \pm 0.32}, \tag{2.6}$$

and on the hypothesis that the central cluster galaxy scales self-similarly with the mass of the cluster itself. Even though these assumptions are certainly very restrictive, they provide us with a definite model that allows a straightforward interpretation of the trends

with mass, and supply some guidance for what to expect in full cosmological simulations. We also note that the recent numerical work of Di Matteo et al. [2003] suggests that, once the $M_{\rm BH}-\sigma$ relation is established with time, the black hole mass is proportional to $M_{\rm DM}^{4/3}$ of the host galaxy.

2.3.1 AGN heating of a massive galaxy cluster

In this section we concentrate on the effects of bubble heating on an isolated galaxy cluster of mass $10^{15}h^{-1}{\rm M}_{\odot}$, while we will discuss the relative importance of AGN heating as a function of mass in the next section. In Figures 2.1 and 2.2, we show maps of the projected mass-weighted temperature of the $10^{15}h^{-1}{\rm M}_{\odot}$ galaxy cluster, focusing on the central regions in order to highlight the morphology of the bubbles with different injection schemes and at various evolutionary stages. Both figures were obtained for simulations with cooling and star formation, and with AGN feedback of the same strength. However, in the left panel of Figure 2.1, the bubbles were placed randomly within a sphere of radius $d_{\rm bub}$, while the remaining three panels illustrate the case of two symmetrical bubbles injected simultaneously, containing half of the energy each, and with the injection axis preserved with time for different bubble cycles.

In Figure 2.2, we show results for simulations with the same feedback energy as in Figure 2.1, but this time the initial radius of the bubbles was two times larger and equal to $60\,h^{-1}$kpc. After being injected, the bubbles rise due to buoyancy and start to assume more elongated, "pancake-like" shapes, as clearly visible in the left panel of Figure 2.1. They continue to rise until the surrounding gas entropy becomes comparable to their entropy content, at which point they settle into an equilibrium and dissolve slowly with time. While rising, they push the intracluster gas above them, and also entrain some of the cooler central gas, transporting it to larger radii.

A closer comparison of Figures 2.1 and 2.2 makes it clear that the smaller bubbles with their significantly higher energy per particle result in more pronounced mushroom-like structures. Nevertheless, they do not shock the surrounding gas which, on the very top of the bubbles, forms cold rims. At late evolutionary stages, corresponding roughly to a quarter of the Hubble time, (see the right panel of Figure 2.2), a characteristic bipolar outflow is visible as a result.

In Figure 2.3, we analyse the global gas properties of the cluster in terms of radial profiles of density, temperature and entropy of the hot gas component, i.e. gas of the cold interstellar medium is not included in the plots[1]. Bubble injection modifies the inner $100\,h^{-1}$kpc substantially, reducing the density and increasing the temperature profile. Accordingly, the entropy of the central gas particles is changed as well, and an entropy floor is formed. The lower right panel of Figure 2.3 shows the mean gas inflow rate in the central $30\,h^{-1}$kpc. After a relatively brief period of time, AGN heating regulates, in a stable fashion, the flow of gas towards the centre, preventing the unrealistically high mass deposition rates of a fully developed cooling flow, which can reach up to $1200\,{\rm M}_{\odot}{\rm yr}^{-1}$ in the case without bubble heating. Even though a repeated injection of bubbles along the same spatial axis ("jet-like") is somewhat more efficient than a random placement within a sphere, the gas

[1]The 'cold' gas component has been defined here as all gas cooler than 1 keV and with a density higher than the star formation density threshold.

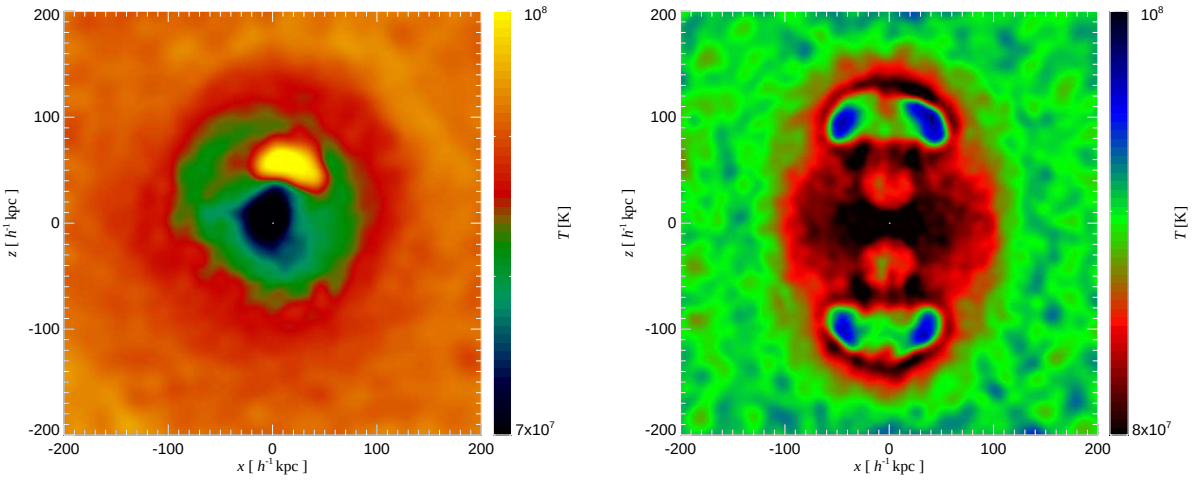

Figure 2.1: Projected mass-weighted temperature maps of the central regions of an isolated galaxy cluster of mass $10^{15}h^{-1}\mathrm{M}_{\odot}$. In the left panel, bubbles have been introduced with a random placement inside a spherical region, while in the right panel, a "jet-like" injection of bubbles is shown where two bubbles are placed opposite of each other, and subsequent generations of bubbles are injected along the same spatial axis. $E_{\rm bub}$, $R_{\rm bub}$ and $d_{\rm bub}$ in both cases are the same, and given by 5×10^{60}erg, $30\,h^{-1}$kpc and $50\,h^{-1}$kpc, respectively. The maps have been constructed for times of $\sim 1.4\,$Gyr and $\sim 0.8\,$Gyr after the beginning of the runs.

profiles have very similar trends in both cases, indicating the robustness of the results with respect to these details of the bubble injection scheme, at least in situations free of secondary effects due to infalling structures and mergers.

In Figure 2.4, we show unsharped masked maps of the X–ray emissivity of one of our cluster models. The X-ray emission has been estimated using the bremsstrahlung approximation,

$$L_{\rm X} = 1.2 \times 10^{-24} \frac{1}{\mu^2 m_p^2} \sum_{i=0}^{N_{\rm gas}} m_{{\rm gas},i}\ \rho_i\ T_i^{1/2} \quad [\mathrm{erg\,s^{-1}}]. \tag{2.7}$$

The unsharp-masking has been performed by subtracting from the original projected $L_{\rm X}$-map the same map smoothed on a $100\,h^{-1}$kpc scale. A large number of centrally concentrated ripples are clearly visible in the result. These ripples in the X–ray emissivity are sound waves generated by the expansion of the bubble after the thermal energy is injected. The sound waves travel through the cluster, and if the IGM has a residual viscosity they can be dissipated, providing a nonlocal heating of the central cluster volume. We note that we have explored different scales over which the smoothing in the unsharped masked technique is performed, obtaining the sharpest and most prominent features for smoothing scales corresponding to approximately $100\,h^{-1}$kpc, which by order of magnitude agrees with the dimension of the ripples themselves.

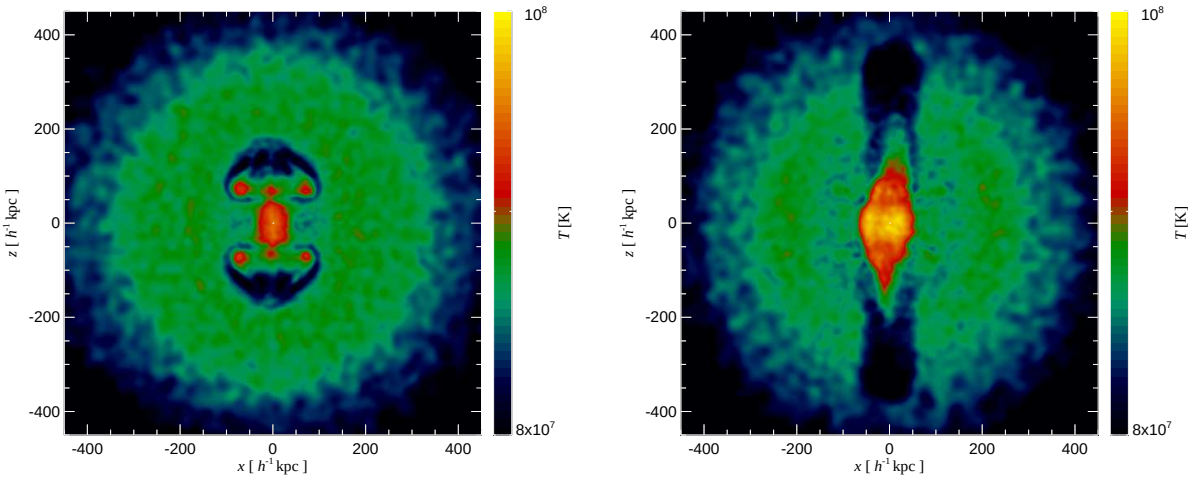

Figure 2.2: Time evolution of the isolated $10^{15}h^{-1}\mathrm{M}_{\odot}$ galaxy cluster with a jet-like AGN heating. The models are the same as in Figure 2.1, only the bubbles have two times bigger radii, namely $60\,h^{-1}$kpc. It can be noticed how the morphology in the central cluster region changes due to bubble-induced motions, from $\sim$ 1.8 Gyr (left panel) to $\sim$ 3.3 Gyr, when a well-defined bipolar outflow is clearly visible (right panel).

We find that the ripples reach distances of $\sim 800\,h^{-1}$kpc after 1 Gyr, translating to a velocity of order $\sim 10^3\,\mathrm{km\,s^{-1}}$, which matches the expected sound speed in the ICM of this cluster. At larger radii, the sound waves are not detectable any more. Note that we also expect that their velocity drops strongly in the outskirts of the cluster, where the temperature and hence the sound speed decline.

Upon closer inspection, it can be seen that the ripples are actually slightly offset from the cluster centre, with their midpoint directly matching the initial coordinates of the injected bubble. Moreover, the ripples progressively lose their intensity at larger radii, both due to a $1/r^2$ dilution of their intensity, and to a lesser extent, due to a damping caused by the residual viscosity of our SPH scheme. Note that some level of numerical viscosity is instrinsic to all SPH schemes, even though we are modelling an ideal gas. Quantifying the exact magnitude of the resulting effective viscosity is not trivial, also because it depends on the spatial resolution achieved in the simulations. However, recent observations of optical Hα-filaments [Fabian et al., 2003b] suggest that the gas in the central region of the cool-core cluster Perseus might be quite viscous, rather then turbulent [but see Ensslin and Vogt, 2005, for estimates of gas turbulence on smaller scales]. If ICM viscosity is relevant, it would imply a high rate of dissipation of the energy contained in the sound waves at small radii. This physical viscosity could be easily higher than the numerical viscosity we have in our simulations. Naturally, it is then desirable to treat the dissipation process accurately, which requires an SPH discretization of the Navier-Stokes equation combined with an assumed level of physical Spitzer-viscosity. Recently, first mesh-based studies of isolated clusters with viscosity and bubble heating have appeared [e.g. Ruszkowski et al.,

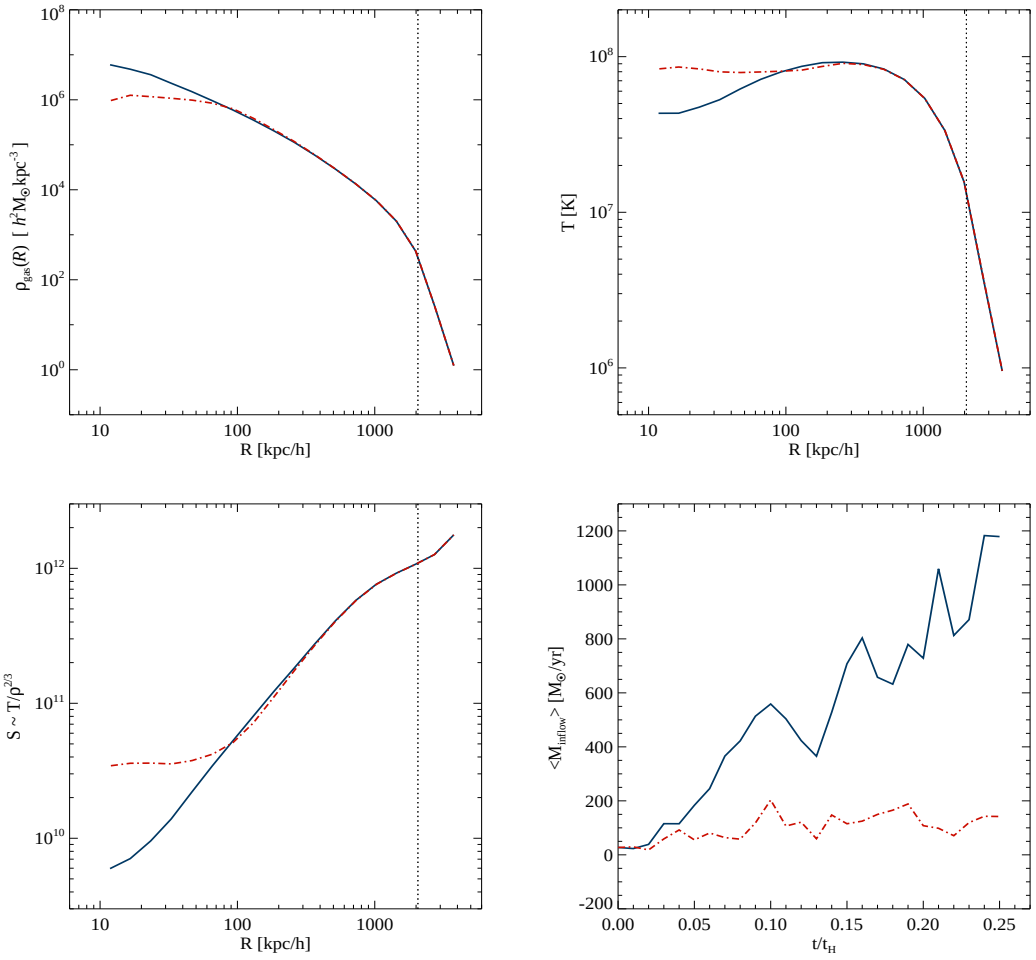

Figure 2.3: Radial profiles of gas density (upper left panel), temperature (upper right panel) and entropy (lower left panel) of the isolated $10^{15}h^{-1}\mathrm{M}_\odot$ halo. Blue lines: run with cooling and star formation. Red lines: AGN feedback mechanism also included (random placement of bubbles). The vertical dotted lines denote R_{200}. Lower right panel: Mean mass inflow rate in the central $30\,h^{-1}$kpc as a function of time, normalised to the Hubble time. It can be seen that the mass deposition rate onto the central galaxy is substantially reduced with AGN heating and stabilised at $\sim 150\,\mathrm{M}_\odot\mathrm{yr}^{-1}$ after a relatively brief period of time.

2004, Reynolds et al., 2005, Brüggen et al., 2005]. We plan to investigate this theoretical issue in a forthcoming study.

In Figure 2.5, we show the locus of selected particles in the $\log S - \log R$ plane, at a time equal to one quarter of the Hubble time (which marks the end of most of our isolated simulations). We selected only particles that at least once belonged to one of the injected bubbles. For easier comparison, the mean radial entropy profile of the AGN heated cluster (the same as in Figure 2.3) is plotted as a red dot-dashed line. The dots

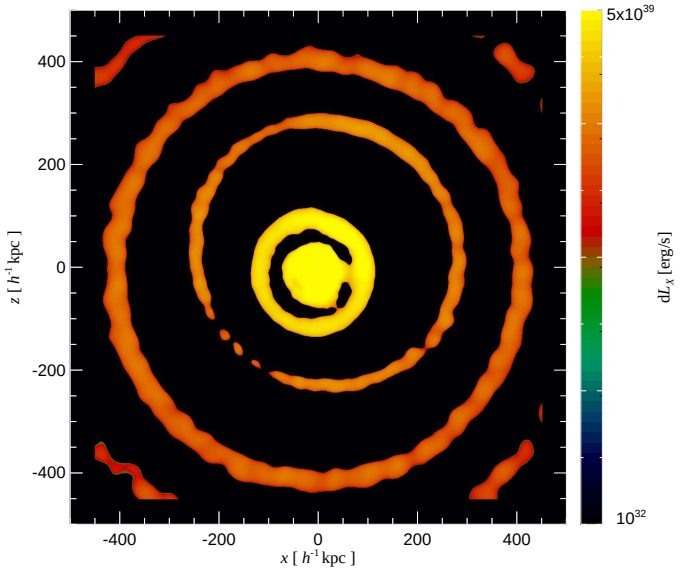

Figure 2.4: Unsharped masked map of the X–ray luminosity in the central region of the $10^{15}\,h^{-1}\mathrm{M}_{\odot}$ isolated halo, at time $\sim 2.2\,\mathrm{Gyr}$. The unsharped masking has been performed by subtracting a smoothed map from the original projected X-ray emissivity map, with the smoothing scale set to $100\,h^{-1}\mathrm{kpc}$. It can be seen that the AGN bubble heating generates a number of sound waves, which could gradually release their energy to the ICM if they are viscously damped on their way to the cluster outskirts.

shown for each individual bubble particle have been colour-coded according to their relative temperature. The particles of a recently injected bubble have the highest temperature values. As expected, their entropy values lie substantially above the average entropy of the cluster for the same range of radii, implying that the bubble will rise due to buoyancy. We thus expect these bubble particles to reach larger radii and to lose some of their thermal energy content during the rise, and this expectation is borne out by the cooler particles from older bubbles.

The radius at which the bubble particles attain the mean cluster entropy level is set by their initial density and thermal content after injection, by their capacity to shed some of the energy to the surrounding ICM, by their radiative cooling efficiency, and by the amount of mixing. Given that the different bubbles at various epochs have very similar initial temperature and mass, Figure 2.5 implies that the bubbles reduce their temperature almost by one order of magnitude, from the injection instant to the final equilibrium position. If we sum up the total energy injected over the entire simulated time, and assume that it gets thermalized over the whole cluster, we obtain that the gas particle temperature is increased by $\sim 0.2\,\mathrm{keV}$, which roughly corresponds to the bubble temperature decrement

mentioned above when the mass fraction of the bubbles is taken into account. Thus, it appears that the radiative cooling is not severe inside the bubbles, even though in the cluster as a whole it approximately balances the AGN feedback mechanism.

We extended our investigation by considering 'jet-like' injection of bubbles and also a scenario in which the bubbles are inflated in a continuous fashion over some time interval $t_{\rm inj}$. We tried values from $t_{\rm inj} = 5 \times 10^7$yrs to $t_{\rm inj} = 5 \times 10^8$yrs, which is significantly longer than the sound crossing time over the scale $R_{\rm bub}$ of the bubble. The maximum radius reached by the bubbles is essentially invariant in all of these cases, yielding $\sim 250 - 300\,h^{-1}$kpc at the final simulated epoch. Also, the heating efficiency of buoyant bubbles remains very similar, although the bubbles are somewhat more energetic in the continuous injection scheme, presumably because cooling losses are reduced here due to the expansion of the bubble before the bulk of the energy us released. This is directly reflected in an even lower mass deposition rate onto the central object, which always occurs in a stable fashion with time, where the gas cooling inflow is balanced by the AGN heating rate.

It is important to point out that the entropy content of the bubbles and the maximum distance they can reach from the cluster centre depend upon the equation of state assumed for the gas belonging to the bubbles. In all our models bubbles have been simulated assuming the equation of state of an ideal gas. However, radio observations indicate that AGN-driven bubbles contain relativistic particles which possibly dominate over the thermal pressure component, implying a softer equation of state. Moreover, the energy contrast of the individual bubbles is not very high in our approach, resulting in a gentle ICM heating, without presence of significant shocks. In fact, most of the observations of AGN-heated clusters point out that strong bubble-induced shocks appear to be absent, although recently a few clusters with moderate shocks in connection with AGN activity have been discovered [Fabian et al., 2003a, Nulsen et al., 2005b, McNamara et al., 2005]. Therefore, due to the assumptions of our model, the maximum possible distance reached by the buoyant bubbles in the cluster atmosphere may be underestimated with respect to the case where the relativistic particle component is modelled as well.

An important question is whether the bubbles are capable of raising cold gas from the cluster centre and mixing it with higher entropy gas at larger radii. Note that the X–ray observations of central metal abundance gradients put a constraint on the amount of gas mixing [Böhringer et al., 2004] in the centre. In order to address this issue, we analysed the gas metallicity distribution in the clusters. Without AGN feedback mechanism, all metals produced in the $10^{15}\,h^{-1}{\rm M}_\odot$ isolated halo are enclosed in the star forming region and are confined to the very centre, where the density is sufficiently high to allow star formation. The bubble heating instead produces both a reduction of the star formation rate by heating some of the gas that would otherwise end-up in the cold interstellar medium, and a spreading of metals away from the cluster centre. Moreover, in our simple model, the metals produced by the central stars are partly entrained and transported along with the bubbles to larger radii. The spatial distribution of the stars themselves is unaffected by the bubbles, however. It is important to note that the metal mixing in our model due to the bubbles represents a lower limit on the induced additional mixing, because fluid dynamical processes that produce small-scale mixing tend to be underresolved in cosmological simulations.

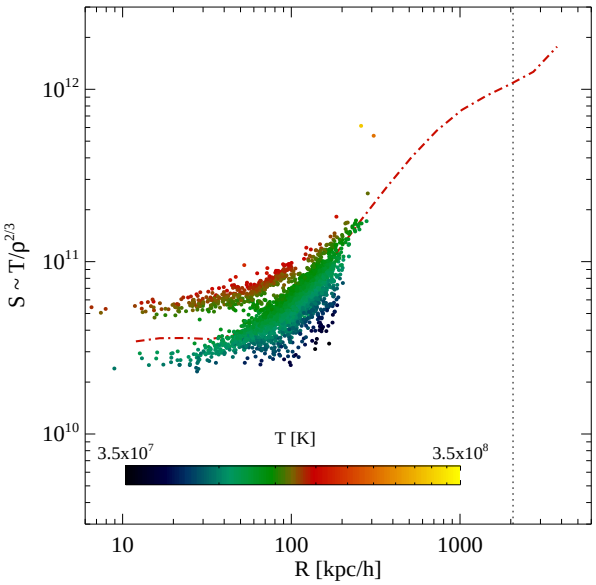

Figure 2.5: Mean radial entropy profile of the $10^{15}\,h^{-1}\mathrm{M}_{\odot}$ isolated halo. The result for the simulation with AGN feedback is given by the red dot-dashed line. The dots show the positions of the bubble particles, and they are colour-coded according to their temperature.

2.3.2 Efficiency of bubble heating in halos of different mass

The radiative cooling times of halos depend on their mass, both because of their different virial temperatures, and because of the temperature dependence of the cooling rate. Given that the masses of supermassive black holes, and hence our assumed bubble feedback, have a mass dependence as well, we expect a complex interplay between the different heating and cooling processes, and as a result a mass-dependent efficiency of the feedback. This non-linear dynamics can be best studied with detailed numerical analysis. To this end, we simulated isolated halos for a range of masses, starting from $10^{12}\,h^{-1}\mathrm{M}_{\odot}$ and reaching up to $10^{15}\,h^{-1}\mathrm{M}_{\odot}$, with the characteristics listed in Table 2.1. The case of the most massive halo has been discussed in some detail in the previous section, so that we can restrict ourselves here to highlight the differences that occur when the mass of the systems is lowered. The study of smaller halos gives also direct insight into the question of how bubble feedback may affect the hierarchical assembly of present-day massive clusters.

In our numerical simulations, the coupled dynamics resulting from cooling, subsequent star formation and a given heating mechanism is quite complex. The introduction of a certain amount of heating can in special situations even trigger an increase of the net cooling rate. For example, let us consider star-forming gas with a density higher than the density threshold set for star formation. If this cold gas component receives an amount of thermal energy from bubble heating that is insufficient to bring it back into the hot phase

(where most of the intracluster gas resides), then a counterintuitive process may occur. In this case, the thermal energy injection prevents the cold gas component from forming stars, but the local gas density will remain comparatively high, which in turn stimulates even larger radiative cooling losses. Thus, such a gentle heating, especially in low mass systems where radiative cooling is more pronounced, can in extreme cases even stimulate an increase of the cold gas component.

Analysing diagnostic phase-space diagrams like the $\log \rho - \log T$ plane, one can notice that for the $10^{15}\, h^{-1}\mathrm{M}_{\odot}$ halo the relative quantity of central cool gas is low, and it is promptly heated once bubble injection is switched on. Moreover, the energy per bubble particle is sufficiently high to push the gas into the "hot-phase" (upwards and to the left in the diagnostic diagram, as illustrated for the $10^{14}\, h^{-1}\mathrm{M}_{\odot}$ halo in Figure 2.6) and the star formation at late simulated epochs is completely quenched.

Examining the $10^{14}\, h^{-1}\mathrm{M}_{\odot}$ isolated halo, we find that bubbles are still very efficient in reducing the star formation rate, e.g. after the time $t_{\mathrm{H}}/4$, only 14% of stars are formed with respect to the run without AGN heating, but the total amount of cold gas, both in the central regions and out to R_{200}, remains very similar. The diagnostic diagram for this cluster is shown in Figure 2.6. The small orange dots are the gas particles for the run without AGN feedback, and they maintain practically the same position even when bubble heating is included. The big blue dots are those gas particles that belong to the 'cold phase', here defined as having temperatures less than 1 keV and densities higher than the density threshold set for star formation (as indicated by the vertical dotted line). With AGN heating included, the red dots denote the bubble particles, while the green star symbols give the locations of cold phase gas particles. Two different features due to the presence of bubble feedback are readily apparent. First, the cold gas fraction for the intermediate temperature range, from 5×10^5 K to 10^7 K, is substantially reduced in the case with feedback, because for most of these particles it is possible to transport them back to the hot phase. In contrast, along the line in the lower-right part of the diagram, there are more particles when bubble heating is included. This can be explained by the fact that this line is determined by the multiphase structure of the ISM, given here in terms of an effective mass-weighted mean temperature, which is a combination of the temperature of cold gas clouds and the one of the hot ISM component [see Springel and Hernquist, 2003a]. Hence, while the feedback mechanism reduces the number of stars formed, it produces a higher amount of interstellar gas with very low temperatures. Note that a large fraction of these cold gas particles have been a part of a bubble at some earlier epoch.

In the lower mass system of mass $10^{13} h^{-1}\mathrm{M}_{\odot}$, the final number of stars is also reduced, this time by only 13%, and, as well as in the previous case, the cold gas fraction is essentially unchanged. In the most extreme case of the $10^{12}\, h^{-1}\mathrm{M}_{\odot}$ halo, the bubble heating of the ICM is radiated away on a very short timescale without producing any substantial modification.

We considered different injection assumptions in order to test whether this effect can be alleviated and the bubble heating efficiency can be increased. Focusing on the most difficult case of the $10^{12}\, h^{-1}\mathrm{M}_{\odot}$ halo, we explored a range of injection energies, from 5×10^{56} erg per bubble, to 3×10^{57} erg. Also, we injected bubbles according to different schemes: in a spatially correlated 'jet-like' fashion, or by inflating the bubbles gradually for $t_{\mathrm{inj}} = 5 \times 10^7$yrs, i.e. by releasing the energy slowly instead of instantaneously. Finally,

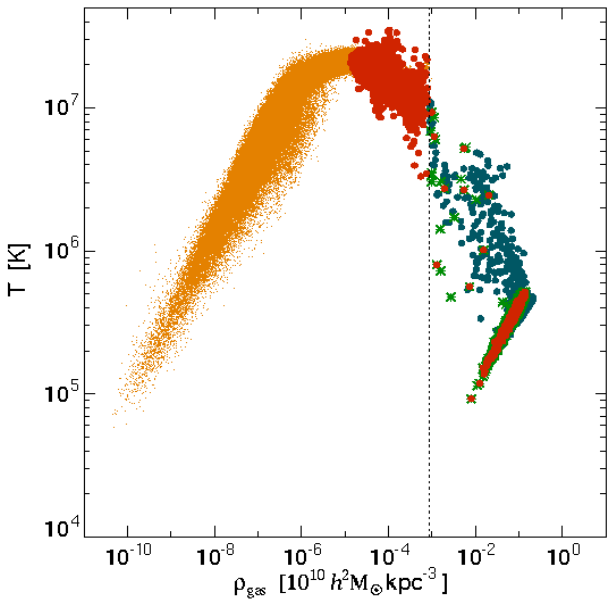

Figure 2.6: Phase-space diagram of gas temperature versus gas density for the $10^{14}\,h^{-1}\mathrm{M}_\odot$ galaxy cluster. Small orange dots are the particles outside the cold star-forming region, while big blue dots denote the gas particles in the run with no feedback, at high overdensities and with temperatures below 1 keV. Green star symbols are the particles satisfying the same criteria, but when the AGN heating is included. Finally, the position of the bubble particles is given by red dots.

we also tried a model where we artificially prevented bubble particles from cooling for $10^7 - 10^8$yrs, motivated by some observational evidences that the bubbles contain a non-thermal component, which would then be able to maintain its pressure longer. From these experiments we conclude that relating the bubble energetics to the underlying dark matter potential by invoking an assumed relation with its black hole mass, does not in general provide stable solutions for an efficient elimination of cooling flows in low mass systems. Unrealistically high bubble energies are required in order to offset the cooling flow, and also their thermal content has to be fine-tuned to a restricted range of values, otherwise AGN heating may easily become so strong that bubbles blow out substantial amounts of mass from the halo or cluster potential well.

This clearly indicates an important deficiency of bubble models like the one studied here. Since there is no internal trigger for bubble activity, a self-regulation loop is missing, but this will be required for stability in more general situations. Therefore, a more detailed physical scenario for the triggering of bubble activity is needed which couples the local physics of the cooling flow with the activity and energetics of AGN feedback. We will discuss a number of possibilities for this in Section 2.5.

2.3.3 Observational X–ray features of simulated bubbles

In the last few years, a growing number of observations performed with the Chandra X-ray telescope have found the presence of so called X–ray cavities in central galaxy cluster regions [e.g. McNamara et al., 2000, Fabian et al., 2000, Sanders and Fabian, 2002, Mazzotta et al., 2002, Bîrzan et al., 2004]. These observations support a scenario where relaxed cooling-flow/cooling-core clusters are heated due to the presence of a supermassive black hole at their centres. Hence, it is interesting to see whether the simulated bubbles produced by our model have morphologies comparable to the observed ones.

In order to perform this comparison accurately, it is necessary to produce artificial emissivity maps which are as similar as possible to realistic observations based on a finite exposure time on an X–ray telescope. Recently, a similar analysis has also been performed by Brüggen et al. [2005]. To this end, we processed selected simulation outputs with the X-MAS software package. A final result of this code is a photon event file quite similar to the one an observer would acquire with the Chandra telescope in ACIS-S3 mode. The instrument background has been included in our images by taking into account an appropriate blank-sky background file [Markevitch et al., 2001]. A detailed description of the X-MAS simulator can be found elsewhere [e.g. Gardini et al., 2004]; here we limit the description to the subsequent analysis steps performed and the significance of the maps obtained.

We have generated event files for different exposure times, ranging from 10 ks to 1 Ms, both for the runs with and without AGN feedback. We then selected a number of different energy bands, performed a Gaussian smoothing on a range of scales, and finally produced unsharp masked images to search for evidence of systematic departures of the flux from the mean. In Figure 2.7, we show photon images of the central region of the $10^{15}\,h^{-1}\mathrm{M}_{\odot}$ isolated halo[2], both in a case with and without additional AGN heating. The physical scale of the maps corresponds to ~ 670 kpc (2048pix), the energy band has been chosen to be $\Delta E = [0.3, 1.5]$ keV, and the maps have been smoothed by summing the pixel fluxes in bins of 4 pixels. For this ΔE, the instrument background is minimised and the features due to the presence of the bubbles are more evident.

The first panel of Figure 2.7 shows a photon image of the AGN-heated cluster after 100 ks of exposure time, before applying any smoothing. The rest of the plots have been created by Gaussian smoothing them first on a small scale (3pix), then re-smoothing the obtained image on a bigger scale (15pix), and finally unsharp masking the two smoothed images (i.e. subtracting off the 15pix smoothed version). The smoothing scales have been selected to maximise flux departures from the mean. The second and the third panel illustrate how the bubbles introduce emissivity irregularities for two different exposure times, 100 ks and 1 Ms, respectively. Finally, the fourth panel presents the cluster photon image after an exposure time of 100 ks and with no AGN feedback.

It is clear that the bubbles generate characteristic fluctuations in the photon counts, both creating bright features and X–ray depressions. The typical dimension of these irregularities is ~ 50 kpc, very similar to the size of the bubbles themselves. The hot spots can be

[2] We decided to perform this analysis on an isolated cluster in order to minimise other features in the X–ray emissivity that would have been imprinted by possible substructures or merger events. Further discussion of this issue in the cosmological framework is given in Section 2.4.5.

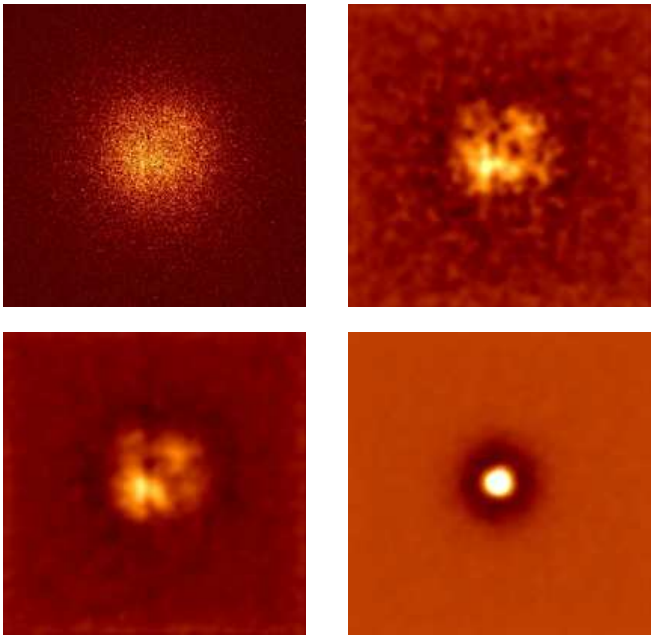

Figure 2.7: Artificial photon images for the $10^{15}\,h^{-1}\mathrm{M}_{\odot}$ isolated galaxy cluster obtained with the X-MAS software package. In all the panels, photons have been selected in the energy band $\Delta E = [0.3, 1.5]\,\mathrm{keV}$, maps were binned in 4pix/bin, and the physical scale of the maps is $\sim 670\,\mathrm{kpc}$. The cluster emissivity map before applying any smoothing is illustrated in the first panel, while all the other panels have been obtained by unsharp masking previously smoothed images, as explained in the text. The second and the third panels show qualitatively very similar features. They are for the run with AGN feedback and differ only in the exposure time. Finally, the fourth panel shows how the same cluster appears when the bubble heating is absent.

associated with the most recent bubble events, containing particles still significantly hotter than the surrounding ICM (as can be also seen from Figure 2.5), whereas the depressions in photon counts can be explained with previous bubble episodes. These peculiarities in emissivity are completely absent in the galaxy cluster without AGN feedback, indicating that they are real features and not artifacts produced by counting statistics or our analysis. The only feature that is present in the fourth panel of Figure 2.7 is the central excess due to the prominent cooling flow of $\sim 100\,\mathrm{kpc}$ size in diameter. Based on these results we conclude that in a relaxed galaxy cluster, departures from the mean flux stemming from bubbles with characteristics as given by our model can be detected, provided the exposure times are long enough, and provided that other sources of photon count deviations are absent or negligible.

2.4 Effect of AGN bubble heating in cosmological simulations

2.4.1 Simulation characteristics

As a next step in our analysis, we consider the importance of AGN feedback in full cosmological simulations of cluster formation. To this end, we selected a number of galaxy clusters with a wide range of masses from a parent dark matter simulation, and resimulated them with higher resolution including gas dynamics. Our hydrodynamical simulations account for cooling and star formation, and additional AGN heating as well. In a subset of our runs, we also included galactic winds powered by star formation, as implemented by Springel and Hernquist [2003a]. Models with winds provide a better description of some galaxy cluster properties, e.g. the distribution of metals, but in order to be able to cleanly identify the effects of bubble heating, we focus most of our analysis on simulations without winds. Where appropriate, we will however briefly discuss any changes of our results when winds are also included.

Our primary series of simulations consist of resimulations of a cluster extracted from the GIF ΛCDM simulation [Kauffmann et al., 1999]. We selected the second most massive galaxy cluster from this simulation and constructed higher resolution initial conditions for it using the "Zoomed Initial Conditions" technique [Tormen et al., 1997]. We carried out two runs with different resolution in order to test numerical convergence of our results. These clusters are equivalent to the ones used by Springel et al. [2001a], but with gas (from now on we will refer to these runs as S1 and S2, respectively). The simulations have been evolved from an initial redshift of $z_{\rm ini} = 30$ for S1, and $z_{\rm ini} = 50$ for S2, producing 25 outputs uniformly spaced in the logarithm of the expansion factor. Additionally, we selected two other clusters with final virial masses substantially smaller (g676) and bigger (g1) than the S1/S2-cluster. These clusters have been extracted form a cosmological ΛCDM simulation of box-size $479\,h^{-1}$Mpc [Yoshida et al., 2001, Jenkins et al., 2001], and again have been resimulated with the ZIC technique at higher resolution [Dolag, 2004].

The simulation of the g1 galaxy cluster includes several other smaller systems in the high-resolution region which we also included in our analysis. Tables 2.2 and 2.3 provide a summary of the main properties of our set of simulated galaxy clusters. In all runs, the cosmological parameters were that of a flat concordance ΛCDM model, with $\Omega_m = 0.3$, $\Omega_\Lambda = 0.7$, $\Omega_b = 0.04$, a normalisation of the power spectrum given by $\sigma_8 = 0.9$, and a Hubble constant at the present epoch of $H = 70$ km s^{-1} Mpc^{-1}.

Unlike simulations of isolated clusters, cosmological simulations require a special algorithmic method for placing bubbles, since the position of the cluster centre and properties like virial mass are not known a priori, and change with time. To address this problem, we run for every AGN duty cycle a fast parallel FOF group finder on the fly as a part of the simulation code, obtaining a list of all halos with their basic properties. We then adopt two different schemes for injecting bubbles. We either consider only the most massive halo found in the high-resolution zone, which can be identified with the most massive progenitor of the final cluster, or we introduce AGN-driven bubbles in all halos above a given fixed mass threshold value. The injection of bubbles in all large halos is motivated by the observational indications that probably most if not all of the spheroidal galaxies harbour a supermassive black hole at their centres. Note that the larger number of bubbles in this second scenario can also cause additional effects during merger events, where bubble

Simulation	$N_{\rm HR}$	$N_{\rm gas}$	$m_{\rm DM}$ $[h^{-1}{\rm M}_\odot]$	$m_{\rm gas}$ $[h^{-1}{\rm M}_\odot]$	$z_{\rm start}$	$z_{\rm end}$	ϵ $[h^{-1}{\rm kpc}]$
S1	450088	450088	5.96×10^9	0.92×10^9	30	0	14.5
S2	1999978	1999978	1.18×10^9	0.18×10^9	50	0	8.5
g676	314518	314518	1.13×10^9	0.17×10^9	60	0	5.0
g1	4937886	4937886	1.13×10^9	0.17×10^9	60	0	5.0

Table 2.2: Numerical parameters of the cosmological galaxy cluster simulations used in this study. The values listed from the second to the fifth column refer to the number and to the mass of high resolution dark matter particles and of gas particles. Note that the actual values of $N_{\rm gas}$ and $m_{\rm gas}$ vary in time due to star formation. The last three columns give the initial and final redshifts of the runs, and the gravitational softening length ϵ.

Cluster	R_{200} $[h^{-1}{\rm kpc}]$	M_{200} $[h^{-1}{\rm M}_\odot]$	$T_{\rm mw}$ $[K]$	$T_{\rm ew}$ $[K]$	$L_{\rm X}$ $[{\rm ergs}^{-1}]$
S1	2427	9.98×10^{14}	5.2×10^7	8.7×10^7	9.8×10^{44}
S2	2466	1.05×10^{15}	5.1×10^7	8.8×10^7	9.9×10^{44}
g676	1176	1.13×10^{14}	1.4×10^7	2.6×10^7	1.6×10^{43}
g1_a	2857	1.63×10^{15}	7.3×10^7	1.3×10^8	1.0×10^{45}
g1_b	1914	4.89×10^{14}	3.1×10^7	4.1×10^7	1.2×10^{44}
g1_c	1448	2.12×10^{14}	1.5×10^7	2.5×10^7	3.0×10^{43}
g1_d	1258	1.39×10^{14}	1.6×10^7	1.9×10^7	1.8×10^{43}
g1_e	1085	8.92×10^{13}	1.1×10^7	1.6×10^7	7.0×10^{42}

Table 2.3: Physical properties of our sample of simulated galaxy clusters at $z = 0$ and at $200\rho_c$. For different galaxy clusters, labeled in the first column, cluster radius, total mass, mass– and emission–weighted gas temperature and X–ray luminosity are listed, respectively. Note that the values refer to the simulations with cooling and star formation, without bubble heating included.

material can be torn apart and mixed into outer regions of the cluster.

2.4.2 Global gas properties of simulated galaxy clusters

Before analysing the properties of simulated galaxy clusters with and without AGN bubble heating, we briefly discuss issues of numerical convergence. For this purpose we consider the S1 and S2 runs, and compare their spherically averaged radial profiles at two epochs, namely at $z = 3$ and $z = 0$[3]. The dark matter and stellar density profiles of the S1 and S2 galaxy clusters are in excellent agreement at both epochs, as well as the gas density profiles, with the residual differences at early times being consistent with what is expected from the increased noise. Both the emission-weighted and the mass-weighted temperature

[3]These two epochs delimit the time interval during which the bubble heating is active, and hence the period of time where our analysis is performed.

profiles do not noticeably differ at low redshifts, while there is a hint a of slightly higher gas temperature for the S2 cluster at early times. Thus, we conclude that for radii larger than the gravitational softening length the properties of our simulated galaxy clusters are numerically robust and have converged quite well.

In Figure 2.8, we compare the gas entropy profiles with and without bubble heating at three different epochs, $z = 1.64$, $z = 0.44$ and $z = 0$. For this comparison, we use both of our AGN heating models, the one based on the Magorrian relationship and the "BHAR model". The entropy has been estimated by calculating the ratio of the emission-weighted temperature to the gas density elevated to the 2/3 power, where the temperature is measured in Kelvin and the gas density is given in $h^2 \mathrm{M}_\odot \mathrm{kpc}^{-3}$. We selected only the hot gas component to compute these profiles, i.e. we avoided the cold, star-forming gas by imposing a cut in density and ionisation level. With this choice, the gas profiles are smoother because they have no contributions from cool substructures at various radii. Nonetheless, it is also important to investigate the fate of the cold gas in the central cluster region, an issue we will address separately in Section 2.4.3. The blue continuous lines are for the run without AGN feedback, the red dot-dashed lines correspond to the "Magorrian model", while the green dashed lines are for the "BHAR model". The vertical dotted lines denote the softening length and the virial radius at the different epochs, respectively. When $E_{\rm bub}$ is computed from the "BHAR model", the effect of bubbles is less prominent at low redshifts than in our other AGN heating scenario. However, at early times the situation is opposite, as expected. Here the "BHAR model" heats the ICM gas more prominently, right from the initial injection epoch ($z = 3$) until $z \sim 0.4$. It is interesting to note that at $z \sim 0.4$ the bubble energy content is already much lower than in the "Magorrian model", indicating that the efficient heating at early times has a prolonged effect on the thermodynamic state of the galaxy cluster. We find that the "Magorrian model" starts to affect the gas entropy from $z \approx 1.6$ in a noticeable way and it becomes very important at late times, where it suppresses the cooling flow completely at $z = 0$.

As a further comparison, we show in Figure 2.9 radial profiles of gas density, temperature, X–ray luminosity, and local cooling time for the S1 galaxy cluster at $z = 0$. AGN heating alters the gas properties out to a radius of $\approx 300\, h^{-1}\mathrm{kpc}$, reducing the central gas density and increasing its temperature. The X–ray emissivity, being more sensitive to the gas density, is substantially lower when bubble feedback is active. In the lower-right panel of Figure 2.9, we show the cooling time of all ICM gas, estimated isobarically as [Sarazin, 1988]

$$t_{\rm cool} = 8.5 \times 10^{10} \left(\frac{n_p}{10^{-3}\,\mathrm{cm}^{-3}} \right)^{-1} \left(\frac{T}{10^8\,\mathrm{K}} \right)^{1/2} [\mathrm{yrs}], \tag{2.8}$$

where n_p is the number density of hydrogen. When AGN heating is not included, the cooling radius, i.e. the radius where $t_{\rm cool} = t_{\rm H}$, lies at $\sim 60\, h^{-1}\mathrm{kpc}$, while it gets reduced to $\sim 25\, h^{-1}\mathrm{kpc}$ in our "BHAR model". However, the cooling radius vanishes for the "Magorrian model", where the bubbles injection heats the gas above 1 keV.

Even though the spatial extent of the bubble particles reaches out to the virial radius of the cluster, they are not capable of heating the gas in outer regions, simply because their entropy content becomes comparable to the entropy of the surrounding ICM gas at intermediate radii. This finding is analogous to the previously discussed case of isolated halos, but the dynamical evolution of the cluster with its associated merger processes

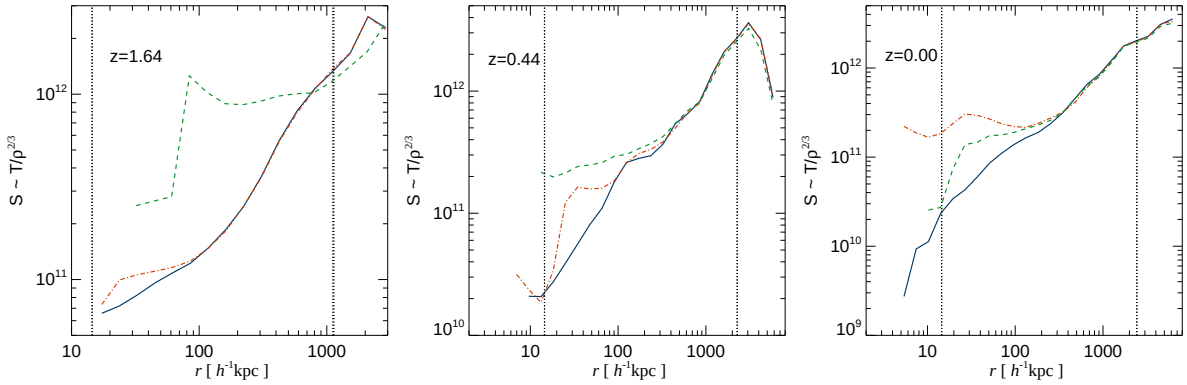

Figure 2.8: Radial profiles of gas entropy of the S1 galaxy cluster simulation. The blue continuous lines are for the run with cooling and star formation only, the red dot-dashed lines refer to the case when AGN heating based on our "Magorrian-like scheme" is included as well, while the green dashed lines are for the BHAR-based model. The dotted vertical lines denote the gravitational softening and the virial radius at the given redshift; the latter is indicated in the upper-left corner. The profiles do not extent down to vanishingly small radii because they have been calculated exclusively from the hot gas component (basically the gas above 1 keV), excluding the cold dense gas in the centre. Note that both the spatial and the entropy scale vary between the three different panels.

makes spreading of bubble material towards the outskirts more efficient.

In Figure 2.10, we show emission-weighted temperature maps of the g676 galaxy cluster at four different epochs, in order to more closely discuss the spatial distribution of bubbles during merger events. The over-plotted dots represent the particles that at least once belonged to a bubble, and they are colour-coded according to their temperature, the darkest ones are particles with $T > 10^8\,\mathrm{K}$, while the lightest have $T < 10^4\,\mathrm{K}$. For this analysis, we have introduced AGN feedback in all halos above $5 \times 10^{10} h^{-1}\mathrm{M}_\odot$ and we scaled the energy content of the bubbles with $M_{200}^{4/3}(z)$ of the host galaxy cluster.

In the first panel at redshift $z = 0.86$, there is a smaller halo on the lower right corner which enters the most massive cluster progenitor at that epoch (which roughly has three times larger mass), which is located at the centre of the panel. Both the massive halo and the smaller one are AGN heated, but the bubbles are less energetic for the infalling halo due to our assumed mass dependence. Moreover, it can be noticed that the bubbles occupying the central regions are hotter, both because they are more recent and thus have had less time to lose their energy content, and also because at later times bubbles are intrinsically more energetic in our "Magorrian scenario". The second panel of Figure 2.10 (at $z = 0.62$) illustrates what happens to the bubble distribution when the smaller halo is crossing the central region of the massive cluster. The bubbles are literally pushed out of the way, upwards and to the right, and they are also heated. The next panel (at $z = 0.48$) shows that the bubble distribution is still quite asymmetric, but at the same time, bubbles have spread efficiently into outer regions and also have cooled. Finally, the last panel

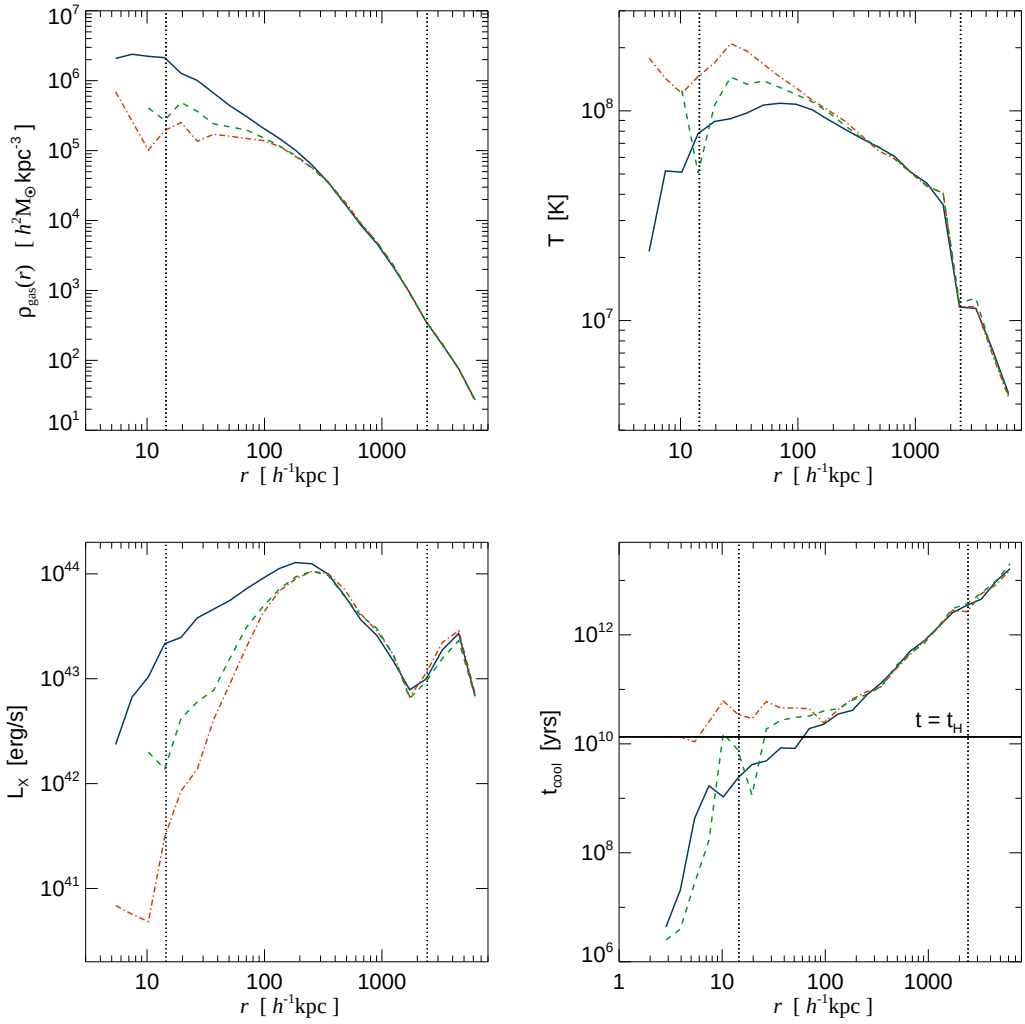

Figure 2.9: Radial profiles at $z = 0$ of gas density (upper-left panel), emission-weighted temperature (upper-right panel), and X–ray luminosity (lower-left panel) estimated with the bremsstrahlung approximation given by eq. (2.7). The lower-right panel shows the cooling time of all gas particles as a function of radius, computed using eq. (2.8). The continuous horizontal line indicates the Hubble time at $z = 0$. The blue continuous lines are for the case without AGN feedback, the red dot-dashed lines are for the model where $E_{\rm bub} \propto M_{200}^{4/3}(z)$, while the green dashed lines are for the scenario where the bubble energy depends on the BHAR given by eq. (2.3).

shows how the cluster appears at $z = 0.20$, where it starts to be fairly relaxed with a quite symmetric distribution of bubbles.

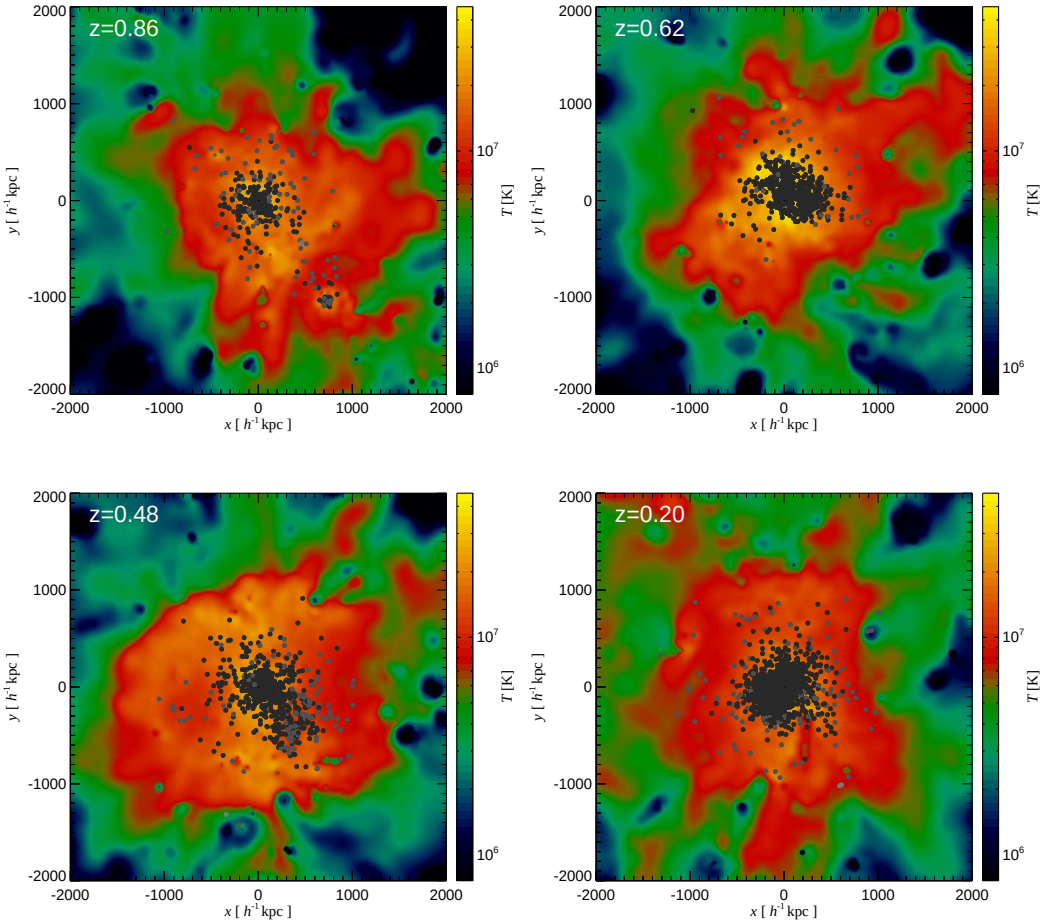

Figure 2.10: Emission-weighted temperature maps of the g676 galaxy cluster simulation during a major merger event at $z = 0.86$, 0.62, 0.48 and 0.20, respectively. Over-plotted dots represent gas particles that have been at least once part of a bubble, and they are colour-coded according to their temperature, the darkest ones being the hottest. It can be noticed that both the spatial distribution of bubbles and their energy content are drastically influenced by the passage of the smaller halo through the central region of the massive cluster.

2.4.3 Stellar properties of galaxy clusters

In this section, we analyse the effects of AGN heating on the properties of the stellar components of galaxy clusters. We concentrate on the properties of the central cluster galaxy, which is the one affected most by the bubble heating. From the initial injection epoch ($z = 3$) until $z = 0$, we compute for this purpose the stellar and gaseous mass, star formation rates, stellar ages, and colours of the cD galaxy that sits in the main progenitor of our final halo.

In Figure 2.11, we show a histogram of the formation times of stars belonging to the cD

galaxy at $z = 0$ of our S1 galaxy cluster. The histograms have been computed by binning the expansion factors that correspond to each stellar formation time, and they have been normalised to the maximum bin. The white histogram is for the run without AGN heating, the grey coloured one for the "Magorrian model", while the hatched histogram gives the result for "BHAR model". When AGN heating is absent, the histogram of stellar formation redshifts clearly shows an extended tail at low redshifts; together with the considerable SFR of order of $100\,\mathrm{M}_\odot\mathrm{yr}^{-1}$, this implies that stars are formed until $z = 0$ in situ. Nevertheless, there is a possibility that some of these stars have been formed elsewhere, e.g. in merging substructures, and that they only ended up later in the cD galaxy by merging. For redshifts less than 0.3 this is certainly not an important mechanism, because in our "Magorrian model", the central SFR is completely suppressed for $z < 0.3$ and at the same time the z_{sf} histogram is truncated. Thus, the difference of $\sim 6 \times 10^{11} h^{-1}\mathrm{M}_\odot$ in the stellar mass of the final cD galaxy in these two cases gives an indication on how many stars have formed in the cD galaxy from $z = 0.3$ until today, when AGN feedback is not present. At the same time, also the mass of the cold gas (below 1 keV) is reduced in the "Magorrian model", from $\sim 2 \times 10^{10}\, h^{-1}\mathrm{M}_\odot$ to zero. Moreover, the suppression of star formation at late times has an immediate effect on colours of the cD galaxy, which becomes redder. To estimate the colours we used Bruzual & Charlot's stellar population synthesis models [Bruzual and Charlot, 2003], computing rest-frame magnitudes in the SDSS bands, assuming Solar metallicity and a Chabrier initial mass function. The u-band magnitude is changed from -23.8 to -22.8 and the $u - r$ colour is increased from 2.0 to 2.6.

In contrast, the star formation of the "BHAR model" proceeds in a quite different manner, as can been seen from the hatched histogram, which is substantially lower for $0.4 < z < 2.0$, but quite similar to the case without AGN feedback at very low redshifts, $z < 0.3$. The first feature arises due to two different processes happening at the same time. The second peak present in the histograms is due to a major merger event that happens roughly at $z = 1$. One consequence of this merger event is a central burst of star formation, which happens to be absent in the "BHAR model" due to its very efficient bubble heating at this epoch. Nonetheless, there are still some stars becoming part of the cD galaxy at $z = 0$ that have formation times in the corresponding time interval. Tracing back these stars in time and considering that the SFR of the cD galaxy in the "BHAR model" during this epoch is practically zero, we see that these stars have been produced in other small galaxies and were indeed accreted onto the central cD galaxy at later times. Assuming that a similar amount of stars accreted onto the cD galaxy also in the case without AGN feedback, a total mass of $\sim 10^{12}\, h^{-1}\mathrm{M}_\odot$ in stars has formed in situ between $z = 2$ and $z = 0.4$, with a considerable part created as part of the central starburst induced by the major merger event.

The tail at low redshifts present in the hatched histogram can be explained by the reduced energy content of the bubbles, which are not efficient any more in suppressing the cooling flow, and consequently the star formation in the central cD galaxy. The total SFR within R_{200} follows a similar trend as the SFR of the cD galaxy, with comparable systematic differences for the different runs, implying that the bubble heating mainly affects the central stellar properties and not the residual star formation in the cluster volume.

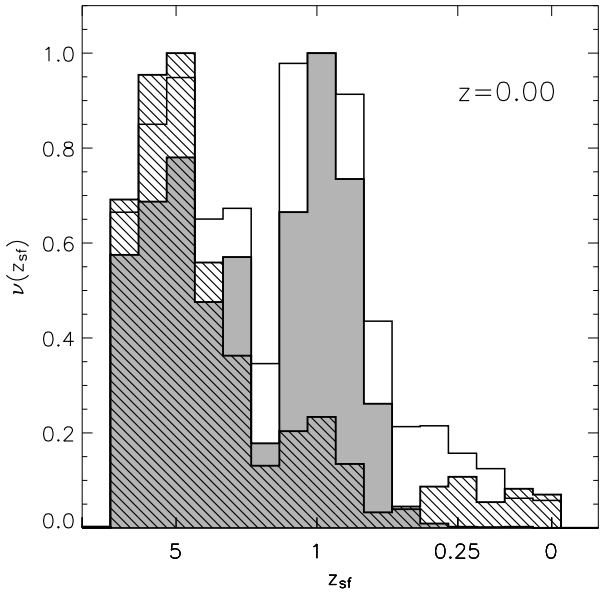

Figure 2.11: Distribution of formation redshifts of the stars belonging to the cD galaxy of the S1 galaxy cluster at $z = 0$. The white histogram corresponds to the case with cooling and star formation only; here it can be seen that stars continue to be formed until $z = 0$. The grey coloured histogram shows how the stellar formation times change when our "Magorrian model" of bubble heating is switched on, which essentially suppresses any central star formation for $z < 0.25$ completely. Finally, the result for the "BHAR model" of AGN feedback is illustrated with the hatched histogram, which shows a considerable suppression of central star formation at intermediate redshifts, $0.3 < z < 2.0$.

2.4.4 The metallicity distribution in the simulated clusters

In this section, we analyse the metal distribution in our simulated galaxy clusters. It is a well known problem that numerical simulations which include cooling and star formation processes in general fail to reproduce the observed shallow metallicity gradients, especially so if efficient feedback mechanisms that help spreading the metals are absent. In particular, metals produced by stars remain locked in the dense, star forming regions, even though supernovae feedback is included which regulates the star formation process itself. As a result, the metallicity distribution remains lumpy and exhibits a rather step gradient. Moreover, most of the metals are produced in the central cD galaxy due to its excessive star formation, which is a manifestation of the cooling flow problem.

This motivates the search for physical feedback processes that can spread and mix metals more efficiently, acting both in the central region and on the scale of the whole galaxy cluster. While the galactic wind model suggested by Springel and Hernquist [2003a] helps in reducing this discrepancy and also diminishes the total SFR over cosmological time,

the model fails to qualitatively change the gas and stellar properties of galaxy clusters discussed in Sections 2.4.2 and 2.4.3. Especially at late times, mixing of metals due to winds from the cD galaxy proves inefficient; here the cluster potential well is simply to deep and the ram pressure of the ICM too high to allow winds to travel far. Bubble heating may fare considerably better in this respect. In the following we therefore analyse the effect of AGN on the metal distribution in our simulations, and we also compare simulations with or without galactic winds of velocity $\sim 480\,\mathrm{km\,s^{-1}}$.

In Figure 2.12, we show radial profiles of the gas metallicity of the S1 galaxy cluster, and in Figure 2.13 we illustrate the corresponding mass-weighted gas metallicity maps. When additional feedback mechanisms are taken into account, the amount of metals in the hot gas component is increased with respect to runs with cooling and star formation only (continuous blue line on Figure 2.12 and left panel of Figure 2.13). Also, the metallicity distribution becomes less lumpy because the metals are more efficiently transported out of the dense regions, increasing the fraction of enriched gas. It can be noticed that already bubble heating without winds (red dot-dashed line in Figure 2.12, and middle panel of Figure 2.13) is capable of producing a more homogeneous metallicity distribution, while the AGN heating coupled with the galactic winds (green dashed line in Figure 2.12 and right panel of Figure 2.13) slightly decreases the radial metallicity gradient and makes the spreading of the metals even more efficient.

Nevertheless, the total amount of metals in the three different ICM phases – hot ICM gas, cold star-forming gas, and stars – remains very similar in all runs, implying that there are no substantial metal-enriched gas outflows from the galaxy cluster itself. The situation can be rather different if winds with similar velocities are present in less massive systems, as demonstrated by Springel and Hernquist [2003a]. When the galactic wind velocities become comparable to the escape velocity from the system in consideration, then the winds may lead to gaseous outflows, eventually polluting the surrounding medium with metals produced by cluster stars. The heating provided by bubbles might help the metal spreading even more. Considering our "BHAR model" at early times where it is very efficient and when the corresponding halo mass is considerably smaller, there is evidence that not only many metals are transfered into the "hot phase", but also that metal enriched gas is pushed towards the cluster outskirts, and in part beyond the virial radius. However, this effect is transitory, because E_{bub} decreases with time, and more importantly, because the forming cluster is so massive that it behaves effectively like a closed box at late times. Consequently, at $z = 0$, the distribution of metals looks quite similar to the "Magorrian model" discussed above. Finally, note that even though bubble heating improves metal spreading in the ICM, at the same time it does not disrupt the central metallicity gradient of the galaxy clusters, as can be clearly seen from Figure 2.12. Therefore, our AGN heating prescription is qualitatively in good agreement with the metallicity gradients observed in cool core clusters [e.g. Böhringer et al., 2002, De Grandi et al., 2004, Böhringer et al., 2004].

2.4.5 Sound waves or merger induced weak shocks?

While the unsharp mask technique is very useful in detecting X-ray cavities and associated sound waves, it is potentially easy to confuse these ripples with shock waves stemming from

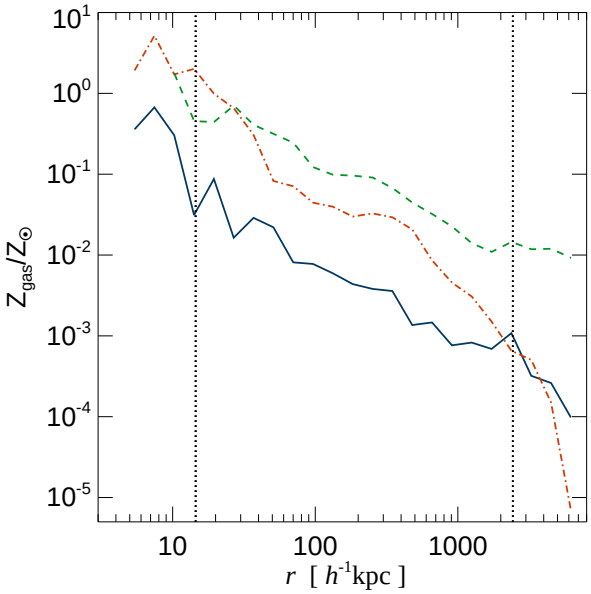

Figure 2.12: Radial profiles of the gas metallicity of the S1 galaxy cluster. Only the diffuse hot gas component has been used to estimate the metallicity, which is given in Solar units. The blue solid line is for the run without AGN heating, the red dot-dashed line is for bubble injection based on our "Magorrian model", while the green dashed line is also for the "Magorrian model" but with additional inclusion of feedback by galactic winds. We can see that the feedback processes manage to better spread the metals into the diffuse ICM gas, and the increased mixing leads to a less clumpy metallicity distribution.

merger events. To demonstrate this danger in interpreting observations, we here analyse a specific case where the presence of smaller systems passing trough the cluster might induce such a misleading conclusion.

To this end, we computed projected maps of the S2 galaxy cluster without AGN heating at $z = 0.13$. At this time, two substructures at radial distances of about half the virial radius are moving towards the centre. These substructures are still visible in the gas density map (upper right panel of Figure 2.14), but almost completely vanish when the X–ray luminosity map is computed. Nevertheless, when the unsharp masking procedure is applied to the L_X map, a two-lobed feature is clearly visible (upper left panel of Figure 2.14). Even though this feature at first glance looks strikingly similar to the ripples produced by bubble heating events, it is exclusively a product of the specific spatial geometry of the substructures in the cluster, and is also enhanced due to projection effects.

In the mass-weighted temperature map (lower left panel of Figure 2.14), two spherical regions can be noticed that are slightly cooler than their surroundings. They correspond to the two substructures. Especially around the substructure in the lower right part of

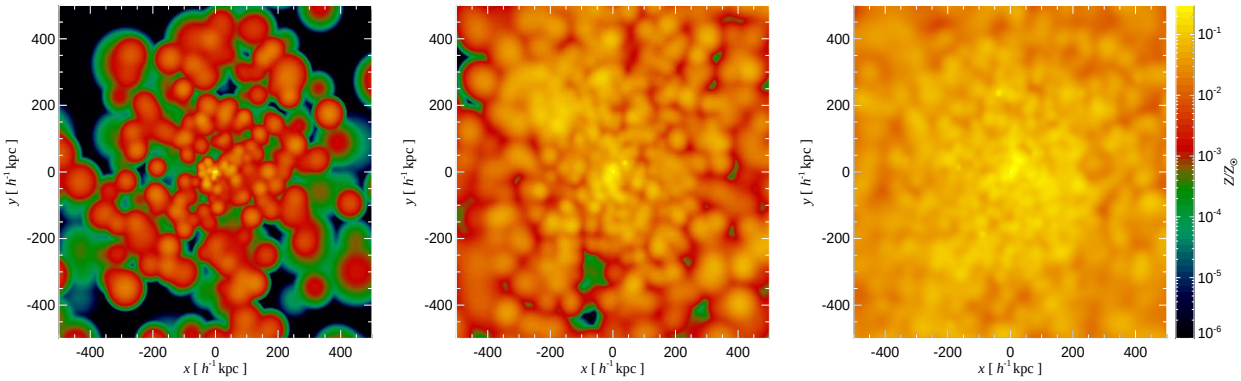

Figure 2.13: Mass-weighted gas metallicity maps of the S1 galaxy cluster at $z = 0$. The left panel corresponds to the case with cooling and star formation only. The middle panel shows how the metallicity of the hot gas component changes when AGN heating (here the "Magorrian model" was assumed) is included, while the right panel illustrates the case where in addition galactic winds with a velocity of $\sim 480\,\mathrm{km\,s^{-1}}$ were included, making the metallicity distribution more homogeneous.

the map, hotter surrounding gas can be seen. To distinguish between a cold front or a shock, we can analyse the pressure of the surrounding gas and compute the Mach number map[4] (lower right panel of Figure 2.14). A clear jump of pressure in the region adjacent to the hot gas around the substructure together with the mildly supersonic motion of the substructure indicates the presence of weak shocks. Note that these shocks cannot be easily identified observationally as being caused by infalling substructures. Thus, if a careful analysis is not performed, these features could be associated mistakingly with sound waves caused by AGN bubbles, especially if at the same time some fossil but unrelated bubble is detected in the cluster by its radio emission.

2.4.6 AGN heating in galaxy clusters of different mass

Here we discuss the effect of AGN heating in clusters spanning a wide range in mass, following their cosmological evolution up to $z = 0$. Their main properties are summarized in Tables 2.2 and 2.3. We analyze how the gas properties of clusters of different mass and at various radii, normalized to R_{200}, change due to the AGN-driven bubbles.

In Figure 2.15, we show for all clusters in our sample at $z = 0$ the cumulative X–ray luminosity and mean gas temperature at four different radii, $r = 0.03\,R_{200}$, $0.1\,R_{200}$, $0.5\,R_{200}$ and R_{200}, marked with different colours and symbols. In this $L_{\mathrm{X}}-T$ plane, clusters are found at different places according to their mass, with less massive systems being located in the lower-left part of the panel and more massive ones in the upper-right part, as indicated in the figure. Also, cluster luminosity and temperature vary systematically

[4] We made a crude estimate of the Mach number by calculating for every gas particle its velocity in the galaxy cluster reference frame and dividing it by the local sound speed.

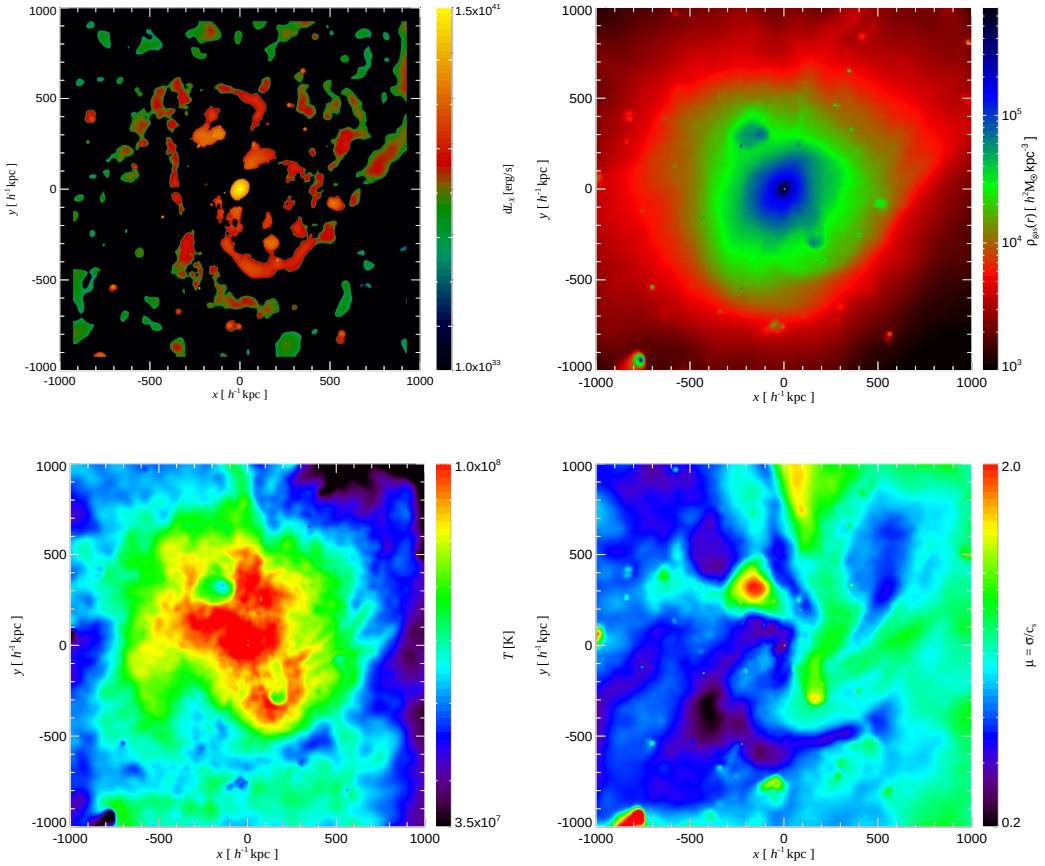

Figure 2.14: Projected maps of different gas properties of the S2 galaxy cluster at $z = 0.13$, where a merger with two smaller subclumps is in progress. AGN heating has not been included in this simulation. The upper left panel shows the unsharped masked image of the X–ray luminosity on a scale of $160\,h^{-1}$kpc, and the upper right panel illustrates the gas density map. On the lower left panel we show a map of mass-weighted cluster gas temperature, while the lower right panel gives a crude estimate of the mass-weighted Mach number.

with increasing radius r, with values at the virial radius occupying the upper-left part of the plot. The arrows attached to each cluster model show how L_X and T change when bubble heating is present. Clearly, there is a systematic trend of decreasing X–ray luminosity for all clusters and at all considered radii. This effect is more pronounced in the most inner regions and it is important both for massive clusters and smaller systems. Thus, in the cosmological simulations the bubble heating efficiency is not as clearly related to the mass of the host cluster as is the case for the isolated halos. From Figure 2.15, it can be seen that the two low mass clusters exhibit prominent imprints caused by AGN activity, highlighting that the bubble heating is more complex in cosmological simulations due to the hierarchical merging histories of clusters.

The gas temperature does not follow an equally clear trend as $L_{\rm X}$ for all the clusters in our sample, but in most cases, and especially for central clusters regions, it is boosted towards higher values, implying that bubble injection leads to en effective heating of the ICM. These trends in $L_{\rm X}$ and T confirm our previous findings for the S1/S2 clusters (presented in Figure 2.9), and show that they are general features of our AGN heating model. Interestingly, recent observational work by Croston et al. [2005] indicates that radio-loud elliptical-dominated groups have $L_{\rm X}-T$ scaling relations systematically different from those of elliptical-dominated radio-quiet groups. Their observed trends in the $L_{\rm X}-T$ plane are qualitatively similar with what we find, showing that for a given X–ray luminosity radio-loud groups have systematically higher gas temperature values. Nevertheless, since they are probing smaller mass systems, simulated galaxy groups with a matching range in mass are needed in order to make a more detailed comparison. Recent observational works [McNamara et al., 2005, Nulsen et al., 2005b] revealed the presence of very powerful outbursts due to the AGN activity, which are also accompanied with large-scale shocks. These clusters are located above the mean $L_{\rm X}-T$ relation, probably because we are witnessing the very early stages of bubble feedback, where pressure equilibrium with the surrounding ICM has not yet been established.

2.5 Discussion and Conclusions

In this work, we discussed a simulation model for AGN heating in the form of hot, buoyant bubbles, which are inflated by active phases of supermassive black holes at the centres of massive halos. The motivation for such a mode of feedback stems from the rich phenomenology of X-ray cavities and radio bubbles observed in clusters of galaxies, and the suggestion that this AGN activity may represent the solution of the 'cooling flow puzzle' posed by clusters of galaxies.

Several previous studies in the literature [e.g. Churazov et al., 2001, Quilis et al., 2001, Brüggen, 2003, Hoeft and Brüggen, 2004, Dalla Vecchia et al., 2004] have analysed bubble feedback in isolated galaxy clusters using hydrodynamical mesh codes. We here present the first implementation of this feedback in a SPH code, so an important goal was to test whether our results are consistent with these previous studies based on very different hydrodynamical techniques. Reassuringly, this is the case, both qualitatively and quantitatively. In particular, for galaxy clusters of similar masses as considered by Quilis et al. [2001], Dalla Vecchia et al. [2004], and with bubbles parametrised in an analogous way, we find changes induced by AGN-heating in gas properties, e.g. density and temperature radial profiles, central mass deposition rates, that are in excellent agreement. Also, the morphology of the bubbles and their time evolution are very similar. This is important because it implies that the SPH technique, which is more easily applicable to full blown cosmological simulations of cluster formation, can be reliably used to study bubble feedback.

In our simulations, we considered both, isolated halos of different mass, and cosmological simulations of the ΛCDM model that follow galaxy cluster assembly from high redshift to the present. The isolated simulations served as a laboratory to study the dynamics of bubbles in detail. By considering halos with masses ranging from $10^{12}\,h^{-1}{\rm M}_{\odot}$ to $10^{15}\,h^{-1}{\rm M}_{\odot}$, they also allowed us to gain some insight in how the coupling of radiative cooling to the

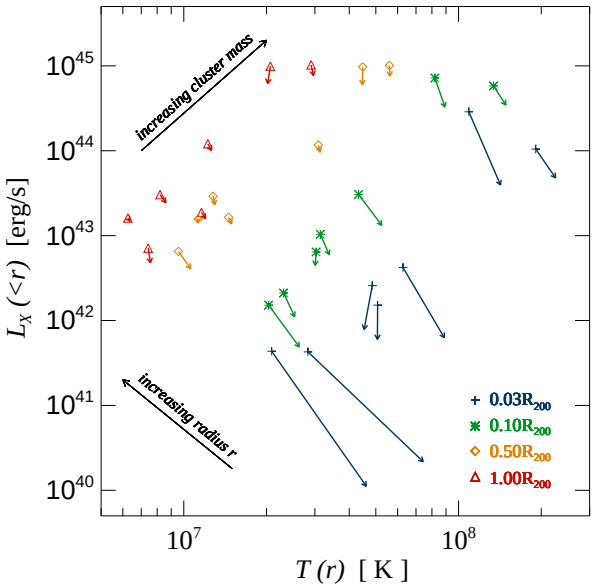

Figure 2.15: Cumulative X–ray luminosity of seven galaxy clusters as a function of their mass-weighted gas temperature. We give results for redshift $z = 0$, and at four different radii. Different symbols and colours denote estimates of $L_{\rm X}$ and T at different radii normalized to R_{200}: blue crosses correspond to $0.03\,R_{200}$, green stars to $0.1\,R_{200}$, yellow diamonds to $0.5\,R_{200}$, and red triangles to R_{200}. The arrows indicate how the cluster luminosity and temperature change when AGN heating is included, i.e. systematically decreasing $L_{\rm X}$ for all the considered radii. More massive clusters are located in the upper-right part of the panel, while less massive systems are found in the lower-left corner of the figure, as indicated.

AGN heating varies with cluster mass. An important conclusion from these experiments is that for systems of mass lower than $\sim 10^{13}\,h^{-1}{\rm M}_\odot$ bubbles with reasonable energy content are not capable of preventing excessive gas cooling. If one nevertheless allows for very large energy in these systems, a stable suppression of the cooling requires a delicate fine tuning of the bubbles. However, the inefficiency of bubble heating in lower mass systems is also caused in part by our injection prescription, which is based on global properties of the host galaxy cluster without accounting for the actual amount of cooling gas present in the very centre.

In our cosmological simulations, we find that bubble injection can substantially affect galaxy cluster properties, especially in massive, relaxed clusters and at late cosmological times. Central cluster gas is efficiently heated, and thus both the amount of cold baryons and the star formation in the central cD galaxy is reduced. Also, an excessive mass deposition rate by cooling flows is prevented. AGN-driven bubbles not only modify the

properties of the most central cluster parts, but alter the whole inner region of massive clusters, out to radii of order $\sim 300\,h^{-1}$kpc, where the gas density is reduced and the temperature is increased. As a result, the X–ray luminosity is considerably reduced, while the gas entropy exhibits a flat core in the central region. These trends are all in the direction required to reconcile hydrodynamical simulations of cluster formation in the ΛCDM model with observations of real galaxy clusters.

We tried several variants of our bubble model in order to explore the dependence of obtained results on the detailed assumptions made about how the energy is released in the bubbles. In particular, we compared an instantaneous injection of energy into the bubbles with a scheme where the energy is released over a certain period of time (from 5×10^7yrs to 5×10^8yrs), we imposed that the bubble particles should not cool during a given time interval (e.g. $\sim 10^8$ yrs), we tried different spatial patterns for the bubble placement, and we also varied the initial epoch where our AGN heating started (from $z = 6$ to $z = 3$). None of these changes was really capable of modifying our results considerably. However, it appears that our findings are much more sensitive to the adopted model for the time evolution of the bubble energy. We explicitly demonstrated this by changing the rate at which the energy is released with time, under the constraint that the total energy injected from $z = 3$ to $z = 0$ was kept constant. When we linked the bubble energy content in this way to a model for the BH accretion rate, the fraction of cold gas and the star formation rate can be noticeably reduced even at early times, but this is compensated by a reduced efficiency of bubble heating at late times, such that cooling flows are not suppressed sufficiently at $z = 0$. The "Magorrian model", where the feedback occurs primarily at low redshift fares better in this respect, and gives therefore a better match to the properties of observed rich clusters of galaxies. In addition, we explored yet another scaling between the energy of the bubbles and the mass of the host galaxy cluster, namely $E_{\rm bub} \propto M_{200}^{5/3}$, which can be motivated by the observed $M_{\rm BH} - \sigma$ relation as well. Also, Ferrarese and Ford [2005] pointed out a relationship between the mass of the black hole and that of the hosting dark matter halo, in the form of $M_{\rm BH} \propto M_{\rm DM}^{1.65}$. Thus, if the energy content of the bubbles is a linear function of the black hole mass, the above scaling is obtained. One also arrives at $E_{\rm bub} \propto M_{200}^{5/3}$ if one assumes that the energy in the bubbles is some small fraction of the total thermal cluster energy, which roughly scales as $M_{200}^{5/3}$. In performing the analysis with the modified slope, we fixed the normalization of the $E_{\rm bub} \propto M_{200}^{5/3}$ relation at redshift $z = 0$ to be equal to the value in our ordinary "Magorrian model". The results of this analysis showed that the change in the slope from 4/3 to 5/3 produces qualitatively very similar results, and hence it follows that the properties of our simulated galaxy clusters are not very sensitive to such a modest change of the AGN heating prescription.

In the newly emerging picture for the joint evolution of galaxies and supermassive black holes, the interplay between AGN and their host galaxies may be composed of two modes. One mode is caused by the quiescent accretion of intracluster gas onto the central BH, provoking periodic AGN activity which manifests itself in jets and radio bubbles. This mode plays a more important role at late cosmological epochs, in massive and more relaxed systems, and it is often referred to as a "radio-mode" [e.g. Croton et al., 2006]. The other mode occurs in merging pairs of galaxies, where strong tidal forces efficiently funnel large amounts of *cold* gas towards the nuclei of the merging galaxies, where it becomes

available for fueling the embedded supermassive BHs [Di Matteo et al., 2005a, Springel et al., 2005a]. The associated intense accretion triggers quasar activity, which is more frequent at higher redshift due to the larger merger rates there. If a small fraction of the bolometric luminosity of the quasar couples thermally to the surrounding gas, a prominent gas outflow can eventually be created during the formation of ellipticals, which then shuts off further accretion and star formation [Springel et al., 2005b] and establishes the $M_{\rm BH}-\sigma$ relationship [Di Matteo et al., 2005a].

The latter process, the 'quasar mode', has already been explored in direct simulation models of galaxy mergers, but not yet in cosmological simulations. It would therefore be extremely interesting to couple these two modes of AGN feedback in a unified simulation model for supermassive black hole growth, and to carry out cosmological simulations with it. In such a model, the energetics of the bubbles and the periods of AGN activity can then be made directly dependent on the current BH mass and on the local physics of accreting gas, removing much of the freedom in our present bubble models. We will present such a model in forthcoming work. In addition, our work suggests that for a more complete picture of the ICM dynamics, additional physical processes should be incorporated as well. This includes thermal conduction, even though it is probably relevant only in the most massive systems. We also suggest that the physical viscosity expected for the ICM gas should be considered as well, since the efficiency of non-local AGN heating by viscous dissipation of sound waves will depend crucially on this input. Finally, radio observations strongly suggest that bubbles are prevalently filled with relativistic particles, which appear as radio lobes, and in many cases are coincident with X–ray cavities. Therefore, it would be important to address, using fully cosmological simulation of cluster formation, the role of non-thermal radio plasma in bubbles for heating of the ICM. It appears that for some time to come clusters of galaxies will remain one of the most interesting places to study complex hydrodynamic phenomena in the Universe.

3

Physical viscosity in smoothed particle hydrodynamics simulations of galaxy clusters

D. Sijacki and V. Springel, 2006, MNRAS, 371, 1025

Abstract

Most hydrodynamical simulations of galaxy cluster formation carried out to date have tried to model the cosmic gas as an ideal, inviscid fluid, where only a small amount of (unwanted) numerical viscosity is present, arising from practical limitations of the numerical method employed, and with a strength that depends on numerical resolution. However, the physical viscosity of the gas in hot galaxy clusters may in fact not be negligible, suggesting that a self-consistent treatment that accounts for the internal gas friction would be more appropriate. To allow such simulations using the smoothed particle hydrodynamics (SPH) method, we derive a novel SPH formulation of the Navier-Stokes and general heat transfer equations and implement them in the GADGET-2 code. We include both shear and bulk viscosity stress tensors, as well as saturation criteria that limit viscous stress transport where appropriate. Our scheme integrates consistently into the entropy and energy conserving formulation of SPH employed by the code. Using a number of simple hydrodynamical test problems, e.g. the flow of a viscous fluid through a pipe, we demonstrate the validity of our implementation. Adopting Braginskii's parameterization for the shear viscosity of hot gaseous plasmas, we then study the influence of viscosity on the interplay between AGN–inflated bubbles and the surrounding intracluster medium (ICM). We find that certain bubble properties like morphology, maximum clustercentric radius reached, or survival time depend quite sensitively on the assumed level of viscosity. Interestingly, the sound waves launched into the ICM by the bubble injection are damped by physical viscosity, establishing a non-local heating process. However, we find that the associated heating is rather weak due to the overall small energy content of the sound waves. Finally, we carry out cosmological simulations of galaxy cluster formation with a viscous intracluster medium. We find that the presence of physical viscosity induces

new modes of entropy generation, including a significant production of entropy in filamentary regions perpendicular to the direction of the clusters encounter. Viscosity also modifies the dynamics of mergers and the motion of substructures through the cluster atmosphere. Substructures are generally more efficiently stripped of their gas, leading to prominent long gaseous tails behind infalling massive halos.

keywords: methods: numerical – hydrodynamics – plasmas – galaxies: clusters: general – cosmology: theory

3.1 Introduction

Studies of the intracluster medium (ICM) provide unique information about the complex interplay of the physical processes that determine the fate of baryons in galaxy groups and clusters. In recent years, remarkable observational progress has in fact unveiled a completely revised picture of the intracluster medium (ICM) where a plethora of non-gravitational physical processes are responsible for key observational phenomena. Indeed, the list of recent discoveries in the field of ICM physics is quite long, and includes cold fronts, long X-ray tails in the wake of late type galaxies passing through the hot cluster environment, or the presence of radio halos and ghosts associated with past AGN activity. Theoretical studies of these phenomena increasingly rely on direct numerical simulations, which are in principle capable of accurately computing the non-linear interplay of all these processes and their consequences for the thermodynamics of the ICM. A prerequisite is that the simulations are capable of representing all the physics relevant for the system, which represents a significant ongoing challenge.

A particularly important question in cluster physics concerns the observed absence of strong cooling flows onto the massive elliptical galaxies at the centres of the potential wells of groups and clusters of galaxies [e.g. Peterson et al., 2001, 2003, Tamura et al., 2001, Balogh et al., 2001, Edge, 2001, Edge et al., 2002, Böhringer et al., 2002]. There is now growing observational evidence for the relevance of AGN heating in these objects [e.g. McNamara et al., 2000, Sanders and Fabian, 2002, Mazzotta et al., 2002, McNamara et al., 2005, Fabian et al., 2006], supporting the widespread theoretical notion that the central AGN is providing enough energy to offset the radiative cooling losses. However, it is still not understood in detail how this energy is coupled into the ICM. X-ray observations with the XMM-Newton and Chandra telescopes [e.g. Blanton et al., 2001, Bîrzan et al., 2004, Nulsen et al., 2005a] have revealed that in many cooling-flow clusters there are so called X-ray cavities which interact with the surrounding intracluster gas. It is believed that these bubbles are inflated by the powerful AGN jets that are generated by an accreting central black hole. The expanding bubbles heat the ICM by mechanical work, and by the buoyant uplifting of cool gas from the central regions and subsequent mixing with the hotter atmosphere at larger radii. At the same time, the bubbles trigger sound waves that travel through the cluster, and they may excite global oscillations modes of the ICM in the cluster potential. It has been suggested that viscous damping of these sound waves may provide an important non-local heating source for the ICM [e.g. Fabian et al., 2003a]. A significant cluster viscosity may in principle exist, but its strength should depend critically on the magnetic field strength and the field topology.

Radio observations [e.g. Owen et al., 2000, Clarke et al., 2005, Dunn et al., 2005] have clearly shown that the X-ray cavities are filled with relativistic gas, and probably have inherited some of the magnetic fields transported by the AGN jet. While the structure of the magnetic fields filling the bubbles is not well known yet, it has by now been firmly established that galaxy clusters are permeated by magnetic fields [for reviews see Carilli and Taylor, 2002, Govoni and Feretti, 2004]. Faraday rotation measurements [Clarke et al., 2001, Clarke, 2004, Eilek and Owen, 2002, Vogt and Enßlin, 2003, 2005] have found that the magnetic fields in clusters appear to be random, with an rms strength of order of $1 - 10\,\mu$G, and with a coherence length of $1 - 20\,$kpc. Assuming a fully ionized plasma [Spitzer, 1962], this implies a very high magnetic Prandtl number for the ICM of order of $\sim 10^{29}$, suggesting that magneto-hydrodynamic (MHD) turbulence is probably relevant. On the other hand, the inferred typical Reynolds numbers for the intracluster gas are quite small, $\lesssim 100$, indicating that the gas viscosity might be quite important. Moreover, the coherence length-scale of the magnetic fields is comparable to the ion mean free path, as well as to the typical size of galaxies and of AGN–driven bubbles that could drive turbulence in the ICM. In fact, there have been some observational studies that found evidence for the presence of turbulence in clusters [Schuecker et al., 2004, Rebusco et al., 2005], suggesting that the injection scale of the turbulence would be of order $\sim 10-100\,$kpc.

All these observational pieces of information do not yet combine to a definitive picture of the magnetic and viscous properties of the ICM, and the theoretical understanding is also not yet mature [for a recent review see Schekochihin and Cowley, 2005]. It is clear, however, that an approximation of the ICM as an ideal, inviscid gas – as usually made in most hydrodynamical simulations of galaxy cluster formation – may be a poor approximation for hot clusters with non-negligible (and perhaps chaotically tangled) magnetic fields. It is therefore the aim of this work to explore the potential imprints of gas viscosity on galaxy cluster properties in a fully self-consistent way, using cosmological simulations of cluster growth from ΛCDM initial conditions. As a prerequisite for such simulations, we develop a numerical scheme capable of accurately solving the Navier-Stokes equations in SPH, which we use instead of the commonly employed much simpler Euler equation. We will assume a simple parameterization of the shear and bulk viscosity tensors, without explicitly dealing with the MHD equations. For this purpose, we adopt Braginskii's parameterization [Braginskii, 1958, 1965] of the shear viscosity, together with a phenomenological suppression factor to mimic the influence of the magnetic fields. The bulk viscosity coefficient is kept constant if included.

In order to test our new hydrodynamical scheme, we apply it to a number of simple test problems with known analytic solutions. These tests yield robust results in agreement with the expectations. We then carry out simulations of galaxy clusters where we include different physics, with or without physical viscosity. These simulations include models with non-radiative hydrodynamics, and models with radiative cooling, star formation and supernovae (SNe) feedback, allowing us to obtain an overview about the interplay of gas dynamics and viscous dissipation in different environments, and the consequences viscosity has for the structure of clusters. We also try to identify potential observational signatures for internal friction processes.

In an additional set of simulations, we analyze the impact of gas viscosity on the AGN–driven bubble heating process. Previous analytic work [e.g. Kaiser et al., 2005] and nu-

merical Eulerian simulations [e.g. Ruszkowski et al., 2004, Reynolds et al., 2005] have suggested that internal friction has a significant impact on bubble properties, stabilizing them against hydrodynamical instabilities that would otherwise readily disrupt them. We explore this issue in some detail with our simulation methodology, in particular studying bubble morphologies, maximum clustercentric distance, and survival times, as a function of the assumed level of shear viscosity. In this context we also examine the total energy in the sound waves triggered by the bubbles. We find that this is rather small, something that could in part be caused by deficiencies in our models, as we discuss later on.

The outline of this paper is as follows. In Section 3.2, we review the fundamental physical laws of viscous fluids, focusing in particular on astrophysical plasmas and a discussion of the role of magnetic fields. The detailed description of our numerical implementation of physical viscosity in SPH is given in Section 3.3, while we illustrate the validity of our numerical scheme with a number of basic hydrodynamical test problems in Section 3.4. In Section 3.5, we analyze the heating effects caused by AGN–driven bubbles rising through viscous intracluster gas, while in Section 3.6, we discuss internal friction during merging episodes and its impact on substructure motion in cosmological simulations of galaxy cluster formation. Finally, we summarize and discuss our results in Section 3.7.

3.2 Theoretical considerations

In the following discussion, we concentrate on viscous gases in the astrophysical context of galaxy and galaxy cluster formation. We briefly review the basic physical equations governing the hydrodynamics of the relevant class of 'real' (as opposed to ideal) fluids, and the constraints that exist for some of the free parameters that describe their properties. This includes a discussion of internal friction processes in the collisional regime and their relevance for astrophysical plasmas. In particular, we examine viscous effects in intracluster gas, assuming that it is fully ionized and that it consists of a primordial mixture of hydrogen and helium. We also describe the differences and difficulties that arise when magnetic fields are present in clusters.

3.2.1 Navier-Stokes equation

To describe real fluids, two of the fundamental equations of hydrodynamics that hold for ideal gases, namely Euler's equation and the energy conservation law, need to be revised. The continuity equation remains in its familiar form, i.e.

$$\frac{\partial \rho}{\partial t} + \frac{\partial (\rho v_k)}{\partial x_k} = 0 \tag{3.1}$$

expresses mass conservation as usual, where ρ is the gas density, v_k denotes the local velocity vector of the fluid, and the summation convention has been employed.

When there is relative motion between different parts of a real fluid, internal friction forces lead to an additional transfer of momentum that is absent in an ideal gas, and which in general will act to reduce velocity differences. The friction forces modify the momentum flux density tensor, which becomes

$$\Pi_{ik} = p\delta_{ik} + \rho v_i v_k - \sigma_{ik} \,. \tag{3.2}$$

In this equation, p is the gas pressure and σ_{ik} represents the viscous stress tensor, which to first approximation can be assumed to be a linear function of the first spatial derivatives of the velocity field. It can be shown [Landau and Lifshitz, 1987] that the most general tensor of rank two satisfying the requested criterion is given by

$$\sigma_{ik} = \eta\left(\frac{\partial v_i}{\partial x_k} + \frac{\partial v_k}{\partial x_i} - \frac{2}{3}\delta_{ik}\frac{\partial v_l}{\partial x_l}\right) + \zeta\delta_{ik}\frac{\partial v_l}{\partial x_l}\,, \tag{3.3}$$

where η is called the coefficient of shear viscosity, and ζ represents the bulk viscosity coefficient. Bulk viscosity becomes important when the fluid is rapidly compressed or expanded on a timescale shorter than the relaxation time of the fluid, in which case considerable energy can be dissipated. The coefficients of viscosity can be functions both of gas pressure and temperature, but not of gas velocity, because of the criterion imposed above on the viscous stress tensor.

The generalized form of Euler's equation describing the motion of viscous fluids can be written as

$$\begin{aligned}\rho\left(\frac{\partial v_i}{\partial t} + v_k\frac{\partial v_i}{\partial x_k}\right) = -\frac{\partial p}{\partial x_i} - \rho\frac{\partial \Phi}{\partial x_i} + \\ + \frac{\partial}{\partial x_k}\left[\eta\left(\frac{\partial v_i}{\partial x_k} + \frac{\partial v_k}{\partial x_i} - \frac{2}{3}\delta_{ik}\frac{\partial v_l}{\partial x_l}\right)\right] + \\ + \frac{\partial}{\partial x_i}\left(\zeta\frac{\partial v_l}{\partial x_l}\right),\end{aligned} \tag{3.4}$$

where Φ is the gravitational potential. When the coefficients of shear and bulk viscosity are assumed to be constant, equation (3.4) is called Navier-Stokes equation.

3.2.2 General heat transfer equation

Unlike ideal gases which are isentropic outside of shock waves, entropy conservation does not hold for viscous fluids. In the latter case, the energy conservation law needs to be augmented with additional terms which depend on the viscous stress tensor and on the temperature gradient [Landau and Lifshitz, 1987]. This results in

$$\frac{\partial}{\partial t}\left(\frac{1}{2}\rho v^2 + \rho\epsilon\right) = -\nabla\left[\rho\mathbf{v}\left(\frac{\mathbf{1}}{\mathbf{2}}\mathbf{v^2} + \mathbf{w}\right) - \mathbf{v}\sigma - \kappa\,\nabla\mathbf{T}\right], \tag{3.5}$$

where w is the heat function given by $w = \epsilon + p/\rho$, and κ is the coefficient of thermal conduction. Using the continuity equation and the Navier-Stokes equation, the energy conservation law can be rewritten as

$$\rho T\frac{\mathrm{d}S}{\mathrm{d}t} = \nabla(\kappa\,\nabla T) + \frac{1}{2}\eta\,\sigma_{\alpha\beta}\sigma_{\alpha\beta} + \zeta(\nabla\,v)^2\,, \tag{3.6}$$

which is called the general heat transfer equation. Here $\sigma_{\alpha\beta}$ denotes the shear part of the viscous stress tensor, or 'rate-of-strain tensor'. This equation expresses how much entropy is generated by the internal friction of the gas and by the heat conducted into the considered volume element. From the general heat transfer equation it is evident that the

coefficients of viscosity and thermal conduction need to be positive, given that the entropy of the gas can only increase, as imposed by the second law of thermodynamics. In the following, we will not consider thermal conduction any further, which has recently been discussed in independent studies that analyzed its impact on cluster cooling flows [e.g. Narayan and Medvedev, 2001, Jubelgas et al., 2004, Dolag et al., 2004].

3.2.3 The viscous transport coefficients in astrophysical plasmas

3.2.3.1 Kinetic theory approach

In the kinetic theory of neutral gases, the viscosity coefficients are kinetic coefficients of the Boltzmann transport equation, and can be estimated by solving this equation under the assumption that the characteristic length-scale of the problem under consideration is much larger than the mean free path l of particles, which is the so-called collisional regime[1]. From this approach it follows [Landau and Lifshitz, 1981] that the shear viscosity coefficient can be expressed as

$$\eta \sim m\,\bar{v}\,n\,l \sim \frac{\sqrt{m\,T}}{\sigma}\,, \tag{3.7}$$

where $\bar{v} \sim \sqrt{T/m}$ is the mean gas velocity, n is the gas number density, and $\sigma \sim 1/(n\,l)$ is the collisional cross-section. Equation (3.7) implies that at a given gas temperature the shear viscosity coefficient does not depend on gas pressure. When the Boltzmann transport equation is solved for the bulk viscosity coefficient, one then obtains that ζ vanishes for the case of a monoatomic non-relativistic gas.

If magnetic fields are absent in a collisional plasma, the main transfer of momentum due to internal friction comes from the motion of ions. Hence, it is sufficient to consider only collisions between ions, neglecting the ones occurring with electrons, in order to estimate the amount of shear viscosity. The cross-section in the limit of small angle scattering in the unmagnetized Coulomb field is given by,

$$\sigma_c \;=\; \frac{4\pi(Ze^2)^2}{\mu^2|\mathbf{v_e}-\mathbf{v_i}|^4}\ln\Lambda\,, \tag{3.8}$$

where μ is the reduced mass of electrons and ions, and $\ln\Lambda$ is the Coulomb logarithm, which can be approximatively taken to be 37.8 for intracluster gas [Sarazin, 1988]. Under the assumption that electrons have much higher velocity than the ions, it follows that $\mu(\mathbf{v_e}-\mathbf{v_i})^2 \sim \mathbf{T_e}$, for the "e–e" and "e–i" collisions, giving an expression for the mean free path of electrons in the form

$$\lambda_e \sim \frac{T_e^2}{4\pi e^4\,n_e\,\ln\Lambda}\,. \tag{3.9}$$

Similarly, the ion mean free path reads

$$\lambda_i \sim \frac{T_i^2}{4\pi(Ze)^4\,n_i\,\ln\Lambda}\,. \tag{3.10}$$

[1] In this study, we will not discuss internal friction processes in the collisionless regime, because the relevant scales for this regime are at best partially resolved (and often completely below the spatial resolution) in current state-of-the-art numerical simulations of galaxy clusters.

Thus, based on the simple derivation of the shear viscosity in the framework of the kinetic theory (eqn. 3.7) and using the expression for the mean free path of ions, one obtains an estimate of the shear viscosity in the case of a fully ionized, unmagnetized plasma [Landau and Lifshitz, 1981], viz.

$$\eta \sim \frac{m_i^{1/2}\, T_i^{5/2}}{(Ze)^4\, \ln\Lambda}\,. \tag{3.11}$$

The exact magnitude of the shear viscosity coefficient is given by [e.g. Braginskii, 1958, 1965],

$$\eta \;=\; 0.406 \frac{m_i^{1/2}\, (k_B\, T_i)^{5/2}}{(Ze)^4\, \ln\Lambda}\,, \tag{3.12}$$

while the bulk viscosity coefficient remains zero.

3.2.3.2 Saturation of the viscous stress tensor

When the length scale on which the velocity is changing becomes similar or smaller than the mean free path of ions, an unphysical situation would occur if the momentum transfer due to viscous forces propagates faster than the information on changes of the pressure forces, i.e. faster then the mean sound speed of ions [Frank et al., 1985, Sarazin, 1988]. Thus, internal friction forces need to saturate at the relevant length scales to a strength of order of the pressure forces. More specifically, let us define a characteristic length-scale l_v such that the shear viscous force[2] obeys

$$F_{\rm visc} \sim \eta \frac{\sigma}{l_v} \sim \eta \frac{v_i}{l_v^2} \sim \eta \frac{c_s}{l_v^2}\,, \tag{3.13}$$

where v_i is the mean velocity of ions, and c_s is the sound speed of the ions. The criterion for viscosity saturation can be expressed as

$$\frac{c_s}{l_v^2} < \frac{c_s}{\lambda_i^2}\,, \tag{3.14}$$

implying that if $l_v < \lambda_i$, the viscous stress tensor has to saturate to a value of the order of c_s/λ_i.

3.2.3.3 Magnetized plasmas

In the presence of magnetic fields, the viscous transport coefficients will depend on the quantity $\omega\,\tau$, where ω is the cyclotron frequency of the considered species (electrons or ions) and τ is the collisional time. The transport coefficients along the field lines will have the same form as in the case of an unmagnetized plasma, because the charged particles can move freely along the magnetic field lines and can cover distances of order of their mean free path. On the other hand, in the case of strong magnetic fields, with $\omega\tau \gg 1$, the transport coefficients will be suppressed in the perpendicular direction to the field lines, and this suppression will be of order of $\omega\tau$ or $(\omega\tau)^2$ for different viscosity terms. If the

[2] An analogous argument holds for the bulk part of the viscous force as well.

temperatures of electrons and ions are similar, as expected for intracluster plasmas, the viscosity will be dominated by ions, even in the presence of strong magnetic fields.

It is worth pointing out that unlike to the case of an unmagnetized plasma, where internal friction of a compressible fluid is determined by two scalar transport coefficients, the viscous transport coefficient becomes a tensor of rank four when there is a non-vanishing magnetic field. Thus, given the symmetry of the viscous transport tensor, there will in general be seven independent viscosity coefficients, five related to the shear, and two to the bulk flows. Therefore, the treatment of viscous flows in magnetized plasmas becomes extremely difficult, and includes the possibility that compressional motions provide additional viscous heating. In fact, a plasma compression in the direction perpendicular to the magnetic field (assuming that the field lines are ordered locally) will produce an excess of transverse pressure, and thus will give rise to a viscous stress with unsuppressed transport coefficient, which is known as gyrorelaxational heating. Potentially, this heating mechanism could operate in the case of AGN–driven bubbles that buoyantly rise in the ICM, pushing the intracluster gas in front of them, as is seen in a number of numerical simulations [e.g. Churazov et al., 2001, Quilis et al., 2001, Hoeft and Brüggen, 2004, Dalla Vecchia et al., 2004, Reynolds et al., 2005, Sijacki and Springel, 2006] and also indicated by recent X–ray observations [e.g. Bîrzan et al., 2004, McNamara et al., 2005, Nulsen et al., 2005a, Fabian et al., 2006]. However, so far it has only been possible to poorly constrain the topology of magnetic field lines in clusters with observations, while theoretical models offer a broad range of possible magnetic field configurations. It will still take some time before fully radiative MHD simulations of galaxy clusters can overcome their present limitations and provide clearer theoretical predictions. Hence, it is presently difficult to put robust constraints on the magnetic field topology in clusters, its evolution over cosmic time, and its dependence on the dynamical state of a cluster, even though some interesting predictions can be made based on non-radiative MHD simulations [e.g. Dolag et al., 2002]. In our numerical modelling of gas viscosity we therefore parameterize the role of magnetic fields by introducing a suppression parameter f in front of the Braginskii viscosity. We will assume f to be constant in time and to be independent of cluster mass.

The discussion above is valid under the assumption that the plasma is in a quasi steady state, where the mean values of relevant quantities change sufficiently slowly in time and space, thus that collisions can establish a Maxwellian distribution on the time scale τ. Otherwise, field fluctuations can significantly change the magnitude of the suppression of the transport coefficients in the direction perpendicular to the field lines.

3.3 Numerical implementation

We use the parallel TreeSPH-code GADGET-2 [Springel, 2005, Springel et al., 2001b] in this study, in its entropy conserving formulation [Springel and Hernquist, 2002]. In addition to gravitational and non-radiative hydrodynamical processes, the code includes a treatment of radiative cooling for a primordial mixture of hydrogen and helium, and heating by a spatially uniform, time-dependent UV background [Katz et al., 1996]. Star formation and associated supernovae feedback processes can also be tracked by the code, using a simple subresolution multiphase model for the ISM [Springel and Hernquist, 2003a].

Even though the bulk viscosity is identical to zero for unmagnetized fully-ionized plas-

mas, there are a number of cases where bulk viscosity may still be important, for example in the presence of magnetic fields where the viscosity tensor contains terms that explicitly depend on the velocity divergence. Also for the sake of completeness, we have therefore implemented a treatment of viscosity in GADGET-2 that accounts both for shear and bulk viscosity. There is a small number of previous studies in the literature that discuss SPH formalisms for internal friction processes [Flebbe et al., 1994, Schäfer et al., 2004]. Our new implementation follows a somewhat different and more complete approach, however, and it is consistent with the entropy-conserving formulation of SPH introduced by Springel and Hernquist [2002]. In the following, we give a brief summary of the SPH method, and then derive the particular formulation of the discretized Navier-Stokes and general heat transfer equations that we adopted.

One of the central aspects of the SPH method is the idea to represent a given thermodynamic function with an interpolant constructed from the values at a set of disordered points. These fluid particles are usually characterized by their position r, mass m, and velocity v [Lucy, 1977, Gingold and Monaghan, 1977, Monaghan and Lattanzio, 1985]. The computation of an interpolant is based on a kernel function, which is often adopted as a simple spline kernel [Monaghan and Lattanzio, 1985],

$$W(r,h) = \frac{8}{\pi h^3} \begin{cases} 1 - 6\left(\frac{r}{h}\right)^2 + 6\left(\frac{r}{h}\right)^3, & 0 \le \frac{r}{h} \le \frac{1}{2}, \\ 2\left(1 - \frac{r}{h}\right)^3, & \frac{1}{2} < \frac{r}{h} \le 1, \\ 0, & \frac{r}{h} > 1. \end{cases} \tag{3.15}$$

where h is the smoothing length. The interpolant $\tilde{Q}(\mathbf{r})$ of a thermodynamic quantity can then be constructed from the values Q_i of the particle set as

$$\tilde{Q}_i = \sum_{j=1}^{N} Q_j \frac{m_j}{\rho_j} W_{ij}(h_i)\,, \tag{3.16}$$

where the sum is evaluated over all particles, $W_{ij}(h_i)$ is an abbreviation for $W(|\mathbf{r_i} - \mathbf{r_j}|, \mathbf{h_i})$, and h_i is the adaptive smoothing length of particle i. A derivative of the interpolant can now be obtained straightforwardly by applying the ∇-operator to the kernel function itself, viz.

$$\nabla_{\mathbf{i}} \tilde{\mathbf{Q}}_{\mathbf{i}} = \sum_{\mathbf{j=1}}^{\mathbf{N}} \mathbf{Q_j} \frac{\mathbf{m_j}}{\rho_{\mathbf{j}}} \nabla_{\mathbf{i}} \mathbf{W_{ij}}(\mathbf{h_i}). \tag{3.17}$$

We use this property of the SPH formalism to derive the viscous accelerations exerted on gas particles. The SPH discretization of the viscous stress tensor can be readily constructed based on standard expressions for velocity gradients and velocity divergence [Monaghan, 1992]. Specifically, the derivative of the α-component of particle i's velocity with respect to x_β (where α and β range from 0 to 2) can be written as

$$\left.\frac{\partial v_\alpha}{\partial x_\beta}\right|_i = \frac{1}{\rho_i} \sum_{j=1}^{N} m_j (\mathbf{v_j} - \mathbf{v_i})|_\alpha \left(\nabla_{\mathbf{i}} \mathbf{W_{ij}}(\mathbf{h_i})\right)|_\beta\,. \tag{3.18}$$

Hence, the velocity divergence can be simply constructed as

$$\nabla{\cdot}\mathbf{v_i} \equiv \left.\frac{\partial \mathbf{v}_\alpha}{\partial \mathbf{x}_\alpha}\right|_{\mathbf{i}} = \frac{\mathbf{1}}{\rho_{\mathbf{i}}} \sum_{\mathbf{j=1}}^{\mathbf{N}} \mathbf{m_j} (\mathbf{v_j} - \mathbf{v_i})|_\alpha \left(\nabla_{\mathbf{i}} \mathbf{W_{ij}}(\mathbf{h_i})\right)|_\alpha\,, \tag{3.19}$$

where the summation notation for repeated Greek indexes was adopted. Therefore, based on equations (3.3), (3.18) and (3.19), the SPH formulation of the viscous stress tensor reads

$$\sigma_{\alpha\beta}\Big|_i = \eta\left(\frac{\partial v_\alpha}{\partial x_\beta}\Big|_i + \frac{\partial v_\beta}{\partial x_\alpha}\Big|_i - \frac{2}{3}\delta_{\alpha\beta}\frac{\partial v_\gamma}{\partial x_\gamma}\Big|_i\right) + \\ + \zeta\,\delta_{\alpha\beta}\frac{\partial v_\gamma}{\partial x_\gamma}\Big|_i . \tag{3.20}$$

Considering equation (3.4) and using the notation introduced in equation (3.17), the following expression for the acceleration of gas particles due to the shear forces can be readily derived

$$\frac{\mathrm{d}\mathbf{v}}{\mathrm{d}t}\Big|_{i,\mathrm{shear}} = \sum_{j=1}^{N} m_j \left[\frac{\eta_i \sigma_\mathbf{i}}{\rho_i^2}\nabla_\mathbf{i}\mathbf{W_{ij}}(\mathbf{h_i}) + \right. \\ \left. + \frac{\eta_j \sigma_\mathbf{j}}{\rho_j^2}\nabla_\mathbf{i}\mathbf{W_{ij}}(\mathbf{h_j})\right], \tag{3.21}$$

where the product of η and σ gives the shear part of the viscous stress tensor, or in the other words, $\sigma_\mathbf{i}$ is now the rate-of-strain tensor of particle i. The previous equation can be written in an explicit component form as follows

$$\frac{\mathrm{d}v_\alpha}{\mathrm{d}t}\Big|_{i,\mathrm{shear}} = \sum_{j=1}^{N} m_j \left[\frac{\eta_i \sigma_{\alpha\beta}|_i}{\rho_i^2}\left(\nabla_\mathbf{i}\mathbf{W_{ij}}(\mathbf{h_i})\right)|_\beta + \right. \\ \left. + \frac{\eta_j \sigma_{\alpha\beta}|_j}{\rho_j^2}\left(\nabla_\mathbf{i}\mathbf{W_{ij}}(\mathbf{h_j})\right)|_\beta\right]. \tag{3.22}$$

We note that this equation conserves linear momentum, but does not manifestly conserve the total angular momentum. A non-conservation of angular momentum can arise due to the fact that even though the force is clearly antisymmetric, the viscous stress tensor can induce torques, and thus the force between two particles is not necessarily central any more. Note that this is a consequence of the tensor nature of the viscous stresses, and not an artificial feature of our numerical scheme. In order to circumvent this apparent inconsistency, one could introduce an additional intrinsic property for every gas particle, namely a spin variable, that would store how much torque has been exerted on it and would itself be a source of shear between two particles which would try to keep this spin close to zero. However, the non-conservation of angular momentum due to viscous forces in our formulation is basically negligible, as has already been discussed in detail in Riffert et al. [1995]. Comparing the discretized form of the SPH equations to the continuum limit shows that the angular momentum is conserved to an accuracy of order $\mathcal{O}(h^2)$, which is comparable to the error made in the usual SPH kernel estimates of other fluid quantities, like the density. In an analogous manner to equation (3.21), the acceleration caused by forces due to bulk viscosity can be estimated as

$$\left.\frac{\mathrm{d}\mathbf{v}}{\mathrm{d}t}\right|_{i,\mathrm{bulk}} = \sum_{j=1}^{N} m_j \left[\frac{\zeta_i \, \nabla\cdot\mathbf{v_i}}{\rho_i^2}\,\nabla_\mathbf{i}\mathbf{W_{ij}}(\mathbf{h_i}) + \right. \\ \left. + \frac{\zeta_j \, \nabla\cdot\mathbf{v_j}}{\rho_j^2}\,\nabla_\mathbf{i}\mathbf{W_{ij}}(\mathbf{h_j})\right]. \tag{3.23}$$

We employ the specific entropy of an SPH particle as independent thermodynamic variable. Instead of using the conventional thermodynamic entropy directly, it is however more convenient to replace the entropy S with an entropic function A, related to the entropy by

$$\frac{\mathrm{d}A(S)}{\mathrm{d}t} = \frac{\gamma-1}{\rho^{\gamma-1}}\,T\,\frac{\mathrm{d}S}{\mathrm{d}t}\,, \tag{3.24}$$

where γ is the adiabatic gas index. Therefore, from the general heat transfer equation it follows that the increase of the entropic function due to internal friction forces is given by

$$\left.\frac{\mathrm{d}A_i}{\mathrm{d}t}\right|_{\mathrm{shear}} = \frac{1}{2}\,\frac{\gamma-1}{\rho_i^{\gamma-1}}\,\frac{\eta_i}{\rho_i}\,\sigma_i^2 \tag{3.25}$$

$$\left.\frac{\mathrm{d}A_i}{\mathrm{d}t}\right|_{\mathrm{bulk}} = \frac{\gamma-1}{\rho_i^{\gamma-1}}\,\frac{\zeta_i}{\rho_i}\,(\nabla\cdot\mathbf{v_i})^\mathbf{2}. \tag{3.26}$$

Clearly, this formulation shows that the entropic function can only increase due the action of internal friction forces if the shear and bulk viscosity coefficients are positive, as desired.

We have implemented different parameterizations of the viscosity coefficients in the simulation code. Besides a model with constant viscosity, we realized a model for cosmological applications where the shear viscosity is parameterized with equation (3.12), modified with an additional prefactor that controls in a simple way the possible shear viscosity suppression due to the presence of magnetic fields, as discussed in Section 3.2.3.3. We follow the literature and vary this prefactor in the range of 0.1 to 1.0. We have also introduced an additional time-step criterion in the code in order to protect against situations where the Courant timestep may not be small enough to guarantee accurate integration of large viscous stresses. We have adopted the maximum allowed time-step as

$$\mathrm{d}t_{\mathrm{max}} \leq \mathrm{d}t_{\mathrm{visc}} \quad \text{with} \quad \mathrm{d}t_{\mathrm{visc}} = \alpha\frac{A}{|\dot{A}_{\mathrm{visc}}|}\,, \tag{3.27}$$

where $\dot{A}_{\mathrm{visc}}$ represents the rate of increase of the entropic function due to shear and bulk viscous forces, and α is a dimensionless time-step parameter that controls the integration accuracy.

Finally, we estimate the characteristic length-scale l_v in the code. Following the arguments expressed in equations (3.13) and (3.14), we adopt a saturation of the relevant viscous stress tensor components to a value given by $\sim c_s/\lambda_i$, provided l_v is found to be smaller than the ion mean free path.

At the end of this Section, we briefly discuss the differences that exist between the functional forms of the physical and the artificial viscosity, bearing in mind their conceptual differences. As discussed in detail in Springel [2005], the GADGET-2 code computes the

acceleration due to the artificial viscosity as follows

$$\left.\frac{\mathrm{d}\mathbf{v_i}}{\mathrm{d}t}\right|_{visc} = -\sum_{j=1}^{N} m_j \, \Pi_{ij} \nabla_{\mathbf{i}} \overline{\mathbf{W}}_{\mathbf{ij}} \,, \tag{3.28}$$

where $\overline{W}_{ij}$ represents the arithmetic mean of $W_{ij}(h_i)$ and $W_{ij}(h_j)$. The entropy increase due to the action of artificial viscous forces is given by

$$\frac{\mathrm{d}A_i}{\mathrm{d}t} = \frac{1}{2}\frac{\gamma-1}{\rho_i^{\gamma-1}} \sum_{j=1}^{N} m_j \, \Pi_{ij} \, \mathbf{v_{ij}} \cdot \nabla_{\mathbf{i}} \overline{\mathbf{W}}_{\mathbf{ij}} \,, \tag{3.29}$$

with $\mathbf{v_{ij}} \equiv \mathbf{v_i} - \mathbf{v_j}$, and Π_{ij} is defined in a slightly different form[3] [Monaghan, 1997] compared to the one that is usually adopted in many SPH codes [Monaghan and Gingold, 1983], namely

$$\Pi_{ij} = -\frac{\alpha}{2}\frac{(c_i + c_j - 3w_{ij})\, w_{ij}}{\rho_{ij}} \,, \tag{3.30}$$

if the particles are approaching each other, otherwise Π_{ij} is set to zero. Here α is a parameter that regulates the strength of the artificial viscosity, c_i and c_j are the sound speeds of particles i and j, respectively, and $w_{ij} = \mathbf{v_{ij}} \cdot \mathbf{r_{ij}}/|\mathbf{r_{ij}}|$. In addition, following the arguments explained in Balsara [1995] and Steinmetz [1996], the strength of the artificial viscosity is reduced in the presence of local shear in order to avoid spurious angular momentum transport. Comparing the equations for acceleration and entropy generation due to artificial viscous forces with the analogous expressions for the case of physical viscosity, it can be seen that the dependences on gas velocity and temperature are quite different. In particular, the Braginskii-parameterization of the shear viscosity coefficient has a much stronger dependence on gas temperature than the artificial viscosity, meaning that the relative importance of the physical viscosity is expected to be be different for objects of different virial temperature. It should also be stressed that the artificial viscosity becomes relevant only when particles are approaching each other, while that is not the case for the physical viscosity. Furthermore, given that the artificial viscosity is suppressed in the presence of significant local shear, the artificial viscosity cannot mimic the behavior of physical shear viscosity, as we explicitly confirmed with a number of test problems that will be discussed in the next Section.

3.4 Illustrative test problems

The purpose of this section is to test the validity and applicability of our new viscosity implementation. To this end, we consider simple hydrodynamical problems with known analytic solutions for real (viscous) fluids. We will first discuss the motion of an incompressible fluid under the action of shear forces in two different situations that illustrate the typical behaviour of viscous fluids. At the end of this section, we then compare the behaviour of shock tube tests when physical shear and bulk viscosity are used to capture shocks instead of the standard artificial viscosity.

[3] For a more sophisticated form of the artificial viscous term see Cleary [1998] and Cleary et al. [2002].

We begin our investigation with the problem of a flow between two moving planes with a finite separation h. While there always exists a flow solution for every particular initial condition, it is interesting to note that it is not guaranteed that the solution will be steady and stable for a different internal viscosity value. In fact, for the case of an ideal fluid the flow is actually always unstable, because any small perturbation in the flow will typically not be damped in this case but rather grow in time. However, stability of the flow can be recovered if the fluid has a sufficiently small Reynolds number, given by

$$\mathcal{R} = \frac{\rho u l}{\eta} = \frac{u l}{\nu}\,, \tag{3.31}$$

where u is the characteristic velocity of the problem, l is its characteristic length-scale, and $\nu = \eta/\rho$ is the kinematic viscosity. It follows that in order to ensure a laminar flow in the 'pipe' between the two planes, the mean velocity times the diameter of the pipe should be of the order of the kinematic viscosity. This condition is satisfied in our numerical tests.

3.4.1 Flow between two sheets with a constant relative velocity

As a first test we simulate the elementary hydrodynamical problem of the motion of a viscous, incompressible fluid between two infinite parallel planes spaced a distant h apart. The space between the planes is uniformly filled with a fluid of constant pressure, having a fixed amount of shear viscosity and bulk viscosity equal to zero. The planes move with a constant relative velocity with respect to each other (along the x-axis, for definiteness), while the fluid is initially at rest. We expect that after a brief time interval a stationary solution should be established, with a laminar flow where all relevant quantities depend only on the position y along the axis orthogonal to the planes. Solving the Navier-Stokes equation for this problem yields that the x-component of the gas velocity should be a linear function of y, with a slope and zero point such that the boundary conditions at the planes are matched, i.e. here the fluid velocity will be equal to the velocity of the planes themselves. If the boundary conditions are given by $v_x(0) = u_1$ and $v_x(h) = u_2$, then the gas velocity is simply

$$v_x(y) = \frac{u_2 - u_1}{h} y + u_1\,. \tag{3.32}$$

The only non-zero component of the viscous shear stress tensor is a linear function of the velocity gradient along the y-axis, namely

$$\sigma_{xy} = \eta \frac{\partial v_x}{\partial y} = \eta \frac{u_2 - u_1}{h}\,. \tag{3.33}$$

Note also that it is directly proportional to the shear viscosity coefficient, allowing us to validate whether the level of viscosity acting in our numerical simulations actually matches the one we intended to put in.

In order to simulate this hydrodynamical problem we have set up initial conditions using a three-dimensional periodic grid with equally spaced gas particles, all of equal mass and pressure, and being initially at rest. The aspect ratio of the box was shorter in the y-direction. The motion of the two planes was imposed by treating the particles in two thin sheets adjacent to the planes as 'boundary particles', giving them the velocity of the

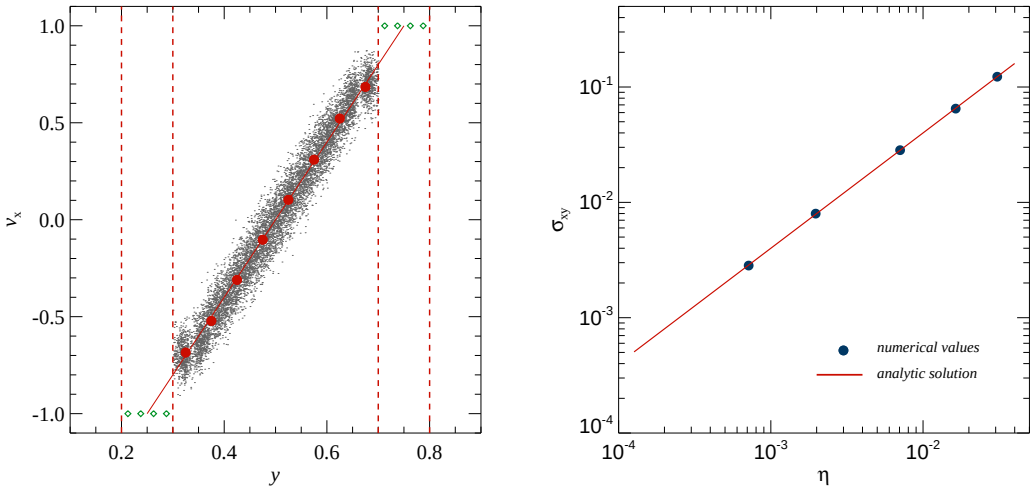

Figure 3.1: The panel on the left shows the stationary-state velocity profile of a viscous flow in between two infinite planes that move relative to each other. The small grey dots represent individual gas particles in the simulation (only every 25th particle has been plotted for clarity). The big red dots are mean v_x-values evaluated in equally sized y-bins. The green diamond symbols show particles that belong to the two thin layers used to impose the boundary conditions, while the continuous solid line is the analytic solution. This run has been performed assuming a shear viscosity coefficient of $\eta \sim 0.002$ in internal code units. The mean value of the viscous stress tensor, σ_{xy}, as a function of the shear viscosity coefficient for a number of similar runs is illustrated in the right panel. In each case, the mean value of σ_{xy} has been estimated once the flow has reached a stationary state and is plotted with a filled circle. The continuous line gives the analytic expectation.

corresponding plane, and preventing them from feeling hydrodynamical forces, i.e. they always keep moving with their initial velocity.

When the simulation is started, the x-component of the gas velocity develops a linear dependence on y under the action of the shear viscosity, and soon the flow becomes stationary. The time needed to reach the stationarity depends on the amount of shear viscosity. The more viscous the medium, the sooner the flow reaches the steady state. Note that the same behaviour cannot be obtained with the standard artificial viscosity. Also, the presence of some amount of artificial viscosity besides the given shear viscosity perturbs the linear dependence of the velocity on the y-coordinate.

In the left panel of Fig. 3.1, we show the x-component of the gas velocity as a function of y when the flow has reached stationarity. The grey little dots represent individual gas particles, while the red big dots denote the mean v_x evaluated in equally sized y-bins. The solid line is the analytic solution, while the diamonds denote particles that are part of the boundary layers of the finite dimension of 0.1, one moving with a velocity $v_x = -1$, the other with $v_x = 1$. It can be seen that the numerical result is reproducing the analytic

solution with good accuracy. Note that the gas velocity near the planes cannot reach the theoretically expected value, because it is here fixed to the value prescribed for the two boundary layers. A finite width of these layers is necessary to impose the boundary conditions in a numerically robust way, but by using a larger particle number, the thickness of this region could be made arbitrarily small, if desired. In the right panel of Fig. 3.1, we show the mean value of the xy-component of the viscous stress tensor as a function of the shear viscosity coefficient adopted in a specific run. The numerical values for the stress tensor have been evaluated once the flow has reached a stationary state. The filled circles give the mean value of σ_{xy} for the different runs, while the solid line is the analytic fit. It can be seen that the analytic solution is recovered with high accuracy for a significant range of shear viscosities.

3.4.2 Flow between two planes with a constant gravitational acceleration

Another elementary hydrodynamic problem involves the viscous flow of a fluid between two planes under the action of a constant gravitational acceleration. This problem is equivalent to the classic example of a flow with a constant pressure gradient [Landau and Lifshitz, 1987]. The initial situation is quite similar to the previous problem, but this time the planes do not move with respect to each other. However, there is a constant gravitational acceleration acting along the x-axis. Again, we consider an incompressible fluid, so that for symmetry reasons all quantities depend only on y if a stationary laminar flow develops. The velocity is expected to exhibit a characteristic quadratic dependence on y, of the form

$$v_x(y) = -\frac{\rho}{2\eta}\frac{\mathrm{d}\Phi}{\mathrm{d}x}y^2 + c_1 y + c_2\,, \tag{3.34}$$

where ρ is the gas density, Φ is the gravitational potential, and c_1 and c_2 are two constants defined by the boundary conditions. Again, the only non-trivial component of the viscous shear tensor is σ_{xy}, and it is related to the velocity field in the same way as in equation (3.33).

The initial conditions for a numerical model of this problem were set up as before, except that a constant gravitational acceleration along the x-axis was imposed. All particles were initially at rest, and the particles of the two boundary layers were made to ignore the gravitational field so that their positions stayed fixed. In Fig. 3.2, we show a measurement of the velocity of the gas particles once the flow reached a stationary state. The grey little dots are individual particles in the simulated region between the planes, while the green diamond symbols represent particles of the boundary layers. The solid line gives the analytic solution, while the big red dot shows the average velocity of gas particles for $y = 0.5$. The central part of the flow matches the characteristic quadratic form of the analytic solution accurately, with a maximum gas velocity corresponding closely to the analytic solution, even though the simulated gas velocity near the planes is a bit lower than the analytic expectation. Again, the latter effect is to be expected due to the finite width of the boundary layers, which also influences the properties of the flow in their immediate vicinity.

We note that the magnitude of the velocity scatter of individual particles around the mean profile depends on the strength of the adopted gas pressure relative to the viscous

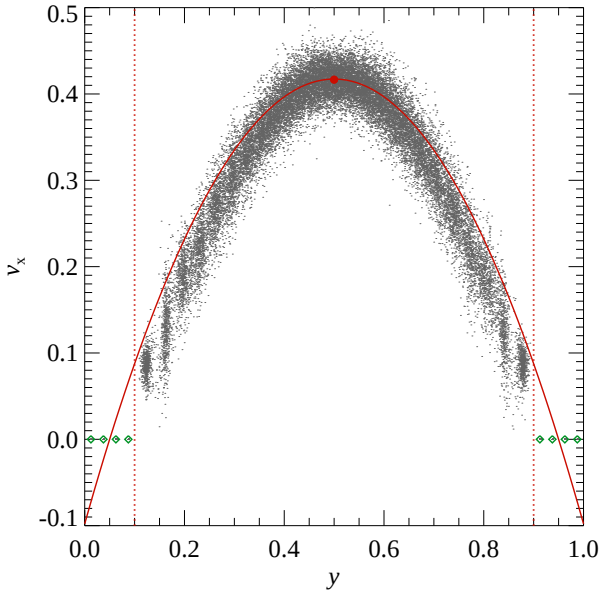

Figure 3.2: Velocity profile for the viscous flow between two fixed planes in a field of constant gravitational acceleration. The little grey dots are the individual particles from the simulation output (only every 25th particle has been plotted for clarity). The analytic solution with its characteristic quadratic velocity dependence on the y coordinate is shown with a red solid line. The big red dot marks the mean velocity of gas particles for $y = 0.5$, while the green diamond symbols represent the particles that belong to the layers of particles used to impose the boundary conditions.

forces. Even for parameter choices where this scatter becomes large, the mean velocity field tracks the analytic solution well in all cases we examined, indicating that our implemented scheme is quite robust.

3.4.3 Shock tube tests

In this section, we examine whether our new implementation of physical viscosity can also be used to capture shocks, and how this fares with respect to results obtained with the standard artificial viscosity. For this purpose, we performed a number of shock tube simulations which have been setup following the standard approach outlined in Sod [1978]. We considered both mild shocks with a Mach number of order 1.5, and also stronger shocks up to a Mach number of 10. These tests allow us to constrain the amount of physical shear and/or bulk viscosity needed to capture the shocks accurately, and hence to assess if and how much artificial viscosity is still required in simulations of viscous gases.

Our initial conditions consist of a three-dimensional periodic box that is elongated in

the x-direction, with a total length L. The box is filled with gas particles of equal mass arranged on a grid. The left half of the box ($x < L/2$) has a higher initial pressure with respect to the right half ($x > L/2$), such that shocks of different strength can be driven into the right side, depending on the initial pressure ratio. The adopted adiabatic index is $\gamma = 1.4$. All gas particles are initially at rest, and we have evolved the simulations until a final time of $t = 3.5$.

Before we discuss the results it should be noted that there is an important conceptual difference between simulations with our new implementation of internal friction and simulations that use the artificial SPH viscosity. In the former case we consider real gases which have different hydrodynamical properties in the region of shocks (where the velocity field has strong gradients) than ideal fluids for which the analytic solutions of shock tubes refer to. In order to properly treat real fluids in shocks, one in principle needs to invoke the kinetic theory of gases, because the mean free path of particles is of the order of the shock width. This is beyond the scope of this work. However, the analytic solutions for ideal gases outside the shock region provide a very good approximation because the viscous forces there are negligible, as we will explicitly confirm below.

In Fig. 3.3, we show the profile of gas density, velocity, entropy and pressure in a shock tube calculation where the gas particles experience a shock of strength $\mathcal{M} = 1.48$. The simulation results are represented by blue circles, the dotted lines denote the initial conditions, and the continuous red lines give the analytic solution, obtained by solving the hydrodynamical equations of an ideal gas with imposed Rankine-Hugoniot conditions [e.g. Courant and Friedrichs, 1976, Rasio and Shapiro, 1991]. The three different columns give results for the standard artificial viscosity with $\alpha = 0.7$ (left panel), physical shear viscosity with $\eta = 0.04$ (middle panel), and physical bulk viscosity of $\zeta = 0.03$ (right panel). The only difference between these three runs lies in the gas viscosity, all the other code parameters and the initial conditions were kept exactly identical in order to facilitate a clear comparison. Fig. 3.3 shows that the numerical model for physical viscosity is capable of capturing the shock, and it results in quite accurate estimates of the post-shock quantities. This holds both for shear and bulk viscosity. Compared to the case with an artificial viscosity, there is more velocity noise in the postshock region, however. Also, the shock front itself is sharper when an artificial viscosity is used, and the analytic solution for the rarefaction wave is recovered more accurately in the transition region to the constant density sections of the flow. In general, the physical viscosity solutions appear more smoothed in the transition regions between the different parts of the flow.

In Fig. 3.4, we examine the viscous stress tensor of gas particles in this problem. The first two panels show the diagonal components of the shear stress tensor, while the last panel gives the bulk viscosity tensor. The viscous stress tensor is different from zero only in the region between the head of the rarefaction wave and the shock wave, implying that the viscous forces are important in that region and are negligible elsewhere. The σ_{yy} and σ_{zz} components of the shear tensor behave almost identically because of the symmetry of the problem, and thus in the middle panel of Fig. 3.4 the dots are for σ_{yy} only. It can be noted that σ_{xx}, σ_{yy} and σ_{zz} have sign and magnitude such that their sum is zero to high accuracy, as it should be given that the shear tensor is traceless. Also, the off-diagonal components of the shear stress tensor are negligible, as expected. The bulk stress tensor shows very similar features as the σ_{xx} component of the shear tensor, due to the fact that

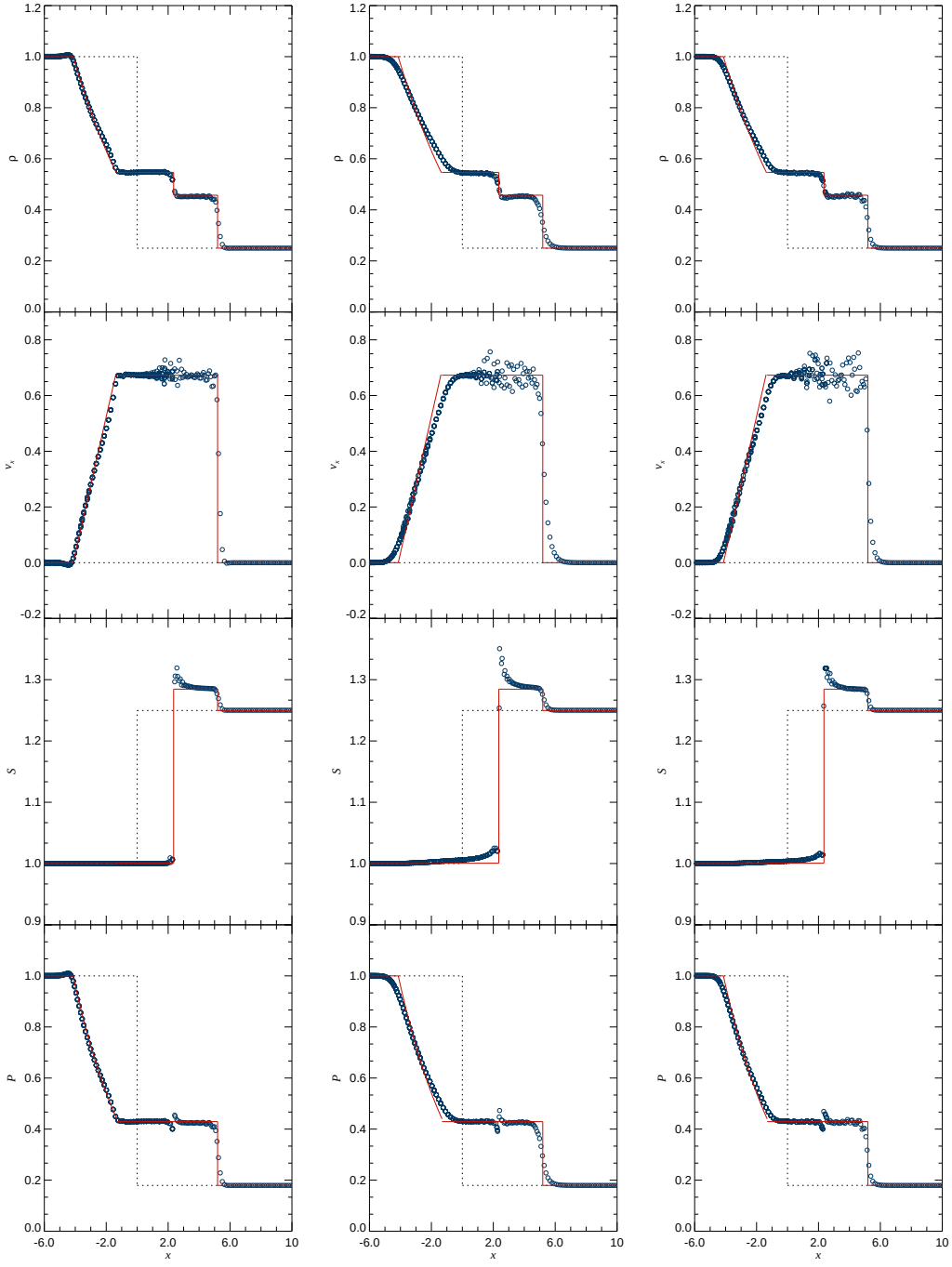

Figure 3.3: Hydrodynamical properties along a shock tube simulation with a shock of Mach number $\mathcal{M} = 1.48$, at time $t = 3.5$. The initial conditions are drawn with doted lines, the analytic solutions are shown with continuous red lines, and the symbols give the SPH result. The three vertical columns refer to a run carried out with the standard artificial viscosity (left column), to one with physical shear viscosity instead (middle column), or to one with physical bulk viscosity (right column). From top to bottom, the individual rows show the profiles of density, velocity, entropy, and pressure, respectively.

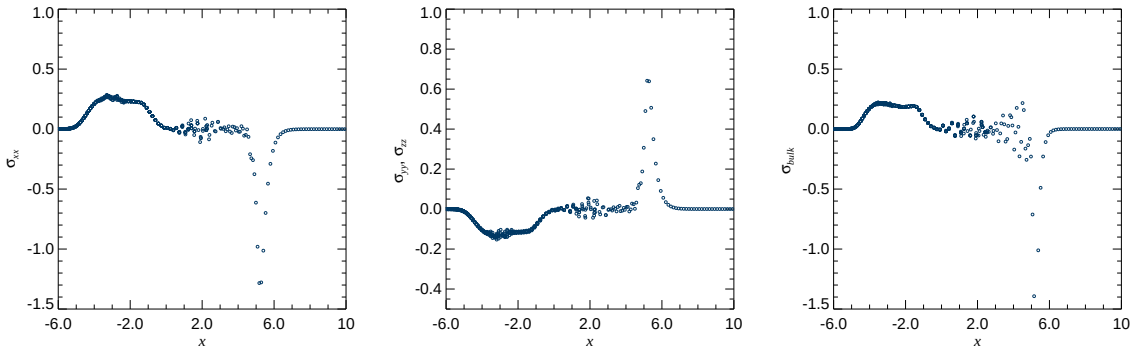

Figure 3.4: Viscous stress tensor profile in the case of a $\mathcal{M} = 1.48$ shock tube simulation. The first two panels refer to the physical shear viscosity, showing diagonal components of the stress tensor, while in the right panel the bulk stress tensor is plotted. In the middle panel, the dots give only results for σ_{yy}, because the σ_{yy} and σ_{zz} components of the shear tensor show a practically identical dependence on the x-coordinate, given the symmetry of the problem.

the dominant term in both cases is $\partial v_x/\partial x$. However, $\sigma_{\rm bulk}$ shows more scatter for $x \in [3, 5]$ because the noise in the remaining velocity derivatives in the corresponding simulation is larger. In our simulations with with larger Mach numbers, we obtained qualitatively very similar results as the ones presented in Fig. 3.4.

The above analysis has shown that both shear and bulk physical viscosity are in principle capable of capturing shocks, provided the viscosity coefficients are sufficiently large. This means that in simulations of low Reynolds number one can probably avoid the use of any additional artificial viscosity. In general however, it seems clear that an artificial viscosity is still needed even when physical viscosity is modelled. This is simply because the strength of the physical viscosity can be quite low, and can vary locally with the flow if a physical parameterization like that of Braginskii is used. Without artificial viscosity, shocks would then not be captured accurately in a narrow shock front, and particle interpenetration would not be properly avoided. Instead, strong fluid instabilities could develop in the shock region, growing to such large enough size that the residual physical viscosity can damp them out. In the rest of our study, we will therefore invoke when necessary an additional artificial viscosity in the standard way when we model physical viscosity in astrophysically interesting situations. This guarantees that shocks are always captured equally well as in standard SPH.

3.5 AGN–driven bubbles in a viscous intracluster medium

In this section, we study the interaction of AGN-induced bubbles with a viscous intracluster medium. This represents an extension of the study of Sijacki and Springel [2006], and we refer to this paper for a detailed description of the models, and the simulation setup, while we here give just a brief overview.

We consider models of isolated galaxy clusters under a range of different physical pro-

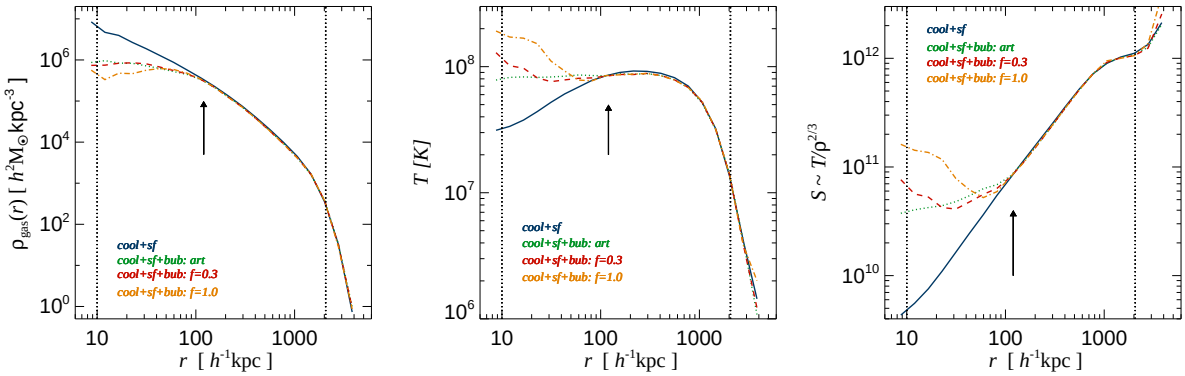

Figure 3.5: Radial gas profiles of a $10^{15}\,h^{-1}\mathrm{M}_\odot$ isolated halo at time $t = 0.15\,t_{\mathrm{Hubble}}$. We show the gas density (left panel), mass-weighted temperature (middle panel), and gas entropy (right panel), and compare runs with cooling and star formation only (blue solid lines) with runs having additional AGN heating as well. The green dotted lines are for simulations with standard artificial viscosity. The red dashed lines give results when the Braginskii parameterization of the shear viscosity is "switched on", with a suppression factor of 0.3. For comparison, the orange dot-dashed lines show the results when no suppression factor is used for the shear viscosity.

cesses. The initial setup consists of a static NFW dark mater halo [Navarro et al., 1996, 1997], and a gas component which is initially in hydrostatic equilibrium. The adopted initial gas density profile closely follows the dark mater profile, except for a slightly softened core. A certain level of rotation has been included as well, described by a spin parameter of $\lambda = 0.05$. AGN heating has been simulated with a phenomenological approach in the form of centrally concentrated hot bubbles that are injected into the ICM in regular time intervals. The basic parameters of the AGN feedback scenario are the bubble radius, distance from the cluster centre, duty cycle and bubble energy content. These parameters have been constrained by recent cluster observations and also by the basic empirical laws of black hole accretion physics.

We used 10^6 gas particles to construct initial conditions for a massive isolated galaxy cluster of mass $10^{15}\,h^{-1}\mathrm{M}_\odot$, with a spatial resolution in the gravitational field equal to $6.5\,h^{-1}$kpc. Starting from these identical initial conditions, we carried out different runs, characterized as follows: (1) radiative cooling and star formation together with standard artificial viscosity; (2) cooling, star formation, and AGN-bubble heating with artificial viscosity; (3) cooling, star formation, AGN-bubble heating, and physical shear viscosity, based on the Braginskii parameterization and with a suppression factor that we varied in the range of 0.3 to 1.0[4]. The radius of the bubbles was chosen as $30\,h^{-1}$kpc, and they

[4]In these runs, we used only the physical viscosity, switching off the artificial viscosity completely. This is here justified because we are simulating an isolated halo where no strong shocks are present, and due to the fact that the bubble heating keeps most of the gas above 10^7K, such that sufficient shear viscosity is present to evolve the hydrodynamics correctly, as we explicitly checked.

were injected into the ICM every 10^8 yrs along a fixed spatial axis, with an energy content equal to 2.5×10^{60} ergs per bubble.

3.5.1 Radial heating efficiency and profiles

In Fig. 3.5, we show radial profiles of our massive galaxy cluster after a simulated time of $0.15\,t_{\rm Hubble}$. Gas density is plotted in the left panel, mass-weighted temperature in the central panel, and gas entropy in the right panel. A number of interesting features can be noticed from the gas profiles. First, regardless of the assumed gas viscosity, the bubble heating prevents the creation of a strong cooling flow, and gas is heated efficiently in the inner regions. Moreover, the spatial extent of the central region in which AGN feedback alters the gas profiles does not depend on the level of gas viscosity - in all the runs, bubbles influence the ICM out to $\sim 150\,h^{-1}$kpc. This scale is indicated with a vertical arrow on the panels. Thus, the radial extent of bubble heating is determined by other factors, like for example by the initial entropy excess of bubbles with respect to the surrounding gas, by the injection mechanism, or by the equation of state of the gas filling the bubbles. Second, it can be seen that an increase of the gas viscosity produces a systematically stronger heating in the innermost $\sim 50\,h^{-1}$kpc, and this trend is also present at subsequent simulation output times until $0.25\,t_{\rm Hubble}$ where we stopped the simulations. The heating is most prominent in the case of unsuppressed Braginskii viscosity (orange dot-dashed lines), where an entropy inversion occurs, and the temperature of the gas keeps increasing until the very centre. Such a temperature profile is not favoured by observational findings, suggesting that if the intracluster gas viscosity is indeed so high than the bubble energy content has to be substantially lower, or the energy transport from the bubbles into the ICM has to be somehow inhibited, possibly by magnetic fields.

Another interesting feature of bubble heating in a viscous ICM can be noticed when the bubble morphologies and the radial heating efficiency are examined in more detail. In Fig. 3.6, we show mass-weighted temperature maps of the central cluster regions, for the case of Braginskii viscosity with suppression factor of 0.3 (upper panel) and for unsuppressed Braginskii shear viscosity (lower panel). The velocity flow pattern is indicated with white arrows on these maps. Even though the radial extent of the bubble heating is similar for different magnitudes of internal friction, the morphologies of evolved bubbles, their maximum clustercentric distance reached and their survival times vary. When the gas viscosity is as high as the full Braginskii value, the bubbles rise up to $\sim 300\,h^{-1}$kpc in the cluster atmosphere without being disrupted, and traces of two up to three past bubble episodes can be detected, indicating that the bubbles survive at least as long as $\sim 2 \times 10^8$ yrs. However, when the gas viscosity is lowered (upper panel of Fig. 3.6) bubbles typically start to disintegrate at $\sim 150\,h^{-1}$kpc and multiple bubble events can typically not be identified.

This suggests that a relatively high amount of gas viscosity may be needed to explain the recent observations of the Perseus cluster [e.g. Fabian et al., 2006], where several bubble occurrences have been detected. However, an alternative explanation could be that the bubbles are stabilized against fluid instabilities by magnetic fields at their interface with the ICM instead of by viscosity. A relativistic particle component (cosmic rays) filling the bubble will also change the dynamical picture. Nevertheless, it is interesting that the

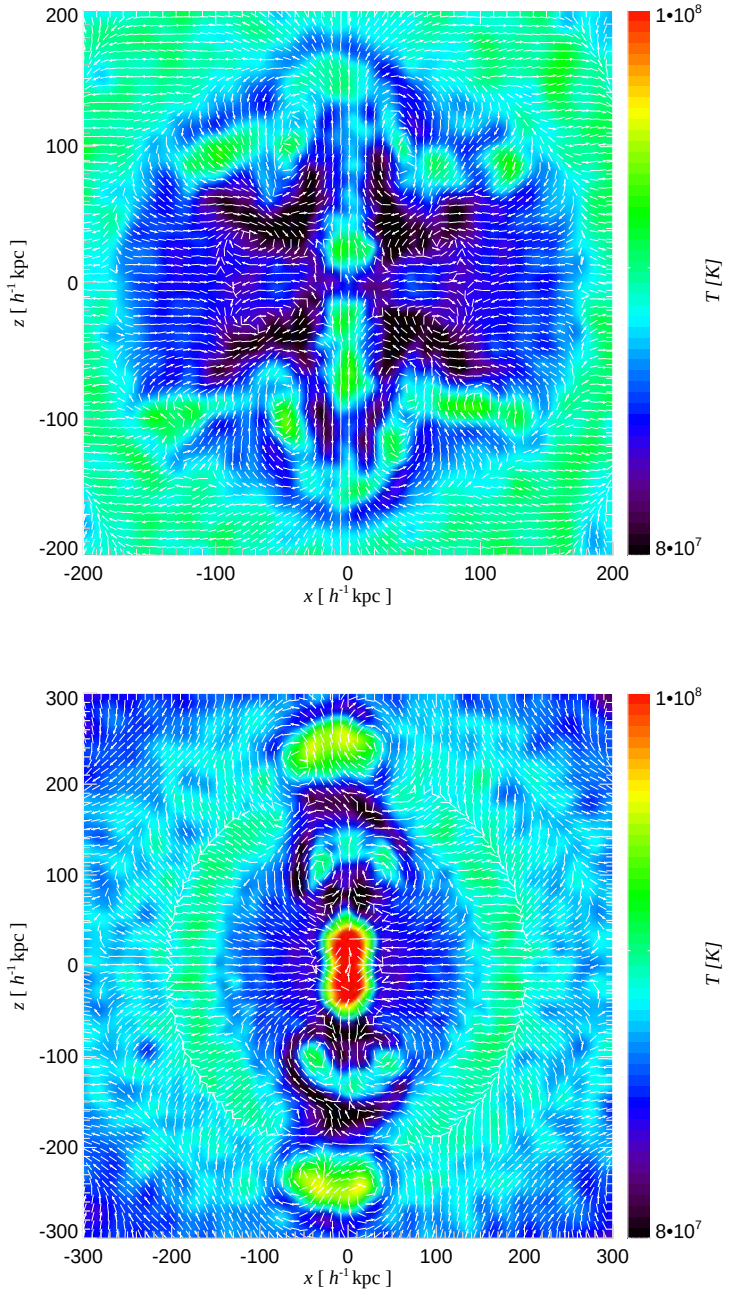

Figure 3.6: Mass-weighted temperature maps of a $10^{15}\,h^{-1}\mathrm{M}_{\odot}$ isolated halo, subject to AGN bubble feedback. The velocity field of the gas is over-plotted with white arrows. The maps show how the morphology, survival time and maximum distance reached of AGN–driven bubbles depend strongly on the amount of physical viscosity assumed: in the upper panel, the Braginskii shear viscosity has been suppressed by a factor 0.3, while in the lower panel, the simulation has been evolved with the full Branginskii viscosity.

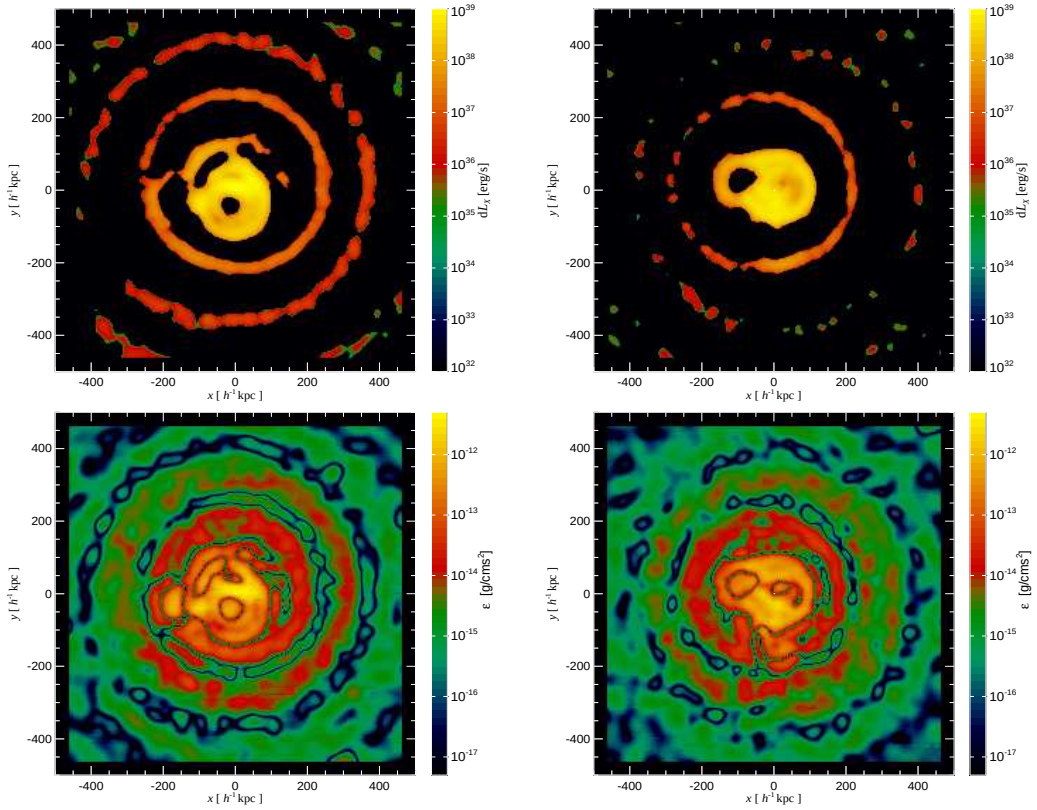

Figure 3.7: The upper panels show unsharp-masked X–ray emissivity maps of a $10^{15}\,h^{-1}\mathrm{M}_{\odot}$ isolated cluster with AGN bubble feedback. On the left, a case with lower viscosity is shown (suppression factor $f = 0.3$), while on the right, a case with the maximum value of the shear viscosity is displayed (suppression factor $f = 1.0$). The sound waves generated by the bubbles in the ICM are clearly more efficiently dissipated when the ICM has a higher viscosity. The panels on the bottom illustrate the projected energy density in sound waves for the same cases, estimated as explained in the text. On these maps, both compressed and rarefied regions are visible, containing a significant amount of acoustic energy density. Nevertheless, the total energy of the sound waves is not substantial in our models, and amounts to only a small fraction of the thermal energy of an injected bubble.

observed morphology of bubbles can in principle constrain the level of ICM viscosity, an aspect that we plan to explore further in a future study.

In the velocity fields shown in Fig. 3.6, it can be seen that the flow of the gas in the wake of the bubbles is approximately laminar, while at the bubble edges the velocity field shows a significant curl component. This perturbed motion is not only present for the most recently injected bubbles, but also for the bubbles that are already $\sim 2 \times 10^8$ yrs old, albeit with a smaller magnitude. In the case of the full Braginskii viscosity the magnitude of the velocity perturbations induced by the bubbles is of the order of $\lesssim 100\,\mathrm{km\,s^{-1}}$ for

Simulation	$N_{\rm HR}$	$N_{\rm gas}$	$m_{\rm DM}$ $[h^{-1}{\rm M}_\odot]$	$m_{\rm gas}$ $[h^{-1}{\rm M}_\odot]$	$z_{\rm ini}$	$z_{\rm fin}$	ϵ $[h^{-1}{\rm kpc}]$
g1/g8	4937886	4937886	1.13×10^9	0.17×10^9	60	0	5.0

Table 3.1: Numerical parameters of the cosmological galaxy cluster simulations used in this study. The values listed from the second to the fifth column refer to the number and to the mass of high resolution dark matter particles and of gas particles. Note that the actual values of $N_{\rm gas}$ and $m_{\rm gas}$ may vary in time due to star formation, if present. The last three columns give the initial and final redshifts of the runs, and the gravitational softening length ϵ.

the recent bubbles, while it decreases to $\lesssim 20\,{\rm km\,s^{-1}}$ for the older ones.

3.5.2 Sound waves dissipation

We also examined how the occurrence of sound waves produced by the bubbles and the associated non-local heating is influenced by different amounts of ICM viscosity. In Fig. 3.7, we show unsharp-masked images of the X–ray emissivity, produced by subtracting a map smoothed on a $50\,h^{-1}$kpc scale from the original luminosity map. It is clear that for higher gas viscosity (right panel, unsuppressed Braginskii value) the damping of sound waves in the central region is stronger than for a simulation with lower viscosity (left panel: 0.3 of Braginskii viscosity). Nevertheless, the radial profiles of the gas entropy show that only in the inner $\sim 50\,h^{-1}$kpc a more efficient heating of the ICM can be observed when the viscosity is increased. This suggests that the energy content of the sound waves produced by the bubbles is not very large and probably not capable of providing significant heating at larger radii.

In order to put more stringent constraints on the influence of the sound waves, we have estimated their energy content by evaluating [Landau and Lifshitz, 1987]

$$\int E_s \,{\rm d}V \;=\; \int \rho_0 v^2 \,{\rm d}V \;=\; \int \frac{\rho'^2}{\rho_0} c_s^2 \,{\rm d}V, \tag{3.35}$$

where E_s is the sound energy density, ρ_0 is the unperturbed gas density, v is the fluid velocity, ρ' is the change in gas density due to the sound waves, and c_s is the sound speed. Strictly speaking, this equation is valid only for travelling plane waves, but it should still provide us with a reliable order of magnitude estimate of the sound waves energy in our geometrically more complex case. We computed projected energy density maps (see lower panels of Fig. 3.7) by taking the smoothed density field for ρ_0, while we estimated ρ' as the difference between the actual density field and the smoothed one. Both compressed regions (which correspond to the rings in the upper panels) and rarefied regions store a considerable amount of energy. However, it should be noted that the sound wave energy in the rarefaction regions is overestimated when computed in this way, because the bubbles themselves contribute to it, being underdense with respect to the background and having similar dimension to the smoothing scale. Nevertheless, when the total sound wave energy is estimated in this way we obtain $\sim 5 \times 10^{59}$ ergs, which is only a small fraction of the

initially injected bubble energy. As pointed out by Churazov et al. [2002], a number of the same order of magnitude is obtained if as a crude estimate of the sound wave energy one considers the sound waves generated by the motion of a solid sphere through a medium of a given density ρ [Landau and Lifshitz, 1987].

Based on these findings, the viscous damping of sound waves provides only an insignificant contribution in coupling the AGN-injected energy into the ICM. Note that in these models of isolated halos we have deliberately included physical shear viscosity only. Thus, our estimate for the damping of sound waves is not affected by any residual artificial viscosity. A caveat, however, is that our simulations do not self-consistently model the initial phase of bubble injection, where the AGN-jet deposits its energy and inflates the bubble. It is conceivable that the associated processes produce energetically more important sound waves and weak shocks, which could then increase the importance of viscous damping of sound waves compared to the result found here.

3.6 Cosmological simulations of viscous galaxy clusters

In this section we discuss the effects of internal friction on clusters of galaxies formed in fully self-consistent cosmological simulations. We have carried out a variety of runs that follow different physical processes, including non–radiative hydrodynamical simulations, described in detail in Section 3.6.1, and runs with radiative gas cooling, star formation and feedback processes, which are discussed in Section 3.6.2. For all these simulations, we carried out matching pairs of runs without physical viscosity and with physical shear viscosity (using the Braginskii parameterization with a suppression factor of 0.3), in order to be able to clearly identify differences due to the viscous dissipation processes.

For our simulations, we selected two massive galaxy clusters that have been extracted from a cosmological ΛCDM model with a boxsize of $479h^{-1}$Mpc [Yoshida et al., 2001, Jenkins et al., 2001], and were prepared by Dolag [2004] for resimulation at higher resolution using the Zoomed Initial Condition technique [Tormen et al., 1997]. In Tables 3.1 and 3.2, we summarize the basic parameters of the simulations and the main physical properties of the galaxy clusters. The cosmological parameters of the simulations correspond to a concordance ΛCDM model with $\Omega_m = 0.3$, $\Omega_b = 0.04$, $\sigma_8 = 0.9$, and $H_0 = 70\,\mathrm{km\,s^{-1}Mpc^{-1}}$ at the present epoch.

3.6.1 Non–radiative simulations

In Fig. 3.8, we show projected gas density maps at different redshifts for our non-radiative cluster simulations. It is evident that already at early times, at around $z \sim 5$, the gas distribution in the presence of shear viscosity (panels on the right) starts to deviate substantially from the corresponding simulation without internal friction (panels on the left). Also, the amount of gas that is bound to dark matter subhalos is reduced, and there appears to be more diffuse gas in the outskirts of massive objects. Furthermore, small structures that are falling into the most massive halo at each epoch (located in the centre of the panels), lose their gas content more quickly due to the shear forces, and feature prominent tails that extend up to several hundred kiloparsec. These general features are present at all epochs from $z \sim 5$ to $z = 0$. At low redshifts, however, the central parts

Cluster	R_{200} $[h^{-1}\mathrm{kpc}]$	M_{200} $[h^{-1}\mathrm{M}_\odot]$	T_{mw} [K]	L_{X} $[\mathrm{ergs}^{-1}]$
g1_csf	2857	1.63×10^{15}	7.3×10^{7}	1.0×10^{45}
g1_csfv	2832	1.58×10^{15}	8.1×10^{7}	1.0×10^{45}
g8_ad	3306	2.52×10^{15}	9.7×10^{7}	1.1×10^{46}
g8_adv	3276	2.45×10^{15}	1.1×10^{8}	4.5×10^{45}

Table 3.2: Physical properties of our sample of simulated galaxy clusters at $z = 0$ and at $200\rho_c$. For two different galaxy clusters, labelled in the first column, and for the different runs, cluster radius, total mass, mass–weighted gas temperature and X–ray luminosity are listed, respectively. Subscripts in the first column denote runs including different physics, namely cooling and star formation for the g1 cluster, and non–radiative gas hydrodynamics for the g8 cluster, in both cases also with Braginskii shear viscosity with suppression factor of 0.3.

of the main halo appear quite similar, although the central density is somewhat reduced in the simulation with physical viscosity, while there appears to be more diffuse gas with a smaller number of prominent gas concentrations in the outskirts. These trends can be readily understood as a consequence of viscous dissipation, which increases the stripping of gas and helps to expel gas from shallow dark matter potential wells in the infall regions of larger structures.

A more quantitative analysis of how viscosity affects the thermodynamics of clusters is obtained by studying the radial profiles of gas density, mass-weighed temperature, and entropy. In Fig. 3.9, we compare these profiles at two different epochs, $z = 1$ and $z = 0$. The solid blue line refers to the non-radiative run, while the dotted green line gives the result when physical shear viscosity is included. The effects of viscosity increase systematically with time, and manifest themselves in a reduction of the gas density throughout the cluster. The suppression is particularly strong in the very centre, where it reaches almost an order of magnitude at $z = 0$. At early times, the temperature is mainly boosted in the outer regions of the cluster, while for $z < 0.5$, also the central gas temperature starts to be significantly increased. As a consequence, the entropy profile shows two different features: At early times, the central rise of entropy is caused by a lower gas density, while at late times, the entropy is even more enhanced in the inner regions, out to a radius of $\sim 100\,h^{-1}\mathrm{kpc}$, because of a lower gas density and an increased temperature. In the outer parts of the halo, the increase of the gas entropy is always a result of the joint action of temperature and density change. We will come back to a discussion of the physical reason for this behaviour in Section 3.6.2.

As a consequence of the strong modification of the density and temperature structure of the cluster in the viscous case, we also find a significant reduction of the X–ray luminosity. This is reflected in Table 3.2, which lists some of the basic properties of these clusters. Interestingly, a similar change of the X–ray luminosity is not found in the case of the simulations that also include cooling and star formation, which we will discuss next.

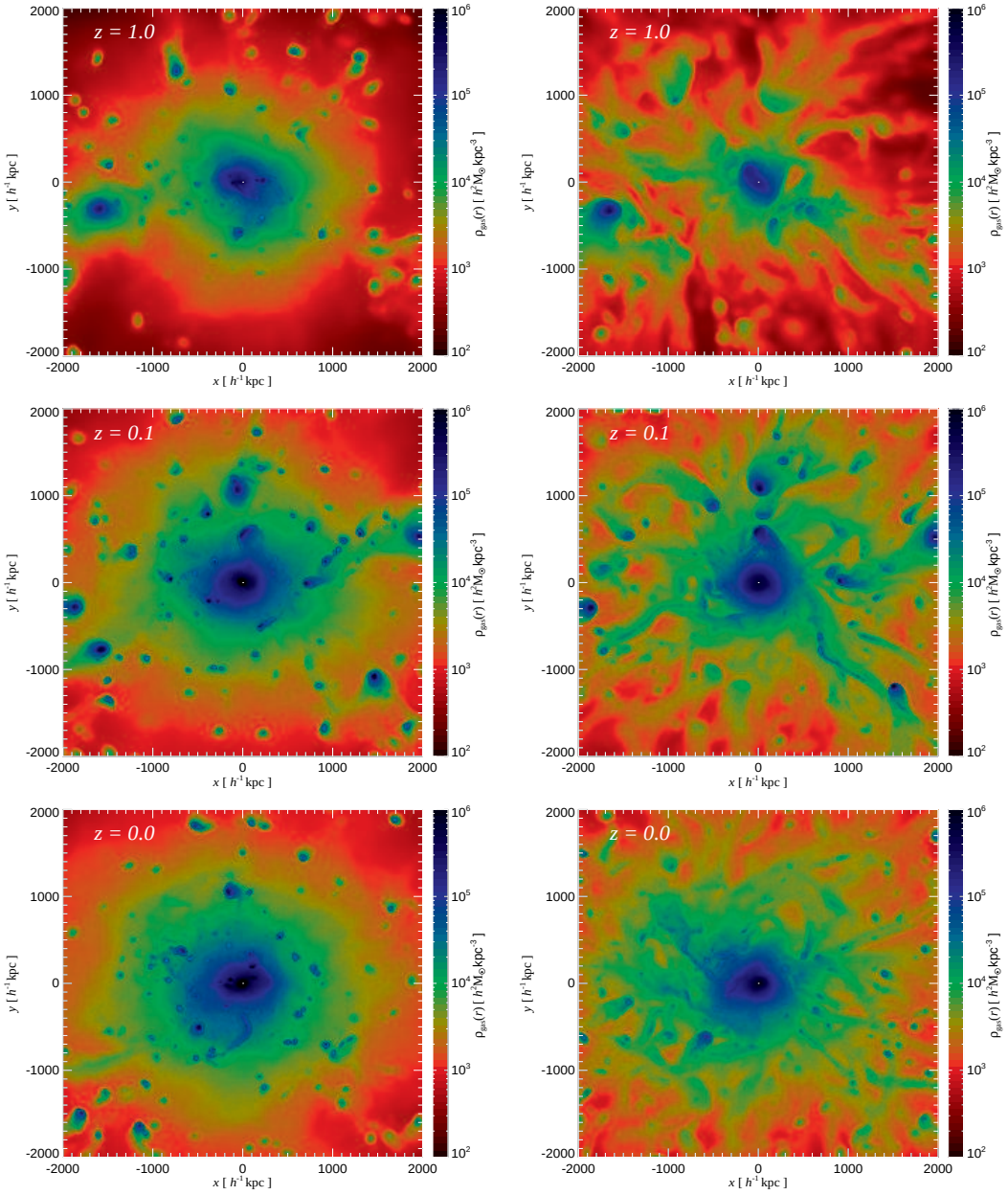

Figure 3.8: Projected gas density maps of the g8 galaxy cluster simulation at redshifts $z = 1.0$, $z = 0.1$ and $z = 0.0$, as indicated in the upper-left corner of the panels. The panels in the left column show the gas density distribution in the case of a non–radiative run, while the panels in the right column give the gas density distribution when Braginskii shear viscosity is "switched-on", using a suppression factor of 0.3. It is evident from these panels that the presence of a modest amount of shear viscosity has a significant impact on the gas distribution, removing more gas from infalling structures when they enter the massive halo, and producing pronounced gaseous tails behind them.

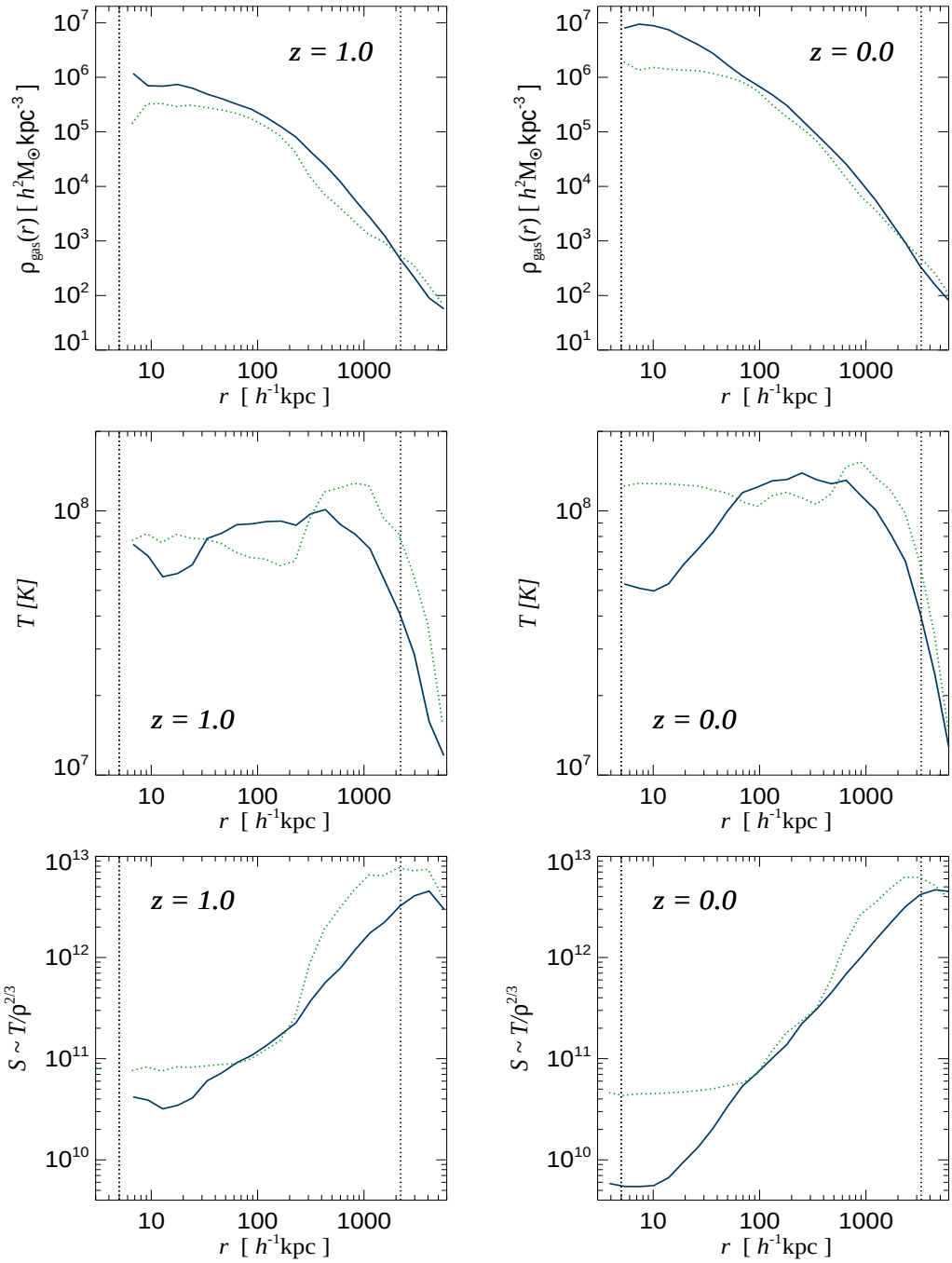

Figure 3.9: Radial profiles of gas density, mass-weighted temperature, and entropy of the 'g8' galaxy cluster simulation. The blue continuous lines are for the non–radiative run, while the dotted green lines are for the run with additional Braginskii shear viscosity with suppression factor of 0.3. The panels in the left column refer to the gas profiles evaluated at $z = 1.0$, while the ones in the right column are for $z = 0$. The dotted vertical lines denote the gravitational softening length and the virial radius at the given redshift.

3.6.2 Simulations with cooling and star formation

In Fig. 3.10, we show the radial gas profiles of basic thermodynamic quantities of our cluster simulations that included radiative cooling and star formation, either without (blue solid line) or with (dotted green line) additional shear viscosity. At high redshifts, the signatures of viscosity are quite similar to the previously considered case where gas cooling was absent. However, the formation of a cooling flow for $z < 0.5$ changes the central gas properties dramatically at later times. Even though viscous dissipation is acting in the cluster centre, the gas cooling times become so short there that all the thermal energy gained from internal friction is radiated away promptly. In fact, the gas starts to cool even more in the central regions in the viscous case, as can been seen from the entropy profiles at $z = 0$. The gas density is increased in the innermost regions as well.

Apparently, while the viscous heating in the centre is not sufficiently strong to raise the temperature significantly, the mild heating does reduce the star formation rate and therefore the associated non-gravitational heating from supernovae. The net result is an increase in the X–ray luminosity due to the sensitive density- and temperature-dependence of the cooling luminosity. Interestingly, there is still a reduction of the X-ray luminosity in the outskirts of the cluster in the viscous simulation, because the gas density is lowered there, but this is just compensated for by a matching increase in the inner parts. Another important aspect of the viscous heating process is that it makes the temperature profile closer to isothermal, suggesting that the viscosity helps to level the temperature of the cluster on large scales. It is interesting to note that our results on the profiles resemble the findings of self-consistent cosmological simulations of cluster formation with thermal conduction [Jubelgas et al., 2004, Dolag et al., 2004]. The transport coefficients of viscosity and heat conductivity have the same temperature dependence, and this fact may contribute to the similarity of the behaviour with respect to the role these transport processes play in shaping the gas properties.

We now turn to a discussion of the radial dependence of viscous dissipation in clusters of galaxies. As can be seen from equation (3.25), the entropy increase due to shear viscosity involves two factors: one is given by the shear viscosity coefficient, which basically has only a dependence on temperature to the 5/2 power, and the other is the ratio of the rate-of-strain tensor squared to that of the gas density elevated to the γ. Thus, viscous entropy injection will be favoured in regions of high temperature, low density and strong velocity gradients. In order to disentangle the relative importance of these different dependencies we show the radial profiles of the shear viscosity coefficient η, the rate-of-strain tensor squared $\sigma^2_{\alpha\beta}$, and of the kinematic viscosity ν in Fig. 3.11, at $z = 0$.

Let us first consider the non–radiative case, which is shown with solid green lines. At all radii, the gas density is reduced in the presence of shear viscosity, and this modification of the density profile influences the rate of entropy production. Nevertheless, the contribution of the shear coefficient is more important in the outer regions, for $r > 100\,h^{-1}$kpc, having a maximum at $\sim 1000\,h^{-1}$kpc, where also the gas temperature is highest. On the other hand, the rate-of-strain tensor is monotonically increasing from the outskirts towards the centre, and this is also true for its individual components, indicating that the velocity gradients are largest in the inner regions.

The dashed red lines show the results when cooling and star formation are included.

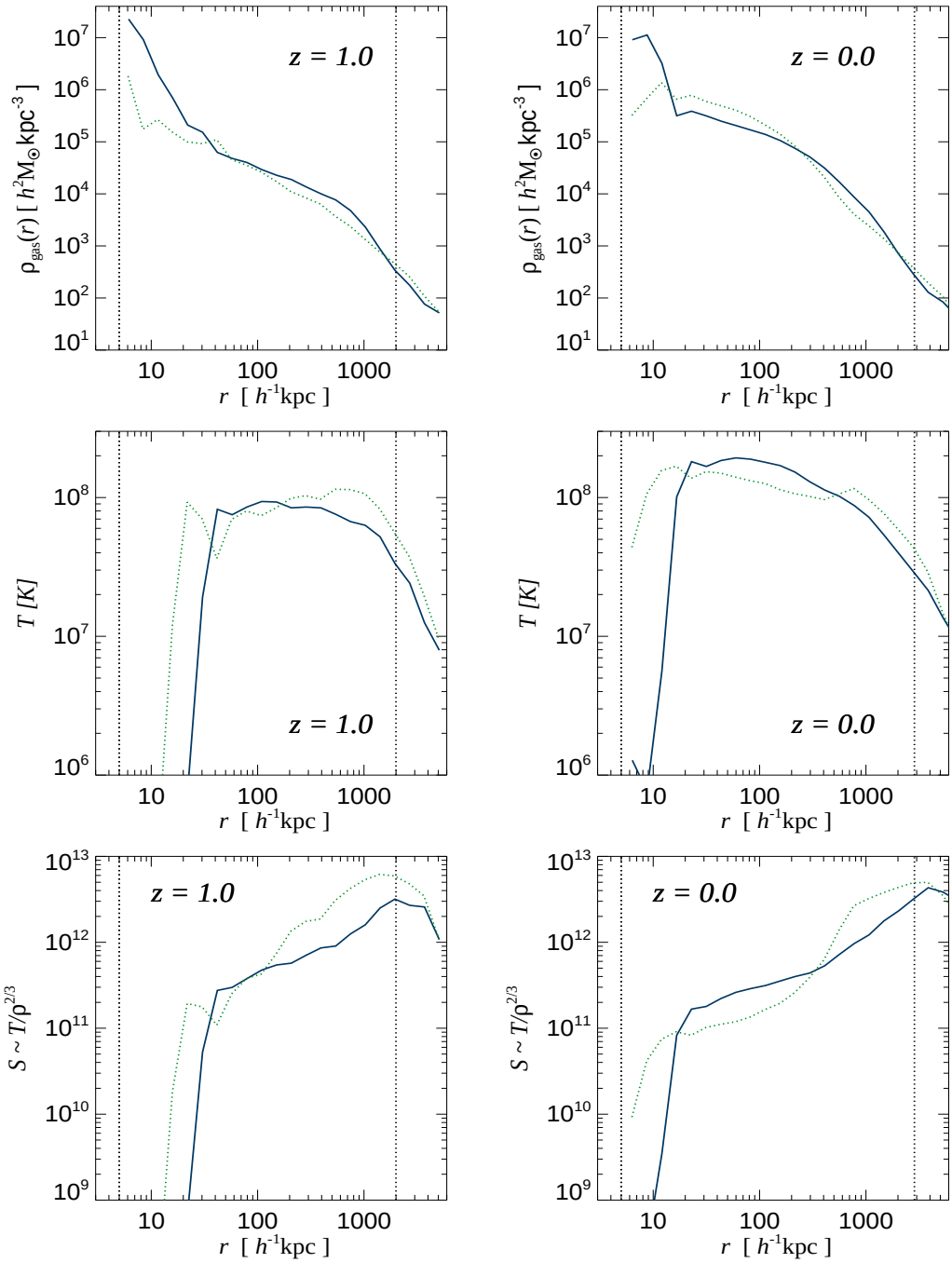

Figure 3.10: Radial profiles of gas density, mass-weighted temperature, and entropy of the 'g1' galaxy cluster simulation. The blue continuous lines are for the run with cooling and star formation, while the dotted green lines are for the run with additional Braginskii shear viscosity with suppression factor of 0.3. The panels in the left column refer to the gas profiles evaluated at $z = 1.0$, while the panels in the right column are for $z = 0$. The dotted vertical lines indicate the gravitational softening length and the virial radius at the given redshift. It can been seen that the viscous effects are similar to the non–radiative case at high redshifts, while they differ significantly at low z due to the formation of a central cooling flow.

The differences that arise in the shear viscosity coefficient compared with the non-radiative case can be simply explained by the different temperature profiles: in the outer regions, for $r > 100\,h^{-1}$kpc, the 'g1' cluster run has lower η because its temperature there is smaller due to the fact that this cluster is somewhat less massive than the 'g8' galaxy cluster. Instead, the temperature of the 'g1' cluster in the innermost regions is larger, because the introduction of radiative cooling increases the central gas temperature, except for the innermost cooling flow region. Also, $\sigma^2_{\alpha\beta}$ of the 'g1' cluster is higher near the centre due to the motions induced by the prominent cooling flow that has formed in it.

Finally, we study the kinematic viscosity in the last panel of Fig. 3.11, which is given by the ratio of the shear viscosity coefficient to the gas density. Both for the 'g1' and 'g8' cluster simulations, the kinematic viscosity coefficient is very similar in the outer regions, and is highest for large radii. In the inner $100\,h^{-1}$kpc, the kinematic viscosity of the 'g1' cluster is higher, due to the efficient gas cooling. Overplotted with a blue arrow is an upper limit for the kinematic viscosity on a scale of 100 kpc estimated for the Coma galaxy cluster by Schuecker et al. [2004]. The kinematic viscosity of the 'g8' galaxy cluster, which is slightly more massive then the Coma cluster, is in agreement with this observational constraint, suggesting that a suppression factor as large as 0.3 is not ruled out observationally. On the other hand, the kinematic viscosity of the 'g1' cluster, with the same suppression factor, is only marginally in agreement with the observational upper limit. However, this comparison needs to be taken with a grain of salt: The intrinsic amount of shear viscosity is certainly overestimated in our simulations, because they suffer from strong central cooling flows which are not observed in real galaxy clusters.

3.6.3 Viscous dissipation during merger events

The radial profiles of gas temperature and entropy discussed above indicate that the gas is heated very efficiently in cluster outskirts by viscous dissipation during accretion and merger events. In this section, we study this phenomenon in more detail. In particular, we analyze the spatial distribution of entropy production just before and during a merger episode. To this end we compare projected density maps, which give us an indication on the exact position and extent of the merging clumps, to entropy maps, which tell us where the heating takes place. In Fig. 3.12, we show an example of these maps for the 'g1' galaxy cluster. The upper panels refer to the run with cooling and star formation only, and the lower panels show the run where shear viscosity was included as well. The panels for the runs with different physics are not at the same redshift because the shear forces influence the dynamics of structure formation sufficiently strongly that timing offsets in the merging histories occur. We tried however to select snapshots with similar merging configuration at comparable cosmic epochs so that the visible differences arise primarily because of the introduction of the shear viscosity. We note that we analyzed a number of different merger configurations at multiple redshifts, also considering the non–radiative simulations. We find that the features visible in Fig. 3.12 are ubiquitous; viscous dissipation of shear motions not only considerably boosts the gas entropy, but also generates this entropy in special spatial regions which have no counterparts in the simulations that only include an artificial viscosity. The relevant regions are located perpendicular to the direction of a halo encounter, and appear as entropy-bright bridges. These regions of enhanced entropy,

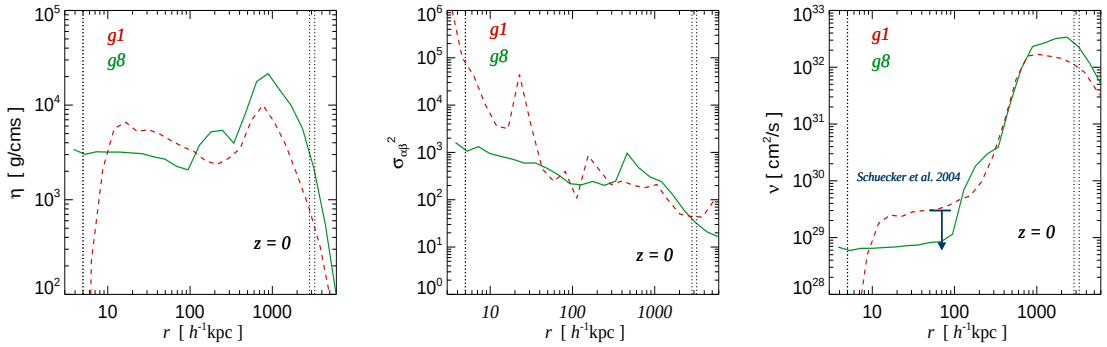

Figure 3.11: From top to bottom, radial profiles of the mass-weighted shear viscosity coefficient, of the rate-of-strain tensor squared, and of the kinematic viscosity coefficient in the 'g1' and 'g8' galaxy cluster simulations, respectively. The red dashed line is for the g1 simulation with cooling, star formation and shear viscosity, while the continuous green line represents the non-radiative g8 simulation with the same amount of shear viscosity. The dotted vertical lines indicate the gravitational softening and the virial radius at $z = 0$, respectively. In the bottom panel, the observational upper limit for the Coma galaxy cluster [Schuecker et al., 2004] at a scale of 100 kpc is shown with a blue arrow.

which are never found in the runs without shear viscosity, are responsible for heating the clusters outskirts, already at early times.

We have also constructed maps of the viscous entropy increase, based on equation (3.25). All the filamentary high entropy regions are corresponding to the ones shown in Fig. 3.12, demonstrating that they are caused by $\eta\,\sigma^2_{\alpha\beta}/\rho^\gamma$. The dominant factor appears to be η/ρ^γ, while the spatial distribution of $\sigma^2_{\alpha\beta}$ is preferentially confined to the regions characterized by relatively high overdensities.

Finally, in order to better understand the gas dynamics in these high entropy regions, we computed the velocity flow field during the merger event, and show it overlaid on the X–ray emissivity map in Fig. 3.13. It can be seen that there are two galaxy clusters approaching each other, one located in the centre of the figure and the other one being above it, at $(x, y) \sim (0, 1000)\,h^{-1}$kpc. The high entropy bridge is lying between the merging clusters, roughly perpendicular to their direction of motion. Considering the velocity flow pattern, it can be noticed that there are two velocity streams: one starting from the lower right corner, and the other from the upper right one. The velocity currents meet in the central region where the merger will occur. Therefore, the gas is not flowing along the high entropy bridge, but rather perpendicular to it. This shows that the material of the high entropy bridge is not funneled towards the centre from the cluster outskirts but rather that it is heated in situ by significant viscous dissipation, creating the entropy bridges between the merging structures.

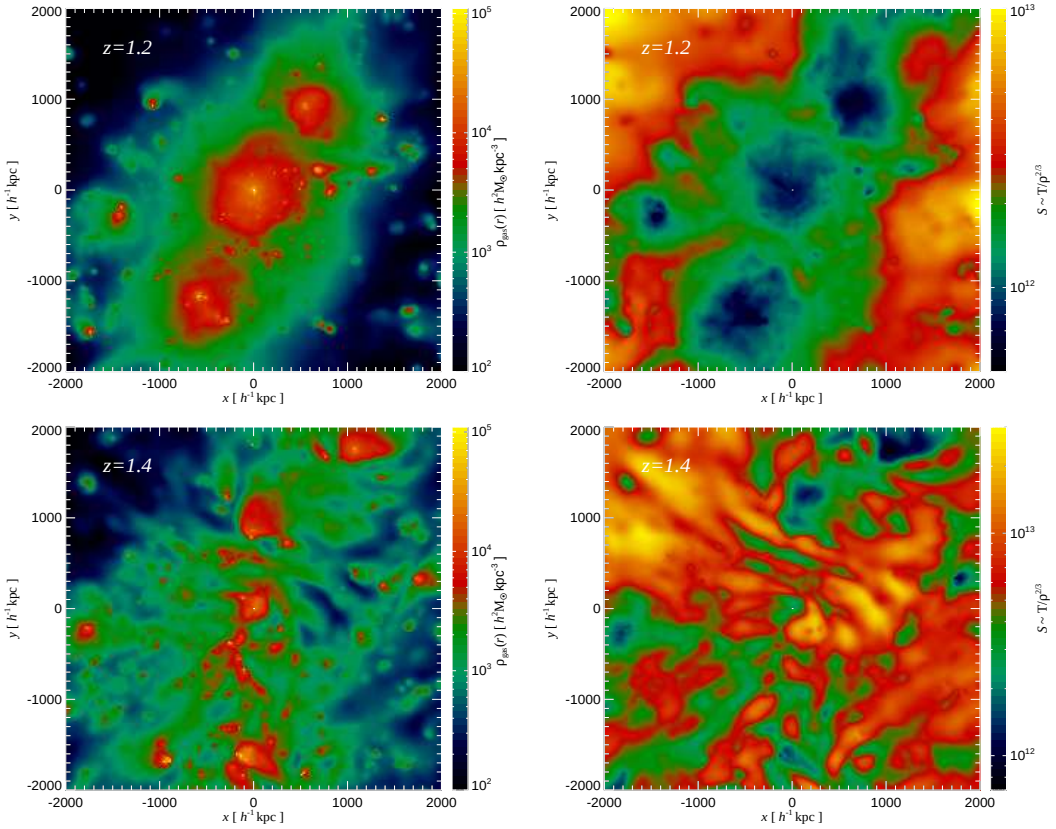

Figure 3.12: Projected maps of gas density and entropy for the g1 galaxy cluster simulation, at an instant just before a merger event. The upper panels are for the run with cooling and star formation, while the lower panels, at somewhat different redshift, are for the run with additional shear viscosity. It can be seen that the entropy of the gas is considerably boosted by internal friction processes (note the different scales of the entropy maps), and in addition it appears that much of this entropy is generated in different regions which have a filamentary kind of structure.

3.7 Discussion and Conclusions

In this study, we discussed a new implementation of viscous fluids in the parallel TreeSPH code GADGET-2, in the framework of a self-consistent entropy and energy conserving formulation of SPH. We presented a discretized form of the Navier-Stokes and general heat transfer equations, considering both shear and bulk internal friction forces, subject to a saturation criterion in order to avoid unphysically large viscous forces. The shear and bulk viscosity coefficients have either been modeled as being constant, or are parameterized in the case of shear viscosity with Braginskii's equation, modified with a suppression factor to describe in a simple fashion a possible reduction of the effective viscosity due to magnetic fields. Our methodology for physical viscosity in SPH extends previous works [Flebbe et al., 1994, Schäfer et al., 2004] that analyzed viscosity effects in the context of SPH

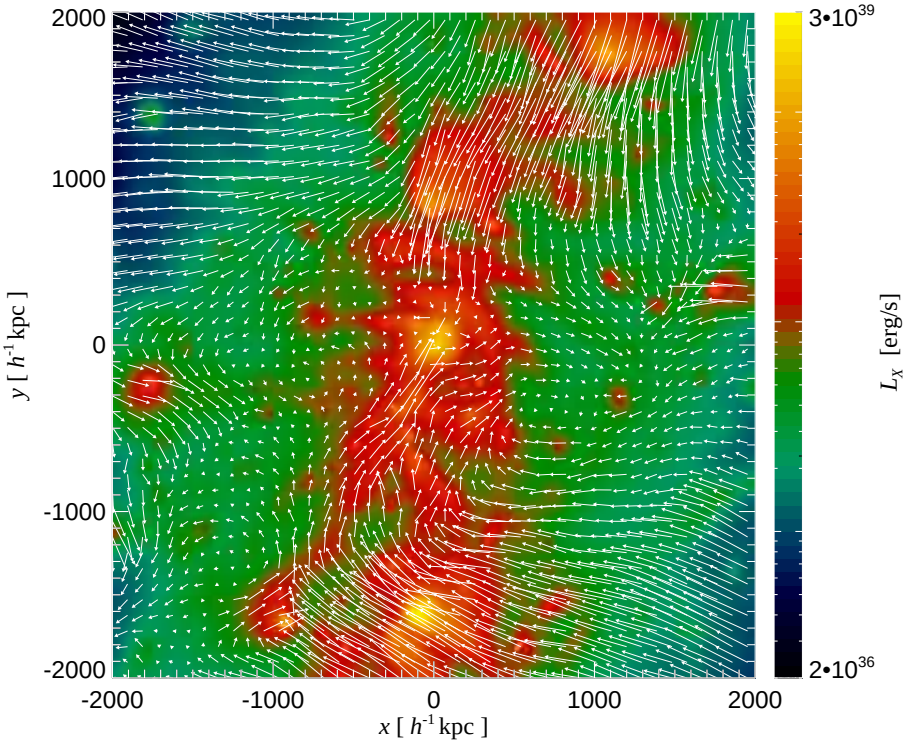

Figure 3.13: Projected X–ray emissivity map of the g1 galaxy cluster, simulated with physical viscosity. The map corresponds to the lower panel of Fig. 3.12, but here the velocity field is overplotted with white arrows. The flow field suggests that the bright entropy bridges are generated in situ due to viscous dissipation.

simulations of planet formation.

We have here applied our new method to simulations of the physics of galaxy clusters, and in particular to their growth in cosmological simulations of structure formation. However, our implementation is general and could, for example, also be used in studies of accretion disks around black holes, or for simulations of planet formation.

We have tested our implementation in a number of simple hydrodynamical problems with known analytic solutions. For example, we simulated flows between two planes that move with a constant relative velocity, or that are fixed and embedded in a constant gravitational field. The stationary solutions we obtained were in good agreement with the analytic expectations and demonstrated the robustness of our scheme. We also performed shock tube tests where we investigated the ability of physical shear and bulk viscosity to capture shocks, instead of using the artificial viscosity normally invoked in SPH codes to this end. We found that for fluids with sufficiently high physical viscosity, shocks can be captured accurately without an artificial viscosity. However, since in practical applications the physical viscosity is often comparatively low, an additional artificial viscosity is still indicated in most cases. In particular, for our applications in cosmological simulations

where we invoked Braginskii's parameterization for the shear viscosity, we are dealing with an effective viscosity which is a strong function of gas temperature. If an artificial viscosity was omitted, simulations would suffer from particle interpenetration at low temperatures.

We have applied our new numerical scheme to study the influence of viscosity on clusters of galaxies. We first considered the physics of hot, buoyant bubbles in the ICM, which are injected by an AGN. In a previous study [Sijacki and Springel, 2006] we have already studied this type of feedback in some detail, but we were here interested in the specific question to what extent the introduction of a certain amount of shear viscosity changes the interaction of the bubbles with the surrounding ICM. We found that the AGN bubbles can still heat the intracluster gas efficiently in the viscous case, but depending on the strength of the viscosity, the properties of the ICM in the inner $\sim 150\,h^{-1}$kpc are altered. The viscous dissipation of sound waves generated by the bubbles does not result in a significant non-local heating of the ICM. To confirm this claim, we estimated the energy budget and the spatial extent of the sound waves for different amounts of viscosity. We found, in agreement with a previous estimate of Churazov et al. [2002], that the total energy in sound waves is only a small fraction of the initial bubble energy. However, a caveat lies in the fact that the initial stages of bubble generation by the AGN-jets are not modeled in our simulation. It is conceivable that these early stages provide stronger sound waves with a potentially bigger impact on the ICM.

We also analyzed bubble morphologies, dynamics and survival times as a function of increasing shear viscosity. Similar to previous analytic and numerical works [Kaiser et al., 2005, Reynolds et al., 2005] we find that an increasing gas viscosity stabilizes bubbles against Kelvin-Helmholtz and Rayleigh-Taylor instabilities, delaying their shredding. Thus, bubbles can rise further away from the cluster centre for the same initial specific entropy content. Because we simulated a long time span, we could follow many bubble duty cycles. This allowed us to conclude that the observation of multiple bubble episodes, as is the case in the Perseus cluster [e.g. Fabian et al., 2006], can be used to infer a minimum value for the ICM gas viscosity, otherwise the bubbles could not survive for such a long time. This constraint is however weakened by the possibility that magnetic fields or relativistic particle populations change the dynamics of the bubbles.

Finally, we addressed the role of gas viscosity in the context of cosmological simulations of galaxy cluster formation. Using a set of non–radiative cluster simulations, we showed that already a modest level of shear viscosity (with a suppression factor of 0.3) has a profound effect on galaxy clusters. The gas density distribution is significantly changed compared to the case where only an artificial viscosity is included, with substructures loosing their baryons more easily, leaving behind a large number of prominent gaseous tails. Only recently XMM-Newton and Chandra observations [Wang et al., 2004, Sun and Vikhlinin, 2005, Sun et al., 2006] have started discovering long (from 60 kpc to 88 kpc) and narrow (< 16 kpc) X-ray tails behind late type galaxies in hot clusters. Further observational studies could put constraints on the amount of gas viscosity by analyzing the X-ray features of the tails. In principle, this could be directly compared with our numerical simulations when synthetic X-ray emissivity maps are constructed. Another interesting imprint of internal friction processes was found in merger episodes of clusters. The entropy of the gas is not just boosted everywhere by a fixed amount due to the viscous dissipation, but instead the entropy increase occurs in filament-like structures which have

no corresponding counterparts in simulations where only artificial viscosity is included.

When the physics of radiative gas cooling is included as well, the effects of internal friction remain similar in the cluster periphery, while in the innermost regions, the radiative cooling timescale becomes so short that the whole energy liberated by internal friction is radiated away. Therefore, in cosmological simulations of cluster formation with radiative cooling, gas viscosity cannot prevent the formation of a central cooling flow. On the other hand, the general tendency of gas viscosity to flatten the temperature profile, and to boost the gas entropy in the outskirts, brings the simulations of galaxy clusters closer to observational results. At least one other physical ingredient is needed to simultaneously solve the over–cooling problem while keeping the benefits of viscous effects. AGN feedback appears to be a promising candidate in this respect, but it remains a complex task to construct a fully self-consistent simulation model that includes all these processes accurately, and with a minimum of assumptions.

4

A unified model for AGN feedback in cosmological simulations of structure formation

D. Sijacki, V. Springel, T. Di Matteo and L. Hernquist, 2007, MNRAS, to be submitted

Abstract

Growing observational and theoretical evidence for a tight link between the evolution of galaxies and their embedded supermassive black holes has been found over the past decade, suggesting that any successful simulation model of structure formation needs to address the joint evolution of galaxies and black holes and include their mutual interaction mechanisms. We here discuss a numerical model for black hole growth and its associated feedback processes that for the first time allows cosmological simulations of structure formation to simultaneously follow the build up of the cosmic population of galaxies and active galactic nuclei. Our model assumes that seed black holes are present at early cosmic epochs at the centres of forming halos. We then track their growth from gas accretion and mergers with other black holes in the course of cosmic time. For black holes that are active, we distinguish between two distinct modes of feedback, depending on the black hole accretion rate itself. Black holes that accrete at high rates are assumed to be in a 'quasar regime', where we model their feedback by thermally coupling a small fraction of their bolometric luminosity to the surrounding gas. The quasar activity requires high densities of relatively cold gas around the black hole, as it is achieved through large-scale inflows triggered by galaxy mergers. For black holes with low accretion rates, we conjecture that most of their feedback occurs in mechanical form, where AGN-driven bubbles are injected into a gaseous environment. This regime of activity, which is subdominant in terms of total black hole mass growth, can be identified with radio galaxies in clusters of galaxies, and

can suppress cluster cooling flows without the requirement of a triggering by mergers. Using our new model, we carry out TreeSPH cosmological simulations on the scales of individual galaxies to those of massive galaxy clusters, both for isolated systems and for cosmological boxes. We demonstrate that our model produces results for the black hole and stellar mass densities in broad agreement with observational constraints, and converges already at moderate numerical resolution. We find that the black holes significantly influence the evolution of their host galaxies, changing their star formation history, their amount of cold gas, and their colours. Also, the properties of intracluster gas are affected strongly by the presence of massive black holes in the cores of galaxy clusters, leading to shallower metallicity and entropy profiles, and to a suppression of strong cooling flows. We conclude that active galactic nuclei are a key ingredient of structure formation simulations. They lead to a self-regulated growth of black holes and bring the simulated properties of their host galaxies into much better agreement with observations.

keywords: methods: numerical – black hole physics – galaxies: formation – galaxies: clusters: general – cosmology: theory

4.1 Introduction

It is now widely believed that most if not all galaxies with a spheroidal component harbour a supermassive black hole (BH) in their centres. Interestingly, the masses of these central BHs are found to be tightly linked with the stellar properties of their host galaxies, as expressed, e.g., in the correlation of bulge velocity dispersion with BH mass [Ferrarese and Merritt, 2000, Gebhardt et al., 2000, Tremaine et al., 2002], or in the relation of bulge stellar mass [Kormendy and Richstone, 1995, Magorrian et al., 1998, Marconi and Hunt, 2003] with BH mass. The existence of these relationships indicates that the formation and evolution of galaxies is fundamentally influenced by the presence of BHs, and vice versa. We thus also expect that the environment and the cosmological evolution of galaxies will affect the way BHs grow.

In fact, there is a plethora of observational and theoretical studies that suggest that several different channels for interaction of BHs with their surroundings exist. At high redshift, mergers of gas-rich galaxies occur frequently and funnel copious amounts of cold gas towards the central regions of galaxies, such that the embedded BHs can reach high gas accretion rates. The radiation energy associated with the accretion can support the enormous luminosities of powerful quasars. Theoretically it has been hypothesized [Silk and Rees, 1998, Fabian and Iwasawa, 1999, King, 2003] that quasars produce high velocity winds, which are expected to affect the properties of the host galaxy. The presence of quasar induced outflows has been observationally confirmed in a number of cases [e.g. Chartas et al., 2003, Crenshaw et al., 2003, Pounds et al., 2003], and has first been demonstrated in simulations of merging galaxy pairs by Di Matteo et al. [2005b]. Several numerical studies dealing with BH microphysics [e.g. Proga, 2003, McKinney, 2006] also predict existence of quasar outflows. Moreover, it appears that tidally disrupted galaxies are preferentially associated with AGN activity [for a review see Barnes and Hernquist, 1992]. Quasar activity hence appears to be directly linked to mergers of galaxies, and should represent the dominant mode of mass growth in the BH population.

Indeed, using semi-analytic models of galaxy formation, Kauffmann and Haehnelt [2000] have demonstrated that BH growth associated with mergers in CDM models can reproduce many properties of the observed quasar population as well as the inferred BH mass density today [see also Volonteri et al., 2003]. Based on the detailed hydrodynamical simulations of BH growth in galaxy mergers [Di Matteo et al., 2005b, Springel et al., 2005b, Robertson et al., 2006a,b, Cox et al., 2006a,b] that have recently become available, Hopkins et al. [2006] have proposed a comprehensive picture of a unified, merger-driven model for the origin of quasars and their relation to spheroid formation. Also, rapid merging of the gas-rich progenitor systems of rare, massive galaxy clusters has been shown [Li et al., 2006] to be a viable formation path for supermassive BHs that are as massive at $z \sim 6$ as those seen in luminous high-redshift SDSS quasars [Fan et al., 2001].

However, there also appears to exist another channel of BH interaction with host galaxies, which is neither related to powerful quasar activity nor associated with galaxy mergers. Evidence for this interaction can be seen in a number of local elliptical galaxies and central cluster galaxies, which contain X-ray cavities filled with relativistic plasma [Bîrzan et al., 2004, McNamara et al., 2005, Forman et al., 2006, Fabian et al., 2006] while harbouring seemingly "dormant" BHs. These X–ray depressions, often referred to as 'bubbles', are thought to be inflated by relativistic jets launched from the central BH. Even though the radiative output from the central BH is not significant, the associated mechanical luminosity can be very important in these systems. There has been considerable effort from the theoretical point of view [e.g. Binney and Tabor, 1995, Churazov et al., 2001, 2002, Quilis et al., 2001, Ruszkowski and Begelman, 2002, Dalla Vecchia et al., 2004, Sijacki and Springel, 2006] to understand the relevance of this mode of AGN feedback, which is widely considered to be leading candidate for resolving the cooling flow problem in groups and clusters of galaxies.

Given the complex physics of AGN-galaxy interactions, is it possible to construct a simple unified model that accounts for the different modes of BH feedback in a cosmological framework? First attempts in this direction have already been made [Churazov et al., 2005, Croton et al., 2006, Merloni and Heinz, 2006], motivated by the observational findings of X-ray binaries [Fender et al., 1999, Gallo et al., 2003]. In particular, it has been shown that X–ray binaries switch between two states: in the so-called "low/hard" state, a steady radio jet is present and the hard X–ray spectrum is observed, while in the "high/soft" state, the jet vanishes and the X–ray spectrum shows a soft, thermal component. The transition between these two states is regulated by the accretion rate onto the BH itself, where the threshold value is of the order of $10^{-2} - 10^{-1} \dot{M}_{\rm Edd}$. The "high/soft" state can be explained by the standard, optically thick and geometrically thin accretion disc [Shakura and Sunyaev, 1973], with BH accretion occurring at high rates and in a radiatively efficient mode. The "low/hard" state on the other hand corresponds to optically thin, geometrically thick, and radiatively inefficient accretion, as described by the theoretical ADAF and ADIOS solutions [Narayan and Yi, 1994, Blandford and Begelman, 1999].

The above suggests a rather simple, yet attractive scenario for distinguishing between different modes of BH feedback in models for the cosmological evolution of active galactic nuclei (AGN): We shall assume that for high accretion rates, a 'quasar-like' feedback occurs, while for states of low accretion, mechanical bubble feedback applies. It is clear that the simplicity of this model will not allow it to explain all kinds of AGN feedback

phenomena, e.g. powerful radio galaxies that accrete at very high rates, as found in some proto-cluster environments, are not well represented in this simple scheme. Moreover, even though the physics of X-ray binaries is expected to be quite similar to the one of AGN [Heinz et al., 2005], an analogous transition between "high/soft" and "low/hard" states in AGN is observationally still not well established, although there are some encouraging observational findings [Maccarone et al., 2003, Körding et al., 2006] in this direction.

With these caveats in mind, we explore in this study a new 'two-mode' AGN feedback scenario in fully self-consistent cosmological simulations of structure formation. Within our numerical model we represent BHs with collisionless "sink" particles and we adopt subresolution methods to compute their gas accretion rate, estimated from a Bondi prescription. Also, we allow BHs to grow via mergers with other BHs that happen to be in their vicinity and that have sufficiently low relative speeds. We assume that BH feedback is composed of two modes, as motived above, and we track their growth and feedback with cosmic time. We consider a vast range of objects harbouring BHs, from galaxies with $\sim 10^8 M_\odot$ stellar mass to massive galaxy clusters with total mass $\sim 10^{15} M_\odot$. Even though our BH growth model is rather simple and crude due to the inevitable numerical limitations, it represents the first attempt to include AGN feedback effects in cosmological simulations of structure formation. As we shall see, this approach produces significant improvements in the properties of simulated galaxies.

The outline of this paper is as follows. In Section 4.2, we describe our numerical method for incorporating the BH growth and feedback in cosmological hydrodynamical simulations. In Section 4.3, we test our model in simulations of isolated galaxy clusters, and explore the numerical parameter space. We then discuss cosmological simulations of galaxy cluster formation and evolution, subject to AGN feedback, in Section 4.4, while in Section 4.5 we consider cosmological simulations of homogeneously sampled periodic boxes. Finally, we summarize and discuss our results in Section 4.6.

4.2 Methodology

We use a novel version of the parallel TreeSPH-code GADGET-2 [Springel, 2005, Springel et al., 2001b] in this study, which employs an entropy-conserving formulation of smoothed particles hydrodynamics [Springel and Hernquist, 2002]. Besides following gravitational and non-radiative hydrodynamical processes, the code includes a treatment of radiative cooling for a primordial mixture of hydrogen and helium, and heating by a spatially uniform, time-dependent UV background [as in Katz et al., 1996]. Star formation and associated supernovae feedback processes are calculated in terms of a subresolution multiphase model for the ISM [Springel and Hernquist, 2003a]. We use a simple prescription for metal enrichment, and optionally incorporate galactic winds powered by supernovae, as implemented by Springel and Hernquist [2003a]. Furthermore, we follow the growth and feedback of BHs based on a new model that combines the prescriptions outlined in Springel et al. [2005c] and Sijacki and Springel [2006].

In the following, we briefly summarize the main features of the BH model relevant for this study [see Springel et al., 2005c, for further details], focusing on extensions that permit us to follow BH growth and feedback in a cosmological simulation of structure formation. We then discuss a new BH feedback prescription at low accretion rates, based

on a 'bubble' heating scenario for representing AGN heating in the radiatively inefficient regime of accretion.

4.2.1 Black hole formation and growth

The BHs in the code are represented by collisionless sink particles, which may accrete gas from their surroundings based on a prescribed estimate for the accretion rate. Two BH particles are also allowed to merge if they fall within their local SPH smoothing lengths and if their relative velocities are smaller than the local sound speed.

In our cosmological simulations of structure formation, we assume that low-mass seed BHs are produced sufficiently frequently such that any halo above a certain threshold-mass contains one such BH at its centre. Whether these seed BHs originate in exploding pop-III stars, in the collapse of star clusters, or are of primordial origin is not important for our analysis, but there needs to be a process that produces initial seed BHs which can then grow to the masses of supermassive BHs by gas accretion in the course of our simulations. For definiteness, in most of our simulations we adopt a seed BH mass of $10^5\,h^{-1}\mathrm{M}_\odot$ and endow all halos with a mass larger than $5\times10^{10}\,h^{-1}\mathrm{M}_\odot$ with a seed if they do not contain any BH already. We identify halos without BHs on the fly during a simulation by frequently calling a fast, parallel friends-of-friends algorithm that is built into our simulation code.

State-of-the-art cosmological simulations of structure formation reach mass resolutions that are at best of order of our initial BH seed mass, while the resolution typically reached is still considerably coarser than that. This would mean that the initial growth of the BH mass could be significantly affected by numerical discreteness effects if the sink particle can only swallow full gas particles, as is the case in our scheme. In order to avoid that the BH growth and the accretion rate estimate is strongly affected by this numerical discreteness limitation, we treat the BH mass M_{BH} as an internal degree of freedom of the sink particle. In the beginning, M_{BH} may differ from the dynamical mass M_{dyn} of the sink particle itself. The variable M_{BH} is integrated smoothly in time based on the estimated accretion rate onto the BH, while M_{dyn} increases in discrete steps when the sink particle swallows a neighbouring gas particle. The latter process is modelled stochastically such that M_{dyn} tracks M_{BH} in the mean, with small oscillations around it. With this prescription for the BH mass, we can follow the early growth of BHs accurately in a sub-resolution fashion even when their mass may be smaller than the mass resolution of the simulation, while at late times (or in the limit of very good mass resolution) the two mass variables coincide. Of course, in the event of a merger of two BH sink particles, both M_{BH} and M_{dyn} are added together.

Following Di Matteo et al. [2005b], we estimate the accretion rate onto a BH particle according to the Bondi-Hoyle-Lyttleton formula [Hoyle and Lyttleton, 1939, Bondi and Hoyle, 1944, Bondi, 1952]

$$\dot{M}_{\mathrm{BH}} = \frac{4\,\pi\,\alpha\,G^2 M_{\mathrm{BH}}^2\,\rho}{(c_s^2+v^2)^{3/2}}\,, \tag{4.1}$$

where α is a dimensionless parameter, ρ is the density, c_s the sound speed of the gas, and v is the velocity of the BH relative to the gas. We account for the possibility that the BH

accretion has an upper limit given by the Eddington rate

$$\dot{M}_{\rm Edd} \, = \, \frac{4\,\pi\,G\,M_{\rm BH}\,m_{\rm p}}{\epsilon_{\rm r}\,\sigma_{\rm T}\,c}\,, \tag{4.2}$$

where m_p is the proton mass, $\sigma_{\rm T}$ is the Thompson cross-section and $\epsilon_{\rm r}$ is the radiative efficiency, that we assume to be 0.1, which is the mean value for the radiatively efficient Shakura and Sunyaev [1973] accretion onto a Schwarzschild BH. In some of our numerical models we specifically explore the imprints of the imposed Eddington limit on the BH properties.

4.2.2 Black hole feedback

In the model of Springel et al. [2005c], it is assumed that a fixed fraction of the BH bolometric luminosity couples thermally to the local gas, independent of the accretion rate and environment. In our model we extend this BH feedback prescription in order to obtain a physically refined model for AGN heating both at high and at low accretion rates. We are motivated by the growing theoretical and observational evidence [Fender et al., 1999, Gallo et al., 2003, Churazov et al., 2005, Heinz et al., 2005, Croton et al., 2006] that AGN feedback is composed of two modes, analogous to states of X-ray binaries. Specifically, at high redshifts and for high accretion rates we assume that the bulk of AGN heating is originating in the luminous quasar activity. In this regime, BHs accrete efficiently and power luminous quasars where only a very small fraction of their bolometric luminosity couples thermally to the gas. On the other hand, at lower redshifts and for BHs accreting at much lower rates than their Eddington limits, AGN heating proceeds via radiatively inefficient feedback in a mostly mechanical form.

To model the transition between these two accretion and feedback modes, we introduce a threshold $\chi_{\rm radio} = \dot{M}_{\rm BH}/\dot{M}_{\rm Edd}$ for the BH accretion rate (BHAR) in Eddington units, above which 'quasar heating' is operating, and below which we deal with 'radio mode' feedback, which we model by injecting bubbles into the host galaxy/cluster. Typically, we adopt a value of 10^{-2} for $\chi_{\rm radio}$, and we impose no other criterion to distinguish between the two modes of feedback.

For BHAR that are higher than $\chi_{\rm radio}$, we parameterize the feedback as in Springel et al. [2005c], i.e. a small fraction of the bolometric luminosity is coupled thermally and isotropically to the surrounding gas particles, with an amount given by

$$\dot{E}_{\rm feed} \, = \, \epsilon_{\rm f}\,L_{\rm r} \, = \, \epsilon_{\rm f}\,\epsilon_{\rm r}\,\dot{M}_{\rm BH}\,c^2\,. \tag{4.3}$$

Here $\epsilon_{\rm f}$ gives the efficiency of thermal coupling. The value of 5% adopted here brings the simulated $M_{\rm BH}-\sigma_*$ relation obtained for remnants of isolated galaxy mergers in agreement with observations, as shown by Di Matteo et al. [2005b].

Below $\chi_{\rm radio}$ we assume that the accretion periodically produces an AGN jet which inflates hot bubbles in the surrounding gas. We clearly lack the numerical resolution for self-consistent *ab initio* simulations of the detailed physics of BH accretion and the involved relativistic MHD that is responsible for the actual jet creation. However, we can nevertheless try to represent the relevant heating mechanism by directly injecting the energy contained in the AGN-inflated bubbles into the ICM. To this end we need to link

M_{200} $[h^{-1}\mathrm{M}_\odot]$	R_{200} $[h^{-1}\mathrm{kpc}]$	c	N_{gas}	m_{gas} $[h^{-1}\mathrm{M}_\odot]$	ϵ $[h^{-1}\mathrm{kpc}]$
10^{13}	444	8.0	3×10^5	4.0×10^6	2.0
10^{14}	957	6.5	3×10^5	4.0×10^7	5.0
10^{15}	2063	5.0	3×10^5	4.0×10^8	10.0
10^{15}	2063	5.0	1×10^6	1.2×10^8	6.5

Table 4.1: Numerical parameters of our simulations of isolated galaxy clusters. The virial masses and radii of the halos, evaluated at $200\,\rho_{\mathrm{crit}}$, are given in the first two columns. The assumed values for the concentration parameter are in the third column, while the number and the mass of the gas particles is shown in the fourth and the fifth column, respectively. The mass of the star particles is half that of the gas particles, because we set the number of generations of star particles that a gas particle may produce to two. Note that there are no parameters for the dark matter particles in these run, because we here modelled the dark halo with a static NFW potential. Finally, in the last column, the gravitational softening length ϵ for the gas and star particles is given.

the bubble properties, like radius, duty cycle and energy content, directly with the BH physics.

Up to now there is no compelling theory that can satisfactorily explain AGN jet formation, bubble inflation by the jet, and the duty cycle of jet activity. On the other hand, a growing body of observational evidence [e.g. Bîrzan et al., 2004, McNamara et al., 2005, Forman et al., 2006, Dunn and Fabian, 2006, Fabian et al., 2006] shows that AGN-driven bubbles are present in many systems, at different redshifts and over a range of masses, which constrains the duty cycle to be of the order of $10^7 - 10^8$ years. However, it is still not clear whether and how AGN activity can be influenced by properties of the host galaxy like its mass, dynamical state, or central gas cooling rate. In light of this uncertainty we propose a simple model for radio feedback where we assume that an AGN-driven bubble will be created if a BH has increased its mass by a certain fraction $\delta_{\mathrm{BH}} \equiv \delta M_{\mathrm{BH}}/M_{\mathrm{BH}}$. Note that with this choice we do not constrain the possible duty cycle of the jet itself. We only conjecture that whenever the BH increases its mass by δM_{BH}, the thermodynamical state of the surrounding gas will be affected by the BH activity, and that this can be represented in the form of the bubbles.

Thus, we relate the energy content of a bubble to the BH properties as

$$E_{\mathrm{bub}} \;=\; \epsilon_{\mathrm{m}}\,\epsilon_{\mathrm{r}}\,c^2\,\delta M_{\mathrm{BH}}\,, \tag{4.4}$$

where ϵ_{m} is the efficiency of mechanical heating by the bubbles. Moreover, we link the bubble radius both to δM_{BH} and to the density of the surrounding ICM, in the following way

$$R_{\mathrm{bub}} = R_{\mathrm{bub},0}\left(\frac{E_{\mathrm{bub}}/E_{\mathrm{bub},0}}{\rho_{\mathrm{ICM}}/\rho_{\mathrm{ICM},0}}\right)^{1/5}, \tag{4.5}$$

where $R_{\mathrm{bub},0}$, $E_{\mathrm{bub},0}$, and $\rho_{\mathrm{ICM},0}$ are normalization constants for the bubble radius, energy content and ambient density, respectively. The scaling of the bubble radius is motivated

by the solutions for the radio cocoon expansion in a spherically symmetric case [Scheuer, 1974, Begelman and Cioffi, 1989, Heinz et al., 1998]. With this parameterization for $R_{\rm bub}$, we mimic a scenario in which a more powerful jet will inflate bigger radio lobes, and where a higher ICM density will confine the size of the buoyant bubbles more. Finally, the spatial injection of the bubbles is random within a sphere with radius twice the bubble radius and centred on the BH particle in consideration.

4.3 Self-regulated bubble feedback in isolated halo simulations

We have first carried out a number of simulations of isolated galaxy clusters in order to test our BH feedback model and to explore its parameter space. These simulations consist of a static NFW dark matter halo [Navarro et al., 1996, 1997] with a gas component initially in hydrostatic equilibrium. The initial gas density profile has a similar form as the dark matter, but with a slightly softened core, as explained in more detail in Sijacki and Springel [2006]. We construct initial conditions for halos with a range of masses (see Table 4.1 for the details of the numerical setup) and evolve them non-radiatively for a time $0.25\,t_{\rm Hubble}$ to damp out possible initial transients. Then, we "switch on" radiative gas cooling and star formation, and also introduce a seed BH particle in the halo centre. In the following subsections, we describe the results for the subsequent growth of the BHs.

4.3.1 Exploring the parameter space

In this section, we analyse the sensitivity of our model and of the resulting BH and host halo properties with respect to the parameter choices we have adopted. We begin by considering an isolated halo of mass $10^{14}\,h^{-1}{\rm M}_\odot$, comparing simulations with and without BHs. For these numerical tests, we only consider AGN feedback in the form of bubbles, while in all full cosmological simulations we will include both modes of AGN feedback introduced in Section 4.2.2.

First, we vary the threshold for bubble triggering in terms of accreted mass, $\delta_{\rm BH}$, from 0.1% to 5%, which will affect both the number of bubble events and their mean energy. The other two free parameters in the BH feedback model, $\epsilon_{\rm m}$ and the normalization value for $R_{\rm bub}$, are kept fixed in this first series of simulations in order to facilitate the comparison. For definiteness, for most of the isolated halo simulations we select $\epsilon_{\rm m} = 1$, $R_{\rm bub,0} = 30\,h^{-1}{\rm kpc}$, $E_{\rm bub,0} = 5 \times 10^{60}{\rm erg}$, and $\rho_{\rm ICM,0} = 10^6\,h^2{\rm M}_\odot{\rm kpc}^{-3}$. Note that our choice for these parameters will be slightly different in cosmological simulations, as we will discuss in Section 4.4. In most of our numerical experiments we start with a small BH seed, typically equal to $10^5\,h^{-1}{\rm M}_\odot$, to establish if the BH growth is self-regulated and whether it leads to a realistic BH mass when a quasi-stationary state is reached. In a number of test simulations we also explore a scenario in which a massive BH is already present at the very beginning.

In panels (a) and (b) of Figure 4.1 we show the BH mass and the accretion rate expressed in Eddington units as a function of time, for three different values of $\delta_{\rm BH} = 0.1\%$, 1% and 5%. It can be seen that the BH is initially growing rapidly starting from the seed mass of $10^5\,h^{-1}{\rm M}_\odot$, and the accretion rate onto the BH is quite high, reaching the Eddington level at $t = 0.06\,t_{\rm H}$. However, after this initial phase of rapid growth, AGN feedback

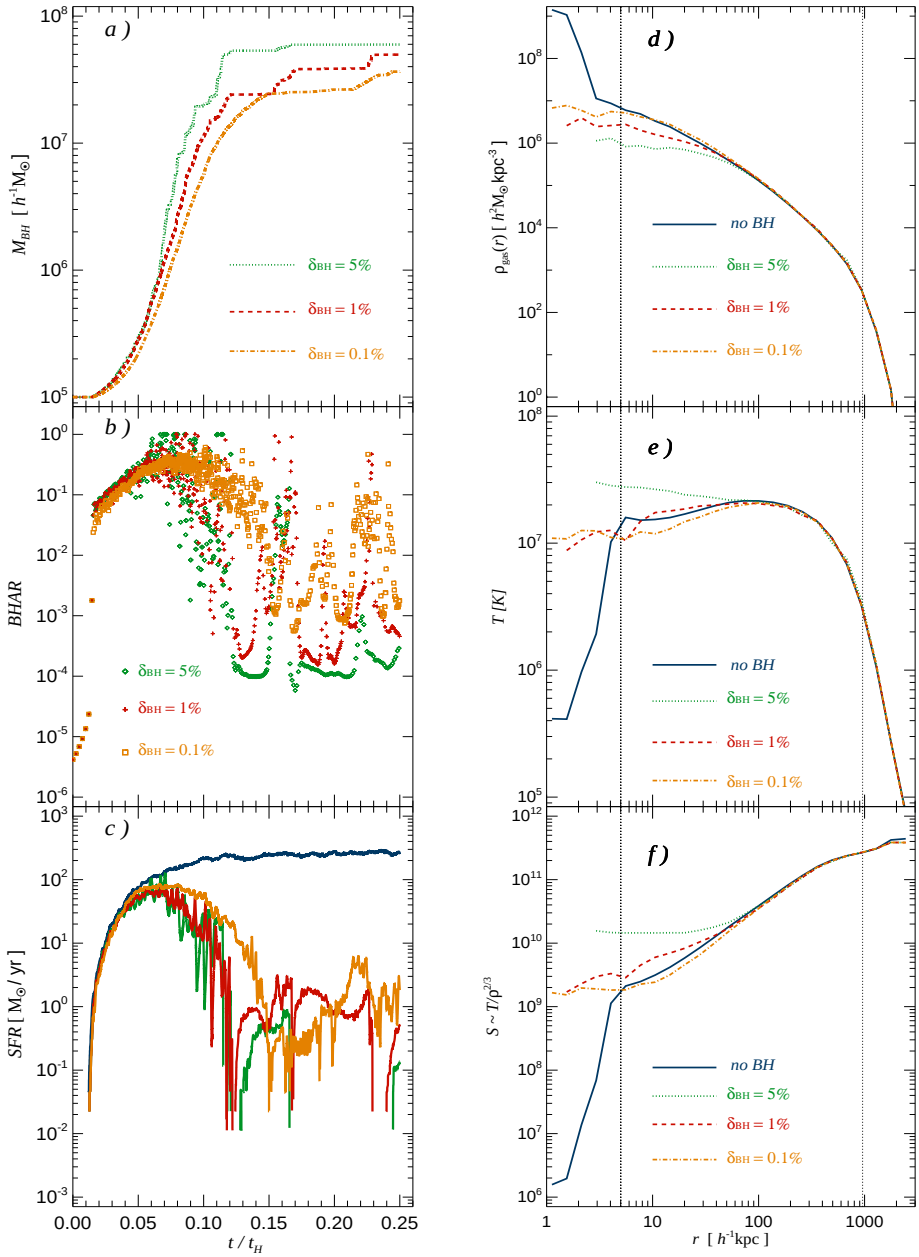

Figure 4.1: Panels (a) and (b) show the time evolution of the BH mass and the accretion rate in Eddington units for a BH that has been introduced in the centre of an isolated cluster of mass $10^{14}\,h^{-1}\mathrm{M}_\odot$. The different curves and symbols give results for increasing $\delta_{\rm BH}$, as labelled in the panels. Panel (c) illustrates the SFR as a function of time for the same set of simulations (same colour-coding as panel (d)). Finally, panels (d), (e) and (f) give the gas density, mass-weighted temperature and entropy radial profiles for this cluster at $t = 0.2\,t_{\rm H}$ in runs without AGN feedback (blue continuous lines) and with AGN heating, where the different curves are for the increasing value of $\delta_{\rm BH}$, as indicated on the panels. The vertical dotted lines mark the gravitational softening length and the virial radius, respectively.

starts to reduce the further BH growth, because at this point enough heating is supplied to the surrounding medium, preventing it to quickly cool and sink towards the most inner regions. Thus, the feedback provided by AGN-driven bubbles reduces the supply of gas available for accretion by the central BH. Consequently, $\dot{M}_{\rm BH}$ drops and the mass of the BH shows no significant growth with time for a while. However, after a certain amount of time which depends on the heating efficiency, the central cluster gas starts to cool again, causing an increase of the BHAR and the triggering of another bubble episode. This mechanism establishes a self-regulated cycle, in which a balance between the gas cooling rate, the bubble heating rate and the residual BHAR is achieved. In panel (b) of Figure 4.1, this cycle of AGN activity can be clearly seen. Here the peaks in BHAR correspond to the bubble injection events. Note that the higher values of $\delta_{\rm BH}$ lead to fewer and more powerful AGN outbursts that cause the accretion rate to drop to very low values of order of $10^{-4}\dot{M}_{\rm Edd}$.

The $\delta_{\rm BH}$ parameter also affects the properties of the ICM. In panels (d), (e) and (f) of Figure 4.1 we illustrate this effect by plotting the radial profiles of gas density, temperature and entropy, for the different values of $\delta_{\rm BH}$ assumed in the simulations, as indicated in the panels. We also show the corresponding profiles for the run without AGN heating, denoted by the continuous blue lines. Clearly, there is a trend in the simulated profiles with $\delta_{\rm BH}$: more frequent and more gentle bubble heating events increase the central cluster entropy less than more powerful but rarer feedback episodes. A similar result has been found in the simulations of Omma and Binney [2004], where a higher jet power was heating the cluster for a longer time interval. However, regardless of the exact value of the $\delta_{\rm BH}$ parameter, the central cooling catastrophe is prevented in our model cluster in all simulated cases with feedback. Once the feedback becomes effective, the BH mass stops growing when it reaches $3-6\times10^{7}\,h^{-1}{\rm M}_{\odot}$. Note however that the final value of the BH mass depends also on the ϵ_m parameter, which we have taken to be as high as possible in these test runs. Consequently, the BH masses obtained here represent a lower limit for the actual BH mass that one would expect in a cluster of this size.

In panel (c) of Figure 4.1, we show how the star formation rate (SFR) is affected by AGN-driven bubbles. Without AGN heating, the SFR of the $10^{14}\,h^{-1}{\rm M}_{\odot}$ isolated cluster grows with time to values as high as $\sim 250{\rm M}_{\odot}/{\rm yr}$. This high SFR results from the large amounts of cool gas that accumulate in the central regions, forming a reservoir for intense star formation activity. However, in the models with AGN feedback, the SFR drops dramatically to values of order of $\sim 1{\rm M}_{\odot}/{\rm yr}$. For these runs it can be also seen that the SFR shows a number of short spikes of somewhat enhanced activity, and these peaks are directly related with episodes of increased BHAR which lead to a triggering of bubbles and a successive reduction of the SFR.

We have also tested to which extent the AGN feedback is affected by changes in the normalization value for the bubble radius. As before, we adopt as default values for bubble energy and ICM density $5\times10^{60}{\rm erg}$ and $10^{6}\,h^{2}{\rm M}_{\odot}{\rm kpc}^{-3}$, respectively, but we vary $R_{\rm bub,0}$ for different runs. In the range of $15\,h^{-1}{\rm kpc}$ to $30\,h^{-1}{\rm kpc}$ for $R_{\rm bub,0}$, our results are not altered significantly by modifications of this parameter. However, for substantially larger values of $R_{\rm bub,0}$, e.g. $60\,h^{-1}{\rm kpc}$, the heating energy per particle drops to considerably smaller values, changing the initial rapid growth phase of the BH. For large values of $R_{\rm bub,0}$, the AGN feedback is less efficient in the early phase of growth such that the BH

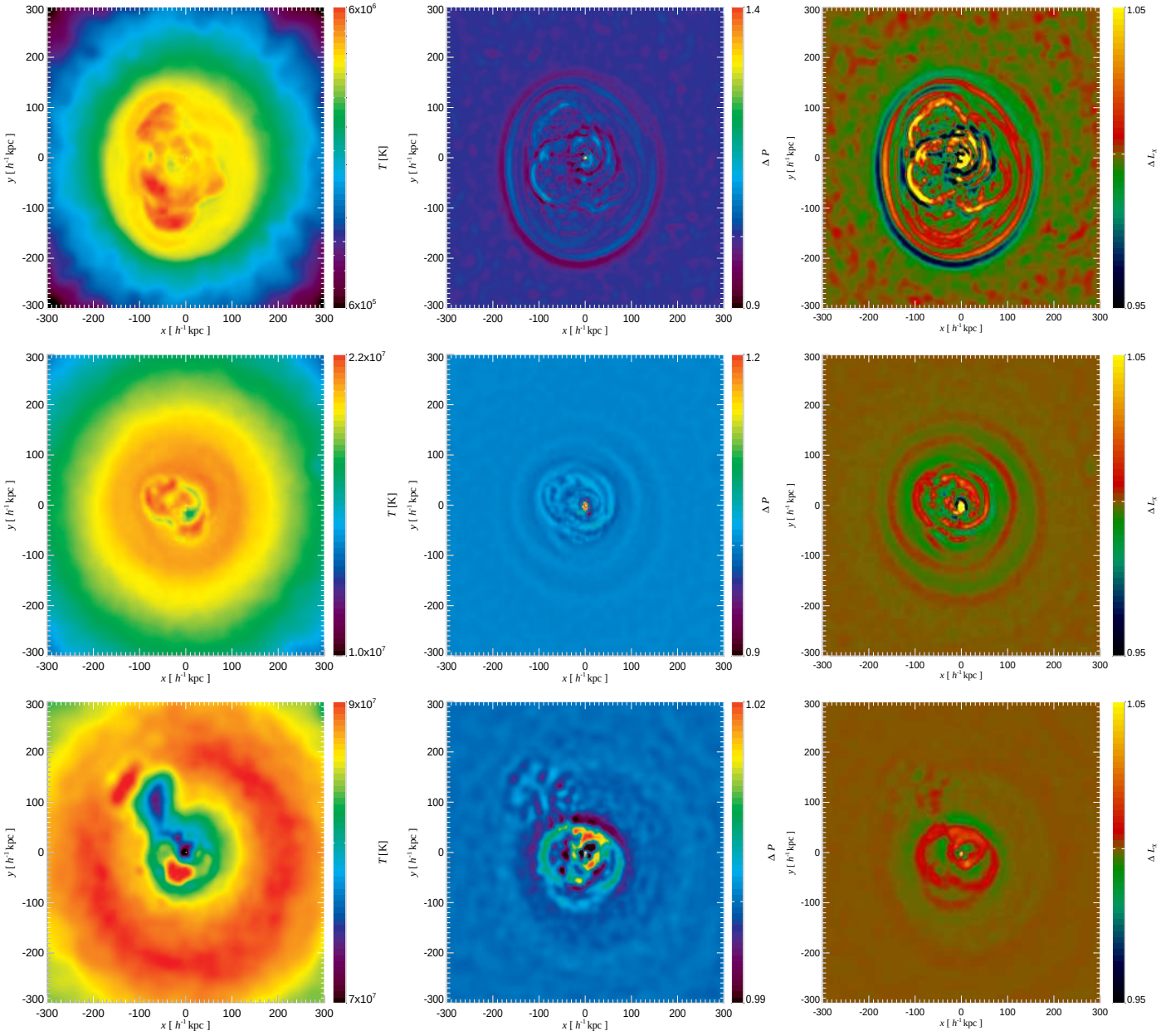

Figure 4.2: The panels on the left-hand side show mass-weighted projected temperature maps of three isolated clusters with increasing mass: $10^{13}\,h^{-1}\mathrm{M}_{\odot}$ (upper-most panel), $10^{14}\,h^{-1}\mathrm{M}_{\odot}$ (central panel) and $10^{15}\,h^{-1}\mathrm{M}_{\odot}$ (lower-most panel). It can be seen that the bubbles injected in the central cluster regions have mushroom-like morphologies and are uplifting residual cool material from the centre (lower-most panel). The middle and right-hand panels give projected pressure and X-ray emission maps, divided by the corresponding map smoothed on a scale of $16\,h^{-1}$kpc. A number of bubble-induced sound waves and weak shocks are clearly visible, and in the case of the $10^{15}\,h^{-1}\mathrm{M}_{\odot}$ cluster, NW from the cluster centre a mushroom-shaped bubble in the pressure map is clearly visible which corresponds to the red blob in the temperature map.

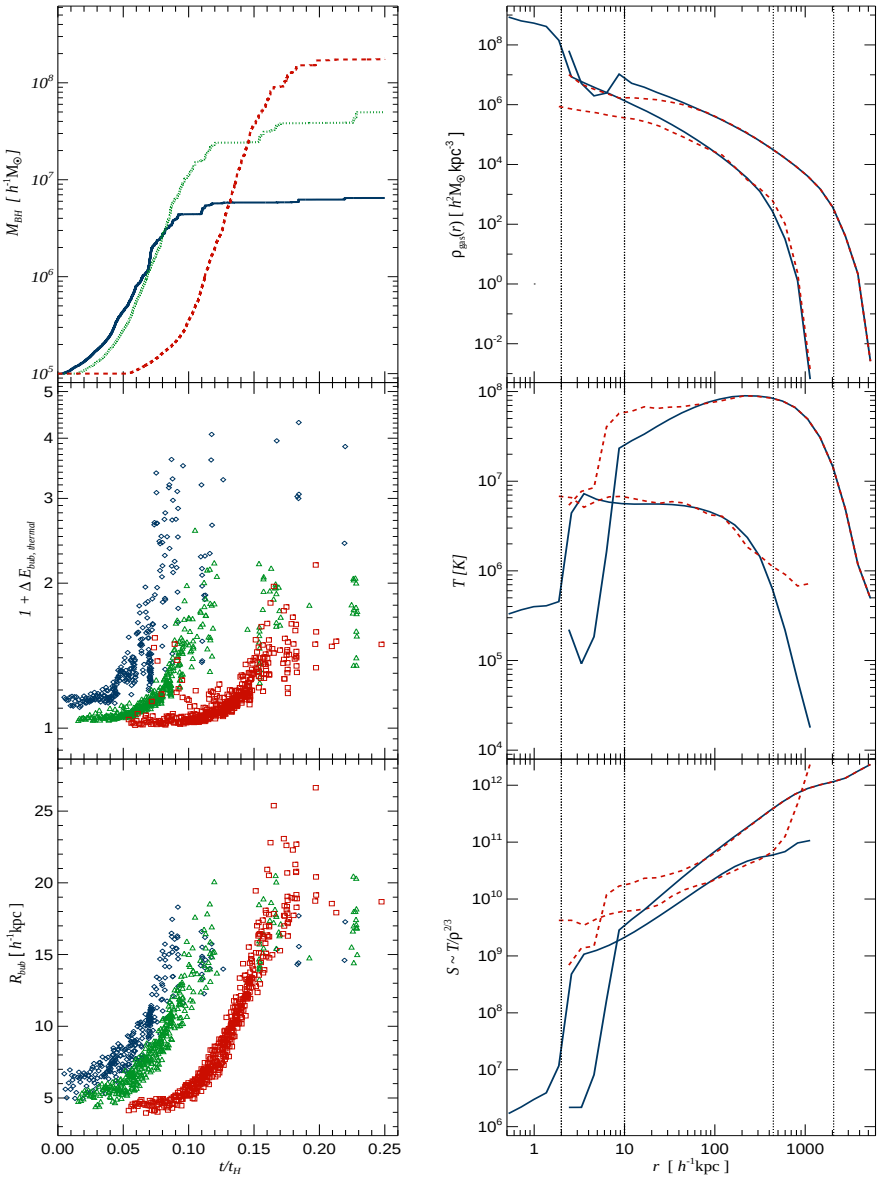

Figure 4.3: Left-hand panels: Growth of the BH mass with time (top panel) for three clusters of different mass. The middle panel shows how the thermal energy contrast, $\Delta E_{\mathrm{bub,\,thermal}}$, depends on time and the BH mass in our cluster simulations. The bubble radius as a function of time is shown in the bottom panel, for the same set of runs. The blue, continuous line and the diamonds are for a cluster of mass $10^{13}\,h^{-1}\mathrm{M}_\odot$, the green, dotted line and triangles are for a $10^{14}\,h^{-1}\mathrm{M}_\odot$ halo, while the red, dashed line and the squares denote results for a $10^{15}\,h^{-1}\mathrm{M}_\odot$ cluster. Right-hand panels: Radial profiles of gas density (upper-most panel), temperature (central panel) and entropy (lower-most panel) for $10^{13}\,h^{-1}\mathrm{M}_\odot$ and $10^{15}\,h^{-1}\mathrm{M}_\odot$ galaxy clusters at $t = 0.2\,t_{\mathrm{H}}$. The blue, continuous lines correspond to the simulations without AGN heating, while red, dashed lines give the case where AGN feedback is present. On every panel, the upper set of profiles are for the more massive cluster. Vertical dotted lines mark the gravitational softening length and the virial radii of these clusters.

can grow to a somewhat larger mass before a self-regulated heating loop is established. We will further discuss the importance of the bubble radius when we consider halos of different mass in Section 4.3.2.

Finally, we have numerically explored scenarios where an already massive BH is introduced at the very beginning of a simulation. For $\delta_{\rm BH}$ equal to 0.1%, the BH mass is found to increase from its initial value of $5 \times 10^7\,h^{-1}{\rm M}_\odot$ to $9 \times 10^7\,h^{-1}{\rm M}_\odot$ over a time span equal to one quarter of the Hubble time. Most of this BH growth, however, can be attributed to the intermittent nature of bubble heating, while in the continuous AGN feedback regime, the BH mass increases by less then 1% over the same simulated time span. Thus, our numerical scheme indeed leads to a stable galaxy cluster solution where overcooling in the central parts is prevented and the BH mass grows to a self-regulated value.

4.3.2 AGN heating in halos of different mass

In this section we examine AGN feedback effects in cluster halos spanning a range in mass, from $10^{13}\,h^{-1}{\rm M}_\odot$ to $10^{15}\,h^{-1}{\rm M}_\odot$. We adopt one set of feedback parameters for all simulations, namely $\epsilon_{\rm m}$, $R_{\rm bub,0}$, $E_{\rm bub,0}$, and $\rho_{\rm ICM,0}$, as in the previous section, and for $\delta_{\rm BH}$ we choose the intermediate value of 1%. We are interested in the question whether for a fixed set of parameters our model produces satisfactory solutions for halos of very different masses.

Before we delve into a detailed quantitative analysis of the cluster simulations, we illustrate the visual morphology of simulated AGN-inflated bubbles in Figure 4.2. For this purpose, we show projected mass-weighted temperature maps (first column), pressure fluctuation maps (middle column) and fluctuation maps of the X–ray luminosity (last column). Different rows are for clusters of increasing mass, from top to bottom. We call the maps in the second and the third columns "fluctuation" maps because they have been constructed by dividing the original map by a version that has been smoothed on a scale of $16\,h^{-1}$kpc. This highlights local departures from the mean ICM properties, similar to what is known as unsharp masking technique in observational analysis.

A number of interesting features can be seen from the panels in Figure 4.2. First, AGN-driven bubbles have characteristic mushroom-like and cap-like morphologies. These are particularly evident for the $10^{13}\,h^{-1}{\rm M}_\odot$ halo, where several bubbles injected briefly after one another can be noticed. Note that the reason why there are so many bubbles in this particular map is in part due to the selected time for the image. At this moment $M_{\rm BH}$ happens to grow rapidly, thus the bubble duty cycle is rather short. In the last row of Figure 4.2, two bubbles can be seen in the central region of the $10^{15}\,h^{-1}{\rm M}_\odot$ cluster, one SW from the cluster centre and the other NW and more distant. The latter one is uplifting some residual cool gas from the cluster centre, which forms a filamentary structure in the wake of the bubble. Looking at the pressure map of this cluster a nicely defined mushroom-like bubble can be seen that corresponds to the NW red blob in the temperature map. In general, the pressure and X-ray luminosity maps show numerous irregularities, sound waves and weak shocks that have been generated by the bubbles. The ripples in these maps become progressively weaker for more massive cluster, which is a consequence of the parameterization adopted in our model, as we will clarify in the following paragraphs.

In the upper-most left-hand panel of Figure 4.3, we show the mass growth of the central

BH as a function of time for the different cluster simulations. It can be seen that halos of increasing mass exhibit a qualitatively similar behaviour for their BH growth: an initial rapid growth phase is followed by self-regulated stagnation. However, the starting point of the rapid growth is dictated by the gas cooling time, which is shortest for the smallest cluster mass considered. Therefore, for the $10^{13}\,h^{-1}\mathrm{M}_{\odot}$ halo, the BH starts growing first, but it is also the first one to reach stagnation, while the BH sitting in the centre of the $10^{15}\,h^{-1}\mathrm{M}_{\odot}$ cluster waits for $\sim 0.05\,t/t_{\mathrm{H}}$ before increasing its mass significantly. At the end of the simulated time-span, all three BHs reach equilibrium states and their final masses are: $\sim 6.5\times10^{6}\,h^{-1}\mathrm{M}_{\odot}$, $\sim 5\times10^{7}\,h^{-1}\mathrm{M}_{\odot}$, and $\sim 1.8\times10^{8}\,h^{-1}\mathrm{M}_{\odot}$, respectively.

In the other two left-hand panels of Figure 4.3, we show how certain bubble properties evolve with time for different cluster simulations. In the middle panel, $\Delta\mathrm{E}_{\mathrm{bub,\,thermal}}$ represents the thermal energy contrast of the bubble just before and after the energy was injected into it. $\Delta\mathrm{E}_{\mathrm{bub,\,thermal}}$ is reflecting mainly the mass growth of the BH, since it determines how much energy will be thermally coupled to the bubbles. It can be seen that $\Delta\mathrm{E}_{\mathrm{bub,\,thermal}}$ initially grows significantly with time, but when the BH growth saturates, it scatters around a constant value. Also, there is a systematic trend of $\Delta\mathrm{E}_{\mathrm{bub,\,thermal}}$ with cluster mass, with smaller mass clusters showing a larger energy contrast for the bubbles. This is primarily due to the smaller radius of bubbles in less massive clusters, as can be seen in the bottom left-hand panel of Figure 4.3. Given that we have adopted the same set of parameters for our different cluster simulations, it follows from Eqn. (4.5) that BHs of smaller mass will generate smaller bubbles. This explains why R_{bub} is growing in time and why it is bigger for more massive halos that harbour larger BHs. This consequence of our model has also repercussions for the presence and intensity of sound waves generated by the inflation of bubbles, as seen in the maps of Figure 4.2. Smaller bubbles with a higher energy contrast relative to the surrounding ICM are more efficient in generating weak shocks and sound waves than large bubbles with low $\Delta\mathrm{E}_{\mathrm{bub,\,thermal}}$.

In Figure 4.3, right-hand panels illustrate radial profiles of gas density, temperature and entropy for our isolated clusters of mass $10^{13}\,h^{-1}\mathrm{M}_{\odot}$ and $10^{15}\,h^{-1}\mathrm{M}_{\odot}$. The radial profiles of the $10^{14}\,h^{-1}\mathrm{M}_{\odot}$ cluster can be found in Figure 4.1 with the same colour-coding. The blue, continuous lines denote the runs without AGN, while the red, dashed curves are for the simulations with AGN heating. The upper set of profiles in each panel are for the more massive cluster. The results show that for a fixed choice of parameters in our AGN heating model the ICM properties of clusters over a range of masses appear satisfactory: (i) the gas density is somewhat suppressed in central regions; (ii) very cool gas in the innermost regions of clusters is absent, and at the same time the AGN heating is not increasing the ICM temperature too much; (iii) the gas entropy is boosted in central regions, but without generating entropy inversions that are typically not observed in real systems. Together with realistic BH masses and BHAR, these promising features of the simulated ICM properties encourage us to proceed studying our model using fully cosmological simulations of galaxy cluster formation, which we consider in the next section.

4.4 Cosmological simulations of AGN feedback in galaxy clusters

We now turn to self-consistent cosmological simulations of galaxy cluster formation, with the aim to understand how AGN feedback influences these objects at different cosmolog-

Simulation	$N_{\rm HR}$	$N_{\rm gas}$	$m_{\rm DM}$ $[h^{-1}{\rm M}_\odot]$	$m_{\rm gas}$ $[h^{-1}{\rm M}_\odot]$	$z_{\rm start}$	$z_{\rm end}$	ϵ $[h^{-1}{\rm kpc}]$
g676	314518	314518	1.13×10^9	0.17×10^9	60	0	5.0
g1	4937886	4937886	1.13×10^9	0.17×10^9	60	0	5.0

Table 4.2: Numerical parameters of the cosmological galaxy cluster simulations analysed in this study. The values listed from the second to the fifth column refer to the number and to the mass of high resolution dark matter particles and of gas particles. Note that the actual values of $N_{\rm gas}$ and $m_{\rm gas}$ vary in time due to star formation. The last three columns give the initial and final redshifts of the runs, and the gravitational softening length ϵ.

ical epochs and how this influence depends on the mass and the evolutionary history of clusters. We focus our analysis on two galaxy cluster simulations that have quite different merging histories and different present-day masses. The clusters have been selected from a cosmological ΛCDM model with a box size of $479\,h^{-1}$Mpc [Yoshida et al., 2001, Jenkins et al., 2001], and were prepared by Dolag [2004] for resimulation at higher resolution using the Zoomed Initial Condition (ZIC) technique [Tormen et al., 1997]. The cosmological parameters of the simulations are those of a ΛCDM concordance cosmology with $\Omega_{\rm m} = 0.3$, $\Omega_\Lambda = 0.7$, $\Omega_{\rm b} = 0.04$, $\sigma_8 = 0.9$, and Hubble constant $H_0 = 70\,{\rm km\,s^{-1}Mpc^{-1}}$ at the present epoch. In respect to the isolated halos simulations we have adopted somewhat different parameters of the BH feedback model, with the normalization values for $E_{\rm bub,0} = 10^{55}$erg, and $\rho_{\rm ICM,0} = 10^4\,h^2\,{\rm M}_\odot\,{\rm kpc}^{-3}$ being lower, with $\delta_{\rm BH} = 0.01\%$, and with a more realistic mechanical feedback efficiency of $\epsilon_m = 0.20$, while the other parameters were kept exactly the same.

The primary numerical parameters of our simulations are summarized in Table 4.2, and the main physical properties at $z = 0$ of the formed clusters are listed in Table 4.3. For both simulated galaxy clusters, the smaller one ("g676") and the more massive one ("g1"), the virial radius, virial mass, total gas mass and stellar mass have been measured in runs without AGN feedback (labelled "csf") and when it is included (labelled "csfbh"). Additionally, the mass– and emission–weighted temperature, X–ray luminosity and total SFR are given in the 6th to the 9th column of Table 4.3, respectively. Looking at the gas properties listed in Table 4.3 it can be seen that AGN feedback does not significantly alter the global gas temperature, or the X–ray luminosity. However, there are still important local changes of these properties when AGN heating is included, as we will discuss in more detail in Section 4.4.3. On the other hand, the global stellar properties are strongly affected by AGN feedback: the total stellar mass is reduced considerably, as well as the total SFR, while the total gas mass is increased. This implies that the relative amount of gas versus stars is a function of AGN heating efficiency.

4.4.1 Black hole growth in clusters

In Figure 4.4, we show a projected gas density map of the g676 galaxy cluster simulation at $z = 0$, with the positions of BHs more massive than $1.5 \times 10^7\,h^{-1}{\rm M}_\odot$ overlaid as black

Cluster	R_{200} $[h^{-1}\mathrm{kpc}]$	M_{200} $[h^{-1}\mathrm{M}_\odot]$	$M_{\mathrm{gas},200}$ $[h^{-1}\mathrm{M}_\odot]$	$M_{\mathrm{stars},200}$ $[h^{-1}\mathrm{M}_\odot]$	T_{mw} $[K]$	T_{ew} $[K]$	L_{X} $[\mathrm{ergs}^{-1}]$	SFR $[\mathrm{yr}^{-1}\mathrm{M}_\odot]$
g676_csf	1176	1.13×10^{14}	9.3×10^{12}	4.7×10^{12}	1.4×10^{7}	2.6×10^{7}	1.6×10^{43}	51
g676_csfbh	1165	1.10×10^{14}	1.1×10^{13}	1.4×10^{12}	1.3×10^{7}	2.4×10^{7}	1.0×10^{43}	1
g1_csf	2857	1.63×10^{15}	1.4×10^{14}	6.3×10^{13}	7.3×10^{7}	1.3×10^{8}	1.0×10^{45}	742
g1_csfbh	2859	1.63×10^{15}	1.7×10^{14}	2.5×10^{13}	7.3×10^{7}	1.3×10^{8}	1.0×10^{45}	144

Table 4.3: Physical properties of our sample of simulated galaxy clusters at $z = 0$, selected with a mean overdensity of $200\rho_c$. For two different galaxy clusters, as labelled in the first column, the cluster radius, total mass, gas mass and stellar mass are given. Also, the mass– and emission–weighted gas temperatures, X–ray luminosity and total SFR are listed, in the 6th to 9th column, respectively. Note that the values give results both for the simulations with cooling and star formation only (denoted with "csf"), and for runs performed with AGN heating (labelled "csfbh").

dots. The density map is $20\,h^{-1}$Mpc on a side and is centred on the most massive cluster galaxy. Interestingly, the surrounding large-scale structure shows many smaller halos with embedded BHs, many of them residing in a filamentary region NW of the central object. In fact, most halos are harbouring a central, massive BH. However, the most massive BH among them is sitting at the centre of the biggest halo, and this is also true at higher redshifts.

The mass as a function of time of this most massive BH is shown in Figure 4.5. To produce this measurement, we have first constructed the full merger tree of all BHs formed in the simulated volume, allowing us to extract the main progenitor trunk corresponding to the most massive BH at $z = 0$, which is plotted as a thick continuous blue line. Also, we show the mass growth of the secondary progenitors that at the moment of their last merger have a mass greater than $5 \times 10^7\, h^{-1}\mathrm{M}_\odot$. It can be seen that the most massive BH at $z = 0$ is not the first one to form, but it merges with two BHs that formed somewhat earlier and that are more massive for $z > 3.5$. The thick, dashed blue line represents the cumulative mass of all secondary progenitors of the most massive BH at $z = 0$. This shows that mergers contribute up to 45% to the final mass of the BH that defines the trunk, while the remaining 55% are due to gas accretion by the BH on the trunk itself. Note however that ultimately all the BH mass is built-up by gas accretion (the mass of the initial seed BHs is negligible), but the part we here attributed to mergers was built up by gas accretion in other systems.

We also note that the mass growth via mergers is more important at higher redshifts, with the last significant merging event occurring at $z \sim 0.7$. The merger events of BHs are mainly driven by the merging history of the host galaxy clusters. Indeed, there is a quite close correspondence between the evolution of the main progenitor of the most massive BH and the main progenitor of the biggest halo in the simulation. In particular, the main progenitor of the g676 galaxy cluster undergoes a number of mergers between redshifts $3.5 < z < 2.8$, when also the BH grows significantly via mergers with other BHs. Then at $z \sim 0.75$, the g676 cluster experiences its last major merger, visible as a jump in

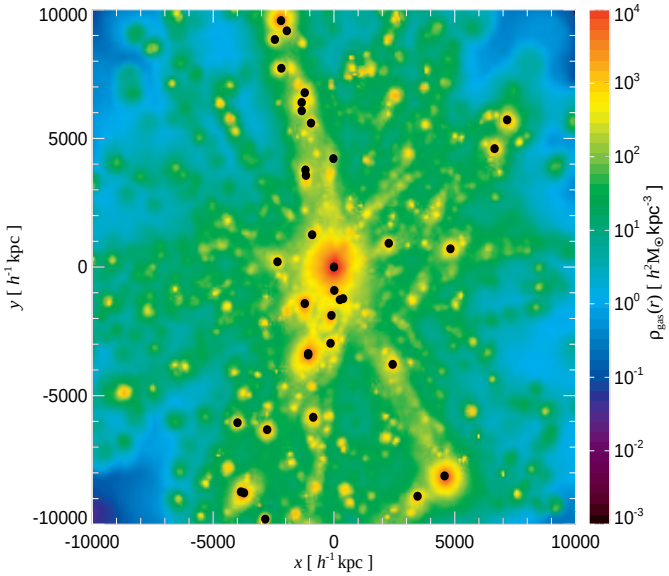

Figure 4.4: Projected gas density map of the g676 galaxy cluster simulation at $z = 0$, subject to AGN heating. Black dots mark the positions of BH particles that are more massive than $1.5 \times 10^7\, h^{-1}\mathrm{M}_\odot$. It can be seen that the BHs are residing not only in the centre of the most massive galaxy cluster, but also in almost all smaller halos that are visible on the map. Interestingly, there is a concentration of BHs in a filament that is extending from the central cluster towards NW, due to the ongoing structure formation there.

the main trunk in Figure 4.5. At lower redshifts, the cluster becomes fairly relaxed and isolated, such that its central BH grows mostly by accreting gas that is cooling off from the hot cluster atmosphere. However, this mode of accretion (at low accretion rates) does not contribute significantly to the overall BH mass growth.

Now we consider in more detail the mass growth and the accretion rate, not only of the most massive BH, but of all the BHs belonging to the simulated volume. Due to the better statistics provided by the g1 galaxy cluster simulation, we focus on this simulation, noting that the results for the g676 cluster are very similar. In Figure 4.6, we plot the BHAR, expressed in Eddington units, as a function of the BH mass. The colour-coding denotes the redshift, over the redshift interval $z = 4.3$ to $z = 0$ considered here. A number of interesting features can be noticed in this plot: (i) at a given BH mass, the accretion rate is decreasing with redshift; (ii) for intermediate redshifts, $2 < z < 3$, the BHAR is lowest for intermediate mass BHs; (iii) at still lower redshifts, the BHAR for intermediate masses keeps falling strongly, while it stays comparatively high for low-mass BHs as well as for very massive BHs; (iv) at the present epoch there is a large population of low-mass BHs that is still accreting efficiently. These features are qualitatively consistent with observational findings both from optical and X-rays surveys [e.g. Steffen et al., 2003, Ueda et al., 2003,

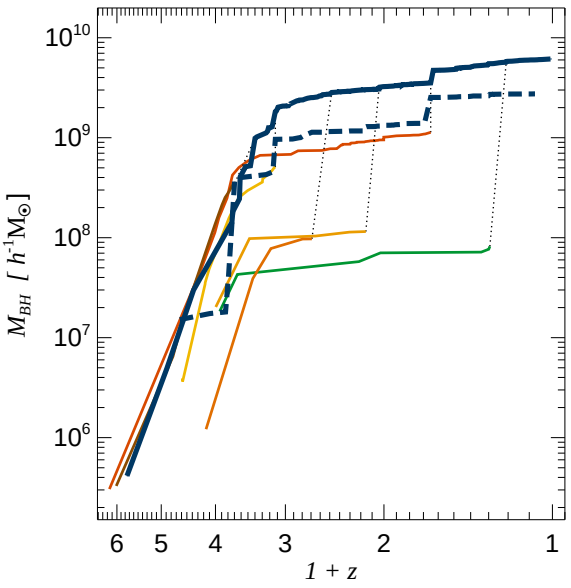

Figure 4.5: Merger tree of the most massive BH at $z = 0$ in the g676 galaxy cluster simulation. The thick blue line is showing the mass growth of the BH's first progenitor as a function of redshift, while the thin lines of different colour represent the evolutionary history of secondary progenitors, until the merger with the main progenitor occurs. For clarity, only secondary progenitors that at the moment of the last merger have a mass greater than $5 \times 10^7\, h^{-1}\mathrm{M}_{\odot}$ are shown. Vertical dotted lines indicate when merger events between the BHs in consideration occur. The dashed, thick blue line represents the cumulative mass of all secondary progenitors.

Heckman et al., 2004, Barger et al., 2005, Hasinger et al., 2005] that indicate that BHs are growing in a so-called 'anti-hierarchical' manner. In Section 4.5, we will come back to this issue, and discuss how the BHAR depends on the BH mass in a galactic environment.

At low redshifts, the increase of the BHAR with mass at the high BH mass end is driven by BHs that sit at the centres of massive galaxy clusters. These BHs are fed by gas from the hot cluster atmosphere, which would develop a strong cooling flow without the periodic heating by the AGN feedback. Interestingly, we also find that our BHAR of massive BHs at $z = 0$ agrees very well with a recent estimate of the Bondi accretion rate for a sample of X-ray luminous elliptical galaxies by Allen et al. [2006].

However, we need to emphasize that the simulations performed in this study were not designed to address the problem of BH formation and growth in the very early universe, for which they lack the required resolution and volume. This becomes also apparent in the plot of Figure 4.6, where the upper right corner is not populated. This means that these simulations cannot account for the existence of supermassive BHs of mass $\sim 10^9\,\mathrm{M}_{\odot}$ already

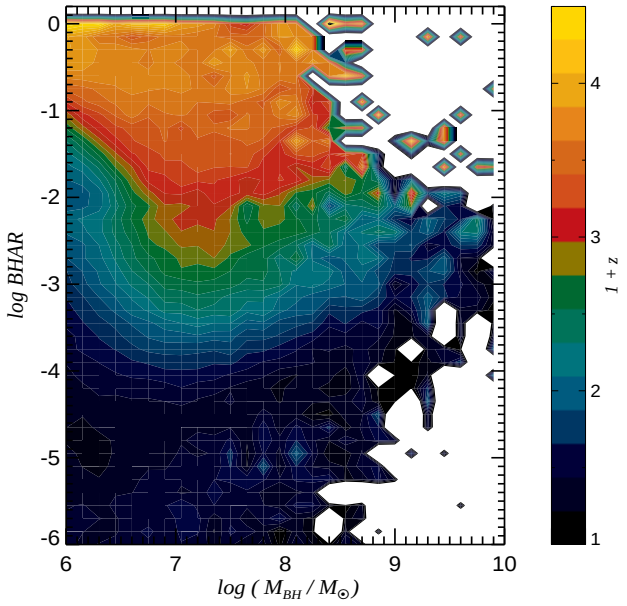

Figure 4.6: BHAR in Eddington units as a function of BH mass, for all BHs belonging to the g1 galaxy cluster simulation. The colour-coding expresses the redshift, and the redshift interval considered here ranges from 4.3 to 0.0. For a given BH mass, the accretion rate is highest at early cosmic times. At lower redshifts, there is an upturn in the BHAR at the massive BH end, corresponding to BHs that are fed by gas that cools off from the atmosphere of the cluster and its massive progenitor systems.

at $z = 6$, as inferred from the luminosity of high redshift quasars [Fan et al., 2001]. Using high-resolution compound galaxy models to populate a merger tree measured from a zoom simulation of a protocluster region, Li et al. [2006] have however recently demonstrated that at least in principle such early supermassive BHs can grow from accretion in gas-rich mergers at high redshift.

4.4.2 Heating the cluster outskirts

In Figure 4.7, we examine the radial dependence of AGN heating in our simulated clusters for different redshift bins. To this end, we evaluate the AGN luminosity at the given epoch and plot it as a function of distance from the centre of the most massive cluster in the simulation. Depending on the BHAR, we decide whether the BH is in the "quasar" or "radio" mode, which we denote with star symbols or circles, respectively (see upper panel). In the lower panel, we plot the total AGN luminosity outside of a given radius, regardless in which mode the BHs accrete. It can be seen that the AGN heating at all redshifts considered and regardless of the feedback mode is most important in the cluster centre. However, at early times, and in particular for $1.5 < z < 4.3$, BHs that happen to reside

in cluster outskirts during this time could provide an important additional source of ICM heating. These BHs are essentially all in the quasar phase where they accrete gas efficiently. Most of these BHs reside in satellite halos that are entering the most massive system for the first time, and thus possibly are preheating the gas of smaller halos prior to and during the merger with the massive cluster. These findings and the spatial distribution of AGN in galaxy clusters, illustrated in Figure 4.4, are in a good agreement with observational evidence [e.g. Cappi et al., 2001, Cappelluti et al., 2005, Ruderman and Ebeling, 2005, Martini et al., 2006] for the presence of AGN in galaxy cluster environments. At low redshifts, though, the AGN sitting at the cluster centre appears to be the dominant source of heating, as we confirm in Section 4.4.3. Interestingly, the feedback luminosity of the central AGN, regardless of its accretion regime, peaks at the similar value for the whole time span considered.

4.4.3 The impact of AGN heating on the ICM

We here analyse how AGN feedback affects the intracluster medium and the stellar properties of the cluster galaxies. In Figure 4.8, we show radial profiles of gas density, temperature and entropy of the g676 cluster at three different epochs, both without (continuous blue lines) and with AGN heating (dashed red lines). Additionally, we have explored a model in which the BHAR was not limited to the Eddington rate, which is drawn with a dotted green line. It can be seen that at all redshifts considered, the central gas density is reduced significantly as a result of AGN feedback. We also observe that the gas temperature in the central regions is fluctuating around the "isothermal" value, sometimes for short time intervals increasing towards the centre, but most of the time being roughly constant or decreasing. These trends in gas temperature are due to the periodic nature of the bubble feedback. If a very energetic bubble is injected in the innermost cluster regions, the gas temperature increases for a short time, and reduces the BHAR considerably. After some time has elapsed, the gas will begin to cool again such that the central gas temperature will gradually start to decrease towards the centre. When enough gas has cooled off from the hot cluster atmosphere and has become available for accretion onto the supermassive BH, a new bubble will be triggered, establishing a self-regulated loop for the growth of the BH and the heating of the ICM. In some sense, this feedback loop acts as a thermometer for the ICM, preventing it to develop strong cooling flows.

On top of our simulated gas temperature profiles, we plot the slopes of the central temperature profiles of the cool core clusters recently found by Sanderson et al. [2006], showing a very encouraging agreement. Indeed, a number of observational studies [e.g. De Grandi and Molendi, 2002, Vikhlinin et al., 2005, Dunn and Fabian, 2006, Pratt et al., 2007] have shown that the central temperature profiles of relaxed, cool core clusters decrease with decreasing radius, while at the same time these systems require an additional source of heating in order to avoid excessive cooling flows. Theoretically, it is not trivial to explain this observed feature of the central cluster temperature – a self-regulated feedback mechanism is apparently needed which is sensitive to the local properties of the intracluster gas. Our model contains such a mechanism and represents to our knowledge the first successful attempt to simulate such a process in a cosmological environment.

As a result of the non-gravitational bubble heating, the ICM entropy is increased in

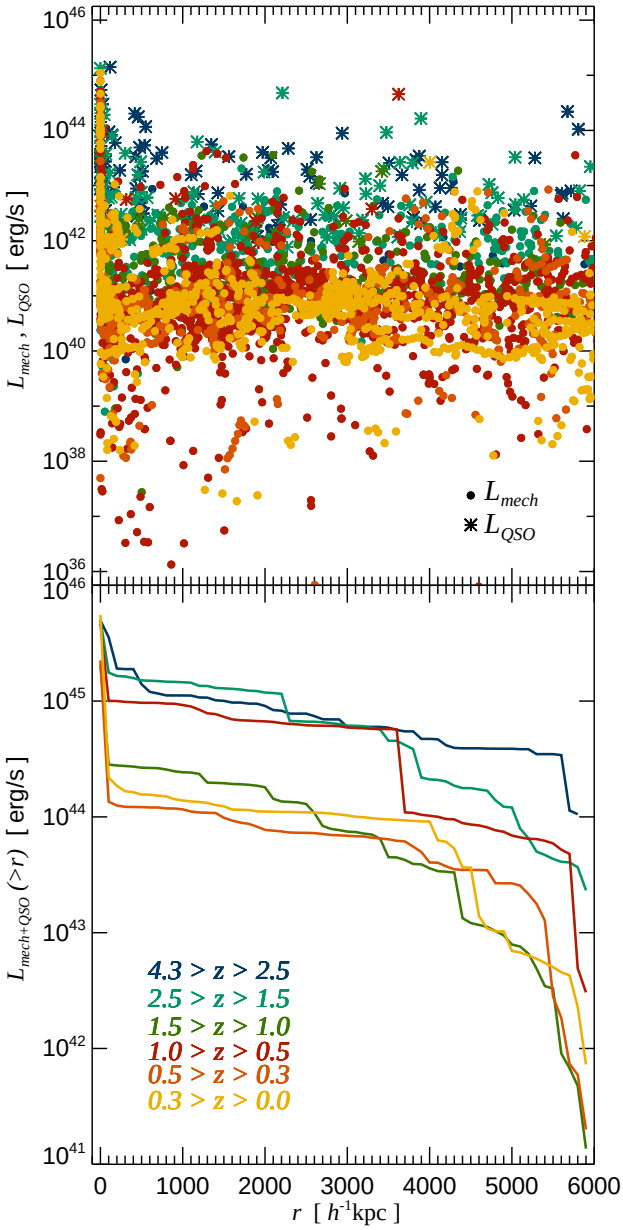

Figure 4.7: In the upper panel, the mechanical and quasar AGN luminosities are plotted as a function of distance from the most massive halo in the g676 galaxy cluster simulation. Depending on the BHAR, a BH is assumed to be either in a "quasar" or in a "radio" mode, and the BH luminosity is calculated accordingly and denoted with different symbols. The colour-coding is according to redshift bins, as indicated in the lower panel. The total AGN luminosity outside a given radius, regardless of the feedback mode, is shown in the lower panel. It can be seen that the highest AGN luminosities always correspond to BHs sitting in the centre of the most massive clusters, and that at higher redshifts (especially $1.5 < z < 4.3$) heating from the quasars in cluster outskirts can be important.

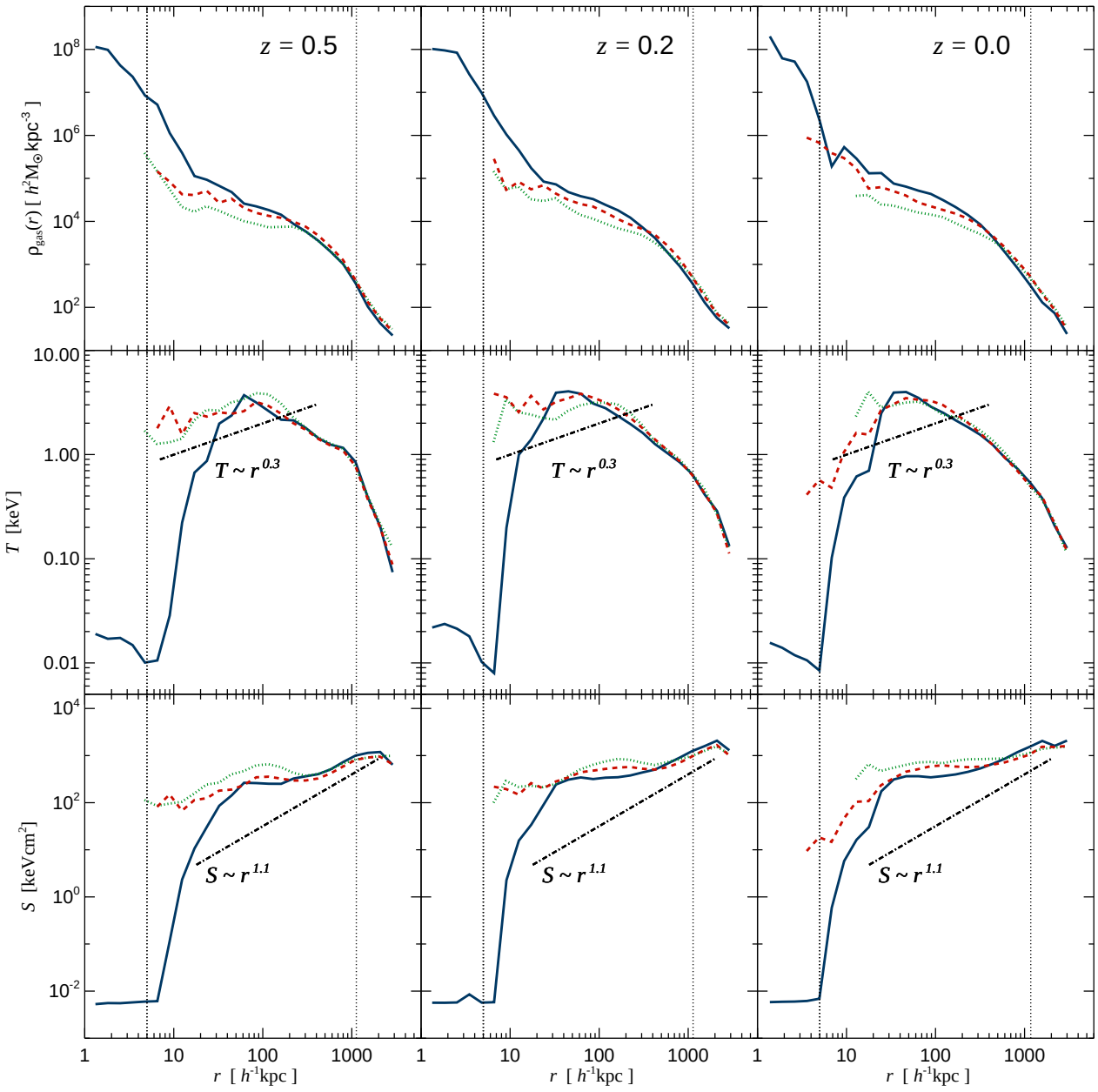

Figure 4.8: Radial profiles of gas density (upper row), mass-weighted temperature (central row) and entropy (lower row) of the g676 galaxy cluster at $z = 0.5$, 0.2 and 0.0, respectively. Continuous blue lines illustrate the case without AGN heating, while dashed red lines are for simulations where AGN feedback is included. The run where the Eddington limit was not imposed on the BHAR is shown with a dotted green line. The vertical dotted lines denote the gravitational softening and the virial radius of this cluster. The dash-dotted lines in the central row of panels show the slope of the central temperature profiles of the cool core clusters found by Sanderson et al. [2006], while the dash-dotted lines in the lower row illustrate the entropy scaling with radius, i.e. $S \propto r^{1.1}$.

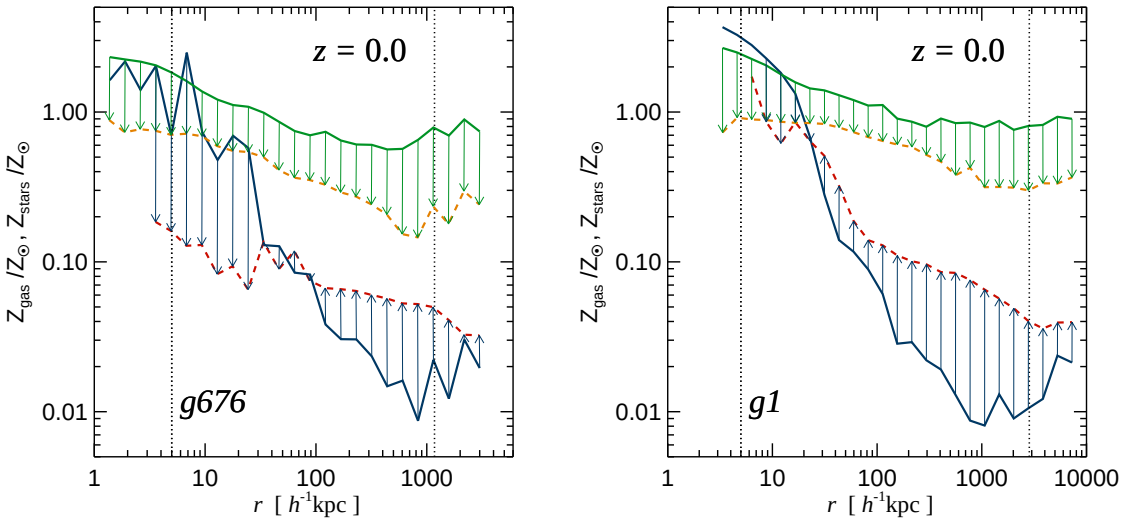

Figure 4.9: Radial profiles of mass-weighted gas metallicity and stellar metallicity of the g676 (left-hand panel) and g1 (right-hand panel) galaxy cluster simulations at $z = 0$. Continuous lines show the metallicity profiles without AGN heating, while dashed lines are for the runs with AGN feedback. The arrows illustrate how the ICM metallicity is affected by the BHs. The stellar metallicity is reduced at all radii, while the gas metallicity shows a tilt in the profile, decreasing in the inner regions and increasing for $r > 30h^{-1}$kpc, while still exhibiting a residual gradient.

the central regions, but maintains a monotonically increasing radial profile. Given the temperature of this cluster, the overall shape and the normalization of the simulated entropy profile are consistent with observational findings [e.g. Pratt and Arnaud, 2003, Ponman et al., 2003]. Observationally, it is found that the entropy scales with radius roughly as $S \propto r^{1.1}$ in the cluster outskirts, while departures from this scaling are seen in the central regions, out to $r \sim 0.1 - 0.2\,R_{200}$. As can be noticed from the bottom row of Figure 4.8, our simulated entropy profiles depart from this scaling out to somewhat larger radii, and this is also found for the 'g1' cluster simulation which has quite similar radial profiles. However, to decide whether this constitutes a real discrepancy between the simulations and observations, a larger set of simulated galaxy clusters is required, which we plan to compile in forthcoming work.

Looking at the radial gas profiles for $r > 400\,h^{-1}$kpc it is clear that the AGN heating does not significantly change the ICM properties at larger radii. Thus, heating of the cluster outskirts does not appear to be relevant for $z < 0.5$, confirming our findings in Section 4.4.2. Moreover, the radial profiles of our simulated galaxy cluster at $z = 0.5$ do not differ significantly from the ones at $z = 0$. This is consistent with observational findings [Bauer et al., 2005], where already formed cool core clusters are seen at $z \sim 0.15 - 0.4$, with similar properties to the local population.

In Figure 4.9, we show radial profiles of gas and stellar metallicity, in Solar units, for

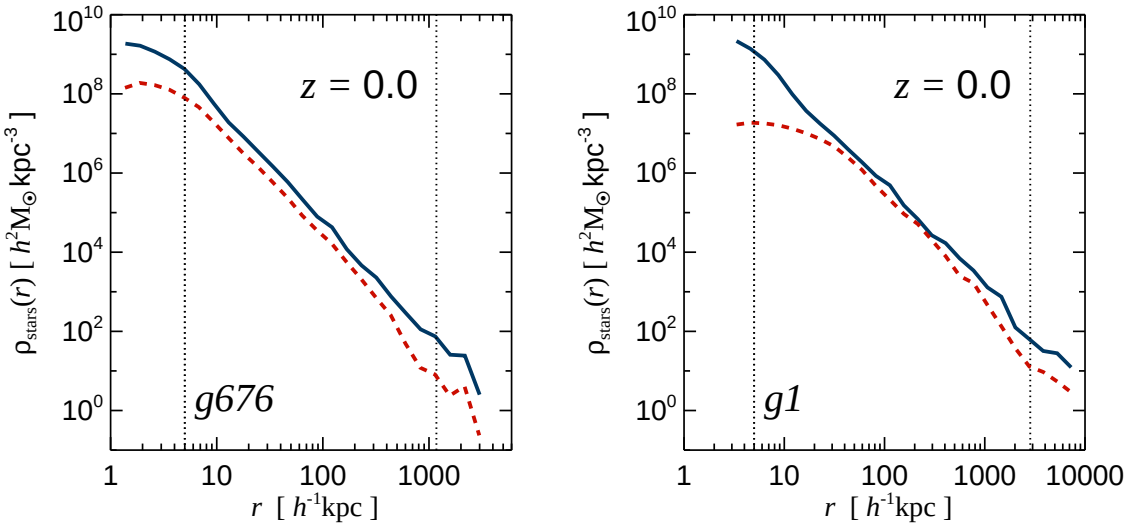

Figure 4.10: Stellar density profile of the g676 (left-hand panel) and g1 (right-hand panel) galaxy cluster simulations at $z = 0$. Continuous blue lines show the case without AGN heating, while dashed red lines are for simulations where AGN feedback is included. It can be seen that the stellar density is decreased at all radii, and in the case of the g1 cluster, the central stellar density develops a core when AGN feedback is operating.

Cluster	$M_{\rm stars}$ $[h^{-1}{\rm M}_\odot]$	$M_{\rm gas}$ $[h^{-1}{\rm M}_\odot]$	$M_{\rm gas,\,cold}$ $[h^{-1}{\rm M}_\odot]$	SFR $[{\rm yr}^{-1}{\rm M}_\odot]$	$M_{\rm r}$	$u-r$	$g-r$
g676_csf	1.3×10^{12}	2.3×10^{10}	1.9×10^{10}	30	-24.64	1.83	0.59
g676_csfbh	3.4×10^{11}	3.5×10^{9}	1.2×10^{9}	0	-22.55	2.68	0.84
g1_csf	4.2×10^{12}	8.4×10^{10}	7.8×10^{10}	163	-26.37	0.76	0.29
g1_csfbh	3.4×10^{11}	7.5×10^{9}	2.5×10^{8}	0	-22.71	2.64	0.83

Table 4.4: Properties of the cD galaxy of the g676 and g1 galaxy clusters at $z = 0$. The listed values refer both to simulations with cooling and star formation only (denoted with "csf"), and to the runs where AGN heating was included (labelled "csfbh"). From the second to the fourth column, we give the stellar mass, the gas mass and the cold gas mass with $T < 1\,{\rm keV}$ of the cD galaxy. The star formation rate of the cD galaxy is found in the fifth column, while the $M_{\rm r}$ magnitude and the $u-r$ and $g-r$ colours are given in the last three columns, respectively.

the g676 and g1 cluster simulations at $z = 0$. The continuous lines show the metallicity profiles without AGN feedback, while the dashed lines illustrate how these profiles change when our BH model is "switched-on". The stellar metallicity is reduced at all radii, while the gas metallicity shows a tilt: it is reduced in the innermost regions, for $r < 30\,h^{-1}{\rm kpc}$,

Simulation	$L_{\rm box}$ $[h^{-1}{\rm Mpc}]$	$N_{\rm part}$	$m_{\rm DM}$ $[h^{-1}{\rm M}_\odot]$	$m_{\rm gas}$ $[h^{-1}{\rm M}_\odot]$	$z_{\rm start}$	$z_{\rm end}$	ϵ $[h^{-1}{\rm kpc}]$
R1	25	2×176^3	1.72×10^8	0.35×10^8	100	1	3.0
R2	25	2×256^3	5.58×10^7	1.14×10^7	100	1	2.0
R3	25	2×384^3	1.65×10^7	0.34×10^7	100	1	1.3

Table 4.5: Numerical parameters of our cosmological simulations in periodic boxes. The values listed in the second to the fifth column refer to the size of the box, to the number of gas and dark matter particles and to their masses. The last three columns give the initial and final redshifts of the runs, and their gravitational softening lengths ϵ.

while it is increased for larger radii. These changes in the metallicity gradients are caused by two effects: first, due to the AGN feedback the total number of stars is reduced, not only in the central regions, but all over the cluster, as illustrated in Figure 4.10; second, some of the metals accumulated in dense, star-forming regions are expelled into the hot ICM. This mechanism drives the tilt in the gas metallicity, increasing the metal content of the hot intracluster gas.

The effect of AGN heating on the metal production and mixing in clusters brings the simulated gradients into a much better agreement with observational results. However, the simulated gas metallicity in the cluster outskirts appears still too low in comparison with the metallicity levels of cool core clusters at similar radii [e.g. De Grandi and Molendi, 2001]. This discrepancy may in part be attributed to the fact that in these simulations we have not included feedback effects from galactic winds and outflows powered by star formation. As we have shown in Sijacki and Springel [2006], galactic winds help spreading metals throughout the cluster environment, especially into the outer parts. Another restriction of our model for metal enrichment lies in its highly simplified treatment of supernovae, where we neglect the time delay of supernovae type Ia. More sophisticated models of chemical enrichment [e.g. Tornatore et al., 2004, Scannapieco et al., 2005] that take this into account might therefore help as well.

We now turn to the effects of AGN feedback on the stellar properties of the simulated clusters. In Figure 4.10, it can be seen that the stellar density is reduced at all radii in both clusters, as we have anticipated above. This reduction is caused not only by the activity of the central cluster BH, but also by other BHs that are harboured at the centres of individual galaxies throughout the cosmic evolution. As we will discuss in more detail in Section 4.5.2, when a BH at the centre of a given galaxy becomes massive enough to influence its host, it acts on the stellar properties by reducing both the instantaneous SFR as well as the integrated total stellar mass by a significant amount.

In Table 4.4, we list a number of properties we have measured for the central cluster galaxy. For the identification of the cD galaxy, we have simply taken its radius to be $20\,h^{-1}$kpc, based on the apparent break in the stellar density profile at this radius. A number of interesting results can be noticed from the values in the table: due to the AGN feedback, the stellar mass of the cD galaxy is significantly reduced, as well as the central total gas mass. There is some residual cold gas in the cD galaxy, but star formation is

completely quenched. This has an immediate and important consequence for the photometric colours of the cD galaxies. In order to estimate the colours, we have used the stellar population synthesis models of Bruzual and Charlot [2003] and computed the rest-frame magnitudes in the SDSS bands, assuming Solar metallicity and a Chabrier initial mass function. Both cD galaxies in our cluster simulations become much less luminous in the r, u and g-bands as a result of AGN feedback, such that the $u-r$ and $g-r$ colour indices are substantially increased. This reflects the fact that the stellar populations of the cD galaxies have become much older in our BH model, with very little recent star formation. With these properties, the simulated cD galaxies are in quite good agreement with observational findings [e.g. von der Linden et al., 2006], in terms of their stellar mass, their SFR and their colours.

Finally, we briefly discuss whether the Eddington limit that we have imposed on the BHAR has a significant effect on the BH growth and the feedback in clusters. For this purpose we have rerun the g676 galaxy cluster simulation with exactly the same feedback parameters, but relaxing the maximum accretion rate assumption. In Figure 4.8, we have included results for the radial profiles of gas density, temperature and entropy in this run as dotted green lines. It can be seen that the ICM properties are modified slightly more strongly in this case with respect to our default model, i.e. the AGN feedback effects appear to be somewhat stronger. A closer look at the detailed mass growth and accretion rate history of the BH as function of redshift shows that the feedback is regulating the BHAR even without an upper limit in the form of the Eddington rate. In fact, the total mass of all BHs at $z = 0$ in the simulated volume increases only by roughly 20% if the Eddington limit is disregarded. The most massive BH in the cluster centre shows an increase of its mass of the same order. This additional growth of the BH mass mostly comes from brief episodes of very high accretion rate, which are quickly terminated by the onset of AGN heating. Without an explicit Eddington limit, a bit more growth can happen before the 'suicidal' AGN activity shuts off the accretion, but the limit itself is not required for establishing a stable self-regulation loop. The Eddington limit therefore does not seem to pose an important restriction on the growth of BHs in clusters. However, this may still be quite different in the early phases of BH accretion at high redshifts, when the BH mass is so low that feedback effects are weak. Then the Eddington limit sets the shortest growth timescale that can be realized, which makes it a challenge to grow BHs quickly enough to the observationally inferred large masses already at very high redshifts. We plan to address this interesting problem in full cosmological simulations in future work.

4.5 Simulations of galaxy formation with AGN feedback

In this section we analyse BH growth and feedback in simulations of cosmic structure formation in homogeneously sampled volumes. We are mainly interested in the question whether our numerical model for a two-mode AGN growth produces realistic results for a range of object masses, from the scales of isolated galaxies to the ones of massive galaxy clusters. In Section 4.4, we have already confirmed that the BH model works well for clusters of galaxies, where it in fact drastically improves the properties of simulated galaxy clusters with respect to observations, and yields at the same time plausible evolutionary histories for the BH masses and the accretion rates. Here, we want to see whether this

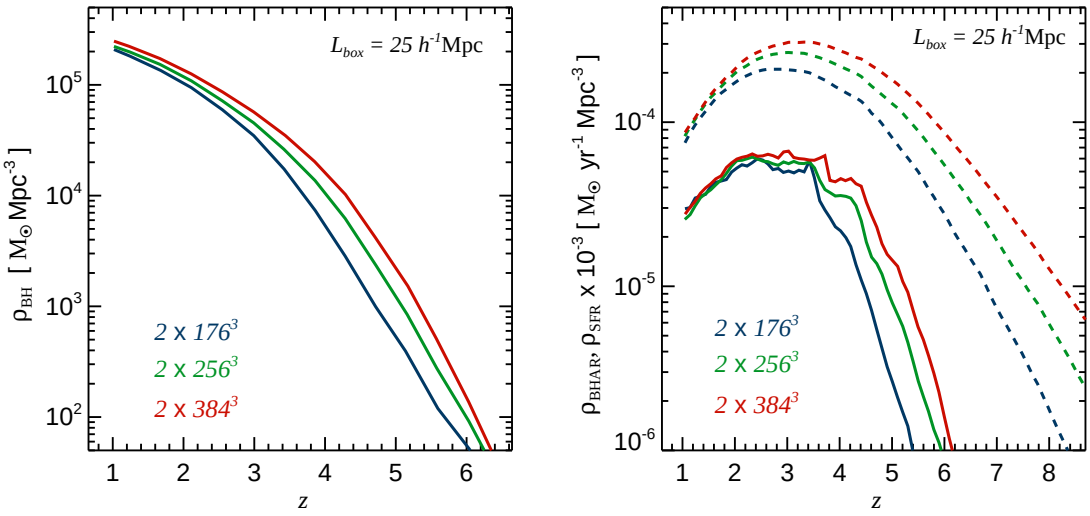

Figure 4.11: Redshift evolution of the comoving BH mass density in a cosmological box of $25\,h^{-1}$Mpc on a side (left-hand panel). The three different curves show runs with increasing resolution as labelled in the panel. The right-hand panel gives the BHAR (continuous lines) and SFR (dashed lines) densities as a function of redshift for the same set of runs. For plotting purposes, $\rho_{\rm SFR}$ has been rescaled by a factor of 10^3 to fit onto the same scale. It can be seen that numerical convergence is achieved at low redshift, where BHAR and SFR densities of the different runs asymptotically approach each other with increasing resolution.

success also carries over to the scale of individual galaxies, where the "quasar" mode of feedback will be dominant.

We have performed hydrodynamical simulations of a cosmological box with $25\,h^{-1}$Mpc on a side, at three different mass resolutions, as summarized in Table 4.5. The small box-size allows us to study comparatively small galaxies with stellar masses in the range of $\sim 10^8 M_\odot$ to $\sim 10^{11} M_\odot$. However, since the fundamental mode of this small box becomes non-linear at around $z = 1$, we had to stop the simulations at this redshift, since they would not be representative any more for the low-redshift universe. For the initial conditions, we have used a 'glass' as unperturbed particle load and the power spectrum fit of Eisenstein and Hu [1999] for imposing initial perturbations with WMAP-3 cosmological parameters [Spergel et al., 2006]. In particular, we have adopted a ΛCDM cosmology with $\Omega_{\rm m} = 0.26$, $\Omega_{\rm b} = 0.044$, $\Omega_\Lambda = 0.74$, $\sigma_8 = 0.75$, and $H_0 = 71\,{\rm km\,s^{-1}Mpc^{-1}}$ at the present epoch, and a primordial spectral index of $n_s = 0.938$.

For all three mass resolutions R1-R3 that we considered, we have computed two runs, one only with cooling and star formation and the other with the BH model included as well. The parameters of the BH model were exactly the same as the ones adopted in our cosmological simulations of galaxy cluster formation. For our intermediate resolution case R2, we have carried out additional simulations to study the influence of further parameters. This includes a run where we used the same cosmological parameters as in Section 4.4 in

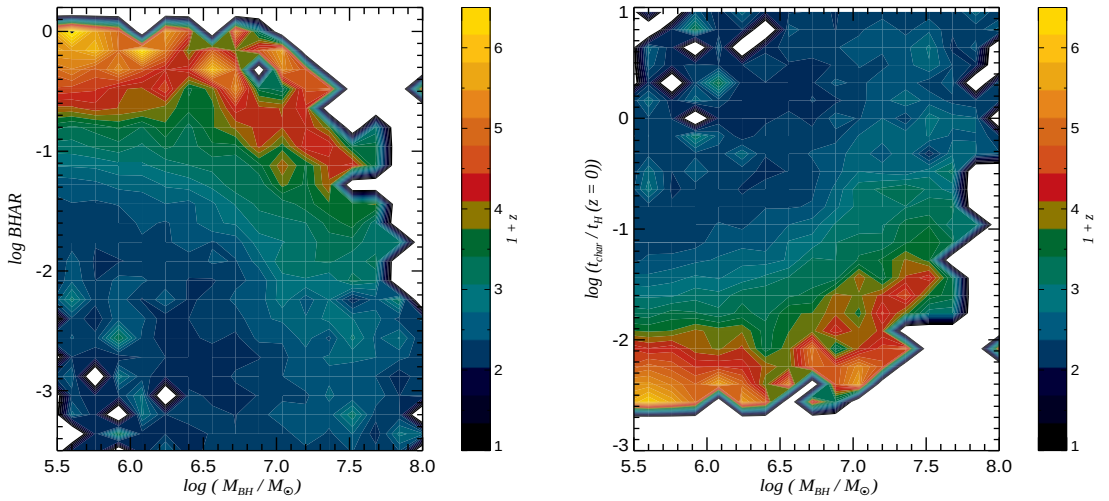

Figure 4.12: Left-hand panel: BHAR in Eddington units as a function of BH mass, for all BHs belonging to the R2 cosmological simulation. The colour-coding expresses the redshift, and the redshift interval considered is from 5.0 to 1.0. Right-hand panel: Characteristic growth time of the BHs as a function of their mass, colour-coded according to redshift. The growth time has been defined as the ratio of the BH mass and the BHAR at the given epoch, normalized to the Hubble time at $z = 0$.

order to gauge the importance of the cosmological model. Also, we have studied the influence of including a model for supernova-driven galactic winds with velocity $v \sim 480\,\mathrm{km/s}$, which can be especially important in low mass systems, as we will discuss below.

4.5.1 Black hole growth

In Figure 4.11, we consider the comoving BH mass density (left-hand panel) and BHAR density (right-hand panel) as a function of cosmic time. For comparison, we also show the redshift evolution of the SFR density (right-hand panel, dashed lines), which we have rescaled by a constant factor of 10^3 to put the curves onto the same plot. It can be seen that the BHAR and SFR densities approach each other asymptotically towards low redshifts when the numerical resolution is increased. The fact that numerical convergence can be more easily achieved at low than at high redshift is not surprising in light of the hierarchical growth of structure. At high redshift, most of the small mass systems that undergo star formation and BH accretion in our highest resolution simulation are unresolved in our low resolution simulation, which hence underpredicts the BHAR and SFR density. However, towards later times, the mass scale where most of the accretion happens shifts to larger mass objects, which can be resolved in all of our simulations, such that approximate convergence can be reached even with moderate resolution. This behaviour is similar to the one seen by Springel and Hernquist [2003b] in a comprehensive simulation study of the cosmic star formation rate history. We consider it highly encouraging that we find such a

behaviour for our BH growth model as well, which shows that the model is numerically well posed and can be meaningfully applied to cosmological volumes with their comparatively poor resolution per galaxy.

Our estimated BH mass density at $z = 1$ in our highest resolution run is $2.5{\times}10^5 \mathrm{M}_\odot\,\mathrm{Mpc}^{-3}$. This is in very good agreement with a number of observational estimates, based both on optical and X–ray data, which typically find values in the range of $2 - 6 \times 10^5 \mathrm{M}_\odot\,\mathrm{Mpc}^{-3}$ [e.g. Fabian and Iwasawa, 1999, Merritt and Ferrarese, 2001, Yu and Tremaine, 2002, Cowie et al., 2003]. The SFR density shows a peak at $z \sim 3$, while the BHAR density peaks at somewhat lower redshift, i.e. $z \sim 2.5$. The BHAR and SFR then decline to lower redshifts, with the SFR density decreasing slightly more steeply. If we extrapolate the BHAR and SFR densities to $z = 0$, the ratio of the two is of order of 2×10^3, a value that is roughly in agreement with the local population of galaxies [Heckman et al., 2004]. By comparing the simulations with and without AGN feedback we conclude that the SFR density starts to be noticeably reduced by BH heating for $z < 4$, and at $z = 1$ this reduction is of order $\sim 20\%$.

In the left-hand panel of Figure 4.12 we show how the BHAR evolves with redshift as a function of the BH mass. We have already considered an analogous plot for our galaxy cluster simulations in Figure 4.6. While the two plots are consistent for the overlapping range of BH masses, the most striking difference can be seen at the high BH mass end: in the galaxy cluster simulation we saw an upturn of the BHAR at low redshifts for very massive BHs, while here instead the BHAR keeps decreasing with increasing BH mass at all redshifts considered. This can be understood as a consequence of the limited size of the cosmological box. As a result of the small volume, rare big objects are absent, and hence massive BHs residing in cluster-sized objects are missing as well.

The characteristic time of BH growth, as a function of the BH mass, is illustrated in the right-hand panel of Figure 4.12. For each BH, we have defined the characteristic growth time as the ratio of its mass to its accretion rate at the given redshift, normalized to the Hubble time at the present epoch. It can be seen that the BH growth time is shortest at high redshifts and for the smallest BHs. At $z = 1$, BHs with mass of order of $10^7 \mathrm{M}_\odot$ reach a characteristic growth time of the order of the Hubble time for the first time. At different redshifts, the $\log t_\mathrm{c} - \log M_\mathrm{BH}$ curve has a similar shape, which is consistent with results obtained for the local galaxy population [Heckman et al., 2004].

4.5.2 Effects on the intergalactic medium

In Figure 4.13, we show projected mass-weighted temperature and metallicity maps of our cosmological box at $z = 1$. In the upper row, the run with cooling and star formation only is plotted, while the other two rows give results for simulations where the AGN feedback was included. In the lower row, feedback by galactic winds was additionally included. The positions of BHs more massive than $2 \times 10^7 h^{-1} \mathrm{M}_\odot$ are marked with black dots. It can be seen that galactic winds modify the gas temperature and metallicity properties more significantly than the BH feedback alone. As expected, galactic winds are especially important in low mass systems, given that they can expel gas from objects with small escape speeds relatively easily due to their shallow potential wells. Galactic winds can therefore pollute a sizable fraction of the volume of the intergalactic medium (IGM) with

metals, to a level of $10^{-3} - 10^{-2}$ of the Solar metallicity, in agreement with a number of observational findings [e.g. Rauch et al., 1997, Cowie and Songaila, 1998, Schaye et al., 2000, Ellison et al., 2000].

However, as can be seen from Figure 4.13, AGN contribute to the process of metal pollution of the low density gas, albeit with lower efficiency. If only AGN feedback is considered, we find that metals can be transported up to a distance of $\sim 1.5\,h^{-1}$Mpc from a galactic centre, but the large-scale metallicity distribution remains extremely patchy. Thus, the main difference relative to enrichment by galactic winds lies not only in the level of IGM metal enrichment, but in the volume filling factor of the metal-enriched regions. Nevertheless, by redshift $z = 3$, AGN feedback is making an important contribution to the enrichment of the IGM, where the characteristic size of high metallicity regions is of the order of $\sim 1\,h^{-1}$Mpc. However, we should point out that the AGN impact on the metal distribution found in our simulations is probably a lower limit, due to the fact that we cannot account for the contribution of very bright quasars powered by massive BHs at high redshifts.

Interestingly, even though AGN heating is affecting the gas metallicity of the IGM, it hardly affects its mean temperature, which is probably a reflection of the small volume filling factor of AGN-driven outflows. In contrast, galactic winds raise the intergalactic temperature significantly. Since this can delay the formation of small galaxies, the number and the mass of galaxies at a given epoch is reduced as well, which in turn slows the growth of the BH mass density.

4.5.3 Galaxy properties and evolution

We now study the question how the properties of galaxies are affected by BH feedback, and how the BH masses relate to their hosts. For this purpose, we identify the galaxies present in our cosmological box at different redshifts using a special group finder, and compute a number of properties for them, e.g. their stellar mass M_*, stellar velocity dispersion σ_*, their total SFR, and their colours in the rest-frame SDSS bands. This also allows us to look for correlations with their central BH masses.

In Figure 4.14, we show the relation between BH mass and stellar velocity dispersion σ_* (left-hand panels), and between BH mass and M_* (right-hand panels), at three different redshifts, $z = 1$, 2 and 3. Here we evaluate M_* and σ_* within the effective radius, R_e, chosen as the half-mass radius. Green star symbols are for the run without galactic winds, while red diamonds are for the simulation that also includes galactic winds. The results shown are from our intermediate resolution box, but we have verified good convergence in these quantities by comparing with the R3 box. With the dashed lines we overplot the locally observed $M_{\rm BH} - \sigma_*$ and $M_{\rm BH} - M_*$ relations, as determined by Tremaine et al. [2002] and Häring and Rix [2004], respectively. A number of interesting features are noteworthy in this figure:

1. Both relations show some evolution with redshift that however seems most prominent at the low BH mass end and for the run with galactic winds. The most massive objects found at every epoch stay very close to the local relation over the redshift interval considered.

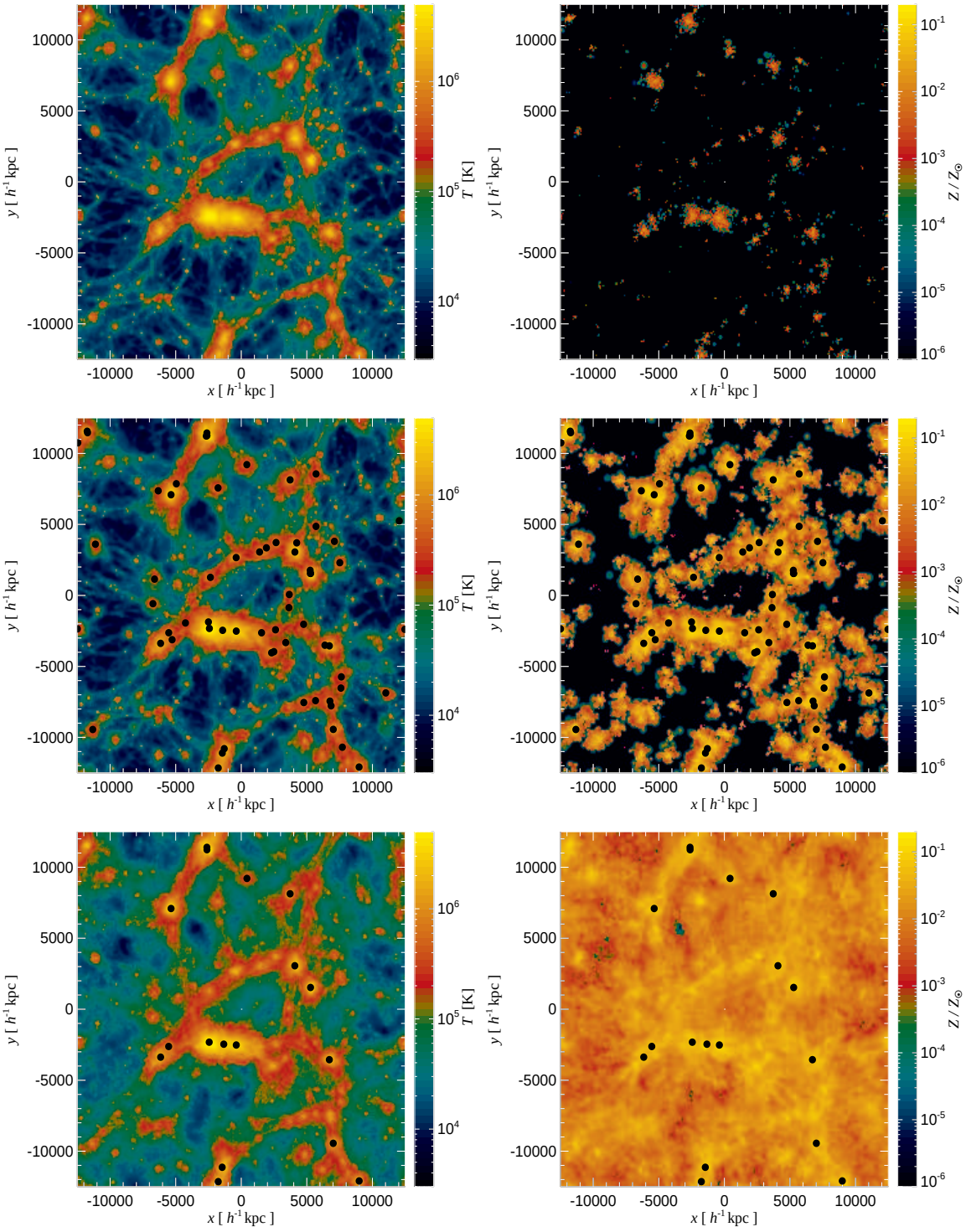

Figure 4.13: Projected mass-weighted temperature maps (left-hand panels) and gas metallicity maps (right-hand panels) at $z = 1$ of the R2 run. Top row: simulation with cooling and star formation only; middle row: simulation with additional BH model; bottom row: run with BH model and galactic winds "switched-on". The positions of BH particles more massive than $2 \times 10^7 h^{-1}\mathrm{M}_\odot$ are marked with black dots.

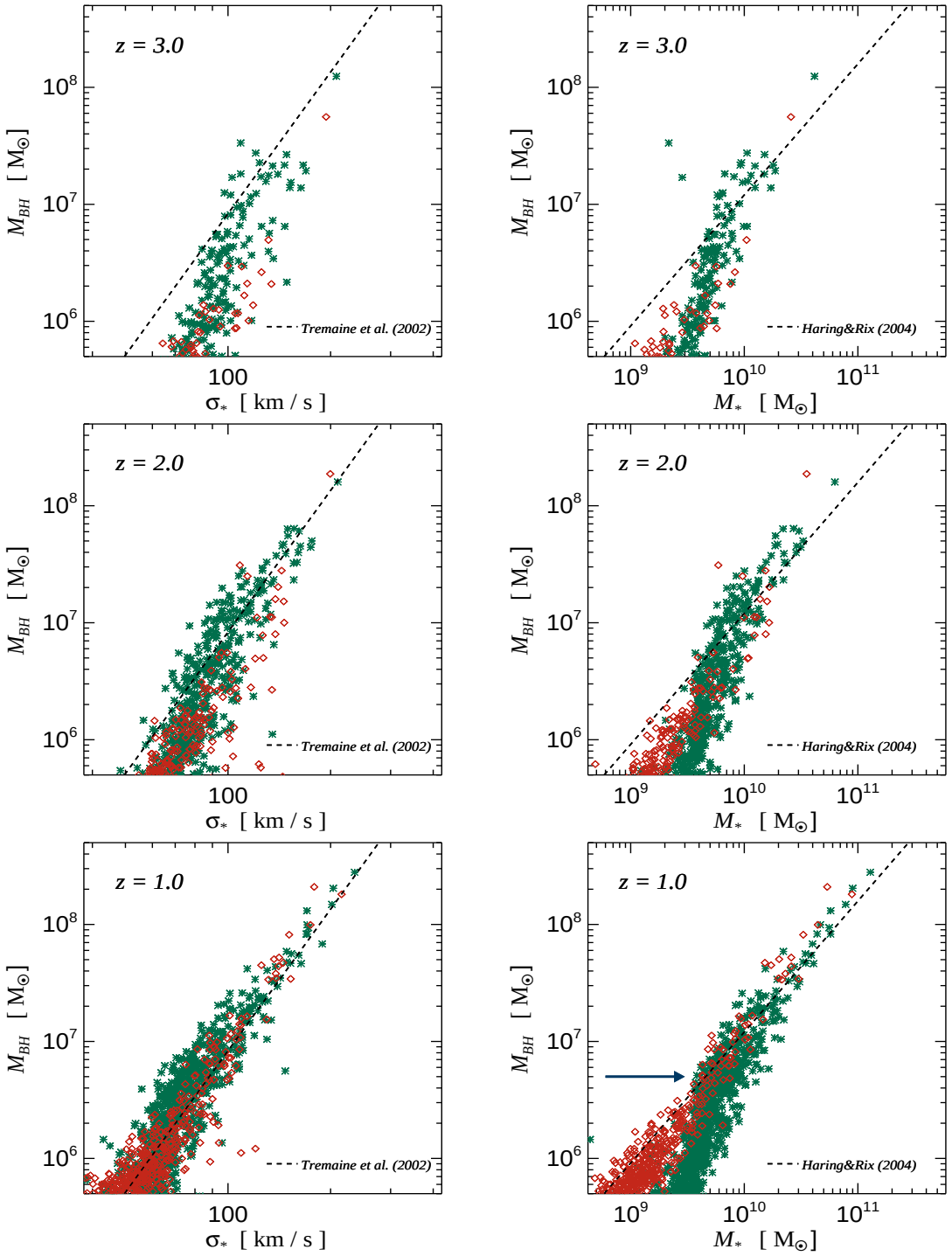

Figure 4.14: BH mass–stellar velocity dispersion relation (left-hand panels) and BH mass–stellar mass relation (right-hand panels), at redshifts $z = 1$, 2 and 3. Green star symbols denote the run without galactic winds, while red diamonds are for a run where galactic winds have been included as well. Both simulations have been performed at the resolution of the R2 cosmological box. The dashed lines give the locally observed relationships between the considered quantities, as determined by Tremaine et al. [2002] and Häring and Rix [2004].

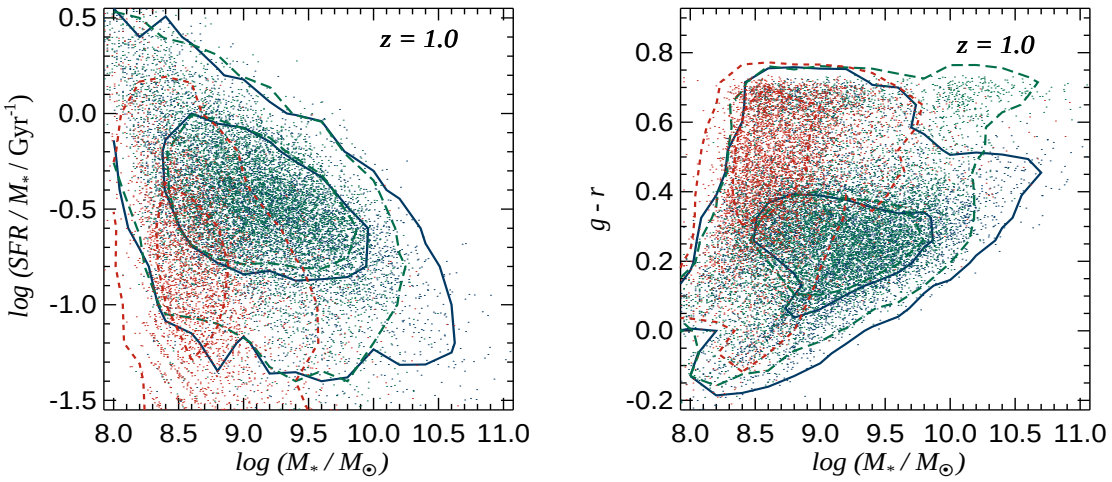

Figure 4.15: Specific SFR (left-hand panel) and $g-r$ colour (right-hand panel) for simulated galaxies as a function of stellar mass at $z = 1$. Blue dots and continuous contours are for the run with cooling and star formation only. Green dots and long-dashed contours indicate the case where our BH model was included, while red dots and short-dashed contours are for the simulation which in addition contains galactic winds.

2. At high redshifts, galactic winds give rise to less massive galaxies with somewhat lower σ_*, and for a given M_* or σ_*, BHs are less massive when the winds are "switched-on". However, by redshift $z = 1$ and for $M_{\rm BH} > 5 \times 10^6 {\rm M}_\odot$, the central BH masses are comparable for a given stellar mass of a galaxy, regardless of the presence of winds. This suggests that the feedback by galactic winds is delaying BH growth by expelling significant amounts of gas at high redshift. However, this gas becomes available for BH accretion at latter epochs, when it has been reincorporated from the IGM back into the galaxies.

3. For BH masses smaller than $5 \times 10^6\,{\rm M}_\odot$ (as indicated with the arrow in Figure 4.14) there is a tilt in both relations, especially noticeable for the $M_{\rm BH} - M_*$ relation. This tilt is significantly reduced in the run with galactic winds. This can be understood by considering that the AGN feedback in these small galaxies is very modest, and does not modify the properties of the hosts significantly. On the other hand, galactic winds are very efficient for these low mass objects, reducing their stellar mass and bringing them into better agreement with the expected relation. However, we caution that this result of our modelling may be sensitive to our prescription for BH seeding and the early initial growth, which could be affected by numerical resolution effects. If small mass galaxies could grow somewhat bigger BHs in their centre, they would also be more affected by BH feedback so that it may not be necessary to invoke galactic winds to match the low mass end of the $M_{\rm BH} - \sigma$ relation. In any case, it is interesting that galactic winds shift these smaller objects in the desired direction

while at the same time more massive galaxies are unaffected and still lie on the local relation.

4. Finally, given that the simulated $M_{\rm BH} - M_*$ and $M_{\rm BH} - \sigma_*$ relations at $z = 1$ match the locally observed relations well it would be interesting to explore how the model will evolve further until $z = 0$. It seems quite likely, especially for more massive galaxies, that not much evolution will occur for $z < 1$, given that these galaxies have a reduced star formation and depleted gas content due to the AGN feedback. However, considering the complex interplay between BHs and galactic winds, a reliable answer of this question will require explicit numerical simulations of a bigger cosmological box at comparable or better resolution, which we will tackle in future work.

In Figure 4.15, we show the specific SFRs and the $g-r$ colours of our simulated galaxies at $z = 1$ as a function of their stellar mass. Blue dots and blue continuous contours show the results when only cooling and star formation is considered. Green dots and long-dashed contours give the results for the run with AGN feedback, while red dots and short-dashed contours represent the case with additional galactic winds. While AGN feedback does not affect the bulk of the population significantly, it is evident that the stellar masses and the SFRs of most massive galaxies are reduced. When feedback by galactic winds is included as well this trend is even more pronounced, and extends to the lower mass systems. Note also that the galaxy colours change in our BH model – a number of galaxies become much redder, forming a red sequence, as it is shown in the right-hand plot of Figure 4.15. However, if the galactic wind model is included, the clearly defined red sequence disappears. Instead, all galaxies are in general less massive and redder. The fact that the red sequence becomes largely unpopulated in the run with galactic winds is not necessarily problematic, however. A larger cosmological box may again fill this region of the diagram with a population of more massive galaxies.

Finally, in order to assess whether the colours of our galaxies in the AGN feedback model are realistic, we have computed the mean $u-r$ colour of the red sequence at $z = 1$, obtaining $u - r \sim 2.2$. We can compare this result to the work of Bell et al. [2004] on the COMBO-17 survey. Using the conversion between $U - V$ and $u - r$ colours suggested by these authors, we find that the colour of our simulated galaxies along the red sequence is in good agreement with the early-type galaxies from the COMBO-17 survey.

4.5.4 Dependence on cosmological parameters

In order to evaluate how sensitively our BH model depends on the underlying cosmological model, we have performed two additional simulations at intermediate resolution (R2) with exactly identical BH parameters. In one case we have adopted cosmological parameters consistent with the WMAP 1st-year data analysis, while for the other run we have selected the updated parameters of WMAP's 3rd year data release. The main difference between the corresponding cosmological models lies in a reduction of the normalization parameter σ_8 ($0.9 \rightarrow 0.75$), a lowering of the matter density Ω_m ($0.3 \rightarrow 0.26$) and in the introduction of a tilt in the primordial power spectrum slope n_s ($1.0 \rightarrow 0.938$).

Our results show that BHs form earlier in the WMAP-1 cosmology, as expected from the fact that host halos above a given mass threshold appear earlier in this model due to the

higher normalization, and are therefore seeded with a BH at higher z. Also, the number density of BHs is higher and there are more high mass BHs at lower redshift with respect to the WMAP-3 run. Consequently, the comoving BH mass density is somewhat higher in the WMAP-1 cosmology. At $z = 1$, it is $3.9 \times 10^5 \mathrm{M}_\odot \mathrm{Mpc}^{-3}$, while for WMAP-3 we obtain $2.2 \times 10^5 \mathrm{M}_\odot \mathrm{Mpc}^{-3}$ at the same numerical resolution. The BHAR density is higher in the WMAP-1 model as well, with its peak shifted to a slightly earlier redshift of ~ 3.5. However, for lower redshifts this is compensated by a steeper decline, such that at $z = 1$ the BHAR densities have a very similar value in both cosmologies. These trends can simply be understood as a result of "delayed" structure formation in the WMAP-3 cosmology. Increasing σ_8 will let the BHs form earlier, evolve faster, and reach their peak activity at higher redshift. Interestingly, within the scatter, the $M_{\rm BH} - \sigma_*$ and $M_{\rm BH} - M_*$ relations are however not significantly affected by the change in the cosmological parameters.

4.6 Discussion and Conclusions

In this study, we have proposed a new model for following BH growth and feedback in cosmological simulations of structure formation. Within our prescription, BH seeds are introduced at early cosmic times in the centres of all halos once their mass exceeds a certain threshold value for the first time. The BH seeding is accomplished by frequently running a FoF algorithm on the fly in our simulation code, which identifies newly formed halos and their properties. The BHs themselves are represented as collisionless sink particles that can grow their mass via two channels, by (1) gas accretion with an accretion rate estimated by a simple Bondi formulae, and (2) via mergers with other BHs that are close enough. Motivated by the observed phenomenology of radio galaxies and quasars, and by analogy with X–ray binaries, we have assumed that the AGN feedback that accompanies gas accretion can be decomposed into two physically distinct modes: BHs accreting at high accretion rates in terms of their Eddington limit are operating in a radiatively efficient "quasar" regime, while BHs accreting at much lower rates live in a radiatively inefficient "radio" mode, which however produces significant mechanical luminosity that gives rise to jet-inflated bubbles.

In our initial tests of the model, we have applied it to simulations of isolated galaxy clusters consisting of a static dark matter potential and gas in hydrostatic equilibrium. Considering a range of cluster masses from $10^{13} h^{-1} \mathrm{M}_\odot$ to $10^{15} h^{-1} \mathrm{M}_\odot$, we have found that the model leads to a self-regulated AGN feedback that produces realistic ICM properties and prevents the overcooling problem in the central cluster regions. At the same time, it yields reasonable BH masses and accretion rates.

We have then applied our model to fully self-consistent cosmological simulations of galaxy cluster formation, where the seeding of BHs and their subsequent growth is followed self-consistently. These simulations are the first cosmological hydrodynamical models that simultaneously follow the growth of structure in the dark matter as well as the baryonic physics of star formation and AGN feedback. These simulations provide information on how the BHs are spatially distributed in the simulated volume, how they grow with cosmic time as a function of their environment, and how they influence the surrounding medium and their host galaxies.

Our analysis of these calculations has focused on the history of the BH in the central cD

galaxy. We have shown that while essentially all the mass in supermassive BHs originates in gas accretion, a large fraction of the mass of the BH in the cD grows from mergers with other BHs, as opposed to being all accreted by a single massive progenitor. This suggests that mergers of supermassive BHs are an important factor for building up very massive BHs. In line with our findings for the isolated cluster simulations we found that feedback from BHs is preventing the formation of excessive cooling flows out of hot cluster atmospheres, and is changing the central ICM properties substantially in the process. These changes are all acting to bring the simulated temperature and entropy profiles into much better agreement with observational findings of cool core clusters [e.g. De Grandi and Molendi, 2002, Pratt and Arnaud, 2003, Ponman et al., 2003, Vikhlinin et al., 2005, Bauer et al., 2005, Dunn and Fabian, 2006, Sanderson et al., 2006, Pratt et al., 2007]. Moreover, the stellar properties of the central galaxy are affected as well, with the forming cD galaxies being less massive, and having older and redder stellar populations which are consistent with the results found in recent studies of a large sample of BCGs in the SDSS survey [von der Linden et al., 2006].

We have also studied our AGN feedback model in simulations of homogeneously sampled cosmological volumes, thereby investigating how successful it is on the scale of galaxies, and with respect to the mean properties of the cosmic population of BHs. In our simulation box of size $25\,h^{-1}$Mpc on a side, we were able to resolve galaxies with stellar masses greater than $\sim 10^8 \mathrm{M}_\odot$. We have found that our model produces a comoving BH mass density equal to $2.8 \times 10^5 \mathrm{M}_\odot \mathrm{Mpc}^{-3}$, which is in very good agreement with observational estimates [Fabian and Iwasawa, 1999, Merritt and Ferrarese, 2001, Yu and Tremaine, 2002, Cowie et al., 2003]. Moreover, the AGN feedback influences the properties and the formation of the host galaxies and vice versa, and this mutual coupling establishes $M_{\mathrm{BH}} - \sigma_*$ and $M_{\mathrm{BH}} - M_*$ relationships already at early epochs. Again, these relations are in broad agreement with observations, at least for the more massive and better resolved systems. Interestingly, a model that besides BH feedback includes feedback from supernova-driven galactic winds produces a better match to the expected relationships at the low mass end. At the same time, this model also leads to a much more widespread enrichment of the IGM, which appears required by the data on quasar absorption line systems. Finally, AGN heating reduces the stellar mass of the most luminous galaxies identified in the simulated volume, and it affects their SFR and colours as well. The galaxies in simulations with AGN feedback show a clearly defined red sequence already at $z = 1$.

These results represent highly encouraging successes for hydrodynamical models of hierarchical galaxy formation in ΛCDM cosmologies, and provide support for the theoretical conjecture that galaxy formation and supermassive BH growth are intimately linked. In spite of these successes we need to emphasize that our BH model clearly represents a drastically simplified picture of BH physics. In part, the simplifications are driven by numerical limitations, because even state-of-the-art simulations of galaxy formation in cosmologically representative regions of the Universe cannot directly resolve the gravitational sphere of influence of individual BHs. We are therefore forced to adopt a subresolution approach for the representation of BH accretion, and also for the modelling of bubble feedback where the initial stages of bubble inflation by a jet are not resolved. However, this subresolution approach can still capture the essential parts of the physics relevant for the coupling of the BHs to their larger-scale environment, and this is what allows us to study their

cosmological significance for galaxy formation.

While we have tried in this study to shed some light onto the entangled histories of galaxies and their central BHs, a number of important questions remain open for future work, and our model appears suitable to help answering them. They include: (i) The early growth of BHs - can the observed 'downsizing' of BH growth be reproduced by our model? (ii) Do the galaxy cluster scaling relations change as a result of the AGN feedback? (iii) Can a galaxy luminosity function with a bright end consistent with observational constraints be reproduced in cosmological simulations, and what is the respective AGN luminosity function? (iv) Do the quasar clustering properties come out right?

Indeed, AGN appear to be a key ingredient of structure formation, and future numerical simulations should be a very helpful theoretical tool to unveil the intriguing and complex picture of their interactions and growth.

5
Conclusions and outlook

The formation and evolution of galaxies represents one of the most important fields of research in physical cosmology. In the last decades, remarkable progress has been achieved, leading to a standard model for structure formation within the concordance ΛCDM cosmology. Indeed, modern technological achievements have permitted us to study the Universe in a whole 'new light'. Observational experiments such as VLA, WMAP, Spitzer, SDSS, Hubble and Chandra, just to name a few, have produced a wealth of information about the evolutionary history of the Universe, from the surface of the last scattering at $z \sim 1100$ until today, and covering a large portion of the electromagnetic spectrum as well. These observational findings have also stimulated much theoretical progress, including the development of ever more sophisticated numerical schemes that have allowed simulations to address a variety of important topics of the complex physics involved. But even though our understanding of the physical processes involved has been greatly enlarged, many aspects of galaxy formation are still poorly understood, and decisive tests of the standard model have yet to be made.

In the last years it has become evident that a large number of physical processes that are mutually intertwined need to be understood in depth in order to explain the richness and complexity of the observed Universe. In particular, it has been realized that supermassive BHs are harboured in the centre of most if not all galaxies with a spheroidal component, and that the masses of these central BHs are strongly related to their hosts. This suggests that BHs are one of the fundamental ingredients of structure formation.

The central aim of this thesis was to explore the ways in which BHs might influence their host galaxies. There are many possible channels of BH interactions with its surroundings, spanning from dynamical to thermal and radiative effects. Here we have concentrated on the specific issue of AGN feedback generated during quasar activity or radio-loud phases. In particular, we have constructed a simplified model where AGN feedback is modelled in terms of thermal energy injection. Thus, we have neglected possible kinetic effects from AGN-driven winds, or shock-heating due to propagating jets in the galactic environment.

Moreover, we have not considered the presence of relativistic particles (cosmic rays) or magnetic fields, that both could in principle be relevant. Finally, we have adopted a subgrid method to follow the BH growth and feedback, because we lack the numerical resolution to resolve all the scales of interest, like the BH's gravitational sphere of influence, in a fully cosmological simulation. While these assumptions are clearly restrictive, our model represents the first attempt to incorporate AGN feedback effects self-consistently into cosmological simulations of structure formation. And despite these simplifications, the complexity of the numerical scheme needed to realistically track dark matter, gas, stellar and BH components at the same time remains very high. Given the promising results of our models, we think that they are an ideal starting point for incorporating gradually more complex modelling, as I will discuss next.

However, before describing important issues for future research, let me briefly summarize the main achievements of this thesis. In Chapter 2, I have discussed a phenomenological model for AGN heating in massive galaxy clusters. The aim of this model was to determine whether AGN heating in cluster cores can indeed provide a solution to the cooling flow problem. Thus, I have studied a heating mechanism in the form of recurrent, hot bubbles, that have been injected in the central cluster regions over the course of cosmic time. The main point that emerged from this study is that the cooling flows can be prevented with a realistic energy budget assumed for the bubbles, consistent with the mass growth expected for the BHs from accretion. More specifically, I have found that AGN heating alters the intracluster gas properties significantly. The gas density is decreased and the entropy increased in the innermost regions. Also, the stellar properties are affected, especially of the central cluster galaxy, whose star formation rate is quenched at low redshifts, thus resulting in much older and redder stellar populations at the present day. Bubbles also induce a modification of the simulated metallicity distribution in clusters, expelling some of the metals from the dense, star-forming regions into the hot ICM, which brings the models in better agreement with observations.

In Chapter 3, I have studied the case in which the intracluster gas is assumed to be a real, viscous fluid, rather than an ideal gas. The motivation for studying this problem comes from several pieces of evidence. Neglecting magnetic fields for the moment, the viscosity of the hot intracluster plasma should be rather high, and is described by Braginskii's parameterization. However, similar to thermal conduction, magnetic fields can suppress the viscosity perpendicular to the direction of magnetic field lines. If the magnetic field is chaotically tangled, the overall strength of this suppression might be not that high in clusters, leaving of order $0.1 - 0.3$ of the viscosity/conductivity of the unmagnetized plasma. Thus, the ICM in hot galaxy clusters may in fact be quite viscous. Furthermore, the detection of ripples in X–ray luminosity maps of the Perseus cluster supports the idea that AGN-driven bubbles, while inflated by the jet, generate weak shocks and sound waves that could be efficiently dissipated if the intracluster medium is viscous, providing a non-local heating process. Thus, in order to explore this interesting possibility I have implemented a treatment for viscous fluids, considering both the Navier-Stokes and general heat transfer equations. I have performed numerical simulations of AGN heated clusters with a viscous intracluster gas that have confirmed that viscous processes provide an efficient way to dissipate AGN-injected energy in the ICM. Moreover, viscosity of the ICM suppresses fluid instabilities acting on buoyantly rising bubbles, prolonging their life-time

and permitting them to reach larger distances from the cluster centre. As a result, the simulated properties of AGN-driven bubbles in the presence of modest levels of gas viscosity are in much better agreement with observational findings than for an ideal gas. However, I should emphasize that magnetic fields might have stabilizing effects on the bubbles as well, which would provide an alternative way to obtain the required stability, with less or no viscosity. I have also performed cosmological simulations of galaxy cluster formation, including effects of shear viscosity. Based on these simulations I found that shear viscosity can boost the entropy in the cluster outskirts. Moreover, satellite galaxies infalling into massive halos are more efficiently stripped from their gaseous content, leaving behind long and narrow tails of gas, similar to features observed in several late-type galaxies.

Given the encouraging results of Chapter 2, it became clear that a self-regulated feedback scheme for AGN heating in clusters, embedded in full cosmological simulations is needed in order to perform more realistic simulations. The need for self-regulation stems from the fact that the local cooling and heating rates need to be tightly coupled, otherwise an overheating or overcooling of the system easily occurs. This motivated the development of a more sophisticated scheme for AGN feedback, which is discussed in detail in Chapter 4. Here, our AGN modelling has been improved in a number of ways: first, a prescription for BH seeding and growth has been adopted from Springel et al. [2005c], where BHs increase their mass by gas accretion or by merging with other BHs that are in a close vicinity; second, the feedback model from Springel et al. [2005c] has been extended to BHs in the radiatively inefficient regime, relating bubble energy content, radius, and duty cycle directly with the BH physics. This model is thus a synthesis of the "radio-mode" feedback studied in Chapter 2, and the "quasar-mode" feedback proposed by Springel et al. [2005c]. With a single set of parameter values, this model reproduces satisfactory results for a range of galaxy cluster masses, alleviating the cooling flow problem. Moreover, when applied to cosmological simulations of galaxy formation, the expected relationships between the BH mass and host stellar properties are reproduced. Also, the comoving BH mass density we obtain is in a good agreement with observational estimates, indicating that the simulated BH population is indeed realistic.

Finally, I would like to comment on future perspectives, highlighting in particular ways in which the modelling of BH growth and feedback could be improved. It would be extremely interesting to numerically explore alternative scenarios of BH formation and growth, considering different physical prescriptions for BH accretion, especially in light of the fact that already at very high redshifts super-massive BHs exist, as seen in the most distant SDSS quasars. If one can reproduce a population of super-massive BHs at high redshifts, it should also be possible to study in some detail the observed "downsizing scenario" of BH accretion. In particular, it would be important to analyse the BH accretion rate as a function of the BH mass and redshift, establishing why massive BHs apparently grow more efficiently at early times, while less massive BHs do so today.

Furthermore, it would be interesting to study alternative modes of BH feedback compared to the ones we considered in cosmological simulations of structure formation. For example, the importance of kinetic feedback by AGN-driven winds could be constrained by studying the metallicity enrichment of the IGM, as a function of wind properties like mass flux and speed. Also, it would be interesting to constrain the relevance of the powerful radio galaxies at high redshifts, which are often associated with proto-cluster environments.

Possibly, such a study could break the degeneracy between the duty cycle of quasars that pass trough the radio-loud phase and the actual fraction of radio galaxies.

Another interesting challenge is to produce simulations that generate AGN-driven bubbles self-consistently in a cosmological setting, by directly following their inflation by a relativistic jet. At the present this is a quite difficult problem for any numerical code, both due to the numerical limitations, and due to the complex physical processes that are involved, including MHD and relativistic hydrodynamics. But once these difficulties are overcome, such simulations could lead to a full understanding of how the bubble size depends on the jet power and gas accretion rate, and the surrounding gas properties.

Yet another unexplored frontier of AGN feedback in cosmological simulations lies in an incorporation of radiative feedback effects from luminous quasars. This would permit studies of how the properties of high redshift galaxies and proto-clusters are affected by radiation pressure effects, which constitutes another possible channel of AGN feedback. In fact, it has been suggested that this type of feedback and not thermal heating may be the primary physical mechanism for quasar feedback, and hence responsible for establishing the $M_{BH} - \sigma$ relationship at high redshifts, and in producing a red and old elliptical galaxy population.

It appears that the study of BH growth and feedback continues to be an exciting and promising field of research in astrophysics, where many challenging problems still need to be understood in depth. At the moment we have only begun to grasp their profound importance.

Acknowledgements

Special thanks go to Volker Springel, my PhD supervisor, for having passed three great years of research together. I am very glad that I had the opportunity to work on highly interesting topics, and that I could use GADGET, one of the best numerical codes currently available. Most importantly, I am grateful for his constant support, encouragement and enthusiasm that stimulated my work. Also, I appreciated a great deal of freedom in pursuing my research and that our scientific discussions always took place in a creative and positive atmosphere.

I am very grateful to Simon White, for providing critical insights into my work, that have always helped me finding the weakest points and strengthening them. I would also like to thank him for all the support during these three years, permitting me to make the first successful steps of my scientific career.

Many thanks are due to Eugene Churazov, with whom I had many interesting and enlightening discussions, which improved my work. Also, I would like to thank Andrea Merloni, Pere Mimica and Brent Groves for having enthusiastic conversations about BH physics and jets.

Finally, life at MPA would not have been the same without the help, company and friendship of many nice persons, whose very fond memories I am bearing in my heart.

Curriculum vitae

Personal data

Debora Sijacki
Born in Belgrade 01.01.1980. Nationality: Serbian.
Current address: Max-Planck-Institut für Astrophysik
Karl-Schwarzschild-Str. 1, 85748, Garching bei München, Germany
Tel.: +49 089 30000 2019
e-mail: deboras@mpa-garching.mpg.de

Education and training

1994-1998	High school "V beogradska gimnazija", Belgrade. Diploma Thesis: *Structure and Evolution of Stars and Galaxies*, final grade: 5/5.
1998-2003	University of Padova, Department of Astronomy. Courses average grade 28/30. Laurea Thesis: *Scaling Laws of Simulated Galaxy Clusters: A Systematic Study*, supervisor: Dott. G. Tormen. Laurea grade: 110/110 e lode (summa cum laude).
2004-2007	PhD studies at the Max Planck Institute for Astrophysics, Garching, supervised by Dr. Volker Springel and Prof. Dr. Simon White.

Scholarships and honours

2001-2002	Student fellowship at University of Padova.
2004-2007	"International Max-Planck Research School on Astrophysics" PhD fellowship at Ludwig-Maximilians University, Munich.
2005	"Marie Curie Host Fellowships For Early Stage Research Training (EST)".

Scientific interests

Cosmic structure formation. Galaxy clusters: hydrodynamical simulations; scaling laws; dynamical properties and merging history. Non-gravitational heating mechanisms: AGN feedback modeling in the cosmological context; viscous dissipation processes during the cosmological growth of structures.

Bibliography

S. W. Allen. The properties of cooling flows in X-ray luminous clusters of galaxies. *MNRAS*, 315:269–295, June 2000. 22

S. W. Allen. Resolving the discrepancy between X-ray and gravitational lensing mass measurements for clusters of galaxies. *MNRAS*, 296:392–406, May 1998. 16

S. W. Allen, A. C. Fabian, A. C. Edge, H. Bohringer, and D. A. White. Cooling flows, central galaxy-cluster alignments, X-ray absorption and dust. *MNRAS*, 275:741–754, August 1995. 22

S. W. Allen, A. C. Fabian, R. M. Johnstone, K. A. Arnaud, and P. E. J. Nulsen. ASCA and ROSAT observations of nearby cluster cooling flows. *MNRAS*, 322:589–613, April 2001a. 22

S. W. Allen, R. W. Schmidt, and A. C. Fabian. The X-ray virial relations for relaxed lensing clusters observed with Chandra. *MNRAS*, 328:L37–L41, December 2001b. 23

S. W. Allen, R. J. H. Dunn, A. C. Fabian, G. B. Taylor, and C. S. Reynolds. The relation between accretion rate and jet power in X-ray luminous elliptical galaxies. *MNRAS*, 372:21–30, October 2006. doi: 10.1111/j.1365-2966.2006.10778.x. 110

L. Bîrzan, D. A. Rafferty, B. R. McNamara, M. W. Wise, and P. E. J. Nulsen. A Systematic Study of Radio-induced X-Ray Cavities in Clusters, Groups, and Galaxies. *ApJ*, 607: 800–809, June 2004. 26, 27, 38, 58, 64, 95, 99

H. Böhringer, K. Matsushita, E. Churazov, Y. Ikebe, and Y. Chen. The new emerging model for the structure of cooling cores in clusters of galaxies. *A&A*, 382:804–820, February 2002. doi: 10.1051/0004-6361:20011708. 18, 22, 48, 58

H. Böhringer, K. Matsushita, E. Churazov, A. Finoguenov, and Y. Ikebe. Implications of the central metal abundance peak in cooling core clusters of galaxies. *A&A*, 416: L21–L25, March 2004. 34, 48

A. Babul, M. L. Balogh, G. F. Lewis, and G. B. Poole. Physical implications of the X-ray properties of galaxy groups and clusters. *MNRAS*, 330:329–343, February 2002. 22

N. A. Bahcall, X. Fan, and R. Cen. Constraining Omega with Cluster Evolution. *ApJ*, 485:L53+, August 1997. doi: 10.1086/310814. 16

M. L. Balogh, F. R. Pearce, R. G. Bower, and S. T. Kay. Revisiting the cosmic cooling crisis. *MNRAS*, 326:1228–1234, October 2001. 22, 58

D. S. Balsara. von Neumann stability analysis of smooth particle hydrodynamics–suggestions for optimal algorithms. *Journal of Computational Physics*, 121:357–372, 1995. 68

A. J. Barger, L. L. Cowie, R. F. Mushotzky, Y. Yang, W.-H. Wang, A. T. Steffen, and P. Capak. The Cosmic Evolution of Hard X-Ray-selected Active Galactic Nuclei. *AJ*, 129:578–609, February 2005. doi: 10.1086/426915. 110

J. Barnes and P. Hut. A Hierarchical O(NlogN) Force-Calculation Algorithm. *Nature*, 324: 446–449, December 1986. 14

J. E. Barnes and L. Hernquist. Dynamics of interacting galaxies. *ARA&A*, 30:705–742, 1992. doi: 10.1146/annurev.aa.30.090192.003421. 94

F. E. Bauer, A. C. Fabian, J. S. Sanders, S. W. Allen, and R. M. Johnstone. The prevalence of cooling cores in clusters of galaxies at z˜ 0.15-0.4. *MNRAS*, 359:1481–1490, June 2005. doi: 10.1111/j.1365-2966.2005.08999.x. 115, 128

M. C. Begelman and D. F. Cioffi. Overpressured cocoons in extragalactic radio sources. *ApJ*, 345:L21–L24, October 1989. doi: 10.1086/185542. 100

E. F. Bell, C. Wolf, K. Meisenheimer, H.-W. Rix, A. Borch, S. Dye, M. Kleinheinrich, L. Wisotzki, and D. H. McIntosh. Nearly 5000 Distant Early-Type Galaxies in COMBO-17: A Red Sequence and Its Evolution since z˜1. *ApJ*, 608:752–767, June 2004. doi: 10.1086/420778. 126

J. Binney and G. Tabor. Evolving Cooling Flows. *MNRAS*, 276:663–+, September 1995. 18, 95

R. D. Blandford and M. C. Begelman. On the fate of gas accreting at a low rate on to a black hole. *MNRAS*, 303:L1–L5, February 1999. 95

R. D. Blandford and M. J. Rees. Extended and compact extragalactic radio sources - Interpretation and theory. *Phys. Scr*, 17:265–274, March 1978. 18

E. L. Blanton, C. L. Sarazin, B. R. McNamara, and M. W. Wise. Chandra Observation of the Radio Source/X-Ray Gas Interaction in the Cooling Flow Cluster Abell 2052. *ApJ*, 558:L15–L18, September 2001. 15, 23, 58

H. Bondi. On spherically symmetrical accretion. *MNRAS*, 112:195–+, 1952. 97

H. Bondi and F. Hoyle. On the mechanism of accretion by stars. *MNRAS*, 104:273–+, 1944. 97

S. Borgani, F. Governato, J. Wadsley, N. Menci, P. Tozzi, G. Lake, T. Quinn, and J. Stadel. Preheating the Intracluster Medium in High-Resolution Simulations: The Effect on the Gas Entropy. *ApJ*, 559:L71–L74, October 2001. 22

S. Borgani, G. Murante, V. Springel, A. Diaferio, K. Dolag, L. Moscardini, G. Tormen, L. Tornatore, and P. Tozzi. X-ray properties of galaxy clusters and groups from a cosmological hydrodynamical simulation. *MNRAS*, 348:1078–1096, March 2004. 22, 23

R. G. Bower. The Entropy-Driven X-ray Evolution of Galaxy Clusters. *MNRAS*, 288: 355–364, June 1997. 22

M. Brüggen. Simulations of Buoyant Bubbles in Galaxy Clusters. *ApJ*, 592:839–845, August 2003. 23, 52

M. Brüggen and C. R. Kaiser. Hot bubbles from active galactic nuclei as a heat source in cooling-flow clusters. *Nature*, 418:301–303, July 2002. 23

M. Brüggen, C. R. Kaiser, E. Churazov, and T. A. Enßlin. Simulation of radio plasma in clusters of galaxies. *MNRAS*, 331:545–555, April 2002. 23

S. I. Braginskii. Transport Phenomena in a Completely Ionized Two-Temperature Plasma. *JETP*, 1958. 33, 459. 59, 63

S. I. Braginskii. Transport Processes in a Plasma. *Reviews of Plasma Physics*, 1965. Vol I, 205. 59, 63

M. Brüggen, M. Ruszkowski, and E. Hallman. Active Galactic Nuclei Heating and Dissipative Processes in Galaxy Clusters. *ApJ*, 630:740–749, September 2005. doi: 10.1086/432112. 32, 38

G. Bruzual and S. Charlot. Stellar population synthesis at the resolution of 2003. *MNRAS*, 344:1000–1028, October 2003. 46, 118

N. Cappelluti, M. Cappi, M. Dadina, G. Malaguti, M. Branchesi, V. D'Elia, and G. G. C. Palumbo. X-ray source overdensities in Chandra distant cluster fields: A new probe to map the cosmic tapestry? *A&A*, 430:39–45, January 2005. doi: 10.1051/0004-6361: 20041534. 112

M. Cappi, P. Mazzotta, M. Elvis, D. J. Burke, A. Comastri, F. Fiore, W. Forman, A. Fruscione, P. Green, D. Harris, E. J. Hooper, C. Jones, J. S. Kaastra, E. Kellogg, S. Murray, B. McNamara, F. Nicastro, T. J. Ponman, E. M. Schlegel, A. Siemiginowska, H. Tananbaum, A. Vikhlinin, S. Virani, and B. Wilkes. Chandra Study of an Overdensity of X-Ray Sources around Two Distant (Z˜0.5) Clusters. *ApJ*, 548:624–638, February 2001. doi: 10.1086/318998. 112

C. L. Carilli and G. B. Taylor. Cluster Magnetic Fields. *ARA&A*, 40:319–348, 2002. doi: 10.1146/annurev.astro.40.060401.093852. 59

G. Chartas, W. N. Brandt, and S. C. Gallagher. XMM-Newton Reveals the Quasar Outflow in PG 1115+080. *ApJ*, 595:85–93, September 2003. doi: 10.1086/377299. 94

E. Churazov, M. Brüggen, C. R. Kaiser, H. Böhringer, and W. Forman. Evolution of Buoyant Bubbles in M87. *ApJ*, 554:261–273, June 2001. doi: 10.1086/321357. 18, 23, 25, 52, 64, 95

E. Churazov, R. Sunyaev, W. Forman, and H. Böhringer. Cooling flows as a calorimeter of active galactic nucleus mechanical power. *MNRAS*, 332:729–734, May 2002. doi: 10.1046/j.1365-8711.2002.05332.x. 18, 23, 81, 91, 95

E. Churazov, S. Sazonov, R. Sunyaev, W. Forman, C. Jones, and H. Böhringer. Supermassive black holes in elliptical galaxies: switching from very bright to very dim. *MNRAS*, 363:L91–L95, October 2005. doi: 10.1111/j.1745-3933.2005.00093.x. 27, 95, 98

T. E. Clarke. Faraday Rotation Observations of Magnetic Fields in Galaxy Clusters. *Journal of Korean Astronomical Society*, 37:337–342, December 2004. 59

T. E. Clarke, P. P. Kronberg, and H. Böhringer. A New Radio-X-Ray Probe of Galaxy Cluster Magnetic Fields. *ApJ*, 547:L111–L114, February 2001. doi: 10.1086/318896. 59

T. E. Clarke, C. L. Sarazin, E. L. Blanton, D. M. Neumann, and N. E. Kassim. Low-Frequency Radio Observations of X-Ray Ghost Bubbles in A2597: A History of Radio Activity in the Core. *ApJ*, 625:748–753, June 2005. doi: 10.1086/429717. 59

P. W. Cleary. Modeling confined multi-material heat and mass flows using SPH. *Applied Mathematical Modeling*, 1998. 22, 981. 68

P. W. Cleary, J. Ha, V. Alguine, and T. Nguyen. Flow modeling in casting processes. *Applied Mathematical Modeling*, 2002. 26, 171. 68

P. Coles and F. Lucchin. *Cosmology. The origin and evolution of cosmic structure*. Chichester: Wiley, —c1995, 1995. 7

H. M. P. Couchman. Mesh-refined P3M - A fast adaptive N-body algorithm. *ApJ*, 368: L23–L26, February 1991. doi: 10.1086/185939. 14

R. Courant and K. O. Friedrichs. *Supersonic Flow and Shock Waves*. Springer-Verlag New York, 1976. 73

L. L. Cowie and J. Binney. Radiative regulation of gas flow within clusters of galaxies - A model for cluster X-ray sources. *ApJ*, 215:723–732, August 1977. 22

L. L. Cowie and A. Songaila. Heavy-element enrichment in low-density regions of the intergalactic medium. *Nature*, 394:44–46, July 1998. doi: 10.1038/27845. 122

L. L. Cowie, A. J. Barger, M. W. Bautz, W. N. Brandt, and G. P. Garmire. The Redshift Evolution of the 2-8 keV X-Ray Luminosity Function. *ApJ*, 584:L57–L60, February 2003. doi: 10.1086/368404. 121, 128

T. J. Cox, T. Di Matteo, L. Hernquist, P. F. Hopkins, B. Robertson, and V. Springel. X-Ray Emission from Hot Gas in Galaxy Mergers. *ApJ*, 643:692–706, June 2006a. doi: 10.1086/503284. 95

T. J. Cox, S. N. Dutta, T. Di Matteo, L. Hernquist, P. F. Hopkins, B. Robertson, and V. Springel. The Kinematic Structure of Merger Remnants. *ApJ*, 650:791–811, October 2006b. doi: 10.1086/507474. 95

D. M. Crenshaw, S. B. Kraemer, and I. M. George. Mass Loss from the Nuclei of Active Galaxies. *ARA&A*, 41:117–167, 2003. doi: 10.1146/annurev.astro.41.082801.100328. 94

J. H. Croston, M. J. Hardcastle, and M. Birkinshaw. Evidence for radio-source heating of groups. *MNRAS*, 357:279–294, February 2005. doi: 10.1111/j.1365-2966.2005.08665.x. 52

D. J. Croton, V. Springel, S. D. M. White, G. De Lucia, C. S. Frenk, L. Gao, A. Jenkins, G. Kauffmann, J. F. Navarro, and N. Yoshida. The many lives of active galactic nuclei: cooling flows, black holes and the luminosities and colours of galaxies. *MNRAS*, 365: 11–28, January 2006. doi: 10.1111/j.1365-2966.2005.09675.x. 24, 27, 54, 95, 98

C. Dalla Vecchia, R. G. Bower, T. Theuns, M. L. Balogh, P. Mazzotta, and C. S. Frenk. Quenching cluster cooling flows with recurrent hot plasma bubbles. *MNRAS*, 355:995–1004, December 2004. doi: 10.1111/j.1365-2966.2004.08381.x. 23, 25, 52, 64, 95

S. De Grandi and S. Molendi. Metallicity Gradients in X-Ray Clusters of Galaxies. *ApJ*, 551:153–159, April 2001. doi: 10.1086/320098. 117

S. De Grandi and S. Molendi. Temperature Profiles of Nearby Clusters of Galaxies. *ApJ*, 567:163–177, March 2002. 23, 112, 128

S. De Grandi, S. Ettori, M. Longhetti, and S. Molendi. On the iron content in rich nearby clusters of galaxies. *A&A*, 419:7–18, May 2004. doi: 10.1051/0004-6361:20034228. 48

T. Di Matteo, R. A. C. Croft, V. Springel, and L. Hernquist. Black Hole Growth and Activity in a Λ Cold Dark Matter Universe. *ApJ*, 593:56–68, August 2003. 26, 29

T. Di Matteo, V. Springel, and L. Hernquist. Energy input from quasars regulates the growth and activity of black holes and their host galaxies. *Nature*, 433:604–607, February 2005a. 55

T. Di Matteo, V. Springel, and L. Hernquist. Energy input from quasars regulates the growth and activity of black holes and their host galaxies. *Nature*, 433:604–607, February 2005b. doi: 10.1038/nature03335. 20, 94, 95, 97, 98

K. Dolag. Next Generation of Galaxy Cluster Simulations. In *The Riddle of Cooling Flows in Galaxies and Clusters of galaxies*, 2004. 40, 81, 107

K. Dolag, M. Bartelmann, and H. Lesch. Evolution and structure of magnetic fields in simulated galaxy clusters. *A&A*, 387:383–395, May 2002. doi: 10.1051/0004-6361: 20020241. 64

K. Dolag, M. Jubelgas, V. Springel, S. Borgani, and E. Rasia. Thermal Conduction in Simulated Galaxy Clusters. *ApJ*, 606:L97–L100, May 2004. doi: 10.1086/420966. 23, 62, 85

M. Donahue, G. M. Voit, C. P. O'Dea, S. A. Baum, and W. B. Sparks. Two Clusters of Galaxies with Radio-quiet Cooling Cores. *ApJ*, 630:L13–L16, September 2005. doi: 10.1086/462416. 27

R. J. H. Dunn and A. C. Fabian. Investigating AGN heating in a sample of nearby clusters. *MNRAS*, 373:959–971, December 2006. doi: 10.1111/j.1365-2966.2006.11080.x. 99, 112, 128

R. J. H. Dunn, A. C. Fabian, and G. B. Taylor. Radio bubbles in clusters of galaxies. *MNRAS*, 364:1343–1353, December 2005. doi: 10.1111/j.1365-2966.2005.09673.x. 59

A. C. Edge. The detection of molecular gas in the central galaxies of cooling flow clusters. *MNRAS*, 328:762–782, December 2001. 18, 22, 58

A. C. Edge and D. T. Frayer. Resolving Molecular gas in the Central Galaxies of Cooling Flow Clusters. *ApJ*, 594:L13–L17, September 2003. 22

A. C. Edge, R. J. Wilman, R. M. Johnstone, C. S. Crawford, A. C. Fabian, and S. W. Allen. A survey of molecular hydrogen in the central galaxies of cooling flows. *MNRAS*, 337:49–62, November 2002. 18, 22, 58

G. Efstathiou, M. Davis, S. D. M. White, and C. S. Frenk. Numerical techniques for large cosmological N-body simulations. *ApJS*, 57:241–260, February 1985. doi: 10.1086/191003. 14

J. A. Eilek and F. N. Owen. Magnetic Fields in Cluster Cores: Faraday Rotation in A400 and A2634. *ApJ*, 567:202–220, March 2002. doi: 10.1086/338376. 59

D. J. Eisenstein and W. Hu. Power Spectra for Cold Dark Matter and Its Variants. *ApJ*, 511:5–15, January 1999. doi: 10.1086/306640. 119

S. L. Ellison, A. Songaila, J. Schaye, and M. Pettini. The Enrichment History of the Intergalactic Medium-Measuring the C IV/H I Ratio in the Lyα Forest. *AJ*, 120:1175–1191, September 2000. doi: 10.1086/301511. 122

T. A. Ensslin and C. Vogt. Magnetic turbulence in cool cores of galaxy clusters. *ArXiv Astrophysics e-prints*, May 2005. astro-ph/0505517. 31

A. C. Fabian. Cooling Flows in Clusters of Galaxies. *ARA&A*, 32:277–318, 1994. 17, 22

A. C. Fabian and K. Iwasawa. The mass density in black holes inferred from the X-ray background. *MNRAS*, 303:L34–L36, February 1999. 94, 121, 128

A. C. Fabian and P. E. J. Nulsen. Subsonic accretion of cooling gas in clusters of galaxies. *MNRAS*, 180:479–484, August 1977. 22

A. C. Fabian, P. E. J. Nulsen, and C. R. Canizares. Cooling flows in clusters of galaxies. *Nature*, 310:733–740, August 1984. 22

A. C. Fabian, J. S. Sanders, S. Ettori, G. B. Taylor, S. W. Allen, C. S. Crawford, K. Iwasawa, R. M. Johnstone, and P. M. Ogle. Chandra imaging of the complex X-ray core of the Perseus cluster. *MNRAS*, 318:L65–L68, November 2000. 38

A. C. Fabian, R. F. Mushotzky, P. E. J. Nulsen, and J. R. Peterson. On the soft X-ray spectrum of cooling flows. *MNRAS*, 321:L20–L24, February 2001. 22

A. C. Fabian, J. S. Sanders, S. W. Allen, C. S. Crawford, K. Iwasawa, R. M. Johnstone, R. W. Schmidt, and G. B. Taylor. A deep Chandra observation of the Perseus cluster: shocks and ripples. *MNRAS*, 344:L43–L47, September 2003a. doi: 10.1046/j.1365-8711.2003.06902.x. 34, 58

A. C. Fabian, J. S. Sanders, C. S. Crawford, C. J. Conselice, J. S. Gallagher, and R. F. G. Wyse. The relationship between the optical Hα filaments and the X-ray emission in the core of the Perseus cluster. *MNRAS*, 344:L48–L52, September 2003b. 31

A. C. Fabian, J. S. Sanders, G. B. Taylor, S. W. Allen, C. S. Crawford, R. M. Johnstone, and K. Iwasawa. A very deep Chandra observation of the Perseus cluster: shocks, ripples and conduction. *MNRAS*, 366:417–428, February 2006. doi: 10.1111/j.1365-2966.2005.09896.x. 18, 19, 58, 64, 77, 91, 95, 99

X. Fan, V. K. Narayanan, R. H. Lupton, M. A. Strauss, G. R. Knapp, R. H. Becker, R. L. White, L. Pentericci, S. K. Leggett, Z. Haiman, J. E. Gunn, Ž. Ivezić, D. P. Schneider, S. F. Anderson, J. Brinkmann, N. A. Bahcall, A. J. Connolly, I. Csabai, M. Doi, M. Fukugita, T. Geballe, E. K. Grebel, D. Harbeck, G. Hennessy, D. Q. Lamb, G. Miknaitis, J. A. Munn, R. Nichol, S. Okamura, J. R. Pier, F. Prada, G. T. Richards, A. Szalay, and D. G. York. A Survey of $z > 5.8$ Quasars in the Sloan Digital Sky Survey. I. Discovery of Three New Quasars and the Spatial Density of Luminous Quasars at $z \sim 6$. *AJ*, 122:2833–2849, December 2001. doi: 10.1086/324111. 95, 111

R. Fender, S. Corbel, T. Tzioumis, V. McIntyre, D. Campbell-Wilson, M. Nowak, R. Sood, R. Hunstead, A. Harmon, P. Durouchoux, and W. Heindl. Quenching of the Radio Jet during the X-Ray High State of GX 339-4. *ApJ*, 519:L165–L168, July 1999. doi: 10.1086/312128. 95, 98

L. Ferrarese and H. Ford. Supermassive Black Holes in Galactic Nuclei: Past, Present and Future Research. *Space Science Reviews*, 116:523–624, February 2005. doi: 10.1007/s11214-005-3947-6. 54

L. Ferrarese and D. Merritt. A Fundamental Relation between Supermassive Black Holes and Their Host Galaxies. *ApJ*, 539:L9–L12, August 2000. doi: 10.1086/312838. 15, 94

O. Flebbe, S. Muenzel, H. Herold, H. Riffert, and H. Ruder. Smoothed Particle Hydrodynamics: Physical viscosity and the simulation of accretion disks. *ApJ*, 431:754–760, August 1994. doi: 10.1086/174526. 65, 89

W. Forman, E. Churazov, C. Jones, M. Markevitch, P. Nulsen, A. Vikhlinin, M. Begelman, H. Bohringer, J. Eilek, S. Heinz, R. Kraft, and F. Owen. Filaments, Bubbles, and Weak Shocks in the Gaseous Atmosphere of M87. *ArXiv Astrophysics e-prints*, April 2006. 18, 95, 99

J. Frank, A. King, and D. Raine. *Accretion power in Astrophysics*. Cambridge University Press, 1985. Cambridge. 63

E. Gallo, R. P. Fender, and G. G. Pooley. A universal radio-X-ray correlation in low/hard state black hole binaries. *MNRAS*, 344:60–72, September 2003. doi: 10.1046/j.1365-8711.2003.06791.x. 95, 98

A. Gardini, E. Rasia, P. Mazzotta, G. Tormen, S. De Grandi, and L. Moscardini. Simulating Chandra observations of galaxy clusters. *MNRAS*, 351:505–514, June 2004. 38

K. Gebhardt, R. Bender, G. Bower, A. Dressler, S. M. Faber, A. V. Filippenko, R. Green, C. Grillmair, L. C. Ho, J. Kormendy, T. R. Lauer, J. Magorrian, J. Pinkney, D. Richstone, and S. Tremaine. A Relationship between Nuclear Black Hole Mass and Galaxy Velocity Dispersion. *ApJ*, 539:L13–L16, August 2000. doi: 10.1086/312840. 15, 94

R. A. Gingold and J. J. Monaghan. Smoothed particle hydrodynamics - Theory and application to non-spherical stars. *MNRAS*, 181:375–389, November 1977. 14, 65

F. Govoni and L. Feretti. Magnetic Fields in Clusters of Galaxies. *International Journal of Modern Physics D*, 13:1549–1594, 2004. doi: 10.1142/S0218271804005080. 59

S. F. Gull and K. J. E. Northover. Bubble Model of Extragalactic Radio Sources. *Nature*, 244:80–+, 1973. 18

N. Häring and H.-W. Rix. On the Black Hole Mass-Bulge Mass Relation. *ApJ*, 604: L89–L92, April 2004. doi: 10.1086/383567. 122, 124

G. Hasinger, T. Miyaji, and M. Schmidt. Luminosity-dependent evolution of soft X-ray selected AGN. New Chandra and XMM-Newton surveys. *A&A*, 441:417–434, October 2005. doi: 10.1051/0004-6361:20042134. 110

T. M. Heckman, L. Armus, and G. K. Miley. Evidence for large-scale winds from starburst galaxies. II - an optical investigation of powerful far-infrared galaxies. *AJ*, 93:276–283, February 1987. doi: 10.1086/114310. 15

T. M. Heckman, G. Kauffmann, J. Brinchmann, S. Charlot, C. Tremonti, and S. D. M. White. Present-Day Growth of Black Holes and Bulges: The Sloan Digital Sky Survey Perspective. *ApJ*, 613:109–118, September 2004. doi: 10.1086/422872. 110, 121

S. Heinz, C. S. Reynolds, and M. C. Begelman. X-Ray Signatures of Evolving Radio Galaxies. *ApJ*, 501:126–+, July 1998. doi: 10.1086/305807. 100

S. Heinz, A. Merloni, T. Di Matteo, and R. Sunyaev. On the Relationship Between the Jets from X-Ray Binaries and Agn. *Ap&SS*, 300:15–21, November 2005. doi: 10.1007/s10509-005-1200-0. 96, 98

M. Hoeft and M. Brüggen. Feedback in Active Galactic Nucleus Heating of Galaxy Clusters. *ApJ*, 617:896–902, December 2004. 23, 52, 64

P. F. Hopkins, L. Hernquist, T. J. Cox, T. Di Matteo, B. Robertson, and V. Springel. A Unified, Merger-driven Model of the Origin of Starbursts, Quasars, the Cosmic X-Ray Background, Supermassive Black Holes, and Galaxy Spheroids. *ApJS*, 163:1–49, March 2006. doi: 10.1086/499298. 95

F. Hoyle and R. A. Lyttleton. The effect of interstellar matter on climatic variation. In *Proceedings of the Cambridge Philisophical Society*, pages 405–+, 1939. 97

A. Jenkins, C. S. Frenk, S. D. M. White, J. M. Colberg, S. Cole, A. E. Evrard, H. M. P. Couchman, and N. Yoshida. The mass function of dark matter haloes. *MNRAS*, 321: 372–384, February 2001. 40, 81, 107

R. M. Johnstone, A. C. Fabian, and P. E. J. Nulsen. The optical spectra of central galaxies in southern clusters Evidence for star formation. *MNRAS*, 224:75–91, January 1987. 22

M. Jubelgas, V. Springel, and K. Dolag. Thermal conduction in cosmological SPH simulations. *MNRAS*, 351:423–435, June 2004. doi: 10.1111/j.1365-2966.2004.07801.x. 23, 62, 85

J. S. Kaastra, C. Ferrigno, T. Tamura, F. B. S. Paerels, J. R. Peterson, and J. P. D. Mittaz. XMM-Newton observations of the cluster of galaxies Sérsic 159-03. *A&A*, 365: L99–L103, January 2001. 22

C. R. Kaiser, G. Pavlovski, E. C. D. Pope, and H. Fangohr. The stability of buoyant bubbles in the atmospheres of galaxy clusters. *MNRAS*, 359:493–503, May 2005. doi: 10.1111/j.1365-2966.2005.08902.x. 59, 91

N. Kaiser. Evolution and clustering of rich clusters. *MNRAS*, 222:323–345, September 1986. 22

N. Kaiser. Evolution of clusters of galaxies. *ApJ*, 383:104–111, December 1991. 22

N. Katz, D. H. Weinberg, and L. Hernquist. Cosmological Simulations with TreeSPH. *ApJS*, 105:19–+, July 1996. doi: 10.1086/192305. 24, 64, 96

G. Kauffmann and M. Haehnelt. A unified model for the evolution of galaxies and quasars. *MNRAS*, 311:576–588, January 2000. 95

G. Kauffmann, J. M. Colberg, A. Diaferio, and S. D. M. White. Clustering of galaxies in a hierarchical universe - I. Methods and results at z=0. *MNRAS*, 303:188–206, February 1999. 40

A. King. Black Holes, Galaxy Formation, and the M_{BH}-σ Relation. *ApJ*, 596:L27–L29, October 2003. doi: 10.1086/379143. 94

A. A. Klypin and S. F. Shandarin. Three-dimensional numerical model of the formation of large-scale structure in the Universe. *MNRAS*, 204:891–907, September 1983. 14

E. G. Körding, S. Jester, and R. Fender. Accretion states and radio loudness in active galactic nuclei: analogies with X-ray binaries. *MNRAS*, 372:1366–1378, November 2006. doi: 10.1111/j.1365-2966.2006.10954.x. 96

J. Kormendy and D. Richstone. Inward Bound—The Search For Supermassive Black Holes In Galactic Nuclei. *ARA&A*, 33:581–+, 1995. doi: 10.1146/annurev.aa.33.090195.003053. 15, 94

L. D. Landau and E. M. Lifshitz. *Fluid Mechanics, Course of Theoretical Physics, Volume 6, 2nd edition*. Elsevier Butterworth-Heinemann, Oxford, 1987. 61, 71, 80, 81

L. D. Landau and E. M. Lifshitz. *Physical Kinetics, Course of Theoretical Physics, Volume 10*. Elsevier Butterworth-Heinemann, Oxford, 1981. 62, 63

S. M. Lea, J. Silk, E. Kellogg, and S. Murray. Thermal-Bremsstrahlung Interpretation of Cluster X-Ray Sources. *ApJ*, 184:L105+, September 1973. 18

G. F. Lewis, A. Babul, N. Katz, T. Quinn, L. Hernquist, and D. H. Weinberg. The Effects of Gasdynamics, Cooling, Star Formation, and Numerical Resolution in Simulations of Cluster Formation. *ApJ*, 536:623–644, June 2000. 22

Y. Li, L. Hernquist, B. Robertson, T. J. Cox, P. F. Hopkins, V. Springel, L. Gao, T. Di Matteo, A. R. Zentner, A. Jenkins, and N. Yoshida. Formation of $z \sim 6$ quasars from hierarchical galaxy mergers. *ArXiv Astrophysics e-prints*, August 2006. 95, 111

L. B. Lucy. A numerical approach to the testing of the fission hypothesis. *AJ*, 82:1013–1024, December 1977. 14, 65

T. J. Maccarone, E. Gallo, and R. Fender. The connection between radio-quiet active galactic nuclei and the high/soft state of X-ray binaries. *MNRAS*, 345:L19–L24, October 2003. doi: 10.1046/j.1365-8711.2003.07161.x. 96

J. Magorrian, S. Tremaine, D. Richstone, R. Bender, G. Bower, A. Dressler, S. M. Faber, K. Gebhardt, R. Green, C. Grillmair, J. Kormendy, and T. Lauer. The Demography of Massive Dark Objects in Galaxy Centers. *AJ*, 115:2285–2305, June 1998. doi: 10.1086/300353. 15, 94

A. Marconi and L. K. Hunt. The Relation between Black Hole Mass, Bulge Mass, and Near-Infrared Luminosity. *ApJ*, 589:L21–L24, May 2003. doi: 10.1086/375804. 15, 94

M. Markevitch, A. Vikhlinin, and P. Mazzotta. Nonhydrostatic Gas in the Core of the Relaxed Galaxy Cluster A1795. *ApJ*, 562:L153–L156, December 2001. 38

P. Martini, D. D. Kelson, E. Kim, J. S. Mulchaey, and A. A. Athey. Spectroscopic Confirmation of a Large Population of Active Galactic Nuclei in Clusters of Galaxies. *ApJ*, 644:116–132, June 2006. doi: 10.1086/503521. 112

P. Mazzotta, J. S. Kaastra, F. B. Paerels, C. Ferrigno, S. Colafrancesco, R. Mewe, and W. R. Forman. Evidence for a Heated Gas Bubble inside the "Cooling Flow" Region of MKW 3s. *ApJ*, 567:L37–L40, March 2002. 38, 58

I. G. McCarthy, M. L. Balogh, A. Babul, G. B. Poole, and D. J. Horner. Models of the ICM with heating and cooling: explaining the global and structural X-ray properties of clusters. *ApJ*, 2004. accepted (preprint astro-ph/0406329). 23

P. J. McCarthy, W. van Breugel, and T. Heckman. Evidence for large-scale winds from starburst galaxies. I - The nature of the ionized gas in M82 and NGC 253. *AJ*, 93:264–275, February 1987. doi: 10.1086/114309. 15

J. C. McKinney. General relativistic magnetohydrodynamic simulations of the jet formation and large-scale propagation from black hole accretion systems. *MNRAS*, 368:1561–1582, June 2006. doi: 10.1111/j.1365-2966.2006.10256.x. 94

B. R. McNamara, M. Wise, P. E. J. Nulsen, L. P. David, C. L. Sarazin, M. Bautz, M. Markevitch, A. Vikhlinin, W. R. Forman, C. Jones, and D. E. Harris. Chandra X-Ray Observations of the Hydra A Cluster: An Interaction between the Radio Source and the X-Ray-emitting Gas. *ApJ*, 534:L135–L138, May 2000. 18, 22, 38, 58

B. R. McNamara, P. E. J. Nulsen, M. W. Wise, D. A. Rafferty, C. Carilli, C. L. Sarazin, and E. L. Blanton. The heating of gas in a galaxy cluster by X-ray cavities and large-scale shock fronts. *Nature*, 433:45–47, January 2005. doi: 10.1038/nature03202. 26, 27, 34, 52, 58, 64, 95, 99

A. Merloni and S. Heinz. Cosmological evolution of the AGN Kinetic Luminosity Function. *ArXiv Astrophysics e-prints*, November 2006. 95

D. Merritt and L. Ferrarese. Black hole demographics from the M_{BH}-σ relation. *MNRAS*, 320:L30–L34, January 2001. 121, 128

J. J. Monaghan. Smoothed particle hydrodynamics. *ARA&A*, 30:543–574, 1992. doi: 10.1146/annurev.aa.30.090192.002551. 65

J. J. Monaghan. SPH and Riemann Solvers. *J. Comp. Phys*, 136:298–307, 1997. 68

J. J. Monaghan and R. A. Gingold. Shock simulation by the particle method SPH. *J. Comp. Phys*, 52:374–389, 1983. 68

J. J. Monaghan and J. C. Lattanzio. A refined particle method for astrophysical problems. *A&A*, 149:135–143, August 1985. 65

O. Muanwong, P. A. Thomas, S. T. Kay, F. R. Pearce, and H. M. P. Couchman. The Effect of Radiative Cooling on Scaling Laws of X-Ray Groups and Clusters. *ApJ*, 552: L27–L30, May 2001. 22

R. Narayan and M. V. Medvedev. Thermal Conduction in Clusters of Galaxies. *ApJ*, 562: L129–L132, December 2001. doi: 10.1086/338325. 23, 62

R. Narayan and I. Yi. Advection-dominated accretion: A self-similar solution. *ApJ*, 428: L13–L16, June 1994. doi: 10.1086/187381. 95

J. F. Navarro, C. S. Frenk, and S. D. M. White. Simulations of X-ray clusters. *MNRAS*, 275:720–740, August 1995. 22

J. F. Navarro, C. S. Frenk, and S. D. M. White. The Structure of Cold Dark Matter Halos. *ApJ*, 462:563–+, May 1996. doi: 10.1086/177173. 27, 76, 100

J. F. Navarro, C. S. Frenk, and S. D. M. White. A Universal Density Profile from Hierarchical Clustering. *ApJ*, 490:493–+, December 1997. doi: 10.1086/304888. 27, 76, 100

M. L. Norman and G. L. Bryan. Cosmological Adaptive Mesh Refinement. In S. M. Miyama, K. Tomisaka, and T. Hanawa, editors, *ASSL Vol. 240: Numerical Astrophysics*, pages 19–+, 1999. 14

P. E. Nulsen, B. R. McNamara, L. P. David, and M. Wise. X-Ray Cavities and Cooling Flows. *The Cosmic Cauldron, 25th meeting of the IAU, Joint Discussion 10, 18 July 2003, Sydney, Australia*, 10, 2003. 23

P. E. J. Nulsen, D. C. Hambrick, B. R. McNamara, D. Rafferty, L. Birzan, M. W. Wise, and L. P. David. The Powerful Outburst in Hercules A. *ApJ*, 625:L9–L12, May 2005a. doi: 10.1086/430945. 58, 64

P. E. J. Nulsen, B. R. McNamara, M. W. Wise, and L. P. David. The Cluster-Scale AGN Outburst in Hydra A. *ApJ*, 628:629–636, August 2005b. doi: 10.1086/430845. 27, 34, 52

R. W. O'Connell and B. R. McNamara. The Fate of Matter in Cooling Flows. *AJ*, 98: 180–+, July 1989. 22

S. P. Oh and A. J. Benson. Entropy injection as a global feedback mechanism. *MNRAS*, 342:664–672, June 2003. 22

H. Omma and J. Binney. Structural stability of cooling flows. *MNRAS*, 350:L13–L16, May 2004. doi: 10.1111/j.1365-2966.2004.07809.x. 102

F. N. Owen, J. A. Eilek, and N. E. Kassim. M87 at 90 Centimeters: A Different Picture. *ApJ*, 543:611–619, November 2000. doi: 10.1086/317151. 15, 19, 23, 59

T. Padmanabhan. *Structure Formation in the Universe*. Structure Formation in the Universe, by T. Padmanabhan, pp. 499. ISBN 0521424860. Cambridge, UK: Cambridge University Press, June 1993., June 1993. 7

J. A. Peacock. *Cosmological Physics*. Cosmological Physics, by John A. Peacock, pp. 704. ISBN 052141072X. Cambridge, UK: Cambridge University Press, January 1999., January 1999. 7

P. J. E. Peebles. *The large-scale structure of the universe*. Research supported by the National Science Foundation. Princeton, N.J., Princeton University Press, 1980. 435 p., 1980. 7

P. J. E. Peebles. *Principles of physical cosmology*. Princeton Series in Physics, Princeton, NJ: Princeton University Press, —c1993, 1993. 7

J. R. Peterson, F. B. S. Paerels, J. S. Kaastra, M. Arnaud, T. H. Reiprich, A. C. Fabian, R. F. Mushotzky, J. G. Jernigan, and I. Sakelliou. X-ray imaging-spectroscopy of Abell 1835. *A&A*, 365:L104–L109, January 2001. 22, 58

J. R. Peterson, S. M. Kahn, F. B. S. Paerels, J. S. Kaastra, T. Tamura, J. A. M. Bleeker, C. Ferrigno, and J. G. Jernigan. High-Resolution X-Ray Spectroscopic Constraints on Cooling-Flow Models for Clusters of Galaxies. *ApJ*, 590:207–224, June 2003. 22, 58

T. J. Ponman, A. J. R. Sanderson, and A. Finoguenov. The Birmingham-CfA cluster scaling project - III. Entropy and similarity in galaxy systems. *MNRAS*, 343:331–342, July 2003. doi: 10.1046/j.1365-8711.2003.06677.x. 115, 128

K. A. Pounds, J. N. Reeves, A. R. King, K. L. Page, P. T. O'Brien, and M. J. L. Turner. A high-velocity ionized outflow and XUV photosphere in the narrow emission line quasar PG1211+143. *MNRAS*, 345:705–713, November 2003. doi: 10.1046/j.1365-8711.2003.07006.x. 94

G. W. Pratt and M. Arnaud. Entropy scaling in galaxy clusters: Insights from an XMM-Newton observation of the poor cluster ¡ASTROBJ¿A1983¡/ASTROBJ¿. *A&A*, 408:1–16, September 2003. doi: 10.1051/0004-6361:20030844. 115, 128

G. W. Pratt, H. Böhringer, J. H. Croston, M. Arnaud, S. Borgani, A. Finoguenov, and R. F. Temple. Temperature profiles of a representative sample of nearby X-ray galaxy clusters. *A&A*, 461:71–80, January 2007. doi: 10.1051/0004-6361:20065676. 112, 128

D. Proga. Numerical Simulations of Mass Outflows Driven from Accretion Disks by Radiation and Magnetic Forces. *ApJ*, 585:406–417, March 2003. doi: 10.1086/345897. 94

V. Quilis, R. G. Bower, and M. L. Balogh. Bubbles, feedback and the intracluster medium: three-dimensional hydrodynamic simulations. *MNRAS*, 328:1091–1097, December 2001. 18, 23, 25, 52, 64, 95

F. A. Rasio and S. L. Shapiro. Collisions of giant stars with compact objects - Hydrodynamical calculations. *ApJ*, 377:559–580, August 1991. doi: 10.1086/170385. 73

M. Rauch, M. G. Haehnelt, and M. Steinmetz. QSO Metal Absorption Systems at High Redshift and the Signature of Hierarchical Galaxy Formation. *ApJ*, 481:601–+, May 1997. doi: 10.1086/304085. 122

P. Rebusco, E. Churazov, H. Böhringer, and W. Forman. Impact of stochastic gas motions on galaxy cluster abundance profiles. *MNRAS*, 359:1041–1048, May 2005. doi: 10.1111/j.1365-2966.2005.08965.x. 59

C. S. Reynolds, B. McKernan, A. C. Fabian, J. M. Stone, and J. C. Vernaleo. Buoyant radio lobes in a viscous intracluster medium. *MNRAS*, 357:242–250, February 2005. doi: 10.1111/j.1365-2966.2005.08643.x. 32, 60, 64, 91

A. G. Riess, L.-G. Strolger, J. Tonry, S. Casertano, H. C. Ferguson, B. Mobasher, P. Challis, A. V. Filippenko, S. Jha, W. Li, R. Chornock, R. P. Kirshner, B. Leibundgut, M. Dickinson, M. Livio, M. Giavalisco, C. C. Steidel, T. Benítez, and Z. Tsvetanov. Type Ia Supernova Discoveries at $z > 1$ from the Hubble Space Telescope: Evidence for Past Deceleration and Constraints on Dark Energy Evolution. *ApJ*, 607:665–687, June 2004. doi: 10.1086/383612. 8

H. Riffert, H. Herold, O. Flebbe, and H. Ruder. Numerical aspects of the smoothed particle hydrodynamics method for simulating accretion disks. *Computer Physics Communications*, 1995. 89, 1. 66

B. Robertson, T. J. Cox, L. Hernquist, M. Franx, P. F. Hopkins, P. Martini, and V. Springel. The Fundamental Scaling Relations of Elliptical Galaxies. *ApJ*, 641:21–40, April 2006a. doi: 10.1086/500360. 95

B. Robertson, L. Hernquist, T. J. Cox, T. Di Matteo, P. F. Hopkins, P. Martini, and V. Springel. The Evolution of the M_{BH}-σ Relation. *ApJ*, 641:90–102, April 2006b. doi: 10.1086/500348. 95

J. T. Ruderman and H. Ebeling. The Origin of the Spatial Distribution of X-Ray-luminous Active Galactic Nuclei in Massive Galaxy Clusters. *ApJ*, 623:L81–L84, April 2005. doi: 10.1086/430131. 112

M. Ruszkowski and M. C. Begelman. Heating, Conduction, and Minimum Temperatures in Cooling Flows. *ApJ*, 581:223–228, December 2002. 18, 23, 95

M. Ruszkowski, M. Brüggen, and M. C. Begelman. Three-Dimensional Simulations of Viscous Dissipation in the Intracluster Medium. *ApJ*, 615:675–680, November 2004. doi: 10.1086/424702. 31, 60

P. Salomé and F. Combes. Mapping the cold molecular gas in a cooling flow cluster: Abell 1795. *A&A*, 415:L1–L5, February 2004. doi: 10.1051/0004-6361:20031744. 22

J. S. Sanders and A. C. Fabian. Spatially resolved X-ray spectroscopy of the core of the Centaurus cluster. *MNRAS*, 331:273–283, March 2002. 38, 58

A. J. R. Sanderson, A. Finoguenov, and J. J. Mohr. Possible AGN Shock Heating in the Cool-Core Galaxy Cluster Abell 478. *ApJ*, 630:191–205, September 2005. doi: 10.1086/431750. 27

A. J. R. Sanderson, T. J. Ponman, and E. O'Sullivan. A statistically selected Chandra sample of 20 galaxy clusters - I. Temperature and cooling time profiles. *MNRAS*, 372: 1496–1508, November 2006. doi: 10.1111/j.1365-2966.2006.10956.x. 112, 114, 128

C. L. Sarazin. *X-ray emission from clusters of galaxies*. Cambridge Astrophysics Series, Cambridge: Cambridge University Press, 1988, 1988. 42, 62, 63

C. Scannapieco, P. B. Tissera, S. D. M. White, and V. Springel. Feedback and metal enrichment in cosmological smoothed particle hydrodynamics simulations - I. A model for chemical enrichment. *MNRAS*, 364:552–564, December 2005. doi: 10.1111/j.1365-2966.2005.09574.x. 117

C. Schäfer, R. Speith, M. Hipp, and W. Kley. Simulations of planet-disc interactions using Smoothed Particle Hydrodynamics. *A&A*, 418:325–335, April 2004. doi: 10.1051/0004-6361:20034034. 65, 89

J. Schaye, M. Rauch, W. L. W. Sargent, and T.-S. Kim. The Detection of Oxygen in the Low-Density Intergalactic Medium. *ApJ*, 541:L1–L4, September 2000. doi: 10.1086/312892. 122

A. A. Schekochihin and S. C. Cowley. Turbulence and Magnetic Fields in Astrophysical Plasmas. *ArXiv Astrophysics e-prints*, July 2005. 59

P. A. G. Scheuer. Models of extragalactic radio sources with a continuous energy supply from a central object. *MNRAS*, 166:513–528, March 1974. 100

P. Schuecker, R. R. Caldwell, H. Böhringer, C. A. Collins, L. Guzzo, and N. N. Weinberg. Observational constraints on general relativistic energy conditions, cosmic matter density and dark energy from X-ray clusters of galaxies and type-Ia supernovae. *A&A*, 402: 53–63, April 2003. doi: 10.1051/0004-6361:20030197. 8

P. Schuecker, A. Finoguenov, F. Miniati, H. Böhringer, and U. G. Briel. Probing turbulence in the Coma galaxy cluster. *A&A*, 426:387–397, November 2004. doi: 10.1051/0004-6361: 20041039. 59, 87, 88

N. I. Shakura and R. A. Sunyaev. Black holes in binary systems. Observational appearance. *A&A*, 24:337–355, 1973. 95, 98

D. Sijacki and V. Springel. Hydrodynamical simulations of cluster formation with central AGN heating. *MNRAS*, 366:397–416, February 2006. doi: 10.1111/j.1365-2966.2005. 09860.x. 64, 75, 91, 95, 96, 100, 117

J. Silk and M. J. Rees. Quasars and galaxy formation. *A&A*, 331:L1–L4, March 1998. 94

A. D. Sod. A Survey of Several Finite Difference Methods for Systems of Nonlinear Hyperbolic Conservation Laws. *Journal of Computational Physics*, 1978. 27, 1-31. 72

D. N. Spergel, L. Verde, H. V. Peiris, E. Komatsu, M. R. Nolta, C. L. Bennett, M. Halpern, G. Hinshaw, N. Jarosik, A. Kogut, M. Limon, S. S. Meyer, L. Page, G. S. Tucker, J. L. Weiland, E. Wollack, and E. L. Wright. First-Year Wilkinson Microwave Anisotropy Probe (WMAP) Observations: Determination of Cosmological Parameters. *ApJS*, 148: 175–194, September 2003. doi: 10.1086/377226. 8

D. N. Spergel, R. Bean, O. Doré, M. R. Nolta, C. L. Bennett, G. Hinshaw, N. Jarosik, E. Komatsu, L. Page, H. V. Peiris, L. Verde, C. Barnes, M. Halpern, R. S. Hill, A. Kogut, M. Limon, S. S. Meyer, N. Odegard, G. S. Tucker, J. L. Weiland, E. Wollack, and E. L. Wright. Wilkinson Microwave Anisotropy Probe (WMAP) Three Year Results: Implications for Cosmology. *ArXiv Astrophysics e-prints*, March 2006. 119

L. Spitzer. *Physics of fully ionized gases*. Plasma Physics Laboratory, Princeton University, 1962. Princeton. 59

V. Springel. The cosmological simulation code GADGET-2. *MNRAS*, 364:1105–1134, December 2005. doi: 10.1111/j.1365-2966.2005.09655.x. 19, 24, 64, 67, 96

V. Springel and L. Hernquist. Cosmological smoothed particle hydrodynamics simulations: a hybrid multiphase model for star formation. *MNRAS*, 339:289–311, February 2003a. doi: 10.1046/j.1365-8711.2003.06206.x. 19, 24, 36, 40, 47, 48, 64, 96

V. Springel and L. Hernquist. Cosmological smoothed particle hydrodynamics simulations: the entropy equation. *MNRAS*, 333:649–664, July 2002. 24, 64, 65, 96

V. Springel and L. Hernquist. The history of star formation in a Λ cold dark matter universe. *MNRAS*, 339:312–334, February 2003b. doi: 10.1046/j.1365-8711.2003.06207. x. 120

V. Springel, S. D. M. White, G. Tormen, and G. Kauffmann. Populating a cluster of galaxies - I. Results at [formmu2]z=0. *MNRAS*, 328:726–750, December 2001a. doi: 10.1046/j.1365-8711.2001.04912.x. 40

V. Springel, N. Yoshida, and S. D. M. White. GADGET: a code for collisionless and gasdynamical cosmological simulations. *New Astronomy*, 6:79–117, April 2001b. doi: 10.1016/S1384-1076(01)00042-2. 19, 24, 64, 96

V. Springel, T. Di Matteo, and L. Hernquist. Modelling feedback from stars and black holes in galaxy mergers. *MNRAS*, 361:776–794, August 2005a. doi: 10.1111/j.1365-2966.2005.09238.x. 55

V. Springel, T. Di Matteo, and L. Hernquist. Black Holes in Galaxy Mergers: The Formation of Red Elliptical Galaxies. *ApJ*, 620:L79–L82, February 2005b. doi: 10.1086/428772. 23, 55, 95

V. Springel, T. Di Matteo, and L. Hernquist. Modelling feedback from stars and black holes in galaxy mergers. *MNRAS*, 361:776–794, August 2005c. doi: 10.1111/j.1365-2966.2005.09238.x. 20, 96, 98, 133

A. T. Steffen, A. J. Barger, L. L. Cowie, R. F. Mushotzky, and Y. Yang. The Changing Active Galactic Nucleus Population. *ApJ*, 596:L23–L26, October 2003. doi: 10.1086/379142. 109

M. Steinmetz. GRAPESPH: cosmological smoothed particle hydrodynamics simulations with the special-purpose hardware GRAPE. *MNRAS*, 278:1005–1017, February 1996. 68

M. Sun and A. Vikhlinin. Revealing the Interaction between the X-Ray Gas of Starburst Galaxy UGC 6697 and the Hot Intracluster Medium of A1367. *ApJ*, 621:718–724, March 2005. doi: 10.1086/427728. 91

M. Sun, C. Jones, W. Forman, P. E. J. Nulsen, M. Donahue, and G. M. Voit. A 70 Kiloparsec X-Ray Tail in the Cluster A3627. *ApJ*, 637:L81–L84, February 2006. doi: 10.1086/500590. 91

T. Tamura, J. S. Kaastra, J. R. Peterson, F. B. S. Paerels, J. P. D. Mittaz, S. P. Trudolyubov, G. Stewart, A. C. Fabian, R. F. Mushotzky, D. H. Lumb, and Y. Ikebe. X-ray spectroscopy of the cluster of galaxies Abell 1795 with XMM-Newton. *A&A*, 365:L87–L92, January 2001. 22, 58

G. Tormen, F. R. Bouchet, and S. D. M. White. The structure and dynamical evolution of dark matter haloes. *MNRAS*, 286:865–884, April 1997. 40, 81, 107

L. Tornatore, S. Borgani, V. Springel, F. Matteucci, N. Menci, and G. Murante. Cooling and heating the intracluster medium in hydrodynamical simulations. *MNRAS*, 342:1025–1040, July 2003. 22

L. Tornatore, S. Borgani, F. Matteucci, S. Recchi, and P. Tozzi. Simulating the metal enrichment of the intracluster medium. *MNRAS*, 349:L19–L24, March 2004. doi: 10.1111/j.1365-2966.2004.07689.x. 117

P. Tozzi and C. Norman. The Evolution of X-Ray Clusters and the Entropy of the Intracluster Medium. *ApJ*, 546:63–84, January 2001. 22

S. Tremaine, K. Gebhardt, R. Bender, G. Bower, A. Dressler, S. M. Faber, A. V. Filippenko, R. Green, C. Grillmair, L. C. Ho, J. Kormendy, T. R. Lauer, J. Magorrian, J. Pinkney, and D. Richstone. The Slope of the Black Hole Mass versus Velocity Dispersion Correlation. *ApJ*, 574:740–753, August 2002. 15, 28, 94, 122, 124

Y. Ueda, M. Akiyama, K. Ohta, and T. Miyaji. Cosmological Evolution of the Hard X-Ray Active Galactic Nucleus Luminosity Function and the Origin of the Hard X-Ray Background. *ApJ*, 598:886–908, December 2003. doi: 10.1086/378940. 109

A. Vikhlinin, M. Markevitch, S. S. Murray, C. Jones, W. Forman, and L. Van Speybroeck. Chandra Temperature Profiles for a Sample of Nearby Relaxed Galaxy Clusters. *ApJ*, 628:655–672, August 2005. doi: 10.1086/431142. 112, 128

C. Vogt and T. A. Enßlin. Measuring the cluster magnetic field power spectra from Faraday rotation maps of Abell 400, Abell 2634 and Hydra A. *A&A*, 412:373–385, December 2003. doi: 10.1051/0004-6361:20031434. 59

C. Vogt and T. A. Enßlin. A Bayesian view on Faraday rotation maps Seeing the magnetic power spectra in galaxy clusters. *A&A*, 434:67–76, April 2005. doi: 10.1051/0004-6361:20041839. 59

L. M. Voigt and A. C. Fabian. Thermal conduction and reduced cooling flows in galaxy clusters. *MNRAS*, 2003. submitted (preprint astro-ph/0308352). 23

L. M. Voigt, R. W. Schmidt, A. C. Fabian, S. W. Allen, and R. M. Johnstone. Conduction and cooling flows. *MNRAS*, 335:L7–L11, September 2002. 23

G. M. Voit. Tracing cosmic evolution with clusters of galaxies. *ArXiv Astrophysics e-prints*, October 2004. astro-ph/0410173. 22

G. M. Voit and G. L. Bryan. Regulation of the X-ray luminosity of clusters of galaxies by cooling and supernova feedback. *Nature*, 414:425–427, November 2001. 22

G. M. Voit and M. Donahue. An Observationally Motivated Framework for AGN Heating of Cluster Cores. *ArXiv Astrophysics e-prints*, September 2005. astro-ph/0509176. 27

G. M. Voit, G. L. Bryan, M. L. Balogh, and R. G. Bower. Modified Entropy Models for the Intracluster Medium. *ApJ*, 576:601–624, September 2002. 22, 23

G. M. Voit, M. L. Balogh, R. G. Bower, C. G. Lacey, and G. L. Bryan. On the Origin of Intracluster Entropy. *ApJ*, 593:272–290, August 2003. 22

M. Volonteri, F. Haardt, and P. Madau. The Assembly and Merging History of Supermassive Black Holes in Hierarchical Models of Galaxy Formation. *ApJ*, 582:559–573, January 2003. doi: 10.1086/344675. 95

A. von der Linden, P. N. Best, G. Kauffmann, and S. D. M. White. How special are Brightest Group and Cluster Galaxies? *ArXiv Astrophysics e-prints*, November 2006. 118, 128

Q. D. Wang, F. Owen, and M. Ledlow. X-Raying A2125: A Large-Scale Hierarchical Complex of Galaxies and Hot Gas. *ApJ*, 611:821–834, August 2004. doi: 10.1086/422332. 91

D. A. White, A. C. Fabian, S. W. Allen, A. C. Edge, C. S. Crawford, R. M. Johnstone, G. C. Stewart, and W. Voges. A ROSAT HRI Observation of the ABELL:478 Cluster of Galaxies. *MNRAS*, 269:589–+, August 1994. 22

D. A. White, C. Jones, and W. Forman. An investigation of cooling flows and general cluster properties from an X-ray image deprojection analysis of 207 clusters of galaxies. *MNRAS*, 292:419–+, December 1997. 22

S. D. M. White, J. F. Navarro, A. E. Evrard, and C. S. Frenk. The Baryon Content of Galaxy Clusters - a Challenge to Cosmological Orthodoxy. *Nature*, 366:429–+, December 1993a. doi: 10.1038/366429a0. 16

S. D. M. White, J. F. Navarro, A. E. Evrard, and C. S. Frenk. The Baryon Content of Galaxy Clusters - a Challenge to Cosmological Orthodoxy. *Nature*, 366:429–+, December 1993b. 22

X. Wu and Y. Xue. The Effect of Radiative Cooling on the Scale Dependence of the Global Stellar and Gas Content of Groups and Clusters of Galaxies. *ApJ*, 572:L19–L22, June 2002. 23

N. Yoshida, R. K. Sheth, and A. Diaferio. Non-Gaussian cosmic microwave background temperature fluctuations from peculiar velocities of clusters. *MNRAS*, 328:669–677, December 2001. 40, 81, 107

N. Yoshida, F. Stoehr, V. Springel, and S. D. M. White. Gas cooling in simulations of the formation of the galaxy population. *MNRAS*, 335:762–772, September 2002. 23

Q. Yu and S. Tremaine. Observational constraints on growth of massive black holes. *MNRAS*, 335:965–976, October 2002. doi: 10.1046/j.1365-8711.2002.05532.x. 121, 128

N. L. Zakamska and R. Narayan. Models of Galaxy Clusters with Thermal Conduction. *ApJ*, 582:162–169, January 2003. 23